DOE-ER-0313/63
Distribution
Categories
UC-423, -424

FUSION MATERIALS
SEMIANNUAL PROGRESS REPORT
FOR THE PERIOD ENDING

December 31, 2017

Prepared for
DOE Office of Fusion Energy Sciences
(AT 60 20 10 0)

DATE PUBLISHED: March 2018

Prepared by
OAK RIDGE NATIONAL LABORATORY
Oak Ridge, Tennessee 37831
Managed by
UT-Battelle, LLC
For the
U.S. DEPARTMENT OF ENERGY

FOREWORD

This is the sixty-third in a series of semiannual technical progress reports on fusion materials science activity supported by the Fusion Energy Sciences Program of the U.S. Department of Energy. It covers the period ending December 31, 2017. This report focuses on research addressing the effects on materials properties and performance of exposure to the neutronic, thermal and chemical environments anticipated in the chambers of fusion experiments and energy systems. This research is a major element of the national effort to establish the materials knowledge base for an economically and environmentally attractive fusion energy source. Research activities on issues related to the interaction of materials with plasmas are reported separately.

The results reported are the products of a national effort involving a number of national laboratories and universities. A large fraction of this work, particularly in relation to fission reactor irradiations, is carried out collaboratively with partners in Japan, Russia, and the European Union. The purpose of this series of reports is to provide a working technical record for the use of program participants, and to provide a means of communicating the efforts of fusion materials scientists to the broader fusion community, both nationally and worldwide.

This report has been compiled under the guidance of F. W. (Bill) Wiffen and Stephanie Melton, Oak Ridge National Laboratory. Their efforts, and the efforts of the many persons who made technical contributions, are gratefully acknowledged.

Daniel Clark
Research Division
Office of Fusion Energy Sciences

TABLE OF CONTENTS

TABLE OF CONTENTS

TABLE OF CONTENTS

TABLE OF CONTENTS

TABLE OF CONTENTS

TABLE OF CONTENTS

TABLE OF CONTENTS

TABLE OF CONTENTS

TABLE OF CONTENTS

TABLE OF CONTENTS

TABLE OF CONTENTS

TABLE OF CONTENTS

TABLE OF CONTENTS

TABLE OF CONTENTS

1. FERRITIC/MARTENSITIC STEEL DEVELOPMENT

1.1 DEVELOPMENT OF CASTABLE NANOSTRUCTURED ALLOYS AS ADVANCED RAFM STEELS—L. Tan and Y. Katoh (Oak Ridge National Laboratory), L.L. Snead (Stony Brook University)

OBJECTIVE

Castable nanostructured alloys (CNAs) are being developed at Oak Ridge National Laboratory to favor the formation of a larger amount of ultrafine stable precipitates in reduced-activation ferritic-martensitic (RAFM) steels using conventional, affordable steelmaking methods. The high density of fine precipitates is expected to improve high temperature strength and radiation resistance of the alloys. The performance of the developed CNAs is compared to the current RAFM steels and ODS-Eurofer.

SUMMARY

Six CNAs were developed as a new generation of RAFM steels, guided by computational thermodynamics to have increased MX Nano precipitates about two to three times that of the current RAFM steels, together with reduced amount of $M_{23}C_6$ precipitates. The CNAs following normalization at 1150°C for 1 h and tempering at 750°C for 1 h with air cooling were characterized by tensile and Charpy impact tests, and by microstructural examination. The six CNAs exhibited comparable yield and tensile strengths, which is significantly greater than P91 and Eurofer97 at temperatures up to 800°C and slightly higher than or comparable to ODS-Eurofer (0.3% Y_2O_3) at temperatures above ~500°C but inferior uniform and total elongation. The CNAs had upper-shelf energies up to ~2.5 times of Grade 91 and the current RAFM, with ductile-brittle transition temperatures comparable to the reference steels. Microstructural characterization indicated a significantly increased amount of MX Nano precipitates, a high density of free dislocations and refined lath structures, leading to the sink strength of CNAs close to that of ODS-Eurofer.

PROGRESS AND STATUS

Introduction

The current RAFM steels, with a limited application temperature range, have yield strength similar to but creep strength noticeably inferior to Grade 91, which is attributable to the significantly lower amount of nano precipitates in the current RAFM steels, insufficient to pin the lath boundaries during recovery processes at temperatures above 600-650°C. CNAs are being developed to favor nanoprecipitates two to three times the amount in the current RAFM steels, leading to improved performance.

Experimental Procedure

A total of six CNAs has been designed using computational thermodynamics to adjust the minor alloying elements and understand their effects on temperature-dependent phase equilibria and constituents. All the CNAs were tempered at 750°C, and the amounts of MX and $M_{23}C_6$ in mole percentages could be obtained from the calculations and converted into volume percentages. Figure 1 shows the calculated mole and volume percentages of MX and $M_{23}C_6$ phases in CNA1 through CNA6 compared with F82H, Eurofer97 and T91 after 750°C tempering, which indicates that MX in the CNAs is about two to three times that in the current RAFM steels. Charpy impact test using half-size V-notch specimens and tensile test using type SS-3 miniature specimens were conducted to screen the performance of the CNAs.

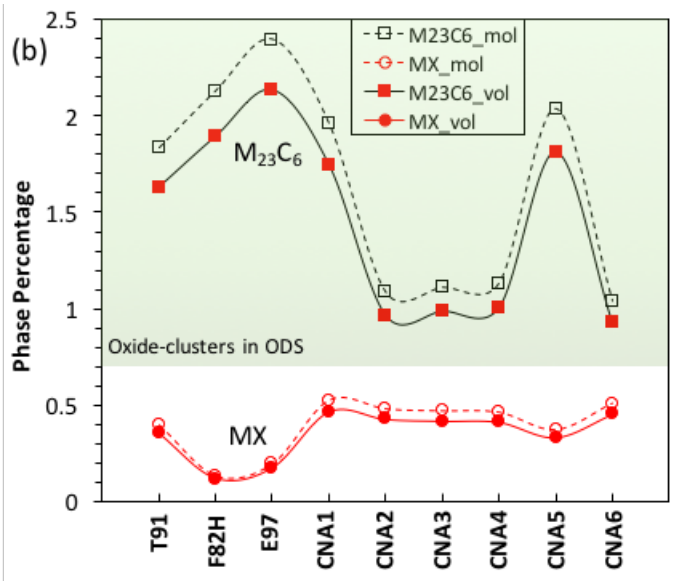

Figure 1. Calculated mole and volume percentages of MX and $M_{23}C_6$ phases in CNAs compared with F82H, Eurofer97 and T91 after tempering at 750°C.

Results

Figure 2a shows temperature-dependent Charpy absorbed energies, normalized to the nominal fracture volume of the half-size specimens of CNAs, full-size specimens of Grade 91 and Euofer97, and KLST type specimens of ODS-Eurofer. This type of normalization was found to minimize the size effects on absorbed energies (but not ductile-brittle transition temperature). The CNAs exhibited significantly increased upper-shelf energies compared to the reference steels. The ultimate tensile strength of the six CNAs, as shown in Figure 2b, are comparable, are noticeably greater than Eurofer97 and P91, and comparable to or slightly greater than ODS-Eurofer at temperatures above ~500°C.

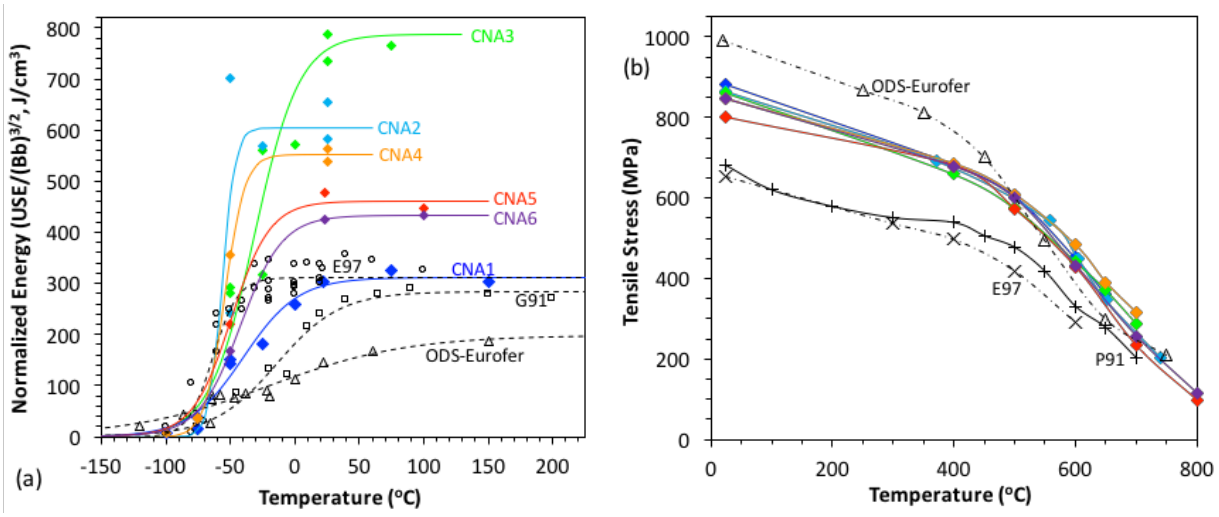

Figure 2. Temperature-dependent (a) normalized absorbed Charpy energies and (b) ultimate tensile strength of CNAs compared to Grade 91, Eurofer97 and ODS-Eurofer.

1.2 MECHANICAL PROPERTY EVOLUTION OF RAFM STEELS NEUTRON-IRRADIATED UP TO 80 DPA—Kun Wang, Kevin G. Field, Lizhen Tan, Xiang Chen, Josina W. Geringer, Yutai Katoh (Oak Ridge National Laboratory), Hideo Sakasegawa, Hiroyasu Tanigawa, Takanori Hirose (National Institutes for Quantum and Radiological Science and Technology)

OBJECTIVE

This work focuses on the post-irradiation examination (PIE) of reduced activation ferritic martensitic (RAFM) steels after neutron irradiation up to 80 dpa in High Flux Isotope Reactor (HFIR) to investigate the evolution of mechanical properties.

SUMMARY

For this reporting period the emphasis is placed on the PIE of neutron-irradiated Eurofer 97 and Oak Ridge National Laboratory {ORNL) 9Cr2WTa RAFM steels, including hardness measurement, tensile tests and fractography observation. In particular, the results of tensile tests are compared with Ni-doped ORNL 9Cr2WTa RAFM steels, to investigate the helium effects on the mechanical properties.

PROGRESS AND STATUS

Introduction

The RAFM steels are the leading candidate structural materials for fusion reactors due to their excellent resistance to void swelling and creep, as well as their good balance of physical and mechanical properties. They also have well-established commercial production and fabrication technologies. When these steels are intensively irradiated by energetic neutrons at irradiation temperatures below 400-450°C in a fusion environment, irradiation hardening accompanied with a decrease of ductility will occur. In a fusion irradiation environment, structural materials will experience production of high quantities of transmutation-induced-helium along with extensive displacement damage, which may result in additional detrimental effects on the mechanical properties. The structural materials will be exposed to 50-80 dpa high irradiation dose every full-power year in the future demonstration (DEMO) fusion reactor. However, the investigating of synergistic effect of helium and displacement damage is still difficult due to the lack of fusion neutron (14 MeV) irradiation facilities. A Ni-doping technique has been used to produce helium contents which are comparable to the helium production in fusion irradiation environment, and RAFM steels have been irradiated for over eight years in HFIR, to obtain a high irradiation dose. In this report period, Eurofer97 and ORNL 9Cr2WTa RAFM steels as well as Ni-doped ORNL 9Cr2WTa RAFM steels were irradiated at various temperatures in HFIR up to 80 dpa. Then, the PIE was conducted in order to interrogate the evolution of mechanical properties of RAFM steels at high irradiation dose and the helium effect on mechanical properties after neutron irradiation.

Experimental Procedure

Miniaturized dog bone-shaped SS-J3 flat tensile specimens with dimensions 16(L) × 4(W) × 0.75(T) mm^3 and gauge section of 5(L) × 1.2(W) × 0.75(T) mm^3 were used in this study. The irradiation conditions of Eurofer97 and (Ni-doped) ORNL 9Cr2WTa RAFM steels are shown in Table 1. The tensile specimens were irradiated in JP28&29 capsules in HFIR. The hardness measurement was performed in Mitutoyo HV120B Hardness Tester; tensile test was conducted using shoulder loading at a strain rate of 10^{-3} s^{-1} on a screw-driven machine. After tensile tests, the fractography of the specimens were observed using Japan Electron Optics Laboratory {JEOL) JSM-6010LA SEM. Hardness tester, tensile machine and Scanning Electron Microscopy {SEM} are located at the Irradiated Materials Examination and Testing (IMET) facility at ORNL.

Table 1. Irradiation parameters (dose and temperature) and testing temperatures of Eurofer97 and (Ni-doped) ORNL 9Cr2WTa irradiated in JP28&29 capsules

Materials	Irradiation dose (dpa)	Irradiation temperature (°C)	Test temperature (°C)
Eurofer97 (9Cr1.1W)	60	300	25 and 300
	50	400	25 and 400
	60	500	25 and 500
ORNL 9Cr2WTa	60	300	25 and 300
ORNL 9Cr2WTa-Ni58	80	300	25 and 300
	50	400	400
ORNL 9Cr2WTa-Ni60	80	300	25 and 300
	50	400	400

Results

Hardness measurement, tensile test and fractography observation

Three Eurofer97 specimens and one ORNL 9Cr2WTa specimen of different irradiation conditions were tested and the hardness results are shown in Table 2. We can see the obvious change of Vickers hardness depends on the radiation temperature. The values of hardness decrease with increasing irradiation temperatures at comparable irradiation dose for Eurofer97 specimens. Figure 1 presents the engineering stress-strain curves of the Eurofer97 specimens tested at RT and irradiation temperatures. All specimens exhibit significant hardening and loss of ductility compared to unirradiated specimens. However, they manifest different hardening levels and loss of ductility under different irradiation and test conditions. The specimens irradiated to 60 dpa at 300°C indicate a large degree of irradiation hardening and show the smallest total elongation tested either at RT or the irradiation temperatures. These specimens also show the smallest uniform elongation at RT (see Figure 1 (a)). While the specimens irradiated at 400°C and 500°C possess fairly large uniform elongation at RT in Figure 1 (a), the uniform elongation of all the specimens decrease to less than 1% when tested at irradiation temperatures in Figure 1 (b).

Table 2. Irradiation conditions and the results of Vickers hardness of Eurofer97 and ORNL 9Cr2WTa

Materials	Irradiation dose (dpa)	Irradiation temperature (°C)	Vickers Hardness (HV1)
Eurofer97 (9Cr1.1W)	60	300	428±19
	50	400	265±16
	60	500	245±37
ORNL 9Cr2WTa	60	300	446±4

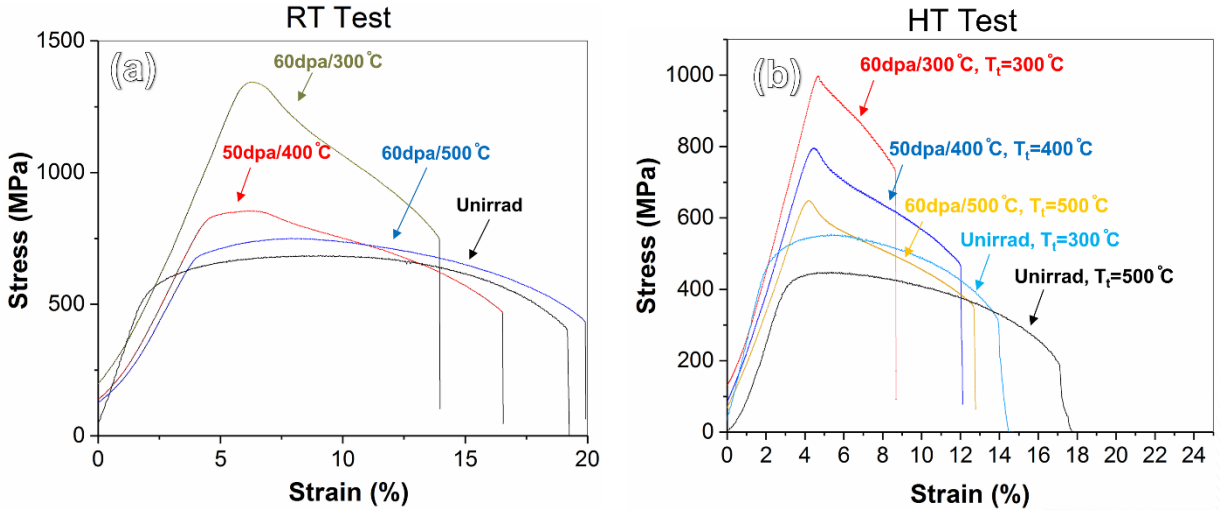

Figure 1. Tensile test results of irradiated Eurofer97 tested at RT (a) or irradiated temperatures (b).

The fracture surfaces of the irradiated Eurofer97 specimens tested at RT are shown in SEM micrographs in Figure 2. Figure 2 (a)-(c) are low magnification images of fracture surfaces of specimens irradiated at 300, 400 and 500°C respectively. Obvious necking has developed before the specimens broke. In addition, it can be seen that the secondary cracks indicated by white arrows exist on the fracture surface. The number of secondary cracks decreases with the increasing irradiation temperature. Figures 2 (d)-(f) are high magnification images of fracture surfaces of specimens irradiated at 300C, 400C and 500°C respectively. On the fracture surfaces many dimples were observed (Figures 2(d)-(f)), indicating the ductile fracture mode of these specimens. Additionally, secondary cracks can be clearly seen in these high magnification micrographs.

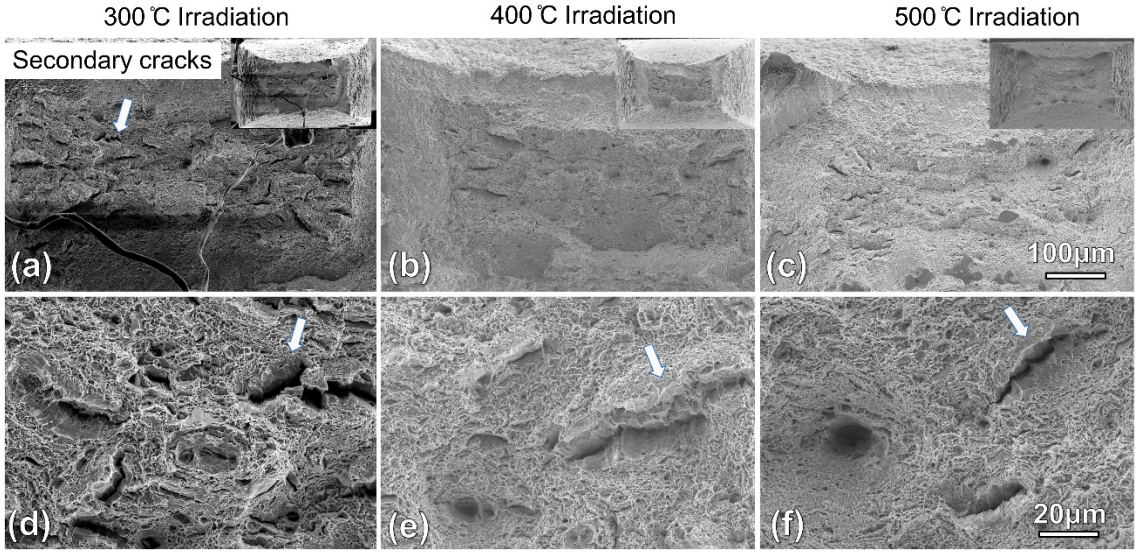

Figure 2. Low magnification (a)-(c) and high magnification (e)-(f) SEM images of fracture surfaces of Eurofer97 specimens irradiated at 300 °C ((a) and (d)), 400 °C ((b) and (e)) and 500 °C ((c) and (f)) and tested at RT.

Figure 3 shows the engineering stress-strain curves of the (Ni-doped) ORNL 9CrTaW specimens tested at RT and irradiation temperatures. All specimens exhibit significant hardening and loss of ductility compared with unirradiated specimens. All the specimens indicate immediate necking after yielding, showing plasticity instability regardless of Ni-doping or not. In particular Ni-58 doped specimens show the highest strength and smallest total elongation at RT, 300 and 400°C. Ni-60 doped specimens do not demonstrate any obvious change of hardening compared to non-doped specimens, even with the difference in the irradiation doses (80 dpa vs. 60 dpa) between Ni-60 doped ORNL 9Cr2WTa and ORNL 9Cr2WTa.

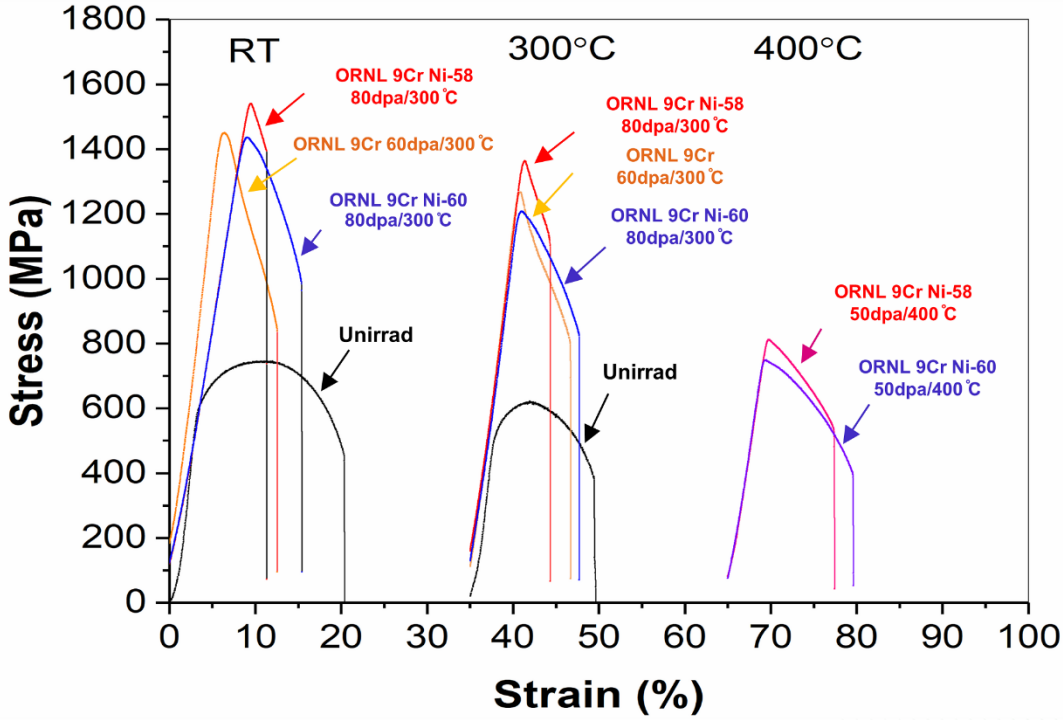

Figure 3. Tensile test results of irradiated (Ni-doped) ORNL 9Cr2WTa tested at RT or irradiated temperatures.

In order to compare the irradiation temperature effect on the irradiation hardening for all RAFM steels, the results of F82H specimens irradiated to 80 dpa and tested at the irradiation temperatures are added for comparison. While the irradiation doses of all RAFM specimens range from 50 to 80 dpa in the high irradiation dose realm, it is assumed that the irradiation hardening has already saturated at such a high range, with the irradiation dose having little effect. Figures 4 and 5 summarize the increase of yield stress and total elongation of all the RAFM steel specimens, including Eurofer97, (Ni-doped) ORNL 9Cr2WTa and (Ni-doped) F82H, irradiated at various irradiation temperatures in JP 28&29 capsules. All the specimens show irradiation hardening. The general trend is that the hardening decreases and total elongation increases with the increasing irradiation temperature in Figures 4 and 5. In Figure 4, Ni-58 doped specimens show the highest stress level compared with other specimens only at 300°C, which may be because of the extra hardening effect contributed by tiny helium bubbles. Ni-60 doped specimens present the lowest stress level at 300, 400 and 500°C. In Figure 5, Ni-60 doped specimens show the largest total elongation at 300 and 400°C, and Eurofer97 indicates the smaller total elongation compared with other RAFM steels.

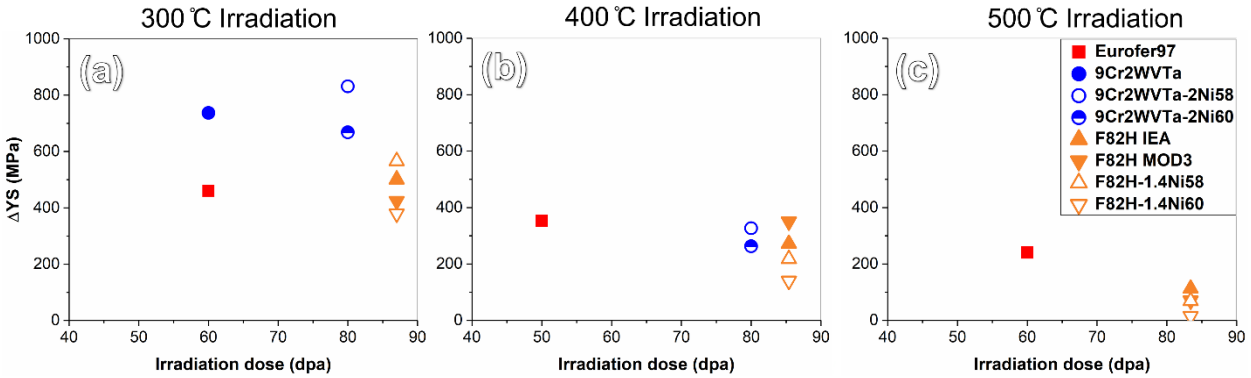

Figure 4. Summary of the increase of yield stress of all RAFM steel specimens irradiated at 300°C (a), 400°C (b) and 500°C (c) in JP 28&29 capsules.

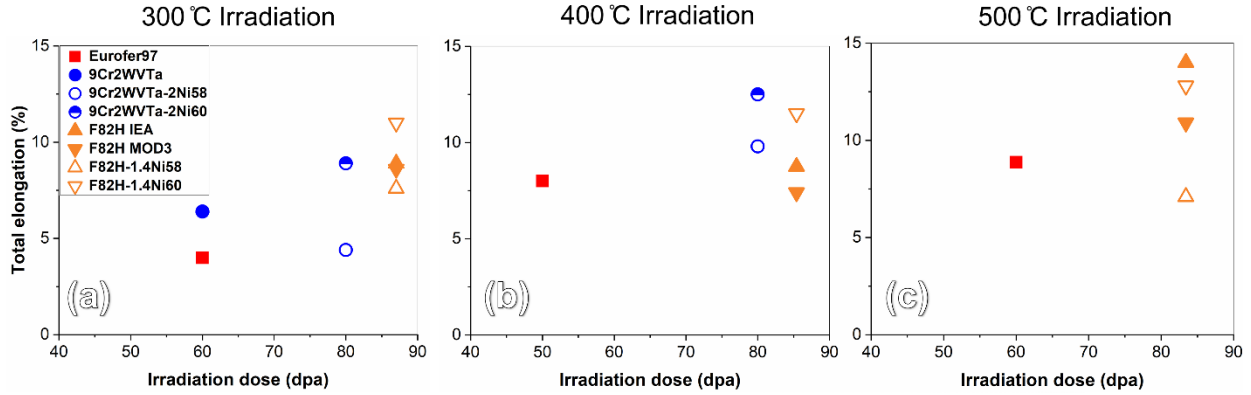

Figure 5. Summary of the total elongation of all RAFM steel specimens irradiated at 300°C (a), 400°C (b) and 500°C (c) in JP 28&29 capsules.

Summary

We have investigated the mechanical property evolution of RAFM steels irradiated up 80 dpa at temperature ranging from 300 to 500°C in HFIR. The specimens were tested at either RT or the irradiation temperature. The results of hardness measurements and tensile tests indicate irradiation hardening in all RAFM steel specimens, while the fracture surfaces still exhibit ductile mode failure. Ni-58 doped RAFM steel only show the highest strength at 300°C, implying the extra hardening induced by helium. Further TEM observations will be performed to thoroughly explore the microstructure evolution, including radiation-induced dislocation loops, cavities, element segregation, precipitation and phase stability.

1.3 PRELIMINARY ANALYSIS OF AN UPDATED IRRADIATION HARDENING 9Cr TEMPERED MARTENSITIC STEEL DATABASE—T. Yamamoto, Y. Wu, G. R. Odette (University of California, Santa Barbara)

OBJECTIVE:

The objective of this work is to expand the University of California Santa Barbara (UCSB) database on irradiation hardening and embrittlement of ≈ 9Cr martensitic steels, update hardening trend curves as and link the mechanical changes to the irradiated microstructure.

SUMMARY

We report on an updated and expanded database on 9Cr tempered martensitic steels. The database currently contains 2233 tensile, 1762 Charpy V-notch impact test, 478 fracture toughness, 264 hardness data and 644 microstructural characterization data points collected from the literature, including results from neutron (NI), spallation proton (SPI) and He ion (HI) and othe charged particle irradiations. In this report, the expanded database is used to fit phenomenological-empirical models of yield stress changes ($\Delta\sigma_y$) as a function of the NI and SPI dose (displacement-per-atom, dpa), irradiation temperature (T_i) and test temperature (T_t), with emphasis on saturation of hardening, higher T_i behavior and the effect of higher He associated with SPI effects.

PROGRESS AND STATUS

Introduction

An important objective for the fusion materials research is to develop a high quality database on the effects of irradiation on the constitutive and fracture properties of 9Cr normalized and tempered martensitic steels (TMS), in terms of irradiation embrittlement characterized by hardening and transition temperature shifts measured in sub-sized Charpy V-notch impact tests (ΔT_c) and fracture toughness tests[1,2] following NI, SPI and HI irradiations.

A high quality database is needed to develop predictive models of the changes in $\Delta\sigma_y$ and ΔT_c (and other properties) as a function of the *combination* of all the significant metallurgical and irradiation variables. The metallurgical variables include the start-of-life alloy composition (wt%), microchemistry and microstructure, including the effects of product form (weld and base metal) and thermo-mechanical processing treatment (TMT). The primary irradiation variables include T_i and the total and rates of production of damaging species, including for displacements-per-atom (dpa), helium (He), hydrogen (H) and a range of solid transmutation products (appm). Post-irradiation testing and data analysis variables are also significant. For example, $\Delta\sigma_y$ depends on the T_t and strain rate. Ultimately a comprehensive and high quality database will be analyzed with physically based, multiscale models [1,3]. Such models will sequentially relate: a) the primary variables to microstructural evolutions; b) the effects of these evolutions on fundamental structure-sensitive constitutive and local fracture properties; c) and the consequences of changes in these fundamental properties to more complex engineering properties, like ΔT_c (and shifts in fracture toughness Master Curve reference temperatures, ΔT_o) [1,3]. We have continued to accumulate tensile and other mechanical property data, especially with a large addition of data from more recent high dose irradiation experiments. Here, we report an update of our analyses of irradiation hardening, including a revised phenomenological-empirical $\Delta\sigma_y$(dpa) model.

There have been many irradiation studies aimed at contributing to such a database. Among the most notable are the International Energy Agency (IEA) round robin project on the Japanese F82H steel [4,5], a large program in Europe, primarily focusing on various heats of the Eurofer steel [6-8] and the US Automotive Materials Partnership (AMP) program as part of the US-Japan Atomic Energy Agency (JAEA) program [9] Accumuled post-irradiation examination (PIE) results on the F82H and Eurofer steels provide high quality data subset at the most common irradiation temperature of $T_i \approx 300°C$ that were treated separately and compared to correspodning trends in other alloys, including 9Cr-1Mo and 9Cr-1-2W steels and other temperature ranges. The analyses also includes results from SPI, which generate very high levels of helium and hydrogen [10-14], as well as HI experiments.

Highlights of the updated database

Our growing database now has 2233 tensile, 1762 Charpy impact, 264 hardness and 478 fracture toughness mechanical test results as well as 644 microstructural characterization data sets. Unfortunatetly many entries are not accompanied by the material, irradiation and testing information needed for extensive analysis. For example, a tensile data entry should have the yield stress (σ_y), ultimate tensile stress (σ_u), fracture stress (σ_f), uniform elongation (ε_u), total elongation (ε_t), reduction in area (RA), all linked to the stress-strain curve, for both the irradiated and unirradiated conditions. Neccesary information on the irradiation variables include T_i, the neutron flux and fluence, and the corresponding dpa rates and totals, and the accumulated He and H. The history of the irradiation conditions must also be considered. The test variables should include the specimen geomerty, T_t and strain rate (ε'). The material variables data needed include composition, product form, TMT history and, ideally, the start of life microstructure. There are few, if any, cases when all this informstion is provided.

Some data sets are aimed at providing detailed basline characterizations for common materials such as F82H and Eurofer97, as illustrated in Figure 1. Here, the red circles are baseline tensile σ_y data included in the database plotted against the test temperature [8,15-18]. The black solid line is the polynomial fit of Eurofer 97 baseline σ_y, that Lucon et al. [18] obtained for their data. There are curently a total of 1442 $\Delta\sigma_y$ data points, which is an increase of ≈ 320 since the database last report [2,19], which are used in the following trend curve analyses.

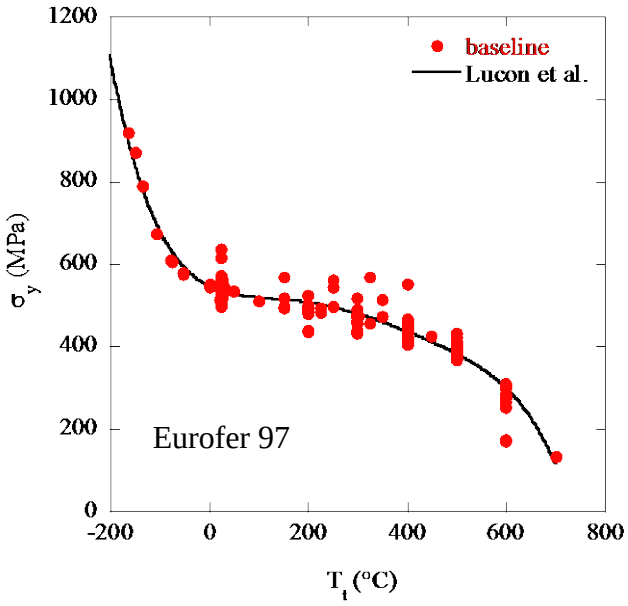

Figure 1. Eurofer97 baseline σ_y verus T_t in the database compared with $\sigma_y(T)$ fit by Lucon et al.[18].

Hardening trend curve analysis [8, 10-18, 20-89]

Hardening $\Delta\sigma_y$ vs. √dpa trends are analyzed by alloy group, irradiation type and temperature. Alloys are divided into four broad categories: a) F82H; b) Eurofer97; c) other 9CrW steels containing 1-2%W; and d) 9CrMo steels containing 0.5 to 1.5%Mo. Two irradiation types are tabulated: a) NI; and b) SPI. Data were grouped into six bins of T_i: a) 20 to 200°C; b) 220 to 280C; c) 300 to 350°C; d) 365 to 390°C; e) 400 to 440°C; and, f) 450°C or higher. Figure 2 summarizes the $\Delta\sigma_y$ - √dpa trends for the a) – f) T_i bins. As shown in the common legend for the plots, the alloy group and irradiation type is coded by color and the symbol for NI and SPI: red circles for F82H; blue squares for Eurofer97; green diamonds for other 9Cr-W steels; and purple triangles for 9Cr-Mo steels; the filled symbols show the NI results and open symbols show the SPI results. Where possible, the data were fit with the simple saturating Makin and Minter model [90,91] as,

$$\Delta\sigma_y = \Delta\sigma_{ys}[1-\exp(-dpa/dpa_o)]^p \qquad (1)$$

Here $\Delta\sigma_{ys}$ is a saturation hardening, dpa_o specifies the dose transient prior to saturation, and p is an effective dispersed-barrier hardening exponent, fixed at the theoretical value of 1/2 this case. The saturating form of Equation 1 can be physically related to the depletion of solutes, in the case of a precipitation hardening, or an excluded volume effect in the case of the accumulation of displacement damage-type defects. The initial rate of hardening is characterized by $[\Delta\sigma_{ys}/dpa_o]^{1/2}$. A simple linear hardening $\Delta\sigma_{ys}$ - $dpa^{1/2}$ fitting model was also used when applicable.

Results

Only a few a new F82H, Eurofer97 and 9Cr-Mo new data points have been added to Figure 2a for low temperature irradiations, mainly SPI data from STIP experiments. For F82H, the high He SPI produced higher hardening than NI. The data from NI and SPI overlap each other for alloys up to to ≈ 6 dpa, at a He

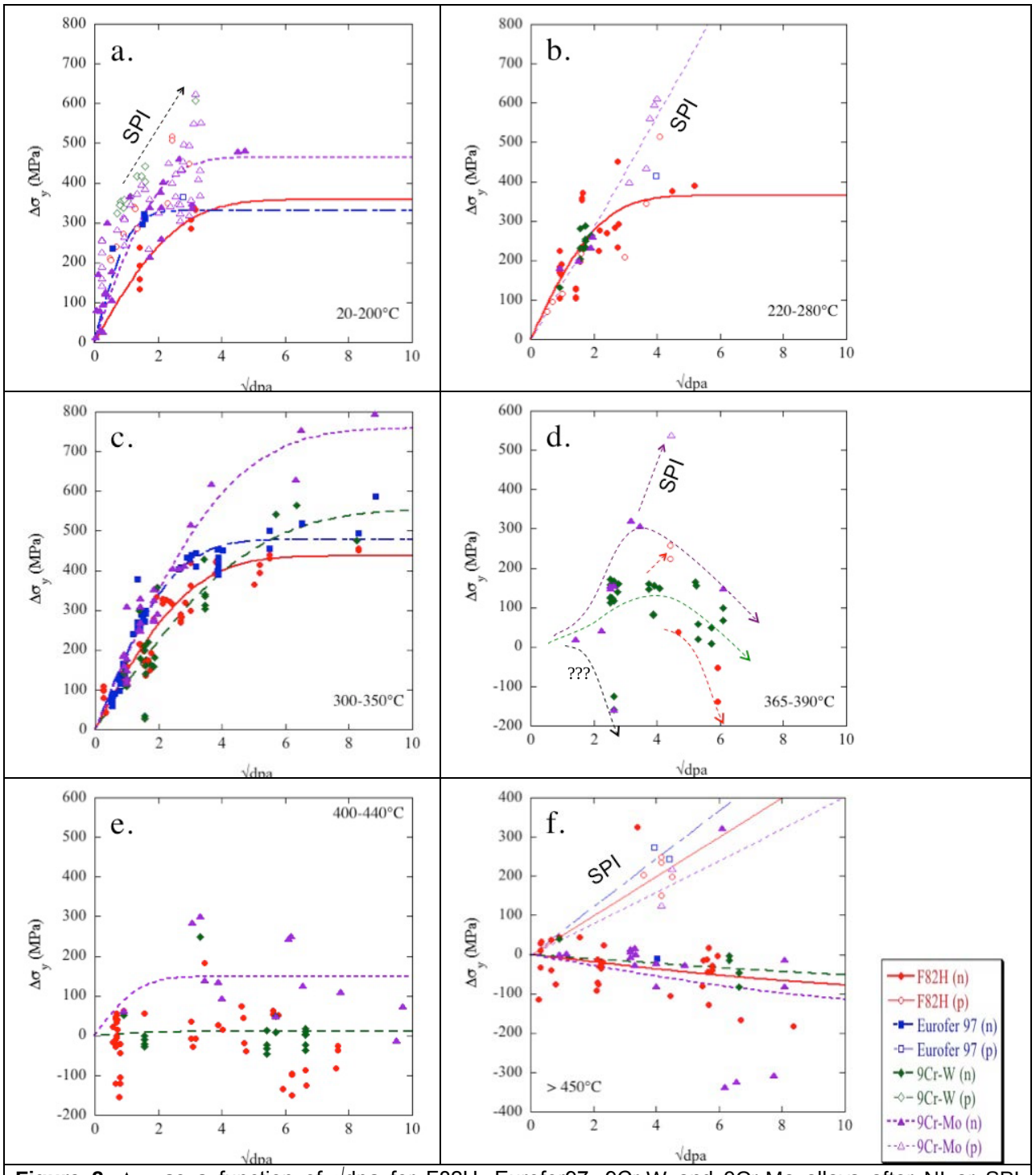

Figure 2. $\Delta\sigma_y$ as a function of √dpa for F82H, Eurofer97, 9Cr-W and 9Cr-Mo alloys after NI or SPI irradiations for T_i bins of a) RT to 200°C; b) 220 to 280°C; c) 300 to 350°C; d) 365 to 390°C; e) 400 to 440°C; and, f) ≥ 450°C.

concentration of ≈ 500 appm. Saturation of NI trends are not very obvious except the highest dpa 9Cr-Mo case. The Cr-W alloys including F82H and Eurofer97 harden less than the Cr-Mo alloys. The SPI data shows a hardening trend that continues to increase beyond the saturating fits for the NI data.

In Figure 2b for 220-280°C, new NI data up to ≈ 30 dpa have been added for F82H that more obviously show a saturation hardening of ≈ 380 MPa. For the other alloys NI data are available only at lower pre saturation dpa, where NI trends for all the alloys are similar. In contrast, SPI data availabe up to 16 dpa of F82H, Eurofer 97 and 9Cr-Mo alloys again show a general trend of higher continuing increases in $\Delta\sigma_y$ at a hardening rate of ≈ 140 MPa/dpa$^{1/2}$.

The 300-350°C bin shown in Figure 2c, where irradiation hardening and resulting embrittilement have been most extensively studied, a larger number of data points have been added to extend maximum dose from ≈ 25 dpa in the the previous database to ≈ 80 dpa. The updated data more clearly show saturation of $\Delta\sigma_{ys}$ at ≈ 436 ± 18 MPa, 479 ± 13 MPa, 555 ± 68 MPa and 760 ± 38 MPa for F82H, Eurofer97, 9Cr-W and 9Cr-Mo, respectively. Notably these saturation $\Delta\sigma_{ys}$ have been revised upwards from our previous analyses, that gave $\Delta\sigma_{ys}$ ≈ 404 ± 48 MPa for all the alloys.

Figure 2d, for the 365-390°C bin, shows apparent softening in all the alloys following an initial hardening peak at ≈ 15 dpa for NI. Note the lines are simply to guide the eye, including upper and lower bounds of the $\Delta\sigma_{ys}$ trends. However, the large softening at low dose in the 9Cr-Mo steels seems somewhat problematic. The reason for softening following peak hardening is not understood, but may in part be due to large uncertainties in a region very dependent on T_i. The few SPI data points at ≈ 20 dpa for 9CrMo and F82H again show much larger hardening than the corresponding NI condition, suggesting strong He effects.

Figure 2e, for the 400-440°C bin, shows similar, but less pronounced hardening-softening NI trends, that also might be viewed as simple large scatter in the results. The 9Cr-Mo alloys again show the largest hardening, while the 9Cr-W show little hardening and the F82H begin to soften at ≈ 36 dpa.

The T_i ≥ 450°C data shown in Figure 2f, also indicate softening for NI of all the alloy groups (with the exception of anomalously high hardening for two F82H points at ≈ 10 dpa), The softening is generally gradual and monotonic, except for one 9Cr-Mo alloy between 36 and 64 dpa, where it is very large. The avarage softening rate is ≈ 1.3 ± 0.7 MPa/dpa for these alloys. In stark contrast, SPI produces a large amount of hardening at ≈ 18 ± 2 dpa and ≈ 1500 ± 250 appm He even in the highest temperature bin

In the previous analysis, a dataset for F82H and Eurofer 97 at 300°C irradiations was used to derive a high quality hardening trend curves with a relatively small amount of scatter. More recent higher dose irradiations of these alloys are available only at 325°C, thus we combined the two Ti (filled and unfilled symbols respectively). The datasets for are well aligned where they overlap. The fitted curves show $\Delta\sigma_{ys}$ of 461 ± 24 MPa, 549 ±19 and 746 ± 42 for F82H, Eurofer 97 and 9Cr-Mo, respectively. The dpa_o ≈ 10 ± 3 dpa at ≈ 80% of saturation is similar for all the alloys.

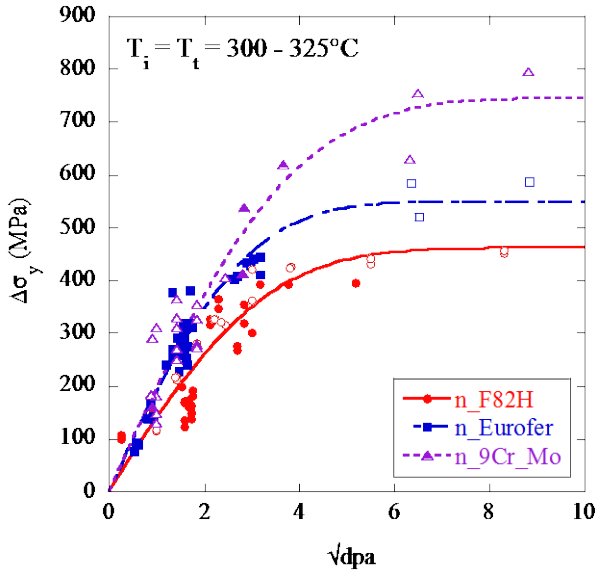

Figure 3. The √dpa dependence of $\Delta\sigma_y$ at $T_i \approx 300$ (filled symbols) and ≈ 325 (open symbols) for F82H, Eurofer 97, and 9Cr-1Mo steels.

Future Research

A large microstrocture database, that has and continues to be constucted, will be combined with the mechanical property data to develop physically based hardening models.

Acknowledgements

The authors explicitly acknowledge the extensive research that produced the data analyzed in this report and thank the researches cited in the references for their major contributions to the development of materials for fusion energy.

References

[1] G.R. Odette, T. Yamamoto, H.J. Rathbun, M.Y. He, M.L. Hribernik, J.W. Rensman, J. Nucl. Mater. 323 (2003) 313.

[2] T. Yamamoto, G. R. Odette, H. Kishimoto, J-W. Rensman and P. Miao, *J. Nucl. Mater.* 356 (2006) 27.

[3] G.R. Odette, B.D. Wirth, D.J. Bacon, N.M. Ghoniem, MRS Bull. (2001) 176.

[4] K. Shiba, A. Hishinuma, A. Toyama, K. Masamura, "Properties of the reduced activation ferritic steel F82H IEA heat," (in Japanese) JAERI-Tech 97-038.

[5] K. Shiba, M. Suzuki, A. Hishinuma, J. Nucl. Mater. 233-237 (1996) 309.

[6] H.E. Hofmans, "Tensile and impact properties of Eurofer97 plate and Bar," NRG Petten 200023/00.381153/P.

[7] J. Rensman H.E. Hofmans, E.W. Schuring, J. van Hoepen, J.B.M. Bakker, R. den Boef, F.P. van den Broek, E.D.L. van Essen, J. Nucl. Mater. 307-311 (2002)250.

[8] J-W. Rensman, "NRG Irradiation Testing: Report on 300ºC and 60ºC Irradiated RAFM Steels," NRG Petten 20023/05.68497/P (2005).

[9] R.J. Kurtz, R.H. Jones, E.E. Bloom, A.F. Rowcliffe, D.L. Smith, G.R. Odette, F.W. Wiffen, Nucl. Fusion 39 (1999) 2055.
[10] K. Farrell, T.S. Byun, J. Nucl. Mater. 296 (2001) 129.
[11] J. Henry, X. Averty, Y. Dai, P. Lamagnére, J. P. Pizzanelli, J. J. Espinas, P. Wident, J. Nucl. Mater. 318 (2003) 215.
[12] S.A. Maloy, M.R. James, G. Willicutt, W.F. Sommer, M. Sokolov, L.L. Snead, M.L. Hamilton, F. Garner, J. Nucl. Mater. 296 (2001) 119.
[13] Y. Dai,X. J. Jia, K. Farrell, J. Nucl. Mater. 318 (2003) 192.
[14] X. Jia, Y. Dai, J. Nucl. Mater. 323 (2003) 360.
[15] J-W. Rensman, H.E. Hofmann, E.W. Schuring, J. van Hoepen, J.B.M. Bakker, R. den Boef, F.P. van den Broek, E.D.L. van Essen, J. Nucl. Mater. 307-311 (2002) 250.
[16] J. Rensman, E. Lucon, J. Boskeljon, J. van Hoepen,R. den Boef, P. ten Pierick, J. Nucl. Mater. 329–333 (2004) 1113.
[17] C. Petersen, A. Povstyanko, V. Prokhorov, A. Fedoseev, O. Makarov, M. Walter, J. Nucl. Mater. 386–388 (2009) 299.
[18] E. Lucon and W. Vandermeulen, "Overview and Critical Assessment of the Tensile Properties of unirradiated and irradiated EUROFER97," SCK•CEN-BLG-1042 (2007).
[19] T. Yamamoto, G.R. Odette, M. Salston, P. Miao, Y. Dai, Transactions of American Nuclear Society vol. 98 (2008) 1111.
[20] A. Kimura, T. Morimura, M. Narui, H. Matsui, J. Nucl. Mater. 233-237 (1996) 319.
[21] P. Spätig, R. Schaublin, S. Gyger, M. Victoria, J. Nucl. Mater. 258-263 (1998) 1345.
[22] Rowcliffe, A.F., Robertson, J.P., Klueh, R.L., Shiba, K., Alexander, D.J., Grossbeck, M.L., Jitsukawa, S., J. Nucl. Mater. 258-263 (1998) 1275.
[23] V.V. Rybin, I.P. Kursevich, A.N. Lapin, J. Nucl. Mater. 258-263 (1998) 1324.
[24] Y. Kohno, A. Kohyama, T. Hirose, M.L. Hamilton and M. Narui, J. Nucl. Mater. 271&272 (1999) 145.
[25] A. Alamo, M. Horsten, X. Averty, E. I. Materna-Morris, M. Rieth, J. C. Brachet, J. Nucl. Mater. 283-287 (2000) 353.
[26] I.V. Gorynin, V.V. Rybin, I.P. Kursevich, A.N. Lapin, E.V. Nesterova, E. Y. Klepikov, J. Nucl. Mater. 283-287 (2000) 465.
[27] R.L. Klueh, M. Sokolov, K. Shiba, Y. Miwa, J.P. Robertson, J. Nucl. Mater. 283-287 (2000) 478.
[28] Y. Dai, S. A. Maloy, G. S. Bauer, W. F. Sommer, J. Nucl. Mater. 283-287 (2000) 513.
[29] R. L. Klueh, J.J. Kai, D.J. Alexander, J. Nucl. Mater. 225 (1995) 175.
[30] R.L. Klueh, D.J. Alexander in "Recent Advances in Fracture Recent Advances in Fracture" TMS, Warrendale, PA, USA (1997) 339.
[31] E.I. Materna-Morris, M. Rieth, K. Ehrlich, Effects of Radiation on Materials: 19th International Symposium, ASTM STP 1366 (2001) 597.
[32] E.V. van Osch, M.G. Horsten, G.E. Lucas, G.R. Odette, Effects of Radiation on Materials: 19th International Symposium, ASTM STP 1366 (2001) 612.
[33] E.V. van Osch, J.B.M. Bakker, R. den Boef, J. Rensman, NRG Petten 20023/99.26974/P
[34] R.L. Klueh, J. Alexander, ASTM STP 1325 (1999) 911.
[35] J. Rensman, J van Hoepen, J.B.M. Bakker, R. den Boef, F.P. van den Broek, E.D.L. van Essen, J. Nucl. Mater. 307-311 (2002) 245.
[36] E.I. Materna-Morris, H.-C. Schneider, B. Dafferner, R. Roll, O. Romer, "Irradiation Influences on Mechanical Properties and Structures of Martensitic Low-Activation Alloys," presented in ICFRM-10.
[37] K. Shiba, personal communication.
[38] H. Kurishita, H. Kayano, M. Narui, A. Kimura, M.L. Hamilton, D.S. Gelles, J. Nucl. Mater. 212-215 (1994)730.
[39] R.L. Klueh, P.J. Matiasz, M. Vitek, J. Nucl. Mater. 141-143 (1986) 960-965.
[40] A. Kohyama, H. Matsui, K. Hamada, H. Simidzu, J. Nucl. Mater. 155-157 (1988) 896.
[41] R. L. Klueh, J. Nucl. Mater. 179-181 (1991) 728.
[42] R. L. Klueh, J. M. Vitek, M.L. Grossbeck, ASTM STP 782 (1982) 648.

[43] J. Russell Hawthorne, J. R. Reeds, J. A. Sprague, ASTM STP 870 (1985) 580.
[44] J.L. Séran, A. Alamo, A. Maillard, H. Trouron, J. C. Brachet, P. Dubuission, O. Rabouille, J. Nucl. Mater. 212-215 (1994) 588.
[45] M.A. Sokolov,IEA Ferritic-martensitic Steel Workshop, Nov. 14, 2002, Garcheing.
[46] M. A. Sokolov, R. L. Klueh, G. R. Odette, K. Shiba and H. Tanigawa, ASTM STP 1447 (2004) 408.
[47] K. Farrell, J. Nucl. Mater. 296 (2001) 129-138.
[48] J. Henry, M.H. Mathon, P. Jung, J. Nucl. Mater. 318 (2003) 249.
[49] J. Henry, J. Nucl. Mater. 318 (2003) 215-227.
[50] R.L. Klueh, P.J. Maziasz, J. Nucl. Mater. 187 (1992) 43.
[51] R.L. Klueh, J. M. Vitek, J. Nucl. Mater. 150 (1987) 272.
[52] K. Farrell, T. S. Byun, J. Nucl. Mater. 318 (2003) 274.
[53] J.L. Séran, V. Lévy, P. Dubisson, D. Gilbon, A. Maillard, A. Fissolo, H. Touron, R. Cauvin, A. Chalony, E. Le Boulbin, ASTM STP1125 (1992) 1209.
[54] R.L. Klueh, J.M. Vitek, J. Nucl. Mater. 132 (1985) 27.
[55] R. L. Klueh, J. Nucl. Mater. 132 (1989) 13.
[56] E. Lucon, M. Decréton, E. van Walle, Fusion Engineering and Design 69 (2003) 373.
[57] M.B. Toloczko, M.L. Hamilton, S.A. Maloy, J. Nucl. Mater. 318 (2003) 200.
[58] A.Alamo, V.Lambard, X.Averty and M.H.Mathon, J. Nucl. Mater. 329-333 (2004) 333.
[59] E. Lucon, R.Chaouadi and M Decreton, J. Nucl. Mater. 329-333 (2004) 1078.
[60] N.Baluc, R.Schaublin, P.Spätig and M.Victoria, ASTM STP 1447 (2004) 341.
[61] M. A. Sokolov, R. L. Klueh, G. R. Odette, K. Shiba and H. Tanigawa, ASTM STP 1447 (2004) 408.
[62] J. Rensman, F. Schmalz et al., "Irradiation Effects in Martensitic Steels under Neutron and Proton Mixed Spectrum," SPIRE, 20564/04.62317/P (2004).
[63] Y. Dai, X. Jia, S.A. Maloy, J. Nucl. Mater. 343 (2005) 241-246.
[64] E. Lucon, A. Almazouzi, "Mechanical Response to Irradiation at 200ºC for EM10, T91, and HT9," SCK-CEN-BLG-986 (2004).
[65] Tavassoli, et al., J. Nucl. Mater. 329-333 (2004) 257-262.
[66] S.A. Maloy, et al., J. Nucl. Mater. 341 (2005) 141-147.
[67] A. Alamo, "Preliminary results of irradiation experiment performed in OSIRIS Reactor at 325°C," IEA workshop, JAERI Tokyo, Japan, 3-4 November 1997, 256.
[68] T.S. Byun et al., J. Nucl. Mater. 303 (2002) 34.
[69] A. Alamo, J. Nucl. Mater. 367 (2007) 54.
[70] R. Klueh, et al., J. Nucl. Mater. 357 (2006) 156.
[71] R.L. Klueh and M.K. Sokolov, J. Nucl. Mater. 367-370 (2007) 102.
[72] M.A. Sokolov, et al., J. Nucl. Mater. 367-370 (2007) 68.
[73] R.L. Klueh, M.A. Sokolov, N. Hashimoto, J. Nucl. Mater. 374 (2008) 220.
[74] F. Kazuyuki, W. Eiichi, M. Kenji, A. Masato, S. Masayoshi, J. Nucl. Mater. 367-370 (2007) 494.
[75] J. Henry, X. Averty, Y. Dai, J.P. Pizzanelli, J. Nucl. Mater. 377 (2008) 80.
[76] R.K. Nanstad, D.A. McClintock, D.T. Hoelzer, L. Tan, T.R. Allen, J. Nucl. Mater. 392 (2009) 331.
[77] T. Zhang, C. Vieh, K. Wang, Y. Dai, J. Nucl. Mater. 450 (2014) 48.
[78] N. Ilchuk, P. Spaetig, G.R. Odette, J. Nucl. Mater. 442 (2013) S58.
[79] E. Materna-Morris, A. Moeslang, H.C. Schneider, J. Nucl. Mater. 442 (2013) S62.
[80] B. Long, Y. Dai, N. Baluc, J. Nucl. Mater. 431 (2012) 85.
[81] E. Gaganidze, C. Petersen, E. Materna-Morris, C. Dethloff, O.J. Weiss, J. Aktaa, A. Povstyanko, A. Fedoseev, O. Makarov, V. Prokhorov, J. Nucl. Mater. 417 (2011) 93.
[82] J. Henry, X. Averty, A. Alamo, J. Nucl. Mater. 417 (2011) 99.
[83] P. Hosemann, E. Stergar, L. Peng, Y. Dai, S.A. Maloy, M.A. Pouchon, K. Shiba, D. Hamaguchi, H. Leitner, J. Nucl. Mater. 417 (2011) 274.
[84] J. Aktaa, C. Petersen, J. Nucl. Mater. 417 (2011) 1123.
[85] Z. Tong, Y. Dai, J. Nucl. Mater. 398 (2010) 43.
[86] H. Tanigawa, R.L. Klueh, N. Hashimoto, M.A. Sokolov, J. Nucl. Mater. 386-88 (2009) 231.
[87] E. Lucon, A. Leenaers, W. Vandermeulen, Fusion Eng.Des., 83 (2008) 620.
[88] R.L. Klueh, D.J. Alexander, J. Nucl. Mater. 212–215 (1994) 736.
[89] R.L. Klueh, D.J. Alexander and P.J. Maziasz, J. Nucl. Mater. 186 (1992) 185.

[90] M.J. Makin, A.D. Whapham, F.J. Minter, Philos. Mag. 7(74) (1962) 285.
[91] M.J. Makin, F.J. Minter, Acta. Metall. Mater. 8 (10) (1960) 691.

1.4 MICROSTRUCTURE BASED PREDICTIONS OF HARDENING IN Fe – 3- to 18%Cr BINARY MODEL ALLOYS IRRADIATED IN THE ATR REACTOR—T. Yamamoto, P. Wells, G. R. Odette (University of California, Santa Barbara), D. Bhattacharyya (Australian Nuclear Science and Technology Organization)

OBJECTIVE

The objective is to develop well calibrated physically based models to predict changes in mechanical properties of irradiated alloys based on microstructural observations, in this case, to predict yield stress ($\Delta\sigma_y$) that occur under irradiation.

SUMMARY

We use a database of Fe-3 to 18%Cr model alloys to derive a dispersed barrier model for irradiation hardening by α' precipitates (α'), solute clusters (sc), and dislocation loops (l). The key model parameters are the individual obstacle strength parameters, α_j (j = α', sc, l) of these dispersed barrier obstacles to dislocation glide. A preliminary analysis of subsets of the database showed that the loops and solute clusters are moderately strong obstacles, while the α' is a weak dislocation barrier. Thus the loop and solute cluster hardening was treated with a root sum square superposition rule, while the hardening contribution of α' was simply added following a linear sum superposition rule. A least square fits to the overall database yielded $\alpha_{\alpha'}$ = 0.031, α_l = 0.2 and α_{sc} = 0.17, with a predicted to measured standard deviation of 39 MPa. These results are compared to those derived by Bergner [1], and various sources of uncertainties are briefly discussed.

PROGRESS AND STATUS

Introduction

There is a large and evolving literature on predicting $\Delta\sigma_y$ from microstructural changes under irradiation that includes both modeling and experiment studies. The general framework is simple, involving [2[a], 3]:

1. First, calculating the hardening contribution due to individual features (j) in the irradiated microstructure that generally include dislocation loops, stacking fault tetrahedra, cavities (bubbles and voids), precipitates of various sorts, solute-defect cluster complexes, and changes in network dislocation and subgrain structures (in some cases).
2. The second step is to properly combine, or superimpose, the individual hardening contributions from the irradiation microstructure with each other, as well as with the unirradiated microstructure of the alloy.

Hardening Contributions of Individual Features

The simple dispersed obstacle approach presented here ignores a number of potential complications such as source hardening, reduction in solid solution contribution due to precipitation (although this can be easily added), hardening by impurity pick-up (such as C under irradiation), complex multi-dislocation dynamics, and so on. The individual models, based on single dislocation-obstacle interaction, can be expressed in various ways but the most frequent and simplest formulations is [3]

$$\sigma_j = M\alpha_j(r_j)Gb/(L - 2r_j). \qquad (1a)$$

Here, the spacing between the centers of the obstacles is

[a] Although published 36 years ago and dated in many details, Martin's short monograph provides a very good description of the mechanisms and models of dispersed barrier hardening and should be reviewed by those interested in the foundations of the topic addressed in this report.

$$L \approx 1/\sqrt{(2N_j r_j)} \ . \qquad (1b)$$

The N_j and r_j are the feature number density and radius, respectively. The α_j is the obstacle-dislocation interaction strength parameter, $M \approx 3.06$ term is the polycrystalline Taylor factor for bcc lattices, G is the shear modulus (≈ 82000 MPa at 25°C), and b = 0.248 nm is the dislocation Burgers vector.

For precipitates and clusters another convenient representation is

$$\sigma_j = 1.68\alpha_j(r_i)Gb\sqrt{f_j/r_j}. \qquad (2)$$

The f_j is the volume fraction of the hardening feature. In the case of network dislocations

$$\sigma_d \approx \alpha_\rho Gb\sqrt{\rho}. \qquad (3)$$

Here, ρ is the network dislocation density.

Additional corrections can be made for simplification, intrinsic to the approximate analytical model. However, the most important and uncertain parameters are the α_j. Various attempts to measure and model α_j are discussed below. But, in summary, the choice of proper value for the various α_j is not at all a settled matter.

Strength Superposition Models

The α_j varies from low values $< \approx 0.05$ for obstacles that are easily sheared by the dislocation, to $\geq \approx 0.8$ for random distributions of strong obstacles that are by passed by the Orowon bowing mechanism. The individual hardening contributions from various obstacles must be combined with one another, as well as with the various contributions from the unirradiated alloy strength. The limiting model for such superposition is a linear sum (LS) and a square root of the sum of the squares (RSS) [2-3]. The RSS law accounts for the spacing of moderate to high strength obstacles with relatively similar α_j. However, if mixtures of high and lower-strength obstacles are present, the high-strength obstacles result in larger dislocation bowing angles. The bowed, thus extended, dislocation line segments encounter more of the lower-strength obstacles than would be the case if only the latter were present. Thus, the net σ_y for mixtures of lower- and higher-strength obstacles is larger than predicted by the simple RSS law. In the limit, numerous, very low strength obstacles do not significantly change the shape of gliding dislocations; hence, they act more like a lattice friction, or long range back stress that simply add to the higher-strength obstacle contributions by an LS law. These concepts are schematically illustrated in Figure 1.

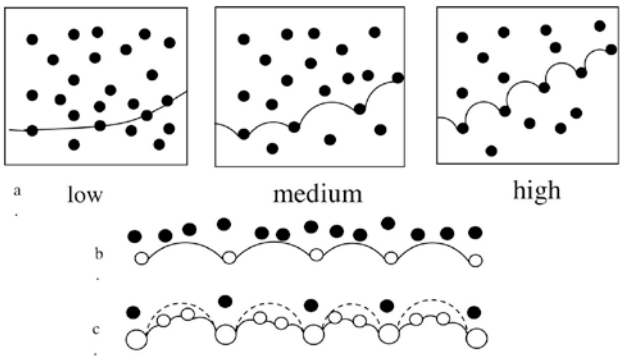

Figure 1. Schematic illustration of the effect of the critical dislocation-bowing angle on strength superposition. (a) Critical dislocation angle shapes for low-, medium- and high-strength obstacles. (b) The bowing for dislocation pinned by five medium-strength obstacles. The dislocation has not yet encountered obstacles shaded black at the critical bowing angle. (c) The dislocation bowing when high-strength obstacles have replaced the medium-strength obstacles. The dislocation is now also pinned by eight medium-strength obstacles instead of five as in Figure 1b. The dashed line shows the bowing for strong obstacles alone at the critical bowing angle.

Computer simulations have been carried out to evaluate the net $\Delta\sigma_y$ [3, 4] for various populations of obstacles with different α_j. The resulting computational database was fitted by a simple analytical model that can be used to calculate the net $\Delta\sigma_y$ based on the individual yield stress contributions from combinations of very weak ($\alpha_w < 0.05$, σ_w), medium ($0.1 < \alpha_m < 0.5$, σ_{ym}) and strong ($\alpha_s > 0.6$, σ_{ys}) obstacles. The net σ_y is given by

$$\sigma_y = \sigma_{yw} + (1\text{-}S)(\sigma_{ym}^{\ 2} + \sigma_{ys}^{\ 2})^{1/2} + S(\sigma_{ym} + \sigma_{ys}) \qquad (5)$$

Here, the superposition factor S is

$$S \approx \alpha_s - \alpha_m(5.0 - 3.3\,\alpha_s) \quad (0.05 < \alpha_m < \alpha_s) \qquad (6)$$

Thus, an RSS superposition model can approximately describe features with similar medium or high strength, while those with very different low and high strength come closer to a LS law. The superposition of the strengthening contributions from medium strength and strong obstacles falls in between. Figure 2 plots the net $\Delta\sigma_y$ ratio ($\Delta\sigma_y/\sigma_i$) versus σ_i, for $\alpha_s = 0.8$ and $\sigma_u = 200$ MPa for various α_i. Note, even for very large σ_i, the $\Delta\sigma_y/\sigma_i$ ratio approaches 1 only for low α_i.

This approach has been applied with great success to irradiation hardening of reactor pressure vessel (RPV) steels that is dominated by Cu-Mn-Ni-Si rich precipitates. The precipitate phase, composition, N, <r> and f depend on the corresponding alloy composition, temperature, fluence and other irradiation variables. In this case, the precipitates, $\alpha_i(r)$, have been measured using combination of small angle neutron scattering (SANS), and hardness or tensile test data. More recently atom probe tomography (APT) has been used to characterize these precipitates. An example of Cu-rich precipitate is shown in Figure 3a, and in Figure 3b shows precipitates that is dominated by Mn-Ni-Si phases. These curves are modified Russell-Brown models [5] fitted to the data. The results are presented in terms of $\sigma_y/\sqrt{f_p}$ versus $<r_p>$. The initial increase in $\sigma_y/\sqrt{f_p}$ is due to the dominance of the increase in $\alpha_p(r)$ with r. The decrease following the peak, at ≈ 1.25 nm, is due to the dominance of the $\sqrt{f}/r$ term in the hardening model. Molecular dynamics simulations by Bacon and Osetsky (B-O) give similar results for coherent Cu precipitates, also shown in Figure 4a [6].

Figure 4 shows predicted versus measured $\Delta\sigma_y$ for one example of many subsets of data [3]. Here, the strong Mo_2C obstacles in the unirradiated alloy are assumed to have individual strength contributions of $\sigma_y = 180$ MPa, and $\alpha_s = 0.9$. The individual irradiated precipitation hardening contributions α_i and α_i are

computed from the fitted RB model. The good predicted versus measure $\Delta\sigma_y$ requires application of the superposition model (Eqs. 5 and 6). The superposition model has been further tested by annealing studies that systematically decrease the σ_{yi}, as well as by measuring $\Delta\sigma_y$ in steels and model alloys that do not contain Mo_2C carbides, that are the dominant dislocation obstacles in unirradiated steels.

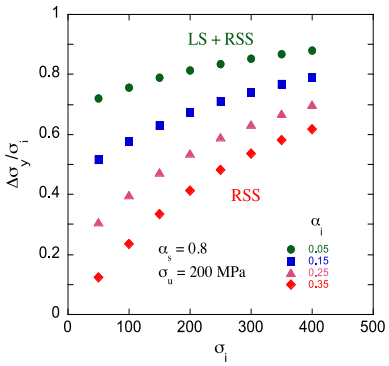

Figure 2. The net yield stress increase, $\Delta\sigma_y$, versus α_m taken as the irradiation contribution, σ_i, for α_s = 0.8 and σ_u = 200 MPa for various α_i and S

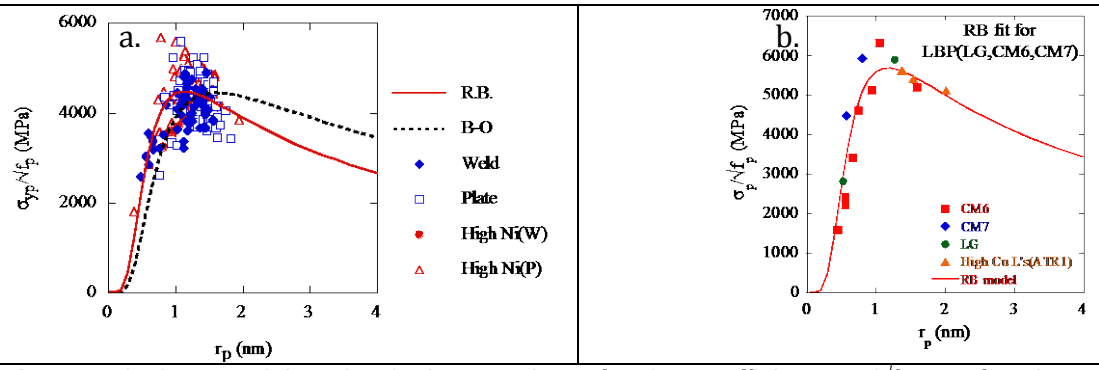

Figure 3. Isolate precipitate hardening to volume fraction coefficients, $\sigma_y/\sqrt{f}$, as a function of precipitate size for a) Cu-rich precipitate and b) Mn-Ni-Si phases.

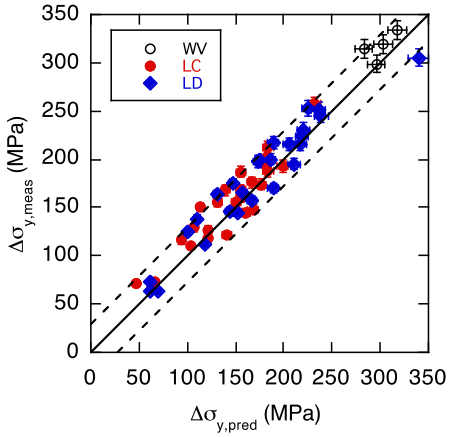

Figure 4. Measured versus predicted $\Delta\sigma_y$ from CRPs based on SANS measurements of f_p and r_p used in a modified Russell-Brown precipitate hardening and computer simulation derived superposition model with addition of weak obstacle matrix feature hardening empirically predicted from alloys with similar compositions, except that they contained little or no Cu.

Analysis of the Fe-3 to18Cr Series Hardening following Irradiation in ATR-1

The observed irradiation hardening ($\Delta\sigma_{yi}$) in the Fe-3 to 18Cr alloys provides an opportunity to evaluate the $\alpha_{\square}$ for various features formed during irradiation without the complication of pre-existing dispersed barrier obstacles (like Mo_2C precipitates and high densities of dislocations in steels). In the Fe-Cr case, the unirradiated σ_{yu} can simply be subtracted from the irradiated σ_{yi}. Figure 5 shows the microhardness increase, ΔH_{vi}, for alloys irradiated in ATR-2 to 1.8 dpa at 320°C, as a function of the alloy Cr content. The corresponding $\Delta\sigma_{yi}$ were evaluated from changes ΔH_{vi}, as $\Delta\sigma_{yi}$ (MPa) = $3.3\Delta H_{vi}$ (kg/mm^2) [7]. In this case, the irradiation hardening features generally consist of α', dislocation loops (DL) and solute clusters (SC), which form on small loops due to segregation.

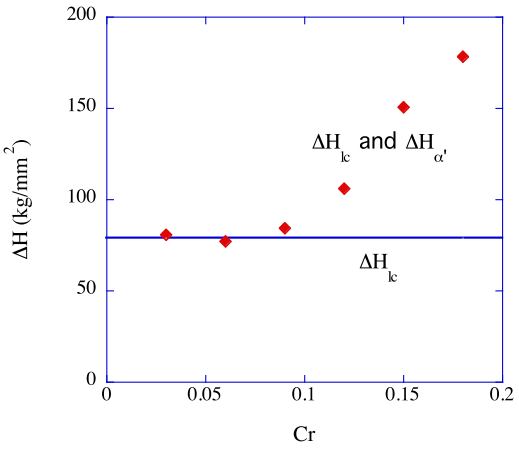

Figure 5. Hardness changes in Fe-3 to 18Cr alloys irradiated to 1.8 dpa at ≈ 320°C in UCSB ATR-1 experiment.

Table 1 summarizes hardening as well as the size and number density of dislocation loops in this work and α' precipitates, that have been previously reported by Bachhav et al. [7].

Table 1. Change in the microhardness, observed microstructure observed using APT and TEM of irradiated Fe-Cr model alloys irradiated to 1.8 dpa at 320°C in the UCSB-ATR1 experiment

Alloy	ΔH_v(kg/mm^2)	α' precipitates [8]		Dislocation loops	
		<d_p> (nm)	N_p (10^{22}m^{-3})	<d_l> (nm)	N_l (10^{22}m^{-3})
Fe-3Cr	81			5.7	4.6
Fe-6Cr	77			7.7	1.2
Fe-9Cr	84	4.8	8.5	13.1	0.112
Fe-12Cr	106	3	95	8.8	0.42
Fe-15Cr	151	2.6	320	12.4	2.2
Fe-18Cr	179	2.4	530	12.4	0.519

It is notable that the loop number densities in Table 1 are a strong function of the alloy Cr content, with a minimum at 9%Cr. This observation is somewhat puzzling, but is supported by a similar trend reported by Bergner for Fe-2.5 -12 Cr model alloys irradiated to 0.6 dpa at 290°C [1]. Note, the actual values N_l and d_l vary somewhat between the two data sets. It is most useful to examine the corresponding trends in $L = 1/\sqrt{(Nd)}$ as shown in Figure 6. The L peaks at 9%Cr in association with the corresponding minimum in N.

Various studies have reported the size and number densities of the Cr-Mn-Si-Ni-P enriched solute clusters (SC) in irradiated Fe-Cr model alloys as well as actual TMS, including: Bergner [1], Bachhav [8,9], Kuksenko [10], Field[11], Wharry [12], Pareige [13], Wu [14]. The SC is believed to be associated with

segregation to the network dislocations and loops. The reported N_{sc} and d_{sc} are scattered, as might be expected. However, the values of $L = 1/\sqrt{(N_{sc}d_{sc})}$ are reasonably consistent. For example, the L reported by Bergner averages ≈ 44.2 ± 7.5 nm, while other data sets average 66 ± 3.7 nm. Thus, here we assume a nominal value 55 nm for estimating the values of α_{sc}. Further details about the solute clusters analysis will be reported in the future.

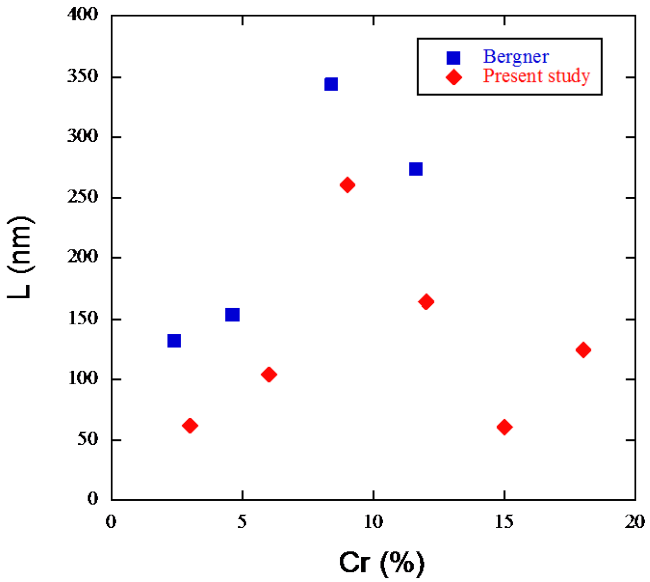

Figure 6. The dislocation loop slip plane spacing, $L_l = 1/\sqrt{Nd}$, versus Cr.

In summary, the L_l for loops in the Fe-3-18Cr model alloys varies from about 50 to 250 nm. The corresponding L_{sc} for the solute clusters is taken as 55 nm for all of the alloys. The α' obstacle spacing, $L_{\alpha'}$, ranges from 2.8 to 15.7 nm.

The hardening data was fitted to determine the corresponding strength factors α_j (j = l, sc and α'). The relatively large values of L_l and L_{sc} in the 3 and 6%Cr alloys indicate that that the contribution of the two stronger (loop and solute cluster) features should be treated with RSS superposition. In contrast, a self-consistent obstacle strength factor with a low value of $\alpha_{\alpha'}$ ≈ 0.05 was estimated from the additional hardening in the 15 an 18%Cr alloys using a LS superposition rule. Note, the lower 9 and 12%Cr alloys with α' precipitates give even lower estimates of $\alpha_{\alpha'}$.

Application of an absolute least squares fit criteria to all the data (unweighted) yielded α_l that are not physically reasonable (< 0.1). This is due to the large variation in the L_l with Cr, which is not consistent with smaller differences in the measured $\Delta\sigma_{yi}$. An average value of α_l ≈ 0.20 for the 3 and 6 Cr data is reasonably consistent with expectation. The corresponding α_{sc} is ≈ 0.17. The overall variation of the SD, α_{sc} and $\alpha_{\alpha'}$, as a function of a fixed α_l, is shown in Figure 7 for least square fits to all of the 3-18 Cr data. A fixed α_l = 0.2 results in α_{sc} = 0.174 and $\alpha_{\alpha'}$ = 0.031, with a standard deviation (SD) of 39 MPa. A larger fixed α_l = 0.25 results in α_{sc} = 0.164 and $\alpha_{\alpha'}$ = 0.029, with a standard deviation (SD) of 59 MPa. Thus α_l = 0.25 is a reasonable upper bound for our 3-18%Cr dataset.

Figure 8a shows a bar plot of the predicted and measured $\Delta\sigma_y$ along with the hardening contributions of the individual components before superposition. Figure 8b shows the corresponding scatter plot.

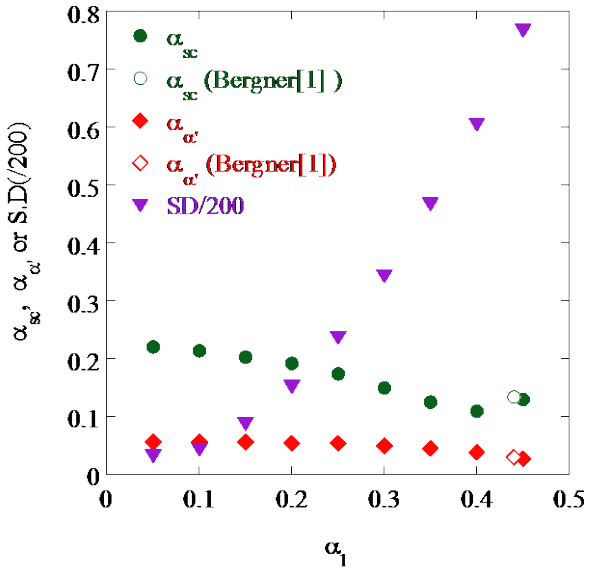

Figure 7. Variation of the standard deviation, α_{sc}, α_{I} and $\alpha_{\alpha'}$ for the least-square fitting of predicted to measured hardening.

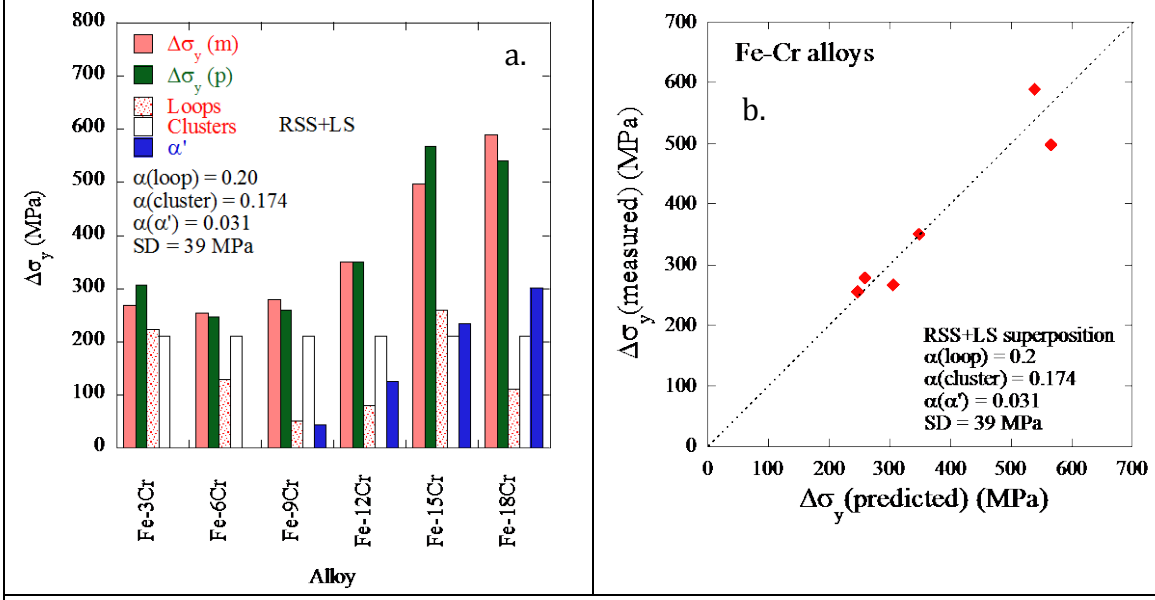

Figure 8. a) The measured and predicted $\Delta\sigma_y$, with the contributions of the individual features for α_{I} = 0.2, α_{sc} = 0.17 and $\alpha_{\alpha'}$ = 0.031; and, b) a corresponding scatter plot.

Discussion

The most comparable study was reported by Bergner et al. [1], who found α_{I} = 0.44, α_{s} = 0.13 and α_{α} = 0.03 for a RSS superposition rule applied to all of the obstacles. It is emphasized that both of these results are consistent with their corresponding data sets. Note, a full RSS model applied to our data results in least square values of $\alpha_{\alpha'}$ = 0.055 and α_{sc} = 0.19 for a fixed α_{I} = 0.2. While Bergner's values of $\alpha_{\alpha'}$ and α_{sc} are similar to those found in this study, the α_{I} = 0.44 value is highly inconsistent with the data reported in this study. This difference is largely attributed to the corresponding differences in the L_I, as shown in in Figure 6.

Finally there are a number of intrinsic sources of uncertainty in these types of analyses. As shown by Bergner, various assumptions in the analytical model used in the fitting can lead to very different results for the α_j. Further, there are uncertainties in both the microstructural (especially for the loops), and mechanical property measurements (like converting ΔH_v to $\Delta\sigma_y$).

Future Work

The approach developed here for the simple Fe 3-18%Cr binary alloys is being extended, in work underway, to modeling microstructure-property relations in multiphase-multiconstituent structural steels following neutron and charged particle irradiations, which result in additional hardening features (such as bubbles and voids as well as other precipitates), and must consider contributions to the strength contributions from features present prior to irradiation (and including their evolution under irradiation).

Acknowledgements

This work was supported by the DOE Offices of Fusion Energy Sciences and Nuclear Energy.

References

[1] F. Bergner, C. Pareige, M. Hern.ndez-Mayoral, L. Malerba, C. Heintze, “Application of a three-feature dispersed-barrier hardening model to neutron-irradiated Fe–Cr model alloys,” J. Nucl. Mater. 448 (2014) 96 – 102.

[2] J. W. Martin, Micromechanisms in Particle-Hardened Alloys, Cambridge University Press (1980).

[3] G. R. Odette, Chapter 2 - Embrittlement Mechanisms and Physical Models Underpinning the TTS Model, in the report E. E. Eason, G. R. Odette, R. K. Nanstad and T. Yamamoto, A Physically Based Correlation of Irradiation-Induced Transition Temperature Shifts for RPV Steels, Oak Ridge National Laboratory ORNL/TM-2006/530 (2007) http://www.info.ornl.gov/sites/publications/files/Pub2592.pdf.

[4] G.R. Odette, G.E. Lucas, G. Tedeski, B.D. Wirth, Development of superposition rules for hardening in alloys containing multiple defect populations, in: F.W. Wiffen (Ed.), Fusion Materials, U.S. DOE Office of Fusion Energy Sciences, Oak Ridge National Laboratory, 1998, 221**.**

[5] K.C. Russell and L.M. Brown, “A Dispersion Strengthening Model Based on Differing Elastic Moduli Applied to the Iron-Copper System”, *Acta Metallurgica* 20 (1972) 969.

[6] D.J. Bacon and Yu.N. Osetsky, “Hardening Due to Copper Precipitates in □-iron Studied by Atomic-Scale Modeling”, *Journal of Nuclear Materials* 329-333 (2004) 1233.

[7] Bachhav M, Odette GR and Marquis EA. "α' precipitation in neutron-irradiated Fe-Cr alloys", Scr. Mater. 2014;74:48–51.

[8] Bachhav M, Yao L, Odette GR and Marquis EA. "Microstructural changes in a neutron-irradiated Fe–6at.%Cr alloy", J. Nucl. Mater. 2014;453(1-3):334–339.

[9] Bachhav M, Odette GR and Marquis EA. "Microstructural changes in a neutron-irradiated Fe-15 at.%Cr alloy", J. Nucl. Mater. 2014;454(1):381–386.

[10] V. Kuksenko, C. Pareige, C. Genevois, P. Pareige, “Characterization of Cr, Si and P distribution at dislocations and grain-boundaries in neutron irradiated Fe-Cr model alloys of low purity,” J. Nucl. Mater. 434 (2013) 49-55.

[11] K.G. Field, X. Hu, K.C. Littrell, Y. Yamamoto, L.L. Snead, “Radiation tolerance of neutron-irradiated model Fe-Cr-Al alloys,” J. Nucl. Mater. 465 (2015) 746-765.

[12] J.P. Wharry, Z. Jiao, V. Shankar, J.T. Busby, G.S. Was, Gary S. “Radiation-induced segregation and phase stability in ferritic-martensitic alloy T 91,” J. Nucl. Mater. 417 (2011) 140.

[13] C. Pareige, V. Kuksenko, P. Pareige," Behaviour of P, Si, Ni impurities and Cr in self ion irradiated Fe–Cr alloys - Comparison to neutron irradiation", J. Nucl. Mater. 456 (2015) 471–476.

[14] Y. Wu et al., private communication.

1.5 WELD PROPERTY EVALUATION OF MODIFIED 3Cr-3WVTa BAINITIC STEEL—Y. Yamamoto (Oak Ridge National Laboratory)

OBJECTIVE

This work aims to develop new bainitic steels, based on 3Cr-3WV(Ta) steels originally developed at Oak Ridge National Laboratory (ORNL). The goal is mechanical properties of both base metal and weldments superior to those of existing commercial bainitic steels or ferritic-martensitic (F-M) steels, together with no requirement for post-weld heat treatment (PWHT). The target applications are high temperature structural components in fusion reactors such as vacuum vessel, structural ring which supports the blanket modules, and magnet shields, to be used at or above the 400-500ºC range. Improvement of long-term creep properties by introducing additional fine, stable second-phase dispersions, as well as maintaining good weldability, is targeted via optimization of alloy composition and thermo-mechanical heat treatment.

SUMMARY

Property evaluation of newly proposed 3Cr-3WVTa base steel with high Mn +Si and low C (ID: MSLC2) with a design strategy for PWHT-free use has been initiated. A gas tungsten arc weld (GTAW) was joined normalized-and-tempered plates of the new steel with compositionally matched weld filler metal. Cross-weld creep-rupture test results indicated that the creep-rupture occurred in the heat affected zone (HAZ) in both as-welded and PWHT specimens and the PWHT resulted in two-orders of magnitude shorter creep-rupture life than the as-welded specimen. This was due to over-tempering of the base metal in the HAZ which led to the loss of creep resistance, suggesting that the microstructural stability during welding is the key to improving the cross-weld creep properties. Another set of welded specimens made using “as-normalized” base metal prior to the weldment was prepared to give better expected microstructural stability in the HAZ and improved cross-weld properties compared to the initial result. In Charpy impact testing, the new steel exhibited temper-embrittlement after standard tempering (700°C/1h). However, over-tempering (760°C/1h) resulted in a ductile brittle transition temperature similar to the as-normalized specimens.

PROGRESS AND STATUS

Introduction

Developmental of new bainitic steels was initiated in the Fusion Materials Program in FY2014, as a modification of the original 3Cr-3WV(Ta) steels developed at ORNL [1, 2, 3]. The target applications include vacuum vessels or structural rings supporting the blanket modules in fusion reactor applications such as the conceptual US Fusion Neutron Sciences Facility (FNSF) [4]. The current alloy design strategy is to produce material usable without post-weld heat treatment (PWHT-free) to lower the capital cost of these permanent, large volume components. A potential concern in the characteristics of the PWHT-free components is the property inhomogeneity of the as-welded material across the weldment. Such inhomogeneity needs to be minimized to avoid any premature failure attributed to itself (e.g. stress concentration). To solve that potential issue, an alloy design was proposed which focused on decreasing the hardness in the normalized condition without losing the high “hardenability” to promote the carbide-free acicular bainite ferrite formation. Based on this design strategy, a steel with 2 wt.% Mn combined with 0.05% C (ID: MSLC2, shown in Table 1) was suggested with guidance from computational thermodynamics. The lab-scale heat of the steel prepared at ORNL successfully showed less hardness in the normalized condition compared to that of the original steel, whereas the hardness after tempering remained comparable to the original. The cross-weld hardness distribution in the steels also indicated a successful reduction of the hardness inhomogeneity across the weld, suggesting that the new design strategy is potentially suitable for PWHT-free behavior. A vacuum induction melted ingot (~30 kg) was commercially procured in early 2017, and then thermo-mechanically processed at ORNL to prepare a hot-rolled plate with 0.5-inch-thickness.

Table 1: Nominal compositions of original 3Cr-3WVTa and MSLC2, balanced Fe

Heat	Composition, wt.%							Remarks
	C	Mn	Si	Cr	V	W	Ta	
Original	0.10	0.40	0.16	3.0	0.2	3	0.1	3WVTa
MSLC2	0.05	2.00	0.5	3.0	0.2	3	0.1	Low C + 2Mn

As reported previously [5], creep-rupture properties of MSLC2 base metal (normalized-and-tempered, NT) at 550°C and 400-480 MPa exhibited similar creep properties to the original steel, suggesting that the high Mn addition successfully compensated for the potential creep degradation due to low carbon content. A gas tungsten arc weld (GTAW) was also produced with the NT plate with compositionally matched weld filler wire for evaluation of the cross-weld properties such as creep and Charpy impact toughness. It was found that the weld strength reduction factor of the MSLC2-NT plate was ~0.8 at 550°C, which was comparable to the low Cr steel weldments reported in the American Society of Mechanical Engineers (ASME) B31.3 [6].

In this report, the cross-weld creep properties with and without PWHT is discussed, in conjunction with the microstructure and simulated creep tests with the over-tempered base metal specimens.

Results

Figure 1 shows the creep-ruptured specimens of the cross-weld MSLC2-NT in “As-welded” and “PWHT (at 700°C for 1h)” conditions, tested at 550°C and 400MPa. The rupture lives were 272 h and 1.5 h, respectively. Both specimens ruptured not in the weld metal but relatively outside of the HAZ. The as-welded specimen showed mostly no changes in the gage diameter in both weld and base metals, and the deformation (and rupture) occurred along a very narrow region of the HAZ (so-called “inter-critical heat affected zone” or “ICHAZ”). On the other hand, the PWHT specimen exhibited large necking inside the HAZ, although the creep rupture propagated in almost the same region (i.e. ICHAZ) in the as-welded specimen. The narrow region corresponded to the base metal additionally annealed below Ac1 temperatures, the region may be equivalent to the over-tempered base metal specimen.

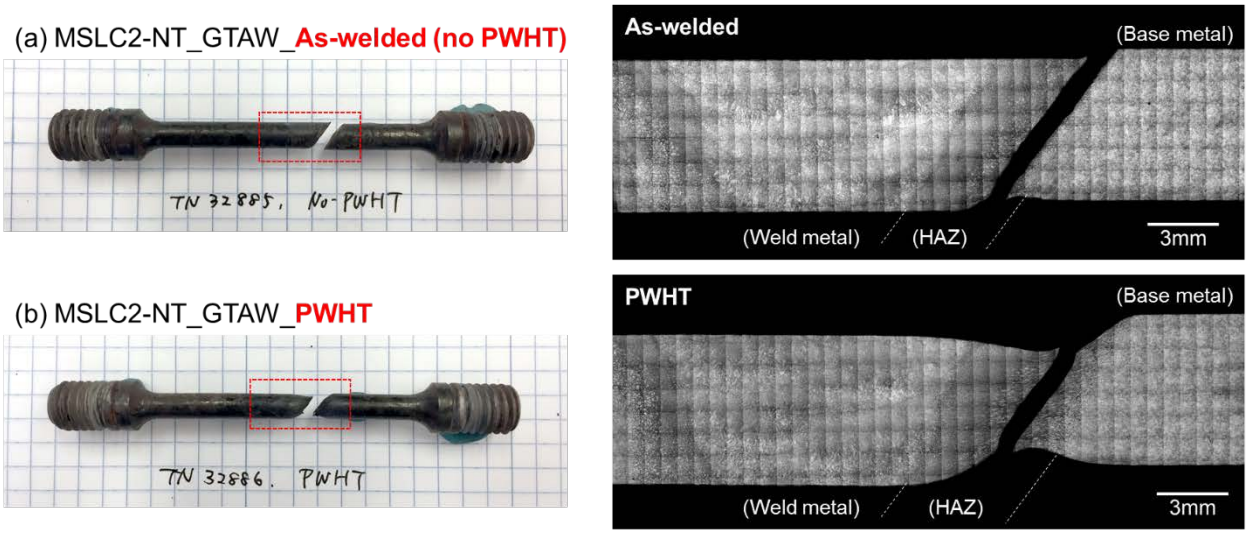

Figure 1. Cross-weld creep-rupture tested specimens of MSLC2-NT at 550°C and 400 MPa; (a) as-welded, and (b) PWHT specimens. The cross-sectional microstructures of the rupture specimens are also shown.

The creep properties of the base metals with over-tempering resulted in significantly lower creep deformation resistance. Figure 2 summarizes the effect of tempering conditions on creep-rupture life at 550°C and 400 MPa (and comparison with the cross-weld creep properties). The standard NT specimen (tempered at 700°C for 1 h) exhibited around 2200 h life at the test condition, whereas the over-tempered specimen (760°C for 1 h) showed only 7.3 h life which was similar to the rupture life of the PWHT specimen. This result indirectly indicated that the over-tempered condition at the HAZ (especially at the ICHAZ) could be the major source of creep degradation of the cross-weld specimens. Since the heat from the weldment would not be eliminated, the potential best condition of the base metal prior to welding could be non-tempered (=as-normalized) condition.

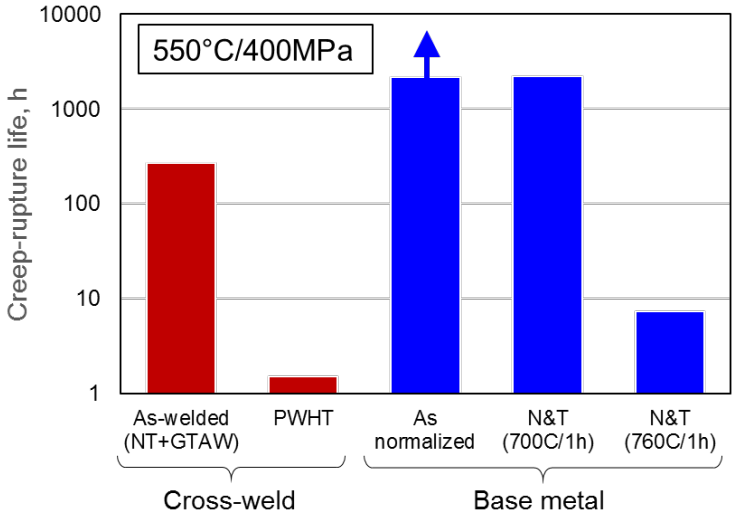

Figure 2. Comparison of creep-rupture lives of MSLC2-NT series (the cross-weld and base metals) at 550°C and 400 MPa.

Figure 3 shows the temperature dependence of Charpy impact absorbed energies of MSLC2 in as-normalized and tempered conditions. The steel was found to show “temper embrittlement” in the standard tempered conditions: the ductile brittle transition temperature (DBTT) increased from 30°C in as-normalized condition to 75°C after tempering at 700°C for 1 h. This could be due to relatively high Si content (combined with the high Mn addition) since it might cause increasing phosphorus segregation at grain boundaries to promote grain boundary cracking [7]. It is suggested that alloy modification may require as one of the potential solution, lowering the Si content. The embrittlement issue of the steel seemed to be resolved by applying over-tempering at 760°C which lowered the DBTT to 22°C. However, as discussed earlier, it would conflict with the creep property degradation.

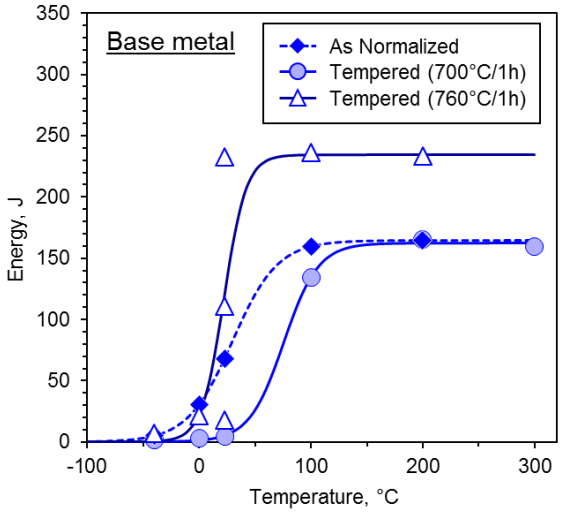

Figure 3. Charpy impact test results of MSLC2 base metal specimens in as-normalized and tempered conditions at 700°C and 760°C for 1 h.

Based on these considerations, additional property screening of the welded plate was proposed which used the "as-normalized" base metal plate to be welded. This could result in better microstructural stability at the HAZ and improved cross-weld properties compared to the initial result. Two different weld plates were prepared as shown in Figure 4: one consisted of a single-V groove weld (Plates A&B), and the other had a custom-shaped groove with one side perpendicular to the plate surface (Plates C&D). The former will be used for cross-weld creep specimens, and the latter will be machined into two different Charpy impact test specimens (ASTM E23) with the V-notch locates on the weld (TS0XW) and the HAZ (TS0XH).

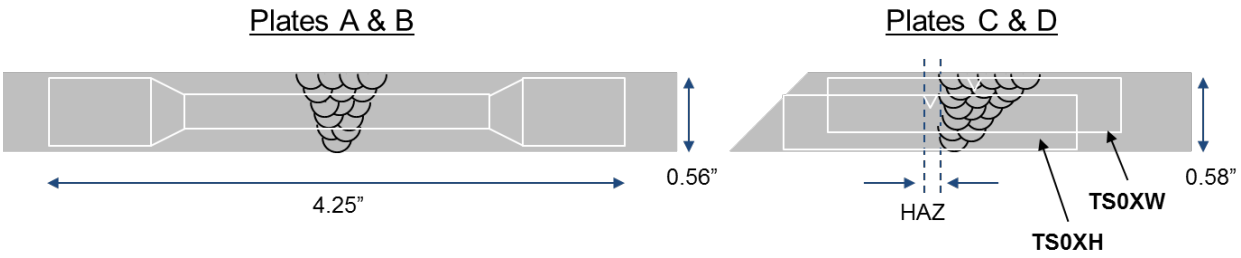

Figure 4. Schematic illustrations of two different welded plates with machining plans for cross-weld creep specimens and Charpy impact test specimens.

Cross-Sectional microstructure and the Vickers hardness distribution were characterized as shown in Figure 5. Both welded plates showed no defects from visual inspections from the surface or the cross-sectional view, and the locations of the weld metals and the HAZ could be easily defined, which helped machining the notches of the Charpy impact test specimens. The contour map of the Vickers hardness indicated the several soft bands corresponding to the tempered beads formed during multiple weld passes, although there were no other specific regions showing "abnormal" features compared to the conventional welded specimens. The specimen machining is currently in progress.

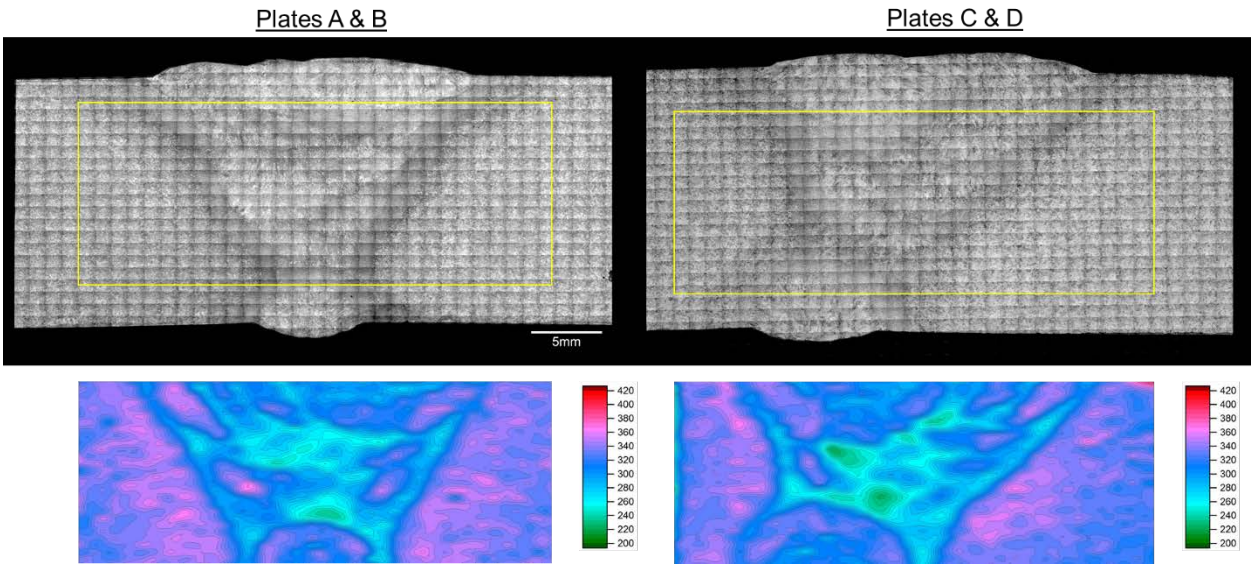

Figure 5. Cross-sectional microstructure of two different welded plates (with as-normalized base metal plates), together with contour maps of the Vickers hardness in the areas designated by the yellow boxes.

References

[1] R.L. Klueh, Elevated-Temperature Ferritic and Martensitic Steels and Their Application to Future Nuclear Reactors, ORNL/TM-2004/176, November 2004.

[2] R.L. Klueh, N.D. Evans, P.J. Maziasz, V.K. Sikka, Creep-rupture behavior of 3Cr-3W-V bainitic steels, International Journal of Pressure Vessels and Piping, 84 (2007) 29-36.

[3] M. Jawad, V.K. Sikka, Development of a New Class of Fe-3Cr-W(V) Ferritic Steels for Industrial Process Applications, ORNL/TM-2005/82, 2005, Oak Ridge National Laboratory.

[4] L. El-Guebaly, et al., Design Challenges and Activation Concerns for Aries Vacuum Vessel, FUSION SCIENCE AND TECHNOLOGY, 64 (2013) 449-454.

[5] Y. Katoh and F.W. Wiffen, ORNL Fusion Materials Program – Annual Report for FY-2017 (2017).

[6] ASME B31.3, ASME Code for Pressure Piping, the American Society of Mechanical Engineering (2008) p.18-19.

[7] J. Yu and C.J. McMahon, Jr., The Effects of Composition and Carbide Precipitation on Temper Embrittlement of 2.25Cr-1 Mo Steel- Part I1. Effects of Mn and Si, Metallurgical Transactions A, 11, (1980) 291-300.

1.6 FATIGUE PRECRACKING M4CVN TYPE STEEL SPECIMENS FOR THE EUROFusion PROJECT—X. Chen, R.L. Swain, E.T. Manneschmidt, K.D. Linton, Y. Katoh (Oak Ridge National Laboratory)

OBJECTIVE

The aim of this task is to perform fatigue pre-cracking of multi-notch bend type specimens (referred to as M4CVN specimens hereafter) for the EUROFusion project. Fatigue pre-cracking results in a sharp initial crack in the specimen, necessary for fracture toughness testing.

SUMMARY

We performed fatigue pre-cracking of M4CVN specimens for the EUROFusion project. The test materials include different variants of reduced activation ferritic and martensitic (RAFM) steels from both Europe and US for the EUROFusion project. This report summarizes fatigue pre-cracking results of the Eurofer 97 baseline material newly received from the sponsor.

PROGRESS AND STATUS

Introduction

In the EUROfusion project, the irradiation effects on transition fracture toughness of Eurofer 97 RAFM steel is one of the core required properties. To fully utilize limited irradiation volume in High Flux Isotope Reactor (HFIR), a M4CVN specimen, which enables four fracture toughness tests in one single specimen, is used. The prerequisite of transition fracture toughness testing is to create a sharp starting crack in the specimen which is realized by high frequency fatigue pre-cracking. The aim of this task is the fatigue pre-cracking on M4CVN specimens for the project. Detailed descriptions of the experimental setup, test procedures, and earlier fatigue pre-cracking results can be found in [1]. This report summarizes fatigue pre-cracking results of the newly received Eurofer 97 baseline material.

Results

The detailed fatigue pre-cracking records for all tested M4CVN specimens are listed in Table 1. The Eurofer 97 baseline material newly received from the sponsor is assigned as material Group E. The final fatigue pre-crack length for each notch was approximately 1.485 mm (0.0585 inch) corresponding to a crack length to specimen width ratio (a/W) of 0.45.

Table 1. Fatigue precracking records for M4CVN steel specimens

Specimen ID	Notch location	Stress intensity (MPa√m)	Peak load (N)	a/W ratio	Fatigue cycles
E000	L	11.9	284	0.451	332,157
	LM	11.9	262	0.450	392,811
	RM	11.9	274	0.450	338,824
	R	11.9	297	0.450	282,684
E001	L	11.9	289	0.450	283,210
	LM	11.9	277	0.450	255,198
	RM	11.9	282	0.450	279,846
	R	11.9	302	0.450	255,200
E002	L	11.9	298	0.450	246,331
	LM	11.9	276	0.451	305,871
	RM	11.9	286	0.450	264,108
	R	11.9	295	0.451	286,433

E003	L	11.9	281	0.450	298,324
	LM	11.9	276	0.450	272,421
	RM	11.9	274	0.450	287,395
	R	11.5	287	0.450	292,118
E004	L	11.5	276	0.450	308,217
	LM	11.5	266	0.450	305,662
	RM	11.5	263	0.450	285,465
	R	11.5	279	0.451	277,359
E005	L	11.5	285	0.450	318,833
	LM	11.5	280	0.450	NA*
	RM	11.5	272	0.450	291,393
	R	11.5	287	0.450	296,130
E006	L	11.5	284	0.450	301,247
	LM	11.5	271	0.450	319,546
	RM	11.5	267	0.451	303,653
	R	11.5	278	0.450	306,798
E007	L	11.5	267	0.451	346,980
	LM	11.5	269	0.450	304,103
	RM	11.5	259	0.450	336,607
	R	11.5	271	0.451	327,204
E008	L	11.5	290	0.450	323,619
	LM	11.5	271	0.450	323,371
	RM	11.5	266	0.450	332,740
	R	11.5	276	0.451	362,080
E009	L	11.5	292	0.450	282,296
	LM	11.5	289	0.450	286,674
	RM	11.5	290	0.450	273,740
	R	11.5	294	0.450	286,365
E010	L	11.5	293	0.450	317,290
	LM	11.5	280	0.451	298,915
	RM	11.5	285	0.450	297,030
	R	11.5	295	0.450	298,431
E011	L	11.5	293	0.450	353,823
	LM	11.5	278	0.450	347,865
	RM	11.5	279	0.450	336,273
	R	11.5	279	0.450	344,346
E012	L	11.5	286	0.451	336,637
	LM	11.5	280	0.450	302,253
	RM	11.5	276	0.450	318,528
	R	11.5	277	0.451	352,324
E013	L	11.5	286	0.450	311,919
	LM	11.5	275	0.450	335,477
	RM	11.5	270	0.450	335,652
	R	11.5	283	0.450	328,985
E014	L	11.5	283	0.450	342,288
	LM	11.5	290	0.450	307,418
	RM	11.5	283	0.450	322,220
	R	11.5	287	0.450	337,775
E015	L	11.5	288	0.450	322,348
	LM	11.5	267	0.450	349,889
	RM	11.5	268	0.450	320,382
	R	11.5	267	0.450	347,383

E016	L	11.5	285	0.450	317,904
	LM	11.5	279	0.450	321,379
	RM	11.5	276	0.450	331,711
	R	11.5	281	0.451	329,941
E017	L	11.5	268	0.450	370,742
	LM	11.5	244	0.450	403,092
	RM	11.5	270	0.450	360,365
	R	11.5	271	0.450	392,557
E018	L	11.5	286	0.450	320,013
	LM	11.5	276	0.451	300,657
	RM	11.5	283	0.450	299,051
	R	11.5	286	0.450	305,922
E019	L	11.5	280	0.450	314,518
	LM	11.5	260	0.451	340,401
	RM	11.5	262	0.451	328,596
	R	11.5	286	0.450	315,838
E020	L	11.5	244	0.450	485,739
	LM	12.1	267	0.450	315,445
	RM	12.1	244	0.450	379,074
	R	11.5	275	0.450	360,529
E021	L	11.5	274	0.450	341,039
	LM	11.5	267	0.450	355,514
	RM	11.5	283	0.450	296,580
	R	11.5	291	0.450	325,395
E022	L	11.5	294	0.451	316,066
	LM	11.5	290	0.450	298,875
	RM	11.5	285	0.450	320,443
	R	11.5	285	0.451	365,174
E023	L	11.5	289	0.450	372,562
	LM	11.5	289	0.450	352,561
	RM	11.5	282	0.450	357,131
	R	11.5	295	0.450	355,516
E024	L	11.5	297	0.451	416,112
	LM	11.5	267	0.450	457,603
	RM	11.5	269	0.450	454,079
	R	11.5	294	0.451	588,006**
E025	L	11.5	283	0.451	389,471
	LM	11.5	249	0.450	435,898
	RM	11.5	277	0.450	408,515
	R	11.5	275	0.453	414,509
E026	L	11.5	293	0.450	385,504
	LM	11.5	278	0.451	388,299
	RM	11.5	269	0.450	373,808
	R	11.5	278	0.450	404,289
E027	L	11.5	280	0.450	392,182
	LM	11.5	276	0.450	374,485
	RM	11.5	275	0.450	378,161
	R	11.5	274	0.450	403,417
E028	L	11.5	278	0.451	414,798
	LM	11.5	273	0.450	413,324
	RM	11.5	265	0.451	388,713
	R	11.5	276	0.450	438,748

E029	L	11.5	275	0.450	473,903
	LM	11.5	245	0.450	643,686
	RM	11.5	270	0.450	437,016
	R	11.5	276	0.450	442,488
E030	L	11.5	285	0.450	412,730
	LM	11.5	288	0.451	379,272
	RM	11.5	285	0.451	396,009
	R	11.5	288	0.450	430,345
E031	L	11.5	280	0.450	412,987
	LM	11.5	270	0.451	431,406
	RM	11.5	271	0.450	414,953
	R	11.5	277	0.450	417,140
E032	L	11.5	267	0.450	491,288
	LM	11.5	267	0.451	449,978
	RM	11.5	270	0.451	411,436
	R	11.5	290	0.450	441,377
E033	L	11.5	290	0.450	397,762
	LM	11.5	291	0.451	361,272
	RM	11.5	270	0.450	428,171
	R	11.5	282	0.450	392,259
E034	L	11.5	278	0.450	371,535
	LM	11.5	286	0.450	371,935
	RM	11.5	285	0.450	368,420
	R	11.5	295	0.451	365,744
E035	L	11.5	276	0.450	418,617
	LM	11.5	287	0.451	383,398
	RM	11.5	278	0.450	376,176
	R	11.5	285	0.450	382,759
E036	L	11.5	279	0.450	431,069
	LM	11.5	295	0.451	358,475
	RM	11.5	290	0.450	368,726
	R	11.5	279	0.450	407,278

*Total fatigue cycles were not recorded for this notch, although the test was successful
**After 180k cycles, no crack growth was observed. The specimen was then compressively loaded to 334 N and resumed fatigue cracking with normal crack growth

References

[1] Fusion Materials Semiannual Progress Report for the Period Ending June 30, 2017, DOE-ER-0313/62, September 2017.

2. ODS AND NANOCOMPOSITED ALLOY DEVELOPMENT

2.1 BASELINE APT STUDIES OF UNIRRADIATED 14YWT ARCHIVE FOR THE IN-SITU HELIUM INJECTION EXPERIMENT—Karen Kruska, Danny Edwards, Richard J. Kurtz (Pacific Northwest National Laboratory)

OBJECTIVE

The objective is to measure the oxide nanocluster distribution in unirradiated 14YWT to compare to the nanoclusters present in the 14YWT after irradiation at 500°C in the High Flux Isotope Reactor (HFIR).

SUMMARY

Atom probe tomography (APT) analysis was conducted on the unirradiated 14YWT archive material, parts of which were used for the in-situ injection helium studies (ISHI) conducted in HFIR. The analysis from three needles revealed an average Y-Ti-O cluster density of ranging from 4.4 to 8.4 x 10^{23} m^{-3} with an average size of 4.4 nm. This analysis agrees with measurements for this alloy in the unirradiated state conducted by the other researchers. Comparing the current results to those obtained from samples of 14YWT neutron irradiated to 21 dpa at 500ºC revealed no measurable changes in the size distribution or the number density of the particles.

PROGRESS AND STATUS

Introduction

Several ferritic alloys were irradiated in an ISHI experiment aimed at exploring the effects of neutron irradiation at 300, 400 and 500ºC with high levels of helium injected via transmutation of a nickel aluminide coating [1]. Recently, post-irradiation examinations (PIE) on two of the ferritic oxygen dispersion strengthened (ODS) alloys, 14YWT and 14YW (21 dpa at 500ºC with a total level of 1230 appm of helium injected over the irradiation cycle) have been presented [2]. The 14YWT analysis was taken from the neutron irradiated side of the sample, i.e. no helium was injected on that side of the sample. Both alloys are oxide dispersion strengthened 14Cr alloys containing yittria additions, the 14YWT also has 0.4 wt% Ti added to refine the oxide dispersion to less than 2 nm with densities approaching 10^{24} particles per m^3. The PIE utilized both APT and aberration-corrected scanning transmission electron microscopy (TEM) to explore the stability of the microstructure after irradiation in HFIR at 500ºC [1], focusing on the alpha prime and small nanoclusters of Y-Ti-O. As a follow-up to this work, we report here the APT analysis of the unirradiated archive 14YWT to help establish the changes in the oxide nanoclusters due to irradiation. Work on the 14YW alloy is being continued and will be reported at later date.

Experimental Procedure

The history of the 14YWT is described in detail elsewhere [3-5], and will only be briefly addressed here. The heat of 14YWT in this study is an early prototype of the nanostructured ferritic alloys that came out of the dissertation work of Aylinger [3,4] and collaborators at the University of California-Santa Barbara (UCSB) and Oak Ridge National Laboratory (ORNL), and was referred to as U14YWT in their publications. Archive material was made available by Professor Robert Odette and his team at UCSB as part of collaborative work on the irradiation effects of the alloy. The nominal composition of this alloy is provided in Table 1.

Several APT needles were extracted from an electro polished TEM disc using a Field Electron and Ion Company (FEI) Quanta 3D. Backscatter electron imaging mode was used to locate a fine-grained region as shown in Figure 1. The APT analysis was conducted in a Cameca Local Electrode Atom Probe (LEAP) 4000HR with a laser wavelength of 255 nm (UV) with a pulse energy of 60 pJ and a frequency of 125 – 250 kHz at a set temperature of 40 K. Cluster analysis was performed using the ordering points to identify the clustering structure (OPTICS) cluster search algorithm developed by Wang et al. [5].

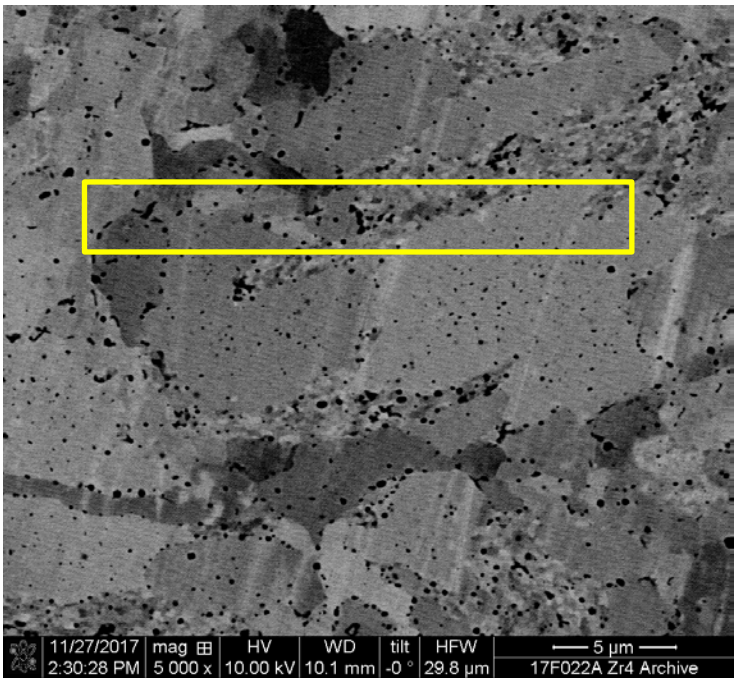

Figure 1. SEM BSE image showing the grain structure in the unirradiated 14YW archive. The APT needles were extracted from the region outlined in yellow, which effectively marks the Pt cap placed on the sample.

Table 1. Composition of 14YWT

Alloy	Composition (wt.%) with Fe balance											
	Al	**Si**	**Ti**	**Cr**	**Mn**	**Fe**	**Ni**	**Y**	**Mo**	**W**	**Re**	**Os**
14YWT	0.82	0.22	0.41	13.76	2.16	79.25	0.09	0.13	0.07	2.04	0.21	0.54

Results

Ion maps are provided in Figure 2 showing the Y-Ti-O distribution of the oxide nanoclusters in each needle based on iso-concentration surfaces of 0.6 at % Y. The spatial distribution is homogenous, and no grain boundaries or interfaces were captured in these three needles. The ion maps indicated small clusters containing Y, TiO as well as CrO ions, all of which were used for the OPTICS cluster search algorithm. The count statistics for each data set are shown in Table 2. Note some variability within the number density of nanoclusters between the three needles, but these values are typical for this class of alloys that include Ti as a particle refinement addition. These nanocluster densities match those reported by Aylinger and coworkers [3,4] based on both APT and small angle neutron scattering experiments. The proxigram taken from one of the larger particles in the one of the needles shows a one to one correlation between the Ti and Y inside the particle. A histogram showing the size distribution for 597 clusters is shown in Figure 4a. The size distribution is almost symmetrical, with an average size of 4.4±0.99 nm, which is essentially identical to the 4.1±0.93 nm measured for the irradiated 14YWT reported previously [2]. A comparison of the size distributions is provided in Figure 4b, clearly demonstrating no significant difference after irradiation to 21dpa at 500ºC.

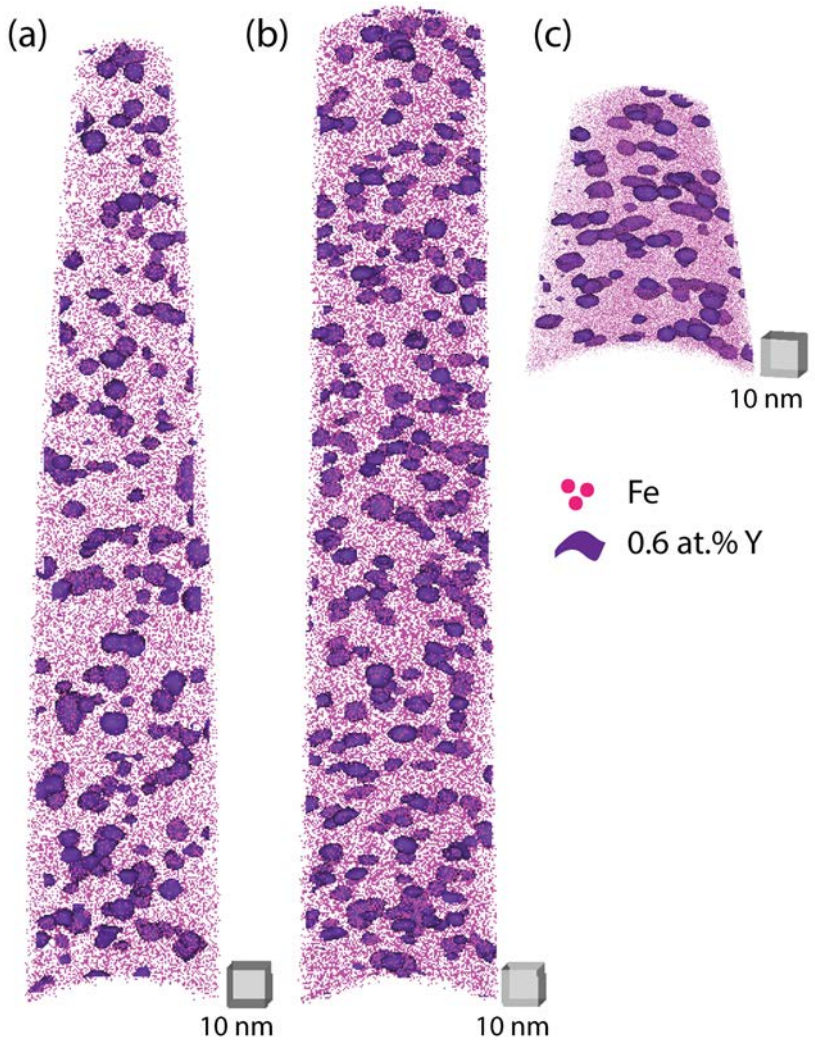

Figure 2. 3D ion maps showing the distribution of Y-Ti-Cr-oxide clusters in 3 APT datasets of unirradiated 14 YWT.

Table 2. Y-TiO-CrO cluster analysis (OPTICS)

Data set	Volume of data set (nm^3)	# of precipitates	Diameter (nm)	Density (m^{-3})
(a)	303,417	239	4.39±0.92	7.88E+23
(b)	451,113	197	4.43±0.94	4.37E+23
(c)	122,634	103	4.35±1.24	8.40E+23

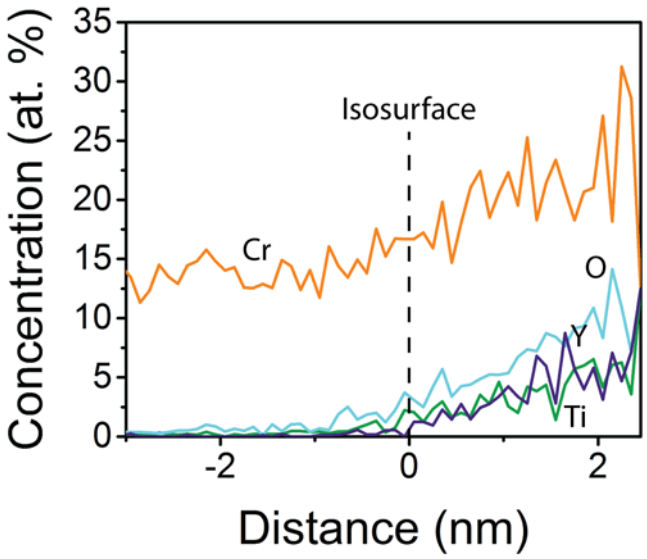

Figure 3. Typical proximity-histogram showing the composition inside one of the larger oxide clusters.

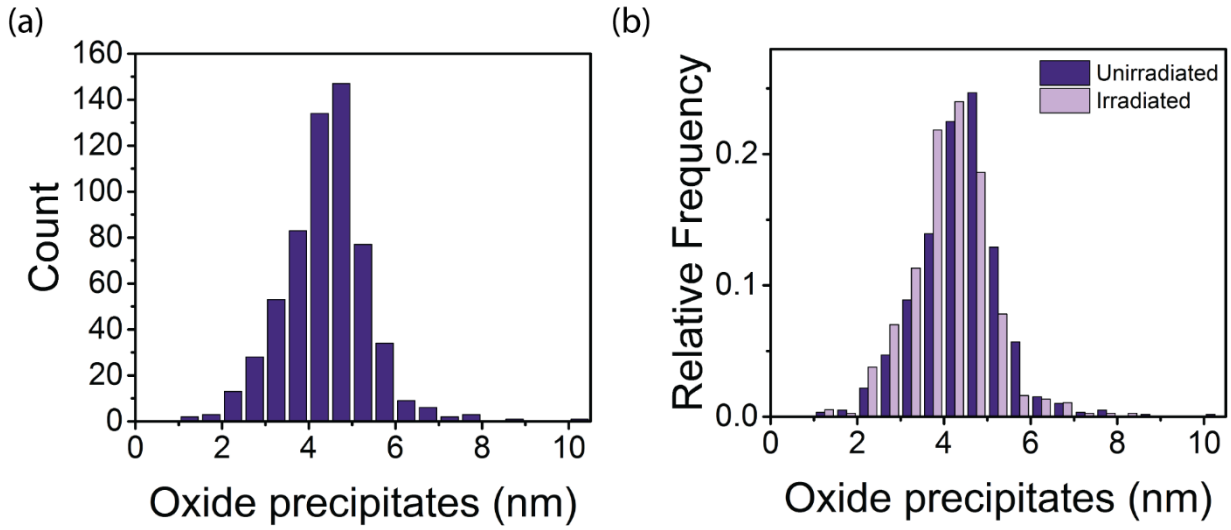

Figure 4. (a) Histogram showing the size distribution of the Y-Ti-Cr-oxide precipitates. (b) Comparison of the relative size distribution before and after neutron irradiation at 500ºC to 21 dpa (no helium injection).

Future Work

1) Complete the matrix of experiments by conducting Scanning Transmission Electron Microsope (STEM) analysis of NIO 14YW, ISHI 14YWT.
2) Explore the relationship between oxide and alpha prime distributions in regions of different gain sizes, perform a correlative STEM analysis in the same region from which 3D-APT dataset are extracted.

3) Conduct TEM imaging/STEM elemental mapping on each APT needle before it is run in the atom probe to develop a correlative analysis of the distribution of cavities, particles and α'-phase particles.
4) Comparison with the archive 14YW material following the same sampling guidelines with respect to grain characteristics.

Acknowledgements

This research was supported by Office of Fusion Energy Sciences, U.S. Department of Energy (DOE) under Contract DE-AC05-76RL01830. A portion of the research was performed using Environmental Molecular Sciences Laboratory (EMSL), a national scientific user facility sponsored by the DOE's Office of Biological and Environmental Research and located at Pacific Northwest National Laboratory (PNNL). The authors thank G. Robert Odette and staff at the UCSB for providing the archival 14YWT material used in this investigation.

References

[1] T. Yamamoto, G.R. Odette, P. Miao, D.T. Hoelzer, J. Bentley, N. Hashimoto, H. Tanigawa, R.J. Kurtz, J. Nucl. Mater. **367-370** (2007) 399.
[2] K. Kruska, D. Edwards and R.J. Kurtz, "APT and TEM characterization of α-phase Formation in Neutron Irradiated 14YW and 14YWT ODS steels Using STEM and 3D-APT", Fusion Semi-Annual Progress Report June 30 (2017) DOE/ER-0313/62.
[3] M.J. Alinger, G.R. Odette and D.T. Hoelzer, J. Nucl. Matls. **329–333** (2004) 382–386.
[4] M.J. Alinger, G.R. Odette and D.T. Hoelzer, Acta Materialia **57** (2009) 392–406.
[5] J. Wang, N. Bailey, P. Hosemann, D.K. Schreiber, J. Liu, M.B. Toloczko, Cluster Analysis in Atom Probe Tomography Data: a New Method Based on The OPTICS Algorithm, presented at Atom Probe Tomography User Meeting 2017, Madison, WI, USA.

2.2 VISCOPLASTIC SELF-CONSISTENT MODELING OF DEFORMATION PROCESSING A 14YWT NANOSTRUCTURED FERRITIC ALLOY—S. Pal, M. E. Alam, G. R. Odette (University of California Santa Barbara)

OBJECTIVE

Viscoplastic self-consistent (VPSC) modeling is used to simulate the texture development of the 14YWT NFA-1 alloy, produced by three different processing routes, and compared to experiment, in order to gain insight of the deformation processing of defect-free product forms.

SUMMARY

Orientation analysis of the texture data measured using electron backscatter diffraction (EBSD) on the hot extruded 14YWT-NFA-1 billet shows a moderate α-fiber texture with a high volume fraction of {111}<110> and {112}<110> components. Annealing and subsequent high-temperature cross-rolling of a hot extruded billet strengthens the α-fiber texture, and the highest texture intensity is shifted towards {001}<110> component. Cross-Rolling aligns a high volume fraction of {001} planes normal to the plate through-thickness direction. In contrast, subsequent hot hydrostatic extrusion of thin wall tubing weakens the α-fiber texture, and shows high texture intensities around the {111}<110> and {112}<110> α-fiber components, versus the dominant {001}<110> brittle component in the cross-rolled plate. Moreover, hot hydrostatic extrusion completely heals micro cracks. Texture evolution of α-Fe during various deformation processing steps was modeled using the VPSC code, developed by Lebarson and Tome et al. [1]. The simulated texture matches the experimental observations. The applied stress state, total strain, slip mode of bcc Fe, and interaction between the polycrystalline grains mediate the overall texture development in NFA-1. Further, τ_{32} and τ_{23} stress components play a key role in texture development.

PROGRESS AND STATUS

Introduction

Nanostructured ferritic 14YWT alloys (NFA) containing 12-14 wt. % Cr, exhibit outstanding thermal stability, an excellent strength and toughness combination, and remarkable radiation tolerance [2]. The NFAs contain ultra-high density ≈ 10^{23}-10^{24}/m^3, 2-4 nm $Y_2Ti_2O_7$ oxides along with a very high dislocation densities and predomminantly μm-sized grains [3]. However, conventional deformation processing of hot extrusions followed by cross-rolling introduces low toughness brittle cleavage texture components, leading to a large population of microcracks on planes normal to the through-thickness direction, thus running parallel to the plate faces [4,5]. Hot hydrostatic extrusion, carried out at Case Western University, successfully produces thin wall tubing from the cross-rolled plate, while eliminating the microcracks [4,6]. Texture and texture component characterization following the three different steps of deformation processing (hot extrusion, cross-rolling and hot hydrostatic extrusion) have been carried out [4,6]. Hot extrusion of a billet produces a mix of <111> (dominant) and <100> texture which transform to a large volume fraction of <100> in the normal direction (ND) of cross-rolled plates, that lead to the formation of microcracks. Notably, subsequent hydrostatic extrusion results in a dominant <111> texture in the radial direction of the tube (equivalent to ND of the plate) [4,6,7]. Clearly, the processing route has a huge impact on texture and damage developed during deformation processing.

Therefore, it is of great interest to model these processing steps in order to optimize deformation paths to produce various NFA product forms. Here, we use the crystal plasticity based VPSC modeling code to simulate the different processing routes to predict the final crystallographic texture and stress-strain response of the alloy that can be compared to experiment. Furthermore, we qualtitatively compare the experimentally observations for the three different deformation paths described above.

Materials

Three different thermo-mechanical processing routes, hot extrusion, hot cross-rolling and hot hydrostatic extrusion of NFA-1 are simulated. Experimental details have been reported elsewhere [6,7]. Figure 1 describes the sample geometry along with sample orientation with respect to the primary deformation axis.

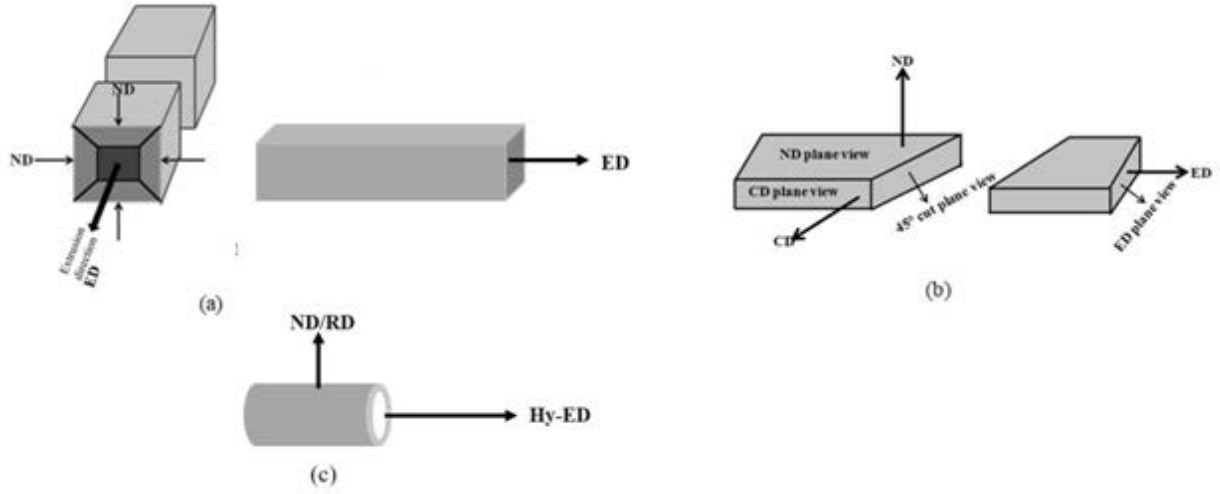

Figure 1. a) Schematic illustrations of the deformation directions and geometries of a) the extruded billet; b) cross-rolled plate; and c) hydrostatically extruded tube. The initial extrusion direction shown for all three deformation steps.

The texture was measured on the polished sections of the different orientation from the three different conditions using the EBSD technique in a Field Electron and Ion Company (FEI) Quanta Scanning Electron Microscopy (SEM) with an Oxford Instruments EBSD camera. Data collection was carried out using the HKL software. The EBSD measurements were carried out at 15kV, with a spot size of 6 and a pixel size of 50 nm. EBSD data were analyzed and plotted using the MTEX software package.

Viscoplastic self-consistent (VPSC) modeling

The macroscopic stress-strain response and texture evolution of crystalline material was modeled using the VPSC code. In this model, each grain is considered as an ellipsoidal viscoplastic inclusion, embedded in an anisotropic homogeneous effective medium, which represents the average properties of all the adjoining grains. The grain-matrix interaction is treated with the inclusion formalism proposed by Eshelby. The model is also able to calculate yield locus, Lankford parameter and material responses such as grain shape, slip, and twin activity. The details formulation of the model is described elsewhere [1]. The kinematics of the VPSC model is briefly described below.

The notation x(X) and X mark the initial and final coordinates of a point in the deformed material, where u=x-X is the total displacement of the point. The local grain and macroscopic (polycrystal) deformation are characterized by the same velocity gradient tensor (L) and deformation gradient tensor (F), defined as:

$$L = \frac{\partial u_i}{\partial x_j} \quad (1)$$

$$F = \frac{\partial x_i}{\partial X_j} \quad (2)$$

The coordinates of the displaced point can be written as

$$x = F \bullet X \tag{3}$$

The strain and rotation rates are the symmetric and skew-symmetric components of the velocity gradient tensor (L_{ij}). Since $\dot{F} = L \bullet F$, the deformation gradient can be updated incrementally by using the following equation

$$F^{New} = (F^{Old} + F'\Delta t) = (I + L\Delta t)F^{Old} \tag{4}$$

In order to determine the texture formation during plastic deformation, the initial texture of the material is subjected to appropriate stress and strain condition boundary conditions. The velocity gradient of the strain rate tensor is given by $L = \begin{pmatrix} L_{11} & L_{12} & L_{13} \\ L_{21} & L_{22} & L_{23} \\ L_{31} & L_{32} & L_{33} \end{pmatrix} \bullet \dot{\varepsilon}$, where $\dot{\varepsilon}$ is a scalar measure of the strain rate (/s). The polycrystal plasticity model calculates the material response in terms of the active slip systems, the resulting resolved stresses and strains, grain reorientation and strain hardening, etc., to predict the anisotropy and texture evolution.

In the VPSC scheme, each grain or orientation is considered as a visco-plastic inclusion embed in a homogeneous effective viscoplastic medium that represents average properties of all other grains and orientations. The response of the medium need not be known a priori; rather, it is adjusted 'self-consistently' to coincide with the average response of all the orientations constituting the aggregate. On the grain level, plastic deformation occurs through crystallographic slip at a shear strain rate of $\dot{\gamma}^s$ on a number of crystallographic slip planes (s), depending upon the critical resolved shear stress value of that particular plane τ^s. The stress and strain tensors are related through a power law plasticity rule. The macroscopic strain rate (d_{ij}) for a given grain is related to the stress tensor (σ_{ij}) by the following relation:

$$d_{ij} = \dot{\gamma_0} \sum_{s=1}^{N} m_{ij} \left(\frac{m_{kl}^s \sigma^{kl}}{\tau_0^s} \right)^n \tag{7}$$

where $\dot{\gamma_0}$ and τ_0^s are the threshold shear strain rate and stress for a slip system *s*, respectively; n is inverse the strain rate sensitivity and N is the number of slip systems. The evolution the critical threshold stress with deformation strain is predicted by the extended Voce law:

$$\tau^s(\Gamma) = \tau_0 + (\tau_1 + \theta_1 \Gamma)(1 - \exp(-\frac{\theta_0 \Gamma}{\tau_1}) \tag{8}$$

$$\text{Here } \Gamma = \int_0^t \sum_s |\dot{\gamma}^s| dt \tag{9}$$

where $\dot{\gamma}^s$ is the shear rate on slip system s. Four parameters, τ_0, τ_1, θ_0 and θ_1, contribute to the hardening on the slip system that models the stage II to IV overall hardening response of the polycrystalline material. The geometric Schmid tensor (m_{ij}^s) is related to the crystallographic slip through the relation: $m_{ij}^s = (b_i^s n_j^s + b_j^s n_i^s)/2$, where b^s and n^s are the direction and normal of the slip system s, respectively. In the VPSC approach, d_{ij} and σ_{ij} are related to the average polycrystal strain rate through an interaction equation:

$$(D - d) = n^{eff} \widetilde{M} : (\sum - \sigma) \tag{10}$$

The tensor $\widetilde{M}$ is a visco-plastic interaction compliance and n^{eff} is an effective inverse rate sensitivity, which tunes the strength of coupling between stress deviation and associated strain rate deviation. Based on the Eq. 10, average stiffness of the matrix increases as the n^{eff} decreases. When, n^{eff} =0, strain rate in the grain will become same as the average irrespective of stress condition; this reproduces the Taylor criteria. Conversely, $n^{eff} = \infty$, gives zero stress deviation to keep the strain rate at infinity, which corresponds to

Sachs model. Therefore, VPSC is a robust scheme to predict texture development during plastic deformation depending upon the range of value chosen for n^{eff}.

Results

Texture of the as-processed: i) as extruded billet; ii) as extruded, annealed and cross-rolled plate; and, iii) hydrostatically extruded thin wall tube were characterized using EBSD. 2D Orientation Density Functions (ODF) plots for a constant Φ_2 = 0 and 45° sections are shown in the Figure 2.

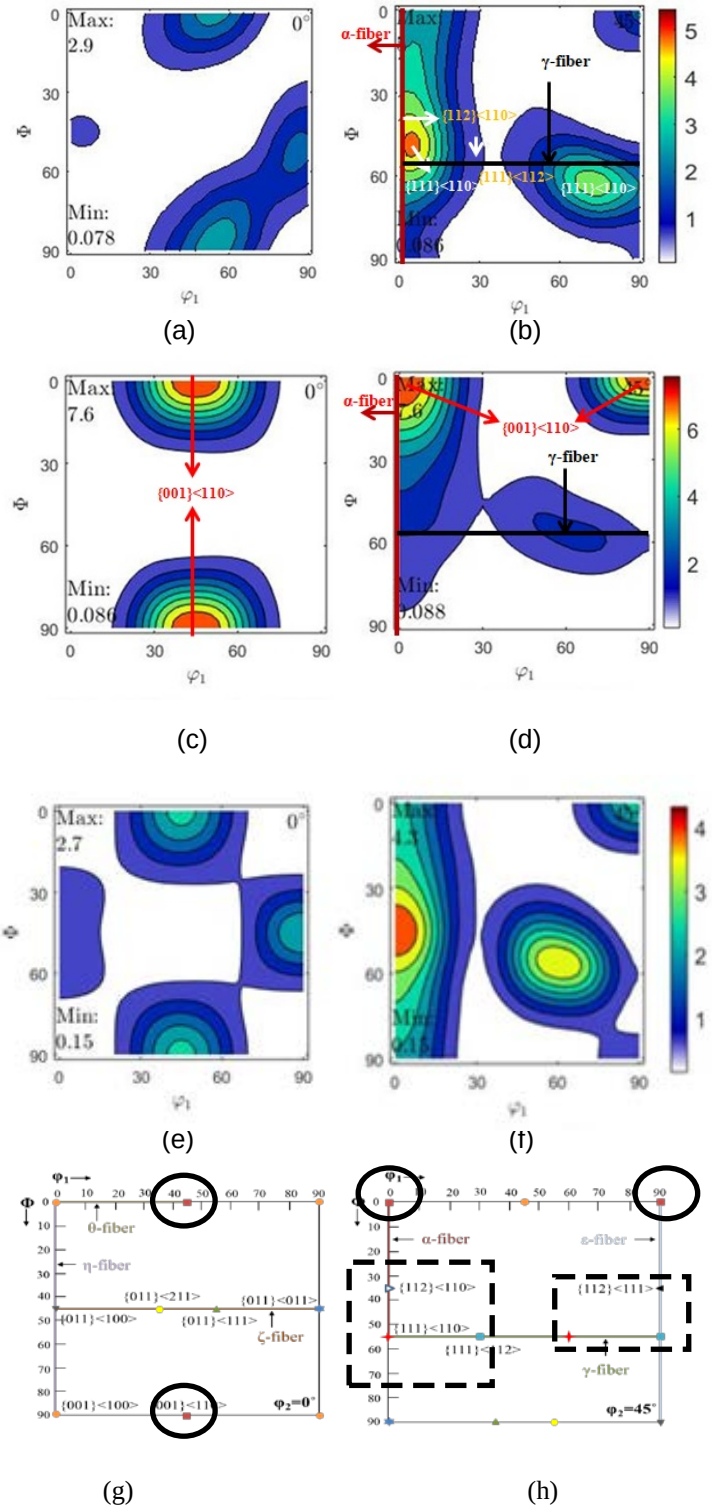

Figure 2. 2D ODF plots for the φ_2 =0 a) and 45° b) sections of the NFA-1 extrusion for the ND plane view. Figures c) and d) are the φ_2 =0 and 45° sections of the 2D ODF plots for the NFA-1 cross-rolled plate. Figures (e) and (f) of the ED plane view of thre ϕ_2 = 0 and 45° texture components for the hydrostatically extruded tube (see Figure 1 for the orientation). Figures g) and h) are the ideal ϕ_2 = 0 and 45° texture components, respectively, for bcc steels, with the highest intensities marked by the circles.

The ODF plots of the Figure 2 reveal that the deformation produces an α-fiber texture, which persist the three stages of deformation. The initial extrusion produces α-fiber with the strongest texture intensities for the {111} <110> and {112}<110> components. Cross-Rolling strengthens the α-fiber texture and produces a very high volume fraction of {001}<110> component. Therefore, a high volume fraction of {001} crystallographic planes of bcc-Fe are aligned on planes normal to the thickness direction and parallel to the plate faces. Previously, it has been shown that alignment of this high volume fraction of {001} type planes normal to the thickness direction of the cross-rolled plate is responsible for producing high density of microcracks in the through-thickness direction of the plate, due to the low value of fracture toughness (≈3-5 MPa√m) value of the {001}<110> cleavage system. Notably, tubing produced a hydrostatic extrusion of the cross-rolled plate does not exhibit any microcracking. The SEM micrographs of the planes perpendicular the original extrusion direction, as shown in Figure 1, also represent the thickness direction of the three deformation conditions, are shown in Figure 3. The SEM observation clearly indicates that cross-rolling introduces microcracks normal to the through-thickness direction of the cross-rolled plate. A detailed micromechanism of the microcracking was described previously in Ref [4,7].

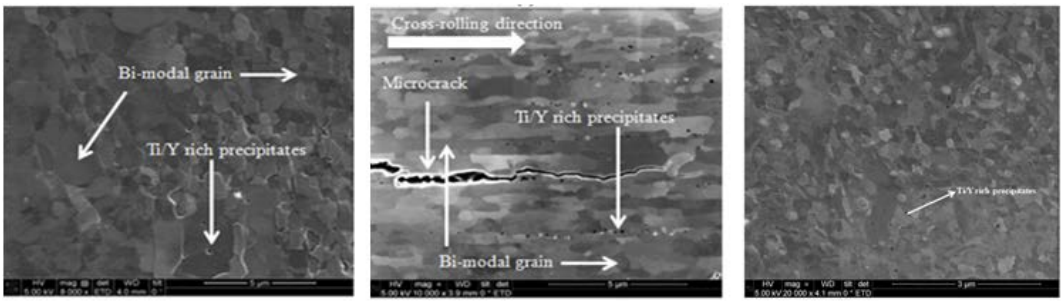

Figure 3. SEM micrographs of the ED plane view of the a) as extruded bar; b) cross-rolled plate; and, c) hydrostatically extruded tube.

The volume fractions of the dominant texture components of three different specimens calculated from the EBSD data using the MTEX program are shown in Table. 1. The angular resolution of volume fraction calculation is 20°.

Table 1. Volume fraction of the texture component (%)

Texture component	Extruded billet	Cross rolled plate	Hydro. extruded tube
{001}<110>	2.23	33.53	4.53
{001}<100>	-	-	
{112}<110>	19.56	3.27	23.14
{111}<110>	26.12	2.51	18.76
{111}<112>	8.21	-	-

Figure 4 shows the true stress-strain curves of the NFA-1 alloy measured in an uniaxial tension test at both 20° and 800°C temperature, taken from the work of Alam et al. [7]. The stress and strain values are plotted from the yield point up to the ultimate tensile strength of the specimen. Figure 4 shows the alloy undergoes isotropic hardening, which is fitted using the Voce hardening law given in Eq. 8. The fitted curves along with the experimental one both are shown in Figure 4. The values of four constitutive parameters in Eq. 8, extracted from the tensile data in Figure 4, are listed in Table 2. The fitted constitutive law at 800°C is used in the VPSC simulation.

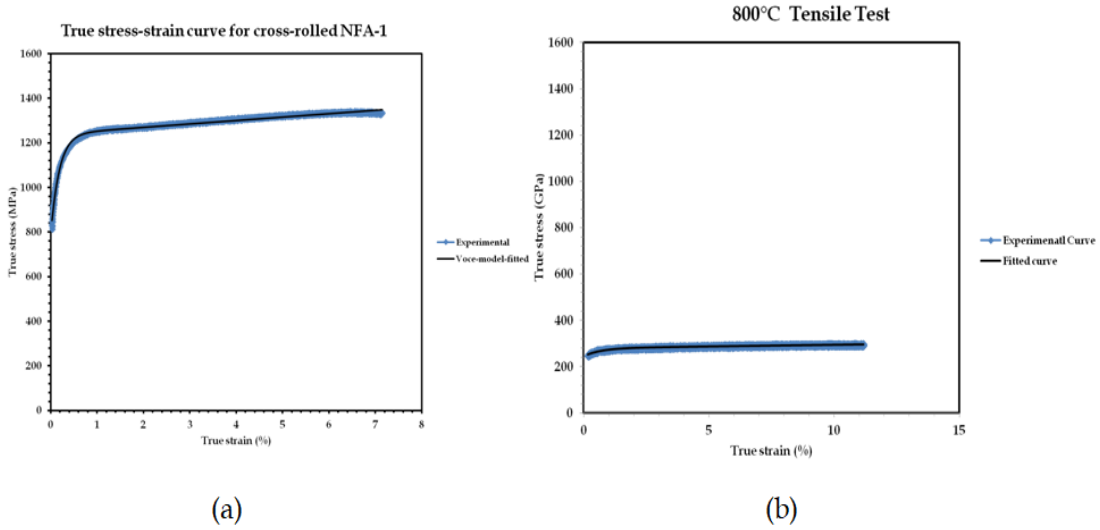

Figure 4. Experimental and Voce hardening law fitted stress-strain curve of NFA-1 alloy tested at: a) 20 and b) 800°C.

Table 2. The hardening parameters extracted from the true stress-strain data shown in Figure 4 for a fitted Voce hardening law

Voce parameters	τ_0	τ_1	Θ_0	Θ_1
20°C	782.2	456.0	2483.7	15.3
800°C	244.4	34.6	51.6	1.4

Simulation of the extrusion process

First, we simulate ideal extrusion process considering randomly oriented α-Fe grains (similar to powder) which subsequently harden during the deformation following a Voce model. The imposed velocity gradient of the strain rate tensor is chosen as $\mathring{u}=\begin{bmatrix}1 & 0 & 0\\ 0 & -0.5 & 0\\ 0 & 0 & -0.5\end{bmatrix}$ for the ideal extrusion process with a total imposed strain of ≈ 1.34. Initially, separate simulations were carried out for both primary slip and pencil glide deformation modes. In case of primary slip of bcc Fe, deformation will only occurs at {110}<111> slip system; whereas, {110}<111>, {112}<111> and {123}<111> slip system can be activated during the pencil glide.

ODF plots shown in Figure 5 suggest that VPSC simulation of hot extruded α-Fe powder successfully captures the formation of α-fiber along with a weak or broken ϒ-fiber; however, the texture intensity of different texture components depend on the mode mediating which crystallographic slip occurs on. Comparing with the Figures 2a and b with the Figures 5b and d, suggests that the pencil glide deformation mode produce texture which closer to that observed in as-extruded NFA-1. However, the highest texture intensity component for the experimentally measured ODF is {111}<110>, which are predicted for the idealized extrusion process, even for the pencil glide deformation mode. Figure 5d, shows the highest α-fiber texture intensity is predicted for the {113}<110> component, along with a

moderate intensity for the {112}<110>. Here, the interaction between the average homogenous viscoplastic medium and individual grains was modeled using affine interaction. Detail of this interaction scheme is described elsewhere [1,8]. However, a near exact simulated texture of the hot extruded billet bar is captured, when the simulation is performed using the secant interaction approach. The corresponding ODF plots of the simulated texture are shown in Figure 6. Although the secant interaction can reproduce the texture, observed experimentally for hot extruded NFA-1, the observed strength of highest intensity {111}<110> texture component does not match perfectly with the simulation results. The reason for this discrepancy is not known.

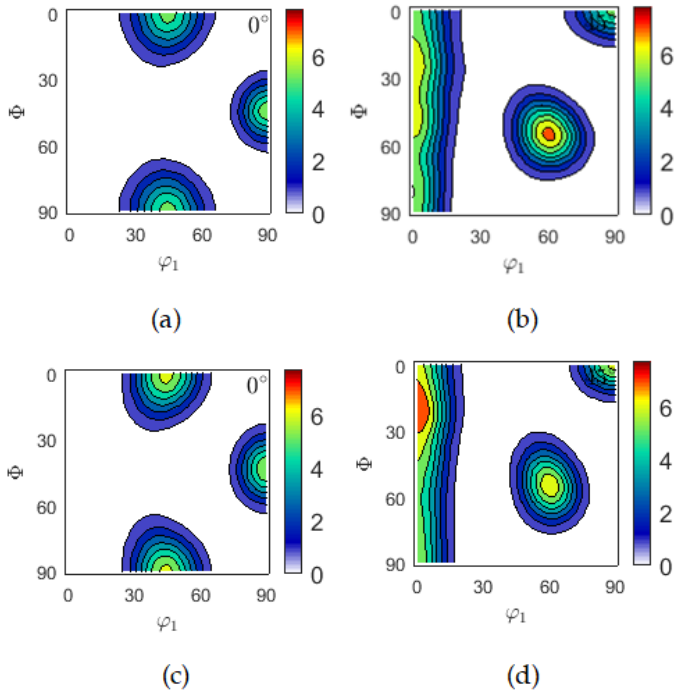

Figure 5. 2D ODF plots for the φ_2 =0 a), and 45° b) sections of the NFA-1 extrusion, simulated using affine interaction scheme and {110}<111> primary slip. Figures c) and d) are the φ_2 =0 and 45° sections of 2D ODF plots of extrusion of NFA-1, simulated using affine interaction scheme and pencil glide slip mode.

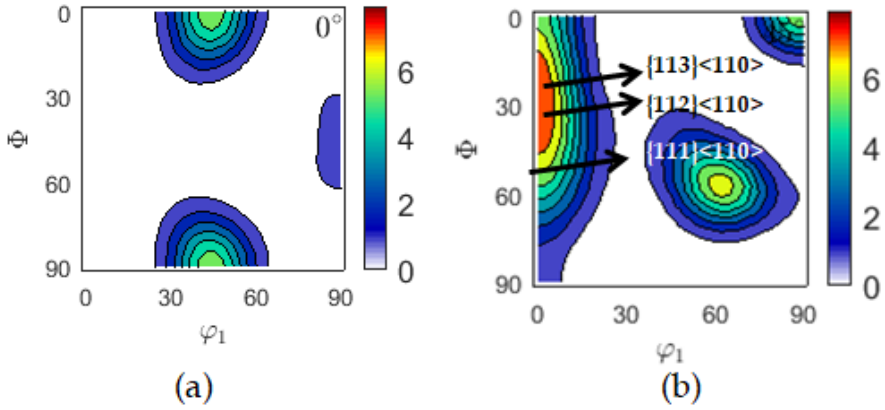

Figure 6. 2D ODF plots of the φ_2 =0 a) and 45° b) sections as extruded NFA-1, simulated using secant interaction scheme and pencil glide deformation mode.

Cross-Rolling simulation

In case of rolling operation, a compressive strain is applied along the thickness (Z) direction of the rolled plate and material starts to flow along the rolling direction, while the strain in the width direction is negligible. For a typical plain strain rolling operation, the velocity gradient tensor (L_{ij}) takes a typical form of, $\dot{u} = \begin{bmatrix} 1 & 0 & 0 \\ 0 & 0.0 & 0 \\ 0 & 0 & -1.0 \end{bmatrix}$. To understand the plastic deformation behavior of the NFA-1 alloy, initially, we simulated the texture development of a randomly oriented α-Fe system, which is subjected to velocity gradient tensor of ideal rolling operation. A plastic strain, up to ε = 2.0, was applied to simulate the rolling, using the pencil glide deformation mode, with both the affine and secant interactions between the inclusion grain and matrix interactions. The simulated ODFs are shown in Figure 7.

Figure 7 indicates that in case of ideal plane-strain deformation, none of the interaction schemes predicts the texture development of NFA-1 during cross-rolling. In both cases, the γ-fiber dominates, with the {111}<110> component (see Figure 6d) showing highest intensity for affine interaction, while the {112}<110> is predominant for the secant interaction.

The cross-rolling was performed on the hot extruded billet in seven sequential 10% thickness reduction steps, to a total 50% of total thickness reduction. The total true strain is ≈ -0.69. Before the cross-rolling, the NFA-1 was extruded up to a true strain of 1.34. The failure of the VPSC prediction of the texture developed during cross-rolling is primarily due to an incorrect assumption of the applied stress state (velocity gradient of strain rate tensor), which can be easily seen in the schematic of the rolling process in Figure 8.

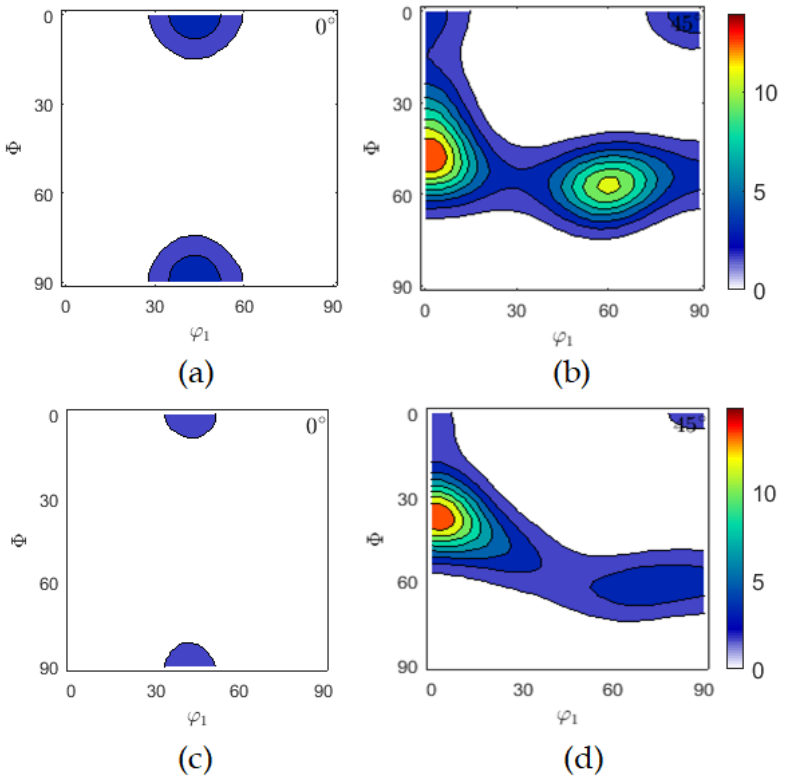

Figure 7. 2D ODF plots of the φ_2 =0 a) and 45° b) sections the cross-rolled NFA-1 plate, simulated using affine interaction scheme. Figures c) and d) are the φ_2 =0 and 45° sections of 2D ODF plots of the cross - rolled NFA-1 plate, simulated using secant interaction scheme. In both the case, the ideal velocity gradient tensor for the rolling process was used.

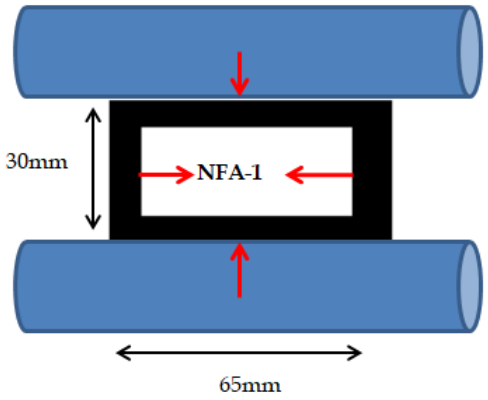

Figure 8. A schematic view of the rolling process.

Specifically, the NFA-1 billet is confined in a mild steel can. Therefore, the assumption of $L_{22} = 0$ and $L_{11} = -L_{33} = 1$ may not be valid for this case. Here, we define the L_{11} component of the velocity gradient tensor as $L_{11} = -(L_{22} + L_{33})$, and the value of L_{22} and L_{33} are chosen as -0.35 and -0.65, respectively, to maintain strain compatibility. During rolling the mild steel can also exerts compressive stress on the NFA-1; hence, the total compressive strain component on the NFA-1 alloy during rolling can be described by adding up both the zz and yy directions axial strain components. The individual values of the components will depend on the dimension of the billet cross-section (35 X 64 mm). As a result, the velocity gradient tensor used for the simulation has the form, $\dot{u} = \begin{bmatrix} 1 & 0 & 0 \\ 0 & -0.35 & 0 \\ 0 & 0 & -0.65 \end{bmatrix}$. The simulation was also performed using both the affine and secant interactions and results are shown in Figure 9. Comparing the simulated ODF with the experimentally measured ODF of the cross-rolled NFA-1 plate (see Figures 2c and d) we conclude that secant interaction accurately predicts the texture development of the NFA-1 alloy during cross-rolling.

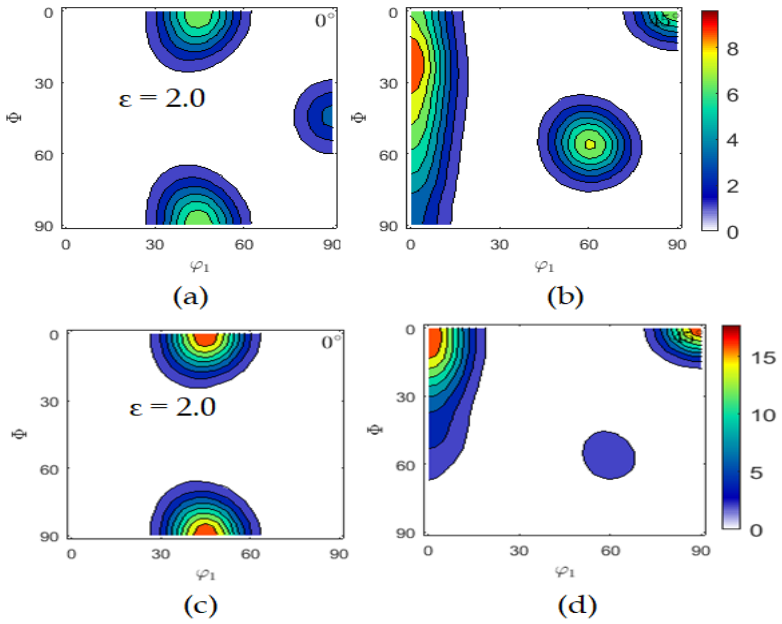

Figure 9. 2D ODF plots of the φ_2 =0 a) and 45° b) sections of the cross-rolled NFA-1 plate, simulated using affine interaction scheme. Figures c) and d) are the φ_2 =0 and 45° sections of 2D ODF plots of cross-rolled NFA-1, simulated using secant interaction scheme.

Although both the affine and secant interaction schemes successfully predict the formation of strong α-fiber texture during the cross rolling; however, the affine interaction underpredicts the highest intensity texture component in the ODF shown in Figure 9b. The highest intensity texture component observed for the cross-rolled plate is {001}<110>, which is successfully predicted by the secant interaction. In contrast, affine interaction predicts {113}<110> as the highest intensity texture component.

The effect of applied true strain on the texture development of the NFA-1 alloy has also been investigated. Simulations were performed to strains of 0.69, 1.34 and 2.0 for the secant interactions. Simulations of the rolling suggest that an increase in the applied strain level increases the intensity of the {001}<110> component increases, while the intensity of {111}<110> component decreases. Both the experimentally observed (Figures 2b and d) and simulated texture (Figure 10) of NFA-1 deformation processing clearly depicts that the overall texture strength increases with increasing applied strain. It was also previously reported that an increase in the applied strain increases the volume fraction of the {001}<110>- texture component of the α-fiber [9].

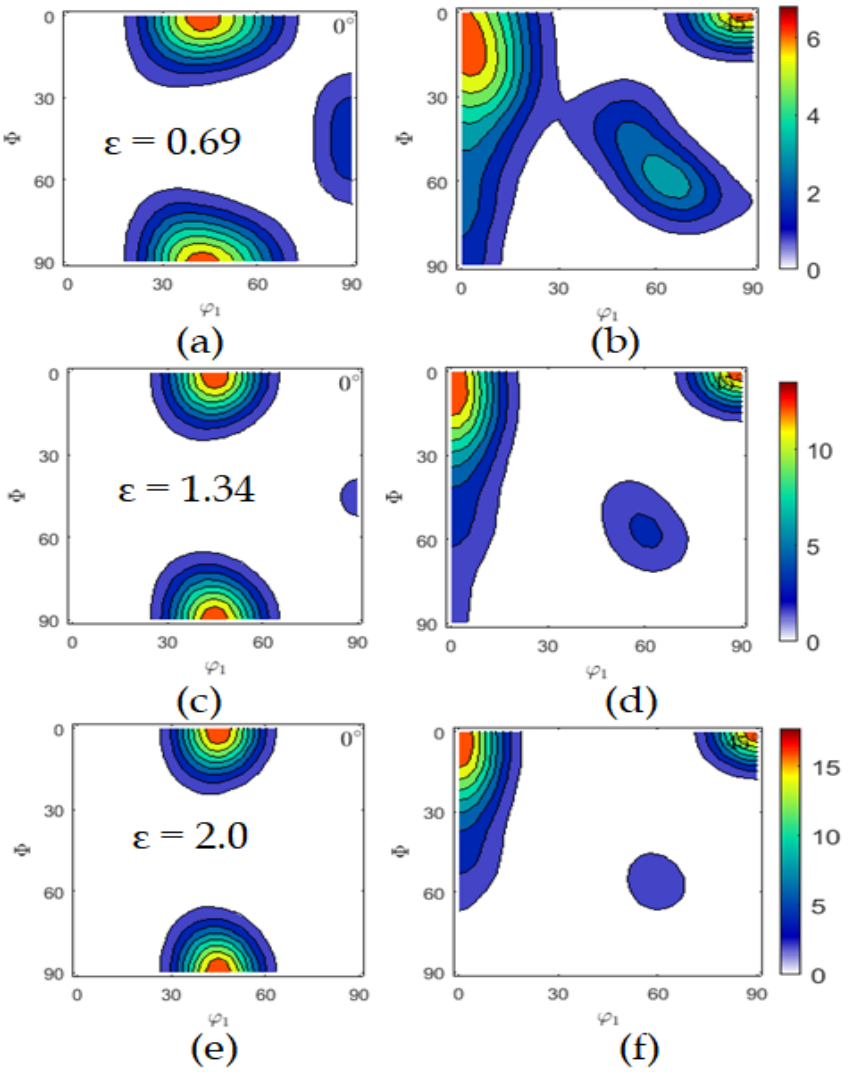

Figure 10. 2D ODF plots of the φ_2 =0 a) and 45° b) sections of VPSC simulated texture of the cross-rolled NFA-1 at an applied true strain of 0.69. Figures c), d) and e), f) are the same φ_2 =0 and 45° ODF sections for applied strains of 1.34 and 2.0, respectively.

Simulation of hydrostatic extrusion

Hydrostatic extrusion was performed on a gun-drilled tube extracted from the cross-rolled plate. The stain introduced during the hydrostatic extrusion is 1.34, while total cumulative strain applied up to the hydrostatic extrusion is ≈ 1.34 (hot extrusion) + 0.69 (cross-rolling) + 1.34 (hydrostatic extrusion) ≈ 3.37. During the extrusion, the material starts to flow plastically along the xx direction, which is out-of-the-plane of the paper in the schematic shown in Figure 11. A non-zero through-thickness shear stress component (τ_{23}= τ_{32}) is also presented during the hydrostatic extrusion. The principle stress components for the hydrostatic extrusion are σ_{11} = $\sigma_{11}/2$= $\sigma_{11}/2$. Based on the Figure 11, the velocity gradient tensor of the process is defined as $\mathring{u} = \begin{bmatrix} 1 & 0 & 0 \\ 0 & -0.5 & 0.05 \\ 0 & 0.05 & -0.5 \end{bmatrix}$. However, the value of L_{23}=L_{32}=0.05 in the velocity gradient tensor is chosen arbitrarily assuming the developed shear strain component will be small and only exists in the through-thickness direction or perpendicular to the extrusion direction. Secant type interaction and pencil glide deformation mode were used in the simulation with an applied true strain 3.37. Simulated texture is shown with the help of 2D ODF plots in Figure 12.

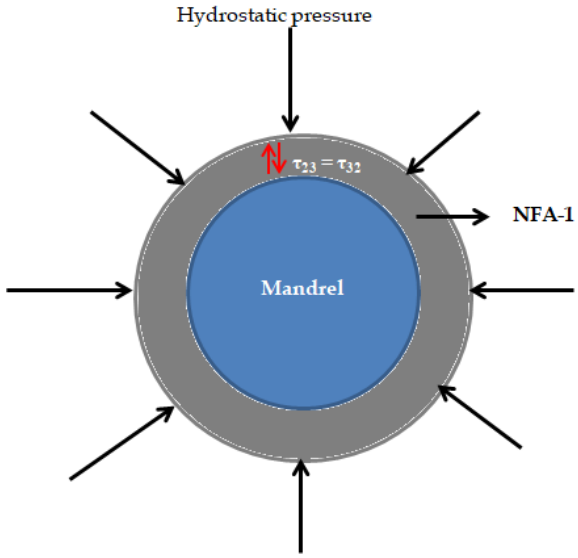

Figure 11. A schematic cross-section view of the hydrostatically extruded tube. The directions of the applied stresses are also shown.

The texture predicted by the VPSC simulation of the hydrostatic extrusion process matches quite the experimentally measured behavior observed on the polished cross-section of the tube. The experimental ODF in Figure 2f shows that the highest intensity texture components is {112}<110>, which is the same texture component, also seen in Figure 12b.

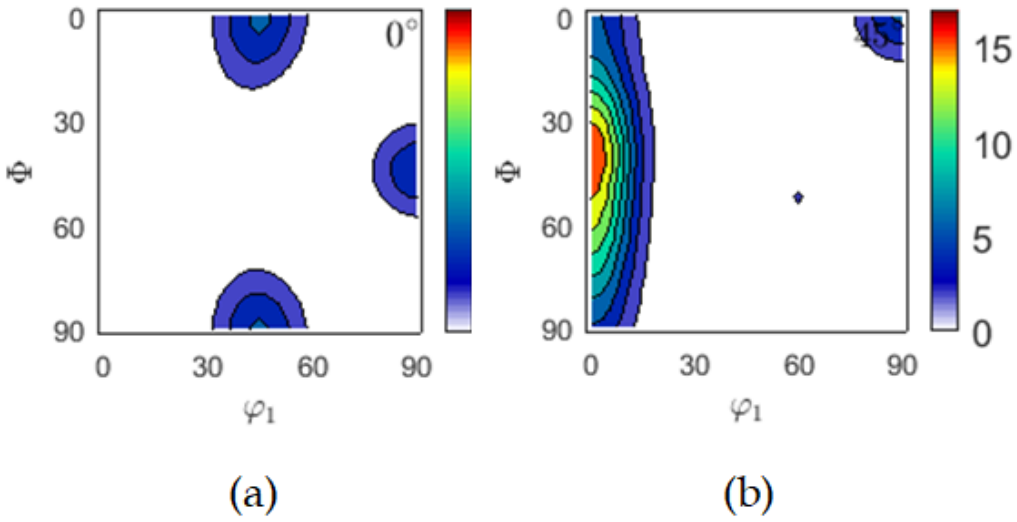

Figure 12. ODF plots of the VPSC simulated hydrostatic extrusion for a) φ_2 =0 and b) 45°.

Conclusions

- The VPSC modeling technique is able to successfully qualitatively predict the texture development during deformation processing of the 14YWT NFA -1.
- A Taylor type deformation model and secant interaction between the polycrystalline orientations (grains) is the most appropriate assumptions for plastic deformation behavior of NFA-1.
- Constraint imposed by the mild steel can during the deformation processing causes a deviation from the ideal value of the velocity gradient tensor of the applied strain rate during cross-rolling, which helps to stabilize the {001}<110> α-fiber texture components.
- An increase in the applied total strain increases in the volume fraction of {001}<110> texture component increases.

Future work

- Other deformation routes processing will be investigated using VPSC for different product forms.
- We will simulate the creep behavior and determine the stress-strain response of the NFA-1 alloy using the MTS hardening model in the VPSC code.

Acknowledgements

We acknowledge U.S. Department of Energy (DOE) through the Office of Fusion Energy Sciences (DE-FG03-94ER54275) for financial support. This work was also partially supported by the DOE Office of Nuclear Energy by a subcontract with Los Alamos National Laboratory (LANL) (simulations of the tube fabrication). We also acknowledge Dr. David Hoelzer, Oak Ridge National Laboratory (ORNL) for providing the as extruded billet and cross-rolled plate, and, Dr, Stuart Maloy and Prof. J.J. Lewandowski for supplying hydrostatically extruded tube. We are also grateful to Prof. Irene Beyerlein for providing the VPSC code and guidance on its use.

References

[1] R.A. Lebensohn, C.N. Tomé, A self-consistent viscoplastic model: prediction of rolling textures of anisotropic polycrystals, Mater. Sci. Eng. A. 175 (1994) 71–82. doi:https://doi.org/10.1016/0921-5093(94)91047-2.

[2] G.R. Odette, On the status and prospects for nanostructured ferritic alloys for nuclear fission and fusion application with emphasis on the underlying science, Scr. Mater. 143 (2018) 142–148. doi:https://doi.org/10.1016/j.scriptamat.2017.06.021.

[3] G.R. Odette, Recent Progress in Developing and Qualifying Nanostructured Ferritic Alloys for Advanced Fission and Fusion Applications, JOM. 66 (2014) 2427–2441. doi:10.1007/s11837-014-1207-5.

[4] S. Pal, M.E. Alam, G.R. Odette, S.A. Maloy, D.T. Hoelzer, J.J. Lewandowski, Microstructure, Texture and Mechanical Properties of the 14YWT Nanostructured Ferritic Alloy NFA-1 BT - Mechanical and Creep Behavior of Advanced Materials, in: I. Charit, Y.T. Zhu, S.A. Maloy, P.K. Liaw (Eds.), Springer International Publishing, Cham, 2017: pp. 43–54.

[5] M.E. Alam, S. Pal, S.A. Maloy, G.R. Odette, On delamination toughening of a 14YWT nanostructured ferritic alloy, Acta Mater. 136 (2017). doi:10.1016/j.actamat.2017.06.041.

[6] E. Aydogan, S. Pal, O. Anderoglu, S.A. Maloy, S.C. Vogel, G.R. Odette, J.J. Lewandowski, D.T. Hoelzer, I.E. Anderson, J.R. Rieken, Effect of tube processing methods on the texture and grain boundary characteristics of 14YWT nanostructured ferritic alloys, Mater. Sci. Eng. A. 661 (2016) 222–232. doi:10.1016/j.msea.2016.02.085.

[7] M.E. Alam, S. Pal, K. Fields, S.A. Maloy, D.T. Hoelzer, G.R. Odette, Tensile deformation and fracture properties of a 14YWT nanostructured ferritic alloy, Mater. Sci. Eng. A. 675 (2016). doi:10.1016/j.msea.2016.08.051.

[8] O. Engler, C.N. Tomé, M.-Y. Huh, A study of through-thickness texture gradients in rolled sheets, Metall. Mater. Trans. A. 31 (2000) 2299–2315. doi:10.1007/s11661-000-0146-7.

[9] B. Hutchinson, Deformation microstructures and textures in steels, Philos. Trans. R. Soc. London. Ser. A Math. Phys. Eng. Sci. 357 (1999) 1471 LP-1485. http://rsta.royalsocietypublishing.org/content/357/1756/1471.abstract.

3. CERAMIC COMPOSITE STRUCTURAL MATERIAL DEVELOPMENT

3.1 MECHANICAL PROPERTY DEGRADATION OF HIGH CRYSTALLINE SIC FIBER–REINFORCED SiC MATRIX COMPOSITE NEUTRON IRRADIATED TO ~100 DISPLACEMENTS PER ATOM - IRRADIATED 3C-SIC—Takaaki Koyanagi, Yutai Katoh (Oak Ridge National Laboratory), Takashi Nozawa (National Institutes for Quantum and Radiological Science and Technology), Lance Snead (Stony Brook University)

Abstract of a manuscript in Journal of the European Ceramic Society (in press).

For the development of silicon carbide (SiC) materials for next-generation nuclear structural applications, degradation of material properties under intense neutron irradiation is a critical feasibility issue. This study evaluated the mechanical properties and microstructure of a chemical vapor infiltrated SiC matrix composite, reinforced with a multi-layer SiC/pyrolytic carbon–coated Hi-NicalonTM Type S SiC fiber, following neutron irradiation at 319 and 629 °C to ~100 displacements per atom. Both the proportional limit stress and ultimate flexural strength were significantly degraded as a result of irradiation at both temperatures. After irradiation at 319 °C, the quasi-ductile fracture behavior of the nonirradiated composite became brittle, a result that was explained by a loss of functionality of the fiber/matrix interface associated with the disappearance of the interphase due to irradiation. The specimens irradiated at 629 °C showed increased apparent failure strain because the fiber/matrix interphase was weakened by irradiation-induced partial debonding.

3.2 DIMENSIONAL STABILITY AND ANISOTROPY OF SiC AND SiC-BASED COMPOSITES IN TRANSITION SWELLING REGIME—Yutai Katoh, Takaaki Koyanagi, Joel McDuffee (Oak Ridge National Laboratory), Lance Snead (Massachusetts Institute of Technology), Ken Yueh (Electric Power Research Institute)

Abstract of a manuscript published in Journal of Nuclear Materials 499 (2018) 471–479.

Swelling, or volumetric expansion, is an inevitable consequence of the atomic displacement damage in crystalline silicon carbide (SiC) caused by energetic neutron irradiation. Because of its steep temperature and dose dependence, understanding swelling is essential for designing SiC-based components for nuclear applications. In this study, swelling behaviors of monolithic CVD SiC and nuclear grade SiC fiber/SiC matrix (SiC/SiC) composites were accurately determined, supported by the irradiation temperature determination for individual samples, following neutron irradiation within the lower transition swelling temperature regime. Slightly anisotropic swelling behaviors were found for the SiC/SiC samples and attributed primarily to the combined effects of the pre-existing microcracking, fiber architecture, and specimen dimension. A semi-empirical model of SiC swelling was calibrated and presented. Finally, implications of the refined model to selected swelling-related issues for SiC-based nuclear reactor components are discussed.

3.3 WIGNER ENERGY IN SILICON CARBIDE—Lance Snead (Stony Brook University*)* Takaaki Koyanagi, Yutai Katoh and Kurt Terrani (Oak Ridge National Laboratory)

OBJECTIVE

This study aims to quantify the amount of stored energy available for release upon annealing in silicon carbide. This fundamental information should prove useful for accident modeling of fusion nuclear systems using SiC/SiC composites.

SUMMARY

High Flux Isotope Reactor (HFIR) irradiated silicon carbide samples, receiving dose from millidpa to tens of dpa near 60-90°C, underwent both microstructural and stored energy release measurements. Above 1 dpa, as expected, amorphization occurs. For doses lower than the amorphization threshold the lattice distortion occurs approximately linear with dose up to a remarkable ~ 8% swelling. Over the same dose the stored energy release upon annealing reaches approximately 2500 J/g at the amorphization threshold. Annealing of the as-amorphized structure yields approximately 1925 J/g. These values are generally comparable with those of graphite and of more engineering consequence as SiC retain a higher level of stored energy at engineering-relevant fusion temperatures.

PROGRESS AND STATUS

Production of interstitial-vacancy pairs in graphite by neutron irradiation was postulated by Eugene Wigner in 1942. Later, Leo Szilard pointed out that upon recombination these defects would relinquish their formation energies (~8 eV) in the form of heat. These two phenomenon became known as the Wigner Effect and the Szilard Complication, respectively, ushering in the new field of *irradiation materials science*. Moreover, the implications of such stored energy release to reactor operation were immediately recognized and later became reality with the 1957 Wind scale reactor fire in Sellafield, United Kingdom.

While *stored energy* is well understood conceptually and has been studied in detail for gas-cooled reactors, the *Szilard Complication* has been generally and practically thought to be unique to graphite. In other words, for practical nuclear systems the combined stored energy due to simple defect production is only an issue for graphite irradiated <200°C, where the subsequent energy release upon annealing greatly exceeds the material's specific heat, driving an autocatalytic temperature rise. However, recent work by Snead et al.[1] on the swelling of various polytypes of silicon carbide has suggested significant Wigner Energy in this system may exist as well. In that paper both lattice dilation and physical swelling for SiC irradiated in thermal contact with the coolant of the HFIR Reactor was measured to reach an extraordinary ~ 7.9% for either single crystal α, β, or the faulted β polytypes. The faulted β polytype is the structure of the most used nuclear-grade SiC, chemically vapor deposited (CVD) SiC. Through simple calculation of Frenkel pair density responsible for such a high volumetric swelling, combined with the energy release when such defects recombined, that work suggested very large stored energy for SiC. For this reason an initial program to measure the stored energy release from these samples was carried out and the potential impact of this release on light water reactor (LWR) systems is presented here.

Experimental Procedure

The experimental approach was conceptually simple, taking advantage of high-purity CVD SiC utilized in previous irradiation capsules irradiated in the HFIR. Doses for samples were: 0.02, 0.1, 0.05, 0.0762, 1.34, 2, and 20 $x10^{21}$ n/cm^2 (E>0.1 MeV.) The samples were irradiated in perforated rabbits within a foil pack in the reactor. The approximate irradiation temperature was 60-90°C.

Energy release was carried out using a Netzch 404C Differential Scanning Calorimetry (DSC) within the Low Activation Materials Development and Analysis (LAMDA) laboratory at Oak Ridge National Laboratory (ORNL). Supporting X-ray and Transmission Electron Microscopy (TEM) was also carried out to provide insight into the microstructure, also in LAMDA.

Results

Figure 1 provides a summary plot of the results of this work. From the figure the as-irradiated swelling is seen to monotonically increase to an extrapolated amorphous transition point of approximately $1x10^{25}$ n/m^2 (E>0.1 MeV). The magnitude of as-amorphized swelling is approximately 10.8-11.7%. This transition point is generally well understood from both ion and neutron irradiation studies. [2; 3] Prior to amorphization and of particular interest, the crystalline SiC structure for this relatively low temperature irradiation achieved a maximum of 8.13% swelling as measured by x-ray lattice dilation. Figure 2 provides a high resolution TEM image of a 6H-SiC structure of a sample irradiated to ~$0.51x10^{25}$ n/m^2 (E>0.1 MeV,) indicated a highly damaged, yet crystalline structure.

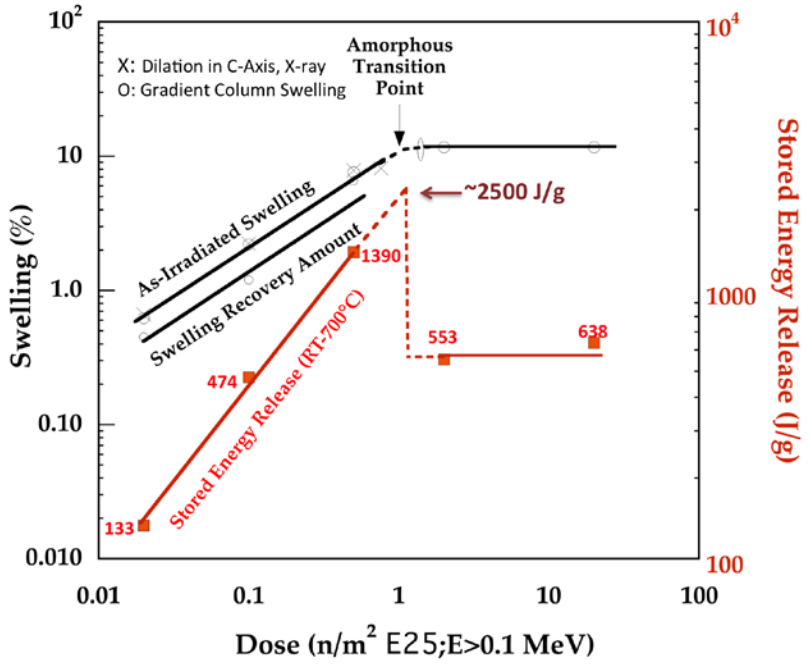

Figure 1. Swelling and Stored Energy Release on annealing of Irradiated SiC to 700°C.

The lower curve of Figure 1 provides the stored energy released upon annealing the irradiated samples to 700°C (the maximum possible in the current experiment). The curve above the release curve provides the associated fractional amount of swelling recovered upon annealing. Based on our current understanding of SiC, in comparison with the nominal ~80% of swelling recovery indicated in Figure 1 following 700°C , nearly all swelling and all stored energy would be released by approximately 1000°C [4].

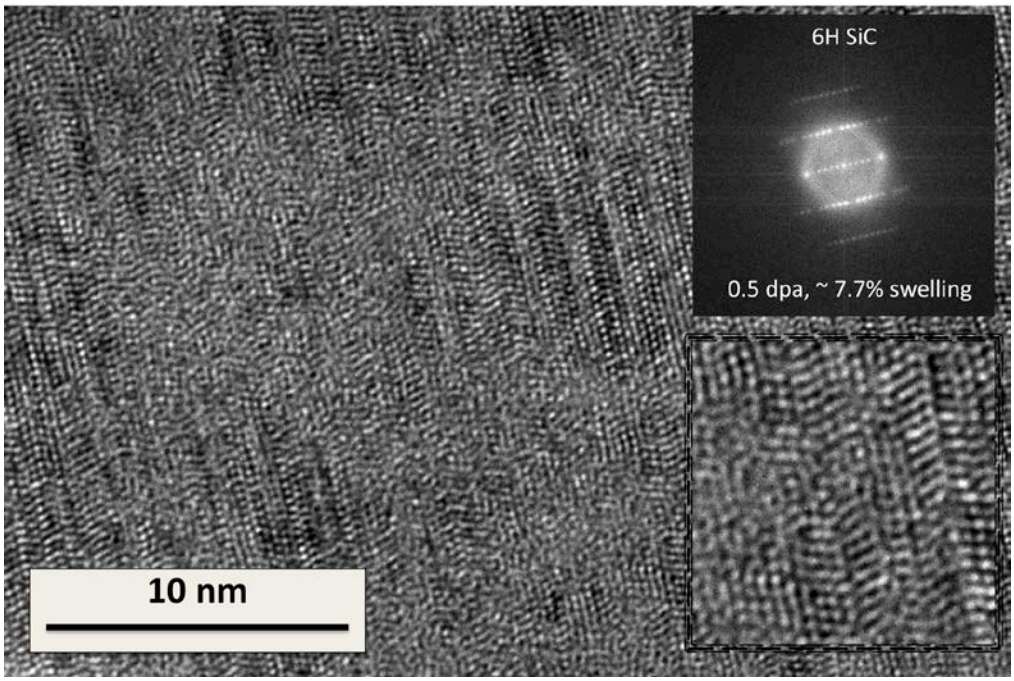

Figure 2. High Resolution TEM Image of Highly Damaged SiC.

The amount of stored energy release in SiC as demonstrated in Figure 1 is comparable to that of graphite, which for highly damaged materials approaches 2500 J/gm. [5] More to the point, the issue is not only the stored energy, but whether the release of that energy occurs at a rate such that it exceeds the materials specific heat and will thereby induce an autocatalytic reaction. Or such an additional heat under accident conditions would cause practical issues to design. Practically, the amount of stored energy in graphite is no longer an issue for present day reactors as the defect kinetics of the graphite crystal will not permit a high concentration of vacancies about a few hundred degrees Celcius.[6] However, while the concentration of simple defects and defect clusters are a strong function of temperature in SiC, their fractional amount (and therefore their associated stored energies), are significant to several hundred degrees Celsius.

Figure 3 provides a comparison of the normalized stored energy in nuclear graphite (after Simmons[5] and Kelly[6]) as a function of temperature as compared to SiC. In this plot a number of assumptions have been made for SiC, including a complete recovery of the lattice swelling for the crystal and importantly that the stored energy as normalized to the swelling is a constant at ~350 J/g per percent swelling. This assumption, while needing to be experimentally validated, has physical support in that other physical properties changes can be similarly normalized to swelling for SiC in the point defect swelling regime, as for example, thermal conductivity (thermal defect resistance) [7] Two important observations can be made from analysis of the previous results. First, significant accumulation and energy release does occur in SiC, on par with highly irradiated graphite for relatively low temperature irradiation. Secondly, as depicted in Figure 3, due to the contrasting nature of defect annihilation in SiC and graphite, a higher level of stored energy is available for release in SiC at intermediate (application relevant) temperatures. However, as shown inset to the figure, the levels of energy for applications such as the dual-coolant lithium-lead (DCLL) blanket SiC module are suggested to be approximately 400 J/g.

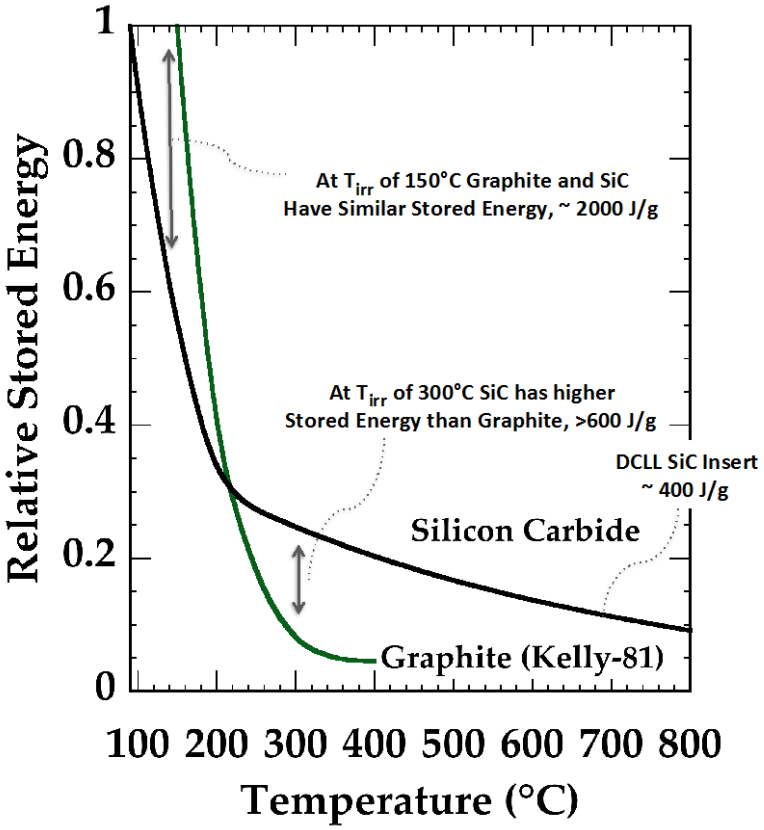

Figure 3. Fractional stored energy comparison: irradiated SiC and Graphite.

Future work

This work has been based on a relatively small number of low temperature irradiations. Both higher temperature irradiation kinetic information as well as a design-basis is needed to understand as what point stored energy release becomes important.

Acknowledgement

The data underlying this work was supported through a 2016 Department of Energy - Nuclear Energy (DOE-NE) National User Facility Rapid Turnaround Experiment. The authors would like to thank Kurt Terrani, Takaaki Koyanagi and Wally Porter of ORNL for assistance with stored energy measurements.

References

[1] Snead, L.L., Katoh, Y., Koyanagi, T., Terrani, K., and Specht, E.D. (2016). Dimensional isotropy of 6H and 3C SiC under neutron irradiation. Journal of Nuclear Materials 471, 92-96.

[2] Snead, L.L., Zinkle, S.J., Hay, J.C., and Osborne, M.C. (1998). Amorphization of SiC under Ion and Neutron Irradiation. Nuclear Instruments and Methods in Physics Research B 141, 123-132.

[3] Snead, L.L., and Hay, J.C. (1999). Neutron irradiation induced amorphization of silicon carbide. Journal of Nuclear Materials 273, 213-220.

[4] Price, R.J. (1972). Annealing behavior of neutron-irradiated silicon carbide temperature monitors. Nucl Tech 16, 536-542.

[5] Simmons, J.W.H. (1965). Radiation Damage in Graphite.(Pergamon Press).

[6] Kelly, B.T. (1981). Physics of Graphite.(London: Applied Science Publishers).

[7] Snead, L.L., Nozawa, T., Katoh, Y., Byun, T.S., Kondo, S., and Petti, D.A. (2007). Handbook of SiC Properties for Fuel Performance Modeling. Journal of Nuclear Materials 371, 329-377.

3.4 MICROSTRUCTURAL EVOLUTION OF 3C-SiC EXPOSED TO SIMULTANEOUS NEUTRON IRRADIATION AND HELIUM IMPLANTATION—X. Hu, T. Koyanagi, Y. Katoh (Oak Ridge National Laboratory), J. Zhao (Lanzhou University), T. Yamamoto (University of California, Santa Barbara)

OBJECTIVE

The objective of this work is to assess the helium-dpa synergisms in silicon carbide (SiC) through investigating the microstructural evolution of 3C-SiC exposed to simultaneous neutron irradiation and helium implantation.

SUMMARY

In this study, we exposed 3C-SiC covered with a 2μm Ni foil to neutron irradiation at 500°C to 30 dpa in the high flux isotope reactor to simulate the simultaneous introduction of helium and irradiation defects into SiC. The combination of transmission electron microscopy (TEM) observations and thermal desorption measurements helps to determine the impact of helium on the microstructural evolution in 3C-SiC through capturing the microstructures of neutron-irradiated 3C-SiC with and without in-situ He implantation before and after thermal desorption measurements. The results indicated that helium desorption spectra from neutron-irradiated and ion-irradiated 3C-SiC are completely different in terms of the desorption peaks' position and intensity. The identification of possible helium trapping sites was attempted. However, the insufficient theoretical studies of helium-defect interactions in SiC limited more detailed analysis. The TEM observation on these samples showed that the presence of helium stabilized the defect clusters and promoted the formation of visible helium bubbles in as-irradiated conditions. Following the subsequent heat treatment during the thermal desorption measurements, large faceted helium bubbles were found along grain boundaries and stacking faults, while the helium bubbles in the grain interior were relatively smaller than the void size in the non-helium neutron-irradiated sample due to the reduced mobility of He-defect clusters. The presented work is expected to provide more insights into the fundamentals of helium-defect interactions in 3C-SiC.

PROGRESS AND STATUS

Introduction

Given its great chemical and thermal stability, good resistance to neutron irradiation, and low cross section for neutron absorption resulting in the low induced activity [1], SiC has been widely applied or considered in nuclear systems as a fuel and structural material since 1960s. Examples include chemical vapor-deposited (CVD) SiC used as pressure vessel materials for the tri-structural-isotropic fuel particles [2], SiC fiber reinforced SiC matrix (SiC/SiC) composites perceived as candidate accident tolerant fuel cladding in light water reactors [3] and primary structural and blanket materials in fusion reactors [4]. The extremely hostile service environment in nuclear systems, characterized by intensive neutron irradiation, corrosive chemical solution, high temperature, high pressure, etc., imposes significant challenges to SiC. Of particular interest is the neutron irradiation, altering the microstructure and the consequential thermo-mechanical properties of SiC. In addition, the presence of gaseous species (e.g., helium, hydrogen isotopes, and fission gases) together with irradiation-induced defects complicates the microstructural evolution of SiC in the real service environments. One of the primary concern is helium effects in SiC for fusion applications. Helium can be introduced into SiC through two major pathways, i.e., (n, α) nuclear reactions and implantation of energetic helium produced elsewhere. For example, the 14MeV-peaked nuclear fusion neutron spectrum induces a large helium generation rate in SiC, up to 150 atomic parts per million (appm) He/dpa [5], due to the large reaction cross section between high energy neutron and Si/C (0.18 and 0.07 barns for reactions between 14.1MeV neutrons and Si, C, respectively). In fission reactors, about 90% of the light nuclei that arise from ternary fission are helium. Helium has negligible solubility in SiC and correspondingly has strong tendency to bind with vacancy and other radiation-induced defects, resulting in the accumulation of He and the subsequent of nucleation and growth of He bubbles. The presence of abundant He bubbles leads to changes in mechanical property and dimensional stability of

SiC [6]. Therefore, it is critically important to understand the interactions of He and irradiation-induced defects in SiC in order to predict the He behavior in SiC, to assess performance and to enable optimized design of SiC devices subject to high flux of fast neutrons. This transmutation effect due to 14MeV neutron is critically important, but its effects on the microstructural evolution and the resulting thermophysical properties of SiC are still poorly understood due to a lack of fusion neutron source.

A wealth of theoretical and experimental efforts has been committed to reveal the fundamentals of the synergisms of He-irradiation defects in SiC. As to theoretical studies, atomistic simulations or other large-scale modeling are expected to provide critical insights into the interactions of helium and irradiation defects in SiC. However, there are very limited simulations of He effects in SiC available in literatures. Van Ginhoven et al. [7] used density functional theory (DFT) to calculate the migration barrier of helium through various diffusion pathways and the binding energy of He to various defect features in 3C-SiC. A more comprehensive first-principles study on the interaction between helium and intrinsic point defects in 3C-SiC has recently been performed by Sun et al. [8]. The stable configurations and energetics of intrinsic point defects, interstitial He, and He cluster, interstitial He-Si, He-C, and multiple He atoms trapped inside a mono-vacancy were investigated. A complete database on the interactions of He and various defects is not available yet.

Parallel to the theoretical studies, experimental studies on He effects in SiC have attracted more attentions. Single-He ion irradiation, dual-ion irradiation, and fission neutron irradiation have been utilized in coordination with various characterization techniques. Olivierdo et al. [9] conducted a comprehensive thermal desorption spectroscopy (TDS) study to characterize helium implantation induced defects in 6H-SiC and 4H-SiC single crystals. The dependence of He implantation energy (100eV to 3 keV) and fluence (10^{13} to 10^{15}/cm^2) on desorption spectra was captured. Two major He desorption peaks were observed at 427 °C and 927 °C, respectively. Helium de-trapping processes responsible for these peaks were identified with the help of the first order desorption model. Svetukhin et al.[10] reported the activation energies of He dissociating from trapping sites through a combination of TDS experiment and an extended first order desorption model. Barbot et al. [11] combined TEM, X-ray diffraction (XRD), and Nano indentation to investigate the microstructure evolution and the consequential mechanical property changes of 4H-SiC single crystals implanted with 50 and 160keV He ions to fluences ranging from 7×10^{15} to 1×10^{17}/cm^2. An isochronal annealing study was also conducted in their study to demonstrate the damage evolution in He-implanted samples. Smith et al. [12] applied both nuclear reaction analysis and elastic recoil detection analysis to acquire the He depth profile and to investigate the retention of He in single crystalline 6H-SiC implanted with 40 keV ^{3}He ions to fluence of ~10^{16}/cm^2. Nogami and Hasegawa [13] compared the hardness, elastic modules and fracture toughness of CVD-SiC after neutron irradiation up to 0.4 dpa at 600°C and up to 0.6 dpa at 800°C and after He implantation up to 800appm at 750°C, although the rationality of such a comparison is in doubt. Kondo et al. [14] compared the microstructure evolution of β-SiC irradiated with single-ion (5.1MeV Si^{2+}) and dual-ion (5.1MeV Si^{2+} and 1MeV He^{+}) to 10 dpa at various temperature to capture the synergistic effect of irradiation damage and He. In this study, it was evident that He promoted the He bubble nucleation and growth. Similar work was also performed for SiC/SiC composites[15]. Moreover, He effect on radiation damage in SiC/SiC composite was studied by Chen and Jung [16]. Their TEM observation of SiC/SiC composite after high energy He (26.3 MeV) implantation and after subsequent thermal annealing showed clear dependence of bubble appearance on the type of boundary. These ion irradiation studies are useful to explore mechanisms, but they do not simulate the real service environment of SiC in fusion reactors because of their highly accelerated damage rate and the strong spatial dependence of He and defect distributions.

Most fission reactor studies of He-irradiation damage synergisms have utilized ^{59}Ni and ^{10}B (n, α) 'alloying element' reactions to produce high levels of He, especially for the studies of steels. As to SiC, Pramono et al. [17] used sintered α-SiC containing B_4C with various ^{10}B concentrations irradiated in the Japan Materials Testing Reactor (300°C, 2.8×10^{24}n/m^2) to mimic the simultaneous production of irradiation defects and He in real fusion environment. Helium release from these irradiated samples, volume swelling and the lattice parameter changes were studied in their work. They also used the same sample to acquire the He migration energy and the diffusion coefficient through the combination of Fick's 2nd law and the

measured He release during an isothermal annealing process [18]. However, B_4C was not homogeneously distributed within SiC and B is not a natural alloying element in SiC. Therefore, although this technique is very useful, it could only provide limited insights into the underlying mechanisms controlling He and defect transport, fate and consequences in pure SiC.

In contrast, in-situ He implantation of materials irradiated in fission reactors [19] is an alternative and very attractive approach to simulate the actual service environment of SiC without introducing non-natural alloying elements . In this study, we report the effects of He on the microstructural evolution in high purity 3C-SiC irradiated in a fission reactor with in-situ He implantation, thus, to assess the effects of He-irradiation damage synergisms in SiC.

Experimental Procedure

High purity polycrystalline CVD 3C-SiC specimens (Rohm & Haas Co., Woburs, USA) were used in this study. A 2μm thick Ni foil worked as implanter to inject high energy α particles from (n, α) reactions into an adjacent sample subject to neutron irradiation. The sample assemblies, SiC stacked with Ni foil, were exposed to neutron irradiation in the High Flux Isotope Reactor (HFIR) at Oak Ridge National Laboratory (ORNL). The SiC samples with and without Ni foil were irradiated under a fast neutron flux of 1×10^{19} n/m^2/s (E>0.1MeV) corresponding to a damage rate of ~1×10^{-6} dpa/s in SiC. Irradiation dose and temperature were 30 dpa and 500 °C, respectively. The irradiation temperature was determined based on annealing behavior of a passive SiC temperature monitor during dilatometry [20]. The uncertainty of temperature determination was ±10°C.

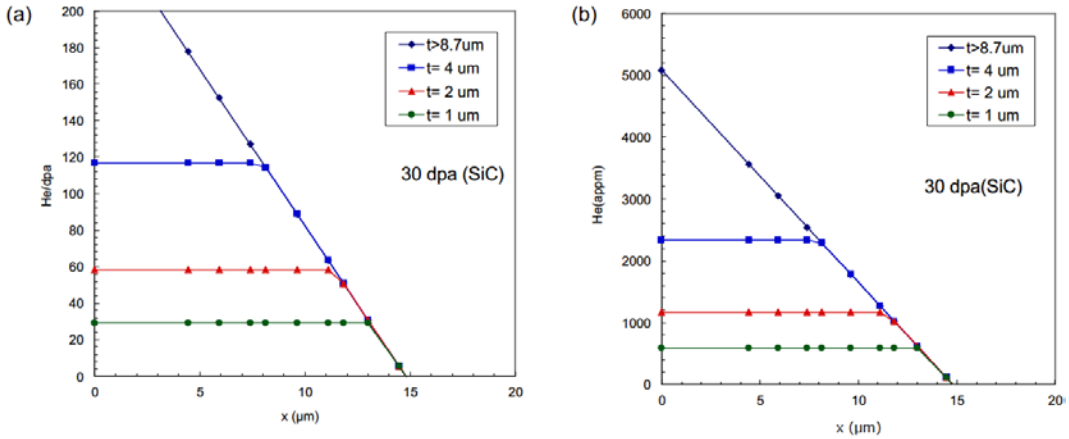

Figure 1. (a) He/dpa ratio and (b) He concentration as a function of depth in SiC wrapped with Ni foils of various thicknesses (1, 2, 4, >8.7μm) irradiated in HFIR.

The 4.76MeV α particles from ^{59}Ni (n, α) reactions has a range of 14.8 μm in SiC for a theoretical density of 3.21 g/cm^3. The concentration of He and He/dpa ratio can be tuned to meet different needs through modifying the thickness of the applied Ni foil. By applying the computing methods stated in [19], the He implantation profiles in SiC are determined in terms of the He/dpa ratio and He concentration as a function of depth in SiC covered with Ni foil implanters of various thicknesses, as shown in Figure 1. A 2μm Ni foil implanter used in this study produces a uniform damage region in an 11 μm thick area with 58 appm He/dpa in SiC. The corresponding He uniform concentration is 1168 appm.

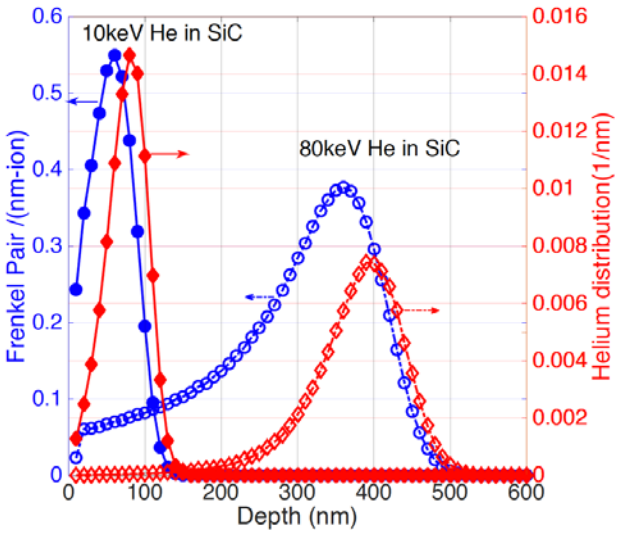

Figure 2 Calculated displacement damage and He distribution as a function of depth from irradiated surface in SiC implanted with 10keV and 80keV He ions by SRIM code.

Helium ion implantations on the same batch of CVD SiC samples were performed at Innovion Inc. to compare the He desorption behavior to that of neutron-irradiated samples. Samples were implanted with 10 keV and 80 keV $^4He^+$ to a fluence of $1\times10^{19}/m^2$ under fluxes of $5.8\times10^{15}/m^2/s$ and $4.8\times10^{16}/m^2/s$, respectively, at room temperature. Depth profiles of displacement damage and retained He ions were calculated by using the Stopping and Range of Ions in Matter (SRIM) assuming displacement threshold energy of 31 and 25 eV for Si and C atoms, respectively, as shown in Figure 2. For 10keV and 80keV He-ion implanted SiC, the maximum production of Frenkel pair occurs at 60 and 360 nm below the implantation surface, while the maximum in the distribution of He occurs at 80 and 400 nm, respectively. The TDS measurements were performed on these two samples by using the gas implantation and thermal desorption system (GITDS) [21] located at low activation materials development and analysis (LAMDA) laboratory at ORNL. Temperature of the sample was increased to 1600°C with a ramping rate of 0.5°C/s. A quadrupole mass spectrometer was used to detect the desorbed He gas. Quantification of the He desorption flux was realized with the help of a standard He leak. More information could be found in Ref. [21].

Following neutron irradiation in HFIR, SiC samples were cleaned with sulfuric acid to remove potential chemical contamination. The TDS measurements were performed on the samples following neutron irradiation and in-situ He implantation to capture the He desorption spectra. Microstructure characterization was performed on the neutron irradiated samples before and after TDS measurements with a Japan Electron Optics Laboratory (JEOL) JEM 2100F field emission gun TEM operating at 200kV. Electron transparent TEM foils were prepared using a focused ion beam system (Field Electron and Ion Company [FEI] Quanta 3D Dual Beam) operated at 30kV for initial milling and at 5 kV for final thinning to minimize the focused ion beam (FIB)-induced artifacts. All samples underwent an additional 900eV Ar ion mill using a Fischione Model 1040 NanoMill to provide final cleaning of the TEM foil prior to microstructure characterizations. Positron annihilation lifetime measurement was also performed on the as-irradiated 3C-SiC without in-situ He implantation to assess the vacancy-type defects, providing complementary information to the TEM observations.

Results

Microstructure of 3C-SiC samples following neutron irradiation and in-situ He implantation

The SiC samples were subject to neutron irradiation at 500°C to 30 dpa. The relatively low irradiation temperature prohibited the formation of large void due to the low mobility of vacancy in SiC, owing to the extremely high migration energies of V_{Si} (2.4 eV) and V_C (3.5 eV) in 3C-SiC [22] [23].

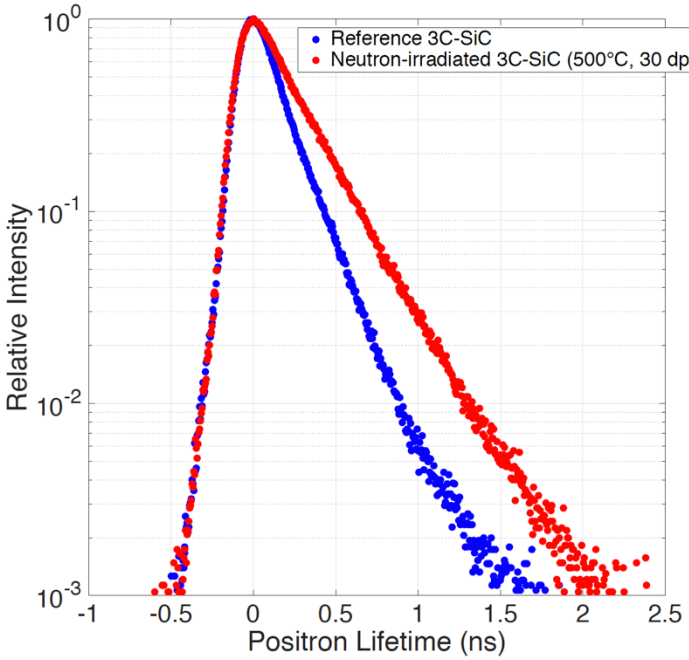

Figure 3. Comparison of measured positron lifetime spectra for reference and neutron-irradiated (500°C, 30 dpa) 3C-SiC without helium injection.

In order to confirm the non-existence of large voids, positron annihilation lifetime spectroscopy (PALS) testing, a powerful technique to characterize vacancy-type defects in materials, was conducted. Figure 3 shows the change of measured positron lifetime spectra before and after neutron irradiation of the 3C-SiC without in-situ He implantation. It is apparent that the long lifetime part of the spectrum was dramatically enhanced due to the production of vacancy and its clusters in the sample subject to high flux neutron irradiation. Fitting the measured positron lifetime by applying trapping model enables the determination of the long lifetime of positrons annihilating within the defects and its corresponding intensity. A widely applied software, PALSfit3 [24], was used for the data fitting by applying two lifetime components. The fitted long lifetime is 287 ps with an intensity of 88%, which is corresponding to the vacancy cluster of $3V_{Si}+2V_C$ with a concentration of 24 appm [25]. We also evaluated the use of three- and four-component fitting, but neither of them reproduced the spectra sufficiently or the fitting values of the parameters are unphysical. Therefore, there are no large voids present within the sample due to the absence of the large positron lifetime (> 400 ps) in the analysis.

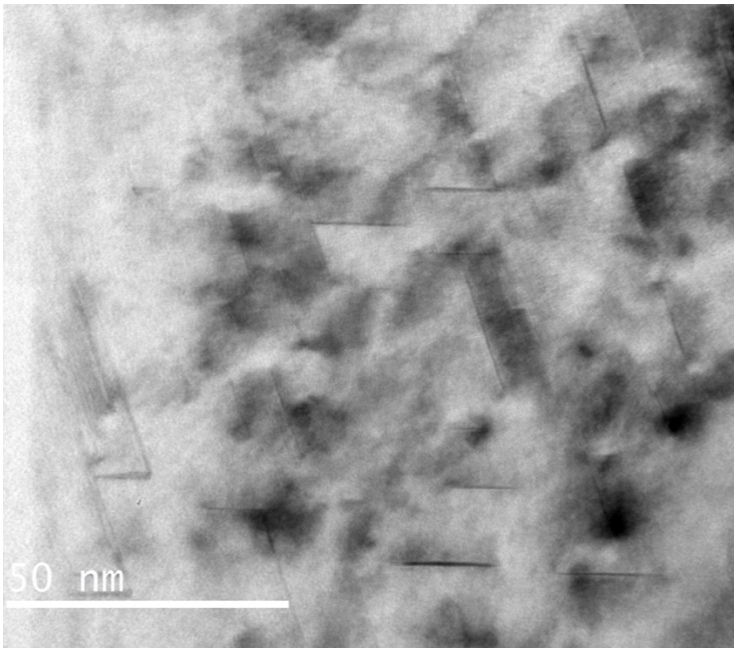

Figure 4. Bright field image of dislocation microstructures in neutron irradiated SiC with in-situ He implantation.

Figure 4 shows the bright field image of SiC irradiated to 30 dpa with a 58 appm He/dpa ratio. The primary irradiation defects observed in this sample is Frank faulted loops, the most commonly observed dislocation microstructure in both ion and neutron irradiated cubic SiC at high temperatures and irradiation doses. Kaoth et al. [26] identified the same type of dislocation microstructures in cubic SiC irradiated by Si^{2+} ions at 1400°C when irradiation dose is higher than 10 dpa. Koyanagi et al. [27] also observed the stacking faults in cubic SiC neutron irradiated at 440°C up to 31 dpa.

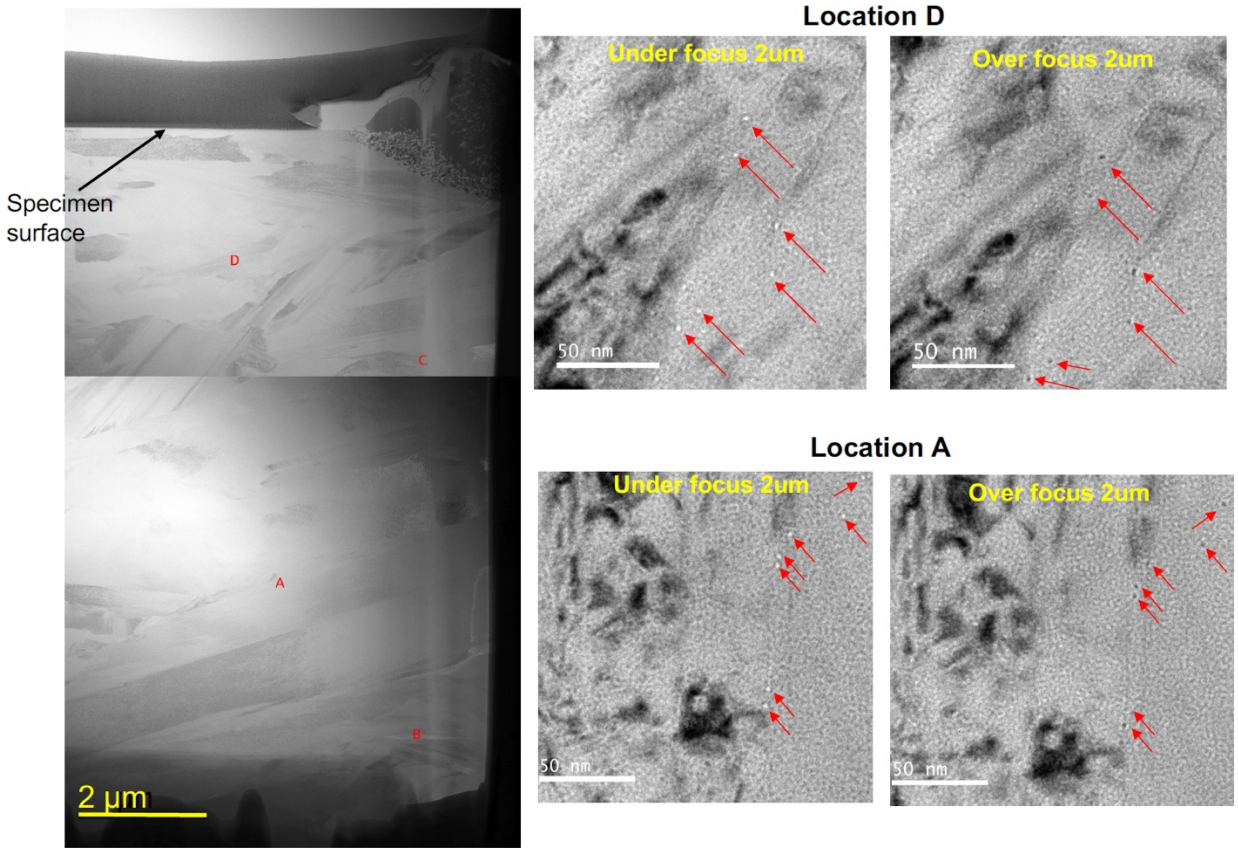

Figure 5. Micrographs of TEM-imaged cavities in neutron irradiated 3C-SiC with in-situ He implantation.

Figure 5 shows the TEM bright field image of the observed area (~10 μm) below the free surface together with the under- and over-focused cavity images of two selected areas, locations D (2 μm below surface) and A (7.5 μm below surface), respectively. Note that the Ni foil implanter created a uniform He/dpa area with a depth of 11μm, covering the current observed areas. It is evident that cavities with a diameter of ~ 2.5 nm were observed, which most likely are helium bubbles due to the homogenous distribution of implanted He within this area. The observation of cavities in SiC at this low irradiation temperature is surprising. Katoh et al. [26] identified the low temperature end for the formation of visible voids in neutron irradiated SiC to be 1100°C. For the samples irradiated under the same condition without in-situ He implantation, no visible voids were observed. In a different study, no voids were either observed in 3C-SiC sample neutron irradiated at 440°C to 31 dpa in the same reactor [27]. Therefore, the introduction of He promoted the nucleation and growth of cavities in 3C-SiC. Actually, Kai et al. [28] also observed the small He bubbles in SiC/SiC composite irradiated with dual-beam (6MeV-Si^{3+} and 1.13MeV-He^{+}) to 100 dpa at 800°C. It is known that He strongly binds with the vacancy defects in SiC [8]. In the sample experiencing neutron irradiation and He implantation, the implanted He is readily captured by the Si or C vacancies surviving the displacement cascade. The He-V_C complex is more predominant due to the relatively smaller formation energy of V_C resulting in more abundant V_C in SiC [22], although the binding energy of He and V_{Si} (1.59 eV) is stronger than that of He-V_C (0.17 eV) [8]. Then the formed He-V complexes are working as nucleation sites to trap mobile defects, consequently, resulting in the formation of the visible cavities shown in Figure 5. Although thermal diffusion of vacancies at this low temperature is negligible due to the large migration energies of Si (2.4eV) and C (3.5eV) vacancies in SiC [22] [23], the radiation enhanced diffusion was supposed to play a more important role in the transportation of involved defects in the sample irradiated up to 30 dpa.

He release during the post-annealing process

Thermal He desorption spectra of both neutron-irradiated with in-situ He implantation and He-implanted samples are shown in Figure 6. The He desorption spectra from the 3C-SiC samples implanted with two different energies (i.e., 10 and 80 keV) to the same fluence (1×10^{19}/m^2) display certain similarities and distinctions. The similarity involves the existence of a major He desorption group in the studied temperature regime, although the peak positions are different. For the sample implanted with 80 keV He ions, the major He desorption peak shifted to 1043°C from 870°C that is the peak position of 10keV He-implanted sample. The peak position shift for high energy implantation has been widely observed in other TDS measurements [9] [29]. This behavior is certainly due to a reduced probability for He to escape to the free surface when the He is implanted deeper. Moreover, for higher energy implantation, more defects are created and thus He is more likely to be trapped in more and larger defect clusters, which require higher temperature to drive He to dissociate. The other difference is that the magnitude of the desorption peak for higher energy He ion implanted sample is smaller than that of low energy implanted sample. The total desorbed He can be acquired by the integration of measured desorbed He flux. The results indicated that 86% and 44% of implanted He were desorbed from the 10keV and 80 keV He ion implanted samples, respectively, implying that more He were trapped in thermally stable H-defect clusters. It is noted that the maximum temperature in the current TDS measurement is 1600°C, 60% of the dissociation point of SiC. Therefore, the contained He will not be completely released until the sample is melting. Actually, He started to be desorbed again at 1400°C following the completion of the major He desorption group, as shown in Figure 6. It is expected that higher temperature beyond 1600°C will continue to enhance the evolution of He-defect clusters and promote the dissociation of He from unstable He-defect clusters. More significant He desorption groups could be observed in the higher temperature regime (>1600°C).

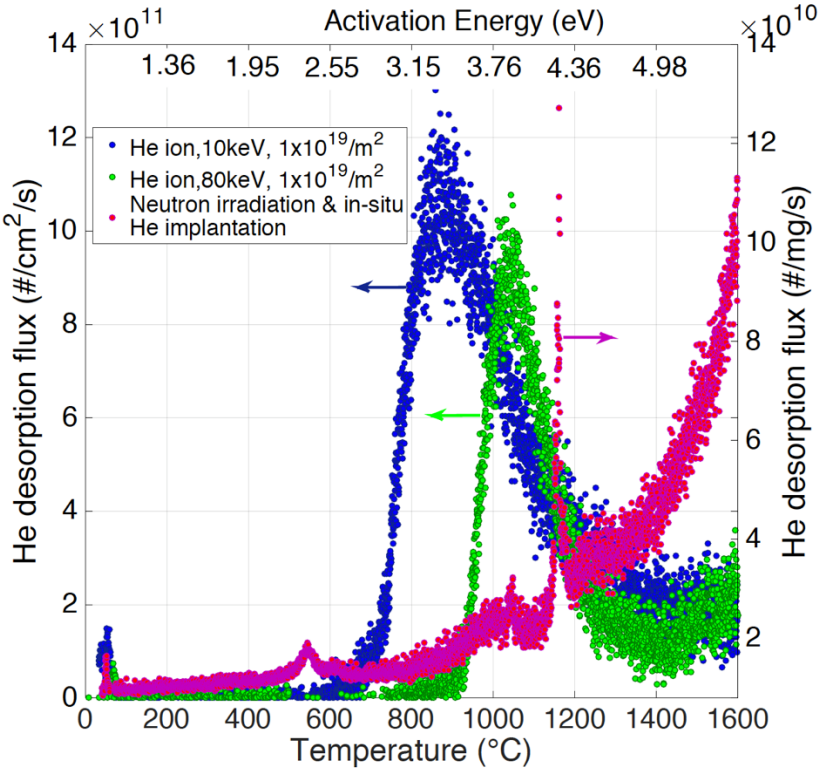

Figure 6. Thermal helium desorption spectra from He implanted 3C-SiC (10keV, 80keV to a fluence of 1×10^{19}/m^2) and neutron-irradiated 3C-SiC with in-situ He implantation (500°C, 30 dpa, 58 appm He/dpa).

Helium desorption spectrum from the neutron irradiated sample with in-situ He implantation was also shown in Figure 6. It displayed a completely different He desorption behavior in comparison with that from He-ion implanted samples. Generally, the desorption spectra showed a continuously increasing He release flux up to the maximum temperature during the TDS measurement, leaving an incompletely developed desorption peak behind. The other noticeable feature is that a sharp peak occurred at 1163°C, and this excessive sharpness is inconsistent with a first order dissociation model as generally adopted in classical rate-theory. Such a sharp peak has also been observed for high purity iron under other implantation conditions [29, 30], which is primarily due to the alpha-gamma phase transformation. However, 3C-SiC is relatively stable below 2100°C without showing any phase transformation [1] . It is unclear what mechanism is responsible for this sharp He release. The average diffusion rate of He within perfect SiC is calculated as 32 nm/s based on the diffusion parameters provided in [31]. Therefore, the fast diffusion of He in the grain interior is not realistic. A possible explanation could be a specific He-defect cluster with significant concentration was fully dissociated in a narrow temperature region around 1163°C while a quick pathway for He diffusion is present to enable the fast release of He (most likely grain boundaries present within the studied SiC).

The significant difference between the He desorption spectra of ion-implanted and neutron-irradiated SiC highlighted the limitation of applying ion irradiation to investigate the synergism of He and irradiation damage in the real service environment. As to neutron irradiation, the damage production is relatively homogeneous due to the small cross section of energy transfer when traveling within materials. The complex mixed neutron energy spectrum created various displacement cascades, resulting in surviving defect clusters with different sizes, accompanied by the introduction of He from the Ni foil implanter. Considering the strong interactions between He and irradiation-induced defects, the implanted He is expected to be readily captured by the adjacent defects, especially the vacancy and its clusters. Therefore, the microstructure of this neutron-irradiated SiC with in-situ He implantation includes homogeneously distributed He-defect clusters with various sizes. Actually, He bubbles with ~2.5nm in diameter were observed as shown in Figure 5. For the He ion-implanted samples, strong spatial dependence of damage production and He distribution resulted in a completely different microstructure. The much higher damage rate (~10^{-3}dpa/s in ion irradiation *vs* ~10^{-7}dpa/s in neutron irradiation) in the ion implanted SiC also posed impacts on the microstructural evolution. For a SiC implanted with 1MeV He ions to 1300 appm He under a He/dpa ratio of 130 at 1000°C, no He bubbles were observed [15]. Therefore, no visible bubbles are expected in the ion implanted samples in this study, which was implanted with 10keV and 80keV He ions to a fluence of 1×10^{19}/m^2 at room temperature. The heat treatment during TDS measurements drives significant evolution of He-defect clusters and intrinsic defect clusters, like the growth of He-vacancy clusters following Ostwald ripening process, dissociation of He-defect clusters due to the thermal instability of the clusters at high temperature, etc. Therefore, the completely different initial microstructures led to the two different evolution routes of the He desorption behavior in the subsequent TDS measurements.

The stability of the He-defect clusters could be evaluated by activation energies of He dissociating from various trapping sites, which could be calculated by applying the simple first order de-trapping mechanism with attempt frequencies of the order of the Debye frequency ($\nu=10^{13}$/s). The evolution of the remaining He content in SiC could be expressed by

$$\frac{dN}{dt} = -Nv exp\left(-\frac{E}{k_B T}\right) \quad (1)$$

where N is the number density of remaining He atoms in the sample, E is the activation energy, kB is the Boltzmann constant, and T is the temperature associated with the desorption peak. By solving $\frac{d^2N}{dt^2} = 0$ under the linear ramp (i.e., $\frac{dT}{dt} = \beta$, β is the ramping rate), the activation energy corresponding to each He desorption peak could be calculated using

$$ln(\beta/T^2) = -\frac{E}{k_B T} + ln\left(\frac{v k_B}{E}\right) \quad (2)$$

In Figure 6, activation energies of He desorption corresponding to each temperature point was labeled in the top x axis. Note that the activation energy of He dissociating from the trapping site is a sum of the binding energy and the migration energy of He. The available migration energies of He in SiC in literature are listed in Table 1. Large discrepancy exists for the results from experiments and modeling. The migration energy of interstitial He in SiC varies in the range from 0.9 to 2.6eV. The binding energy of He to the corresponding trapping sites could then be obtained by subtracting the migration energy from the calculated activation energy. By comparing with the theoretical analysis, one could identify the possible trapping site for He at each temperature point. If taking the He migration energy as 2.5eV, the binding energy of He and the trapping site responsible for the sharp He desorption peak is 1.7eV, close to the He binding energy of He_4V_{Si} cluster (1.6eV) [8]. Similarly, the binding energies of He and trapping sites responsible for the major desorption peaks of the two He-implanted samples are calculated as 0.9 and 1.4 eV, corresponding to the clusters of He_9V_{Si} and He_2V_{Si}, respectively. It is emphasized here that the binding energy of He-vacancy is a function of He/V ratio, implying that the clusters with same He/V ratio might have the same He binding energies. Additionally, the observed He desorption is a collective result of complex evolution of all clusters present in the materials. Therefore, these listed clusters are only a part of the He-defect clusters responsible for each desorption peaks. The lack of comprehensive theoretical study on the interactions between He and defects in 3C-SiC limited our further interpretation of the observed He desorption spectra. A complete picture of the evolution of He-defect clusters could not be obtained at this moment.

Table 1. Migration energy of interstitial helium in SiC

Sample type	Migration Energy of Helium (eV)	Method	Reference
Unknown SiC	1.1	Helium release measurement	[32]
Sintered α-SiC	0.9	Post-irradiation helium release experiment	[18]
4H-SiC	2.6	Neutron reaction analysis	[31]
3C-SiC	2.5	DFT simulation	[7]

Microstructure of neutron irradiated samples following TDS measurements

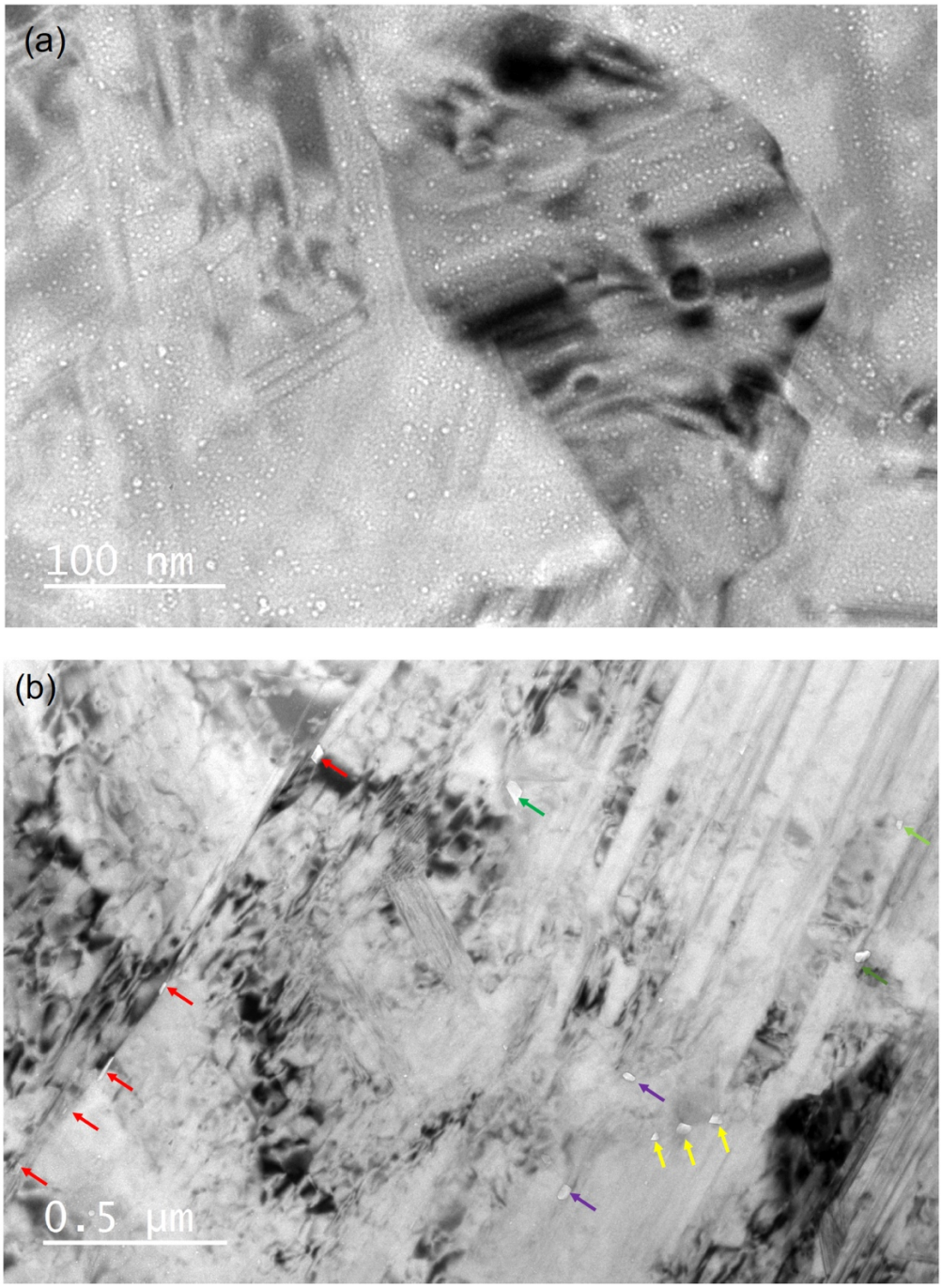

Figure 7. TEM bright field images of neutron irradiated 3C-SiC (a) without and (b) with in-situ helium implantation following the heat treatment in TDS measurements. The large helium bubbles along grain boundaries are labeled with arrows.

The TEM observations were further performed on the neutron-irradiated 3C-SiC samples with and without in-situ He implantation to capture the impact of in-situ He implantation on the microstructural evolution following the heat treatment during TDS measurements. The TEM bright field images and the corresponding cavity size distributions are shown in Figure 7 and Figure 8, respectively. As shown in Figure 7 (a), it is apparent that a great number density of cavities were distributed homogeneously throughout the grain interior in the neutron irradiated 3C-SiC without in-situ He implantation following the TDS heat treatment. No cavities were observed along the grain boundaries, implying these cavities are actually voids. It is noted that most of the large visible voids are faceted. The void size distribution basically falls in a Gaussian pattern, as shown in Figure 8 (a). The maximum annealing temperature used in the current study is 1600°C. Therefore, it is not surprising that abundant visible voids were observed within the samples, owing to the enhanced mobility of vacancies when temperature was greater than 1100°C.

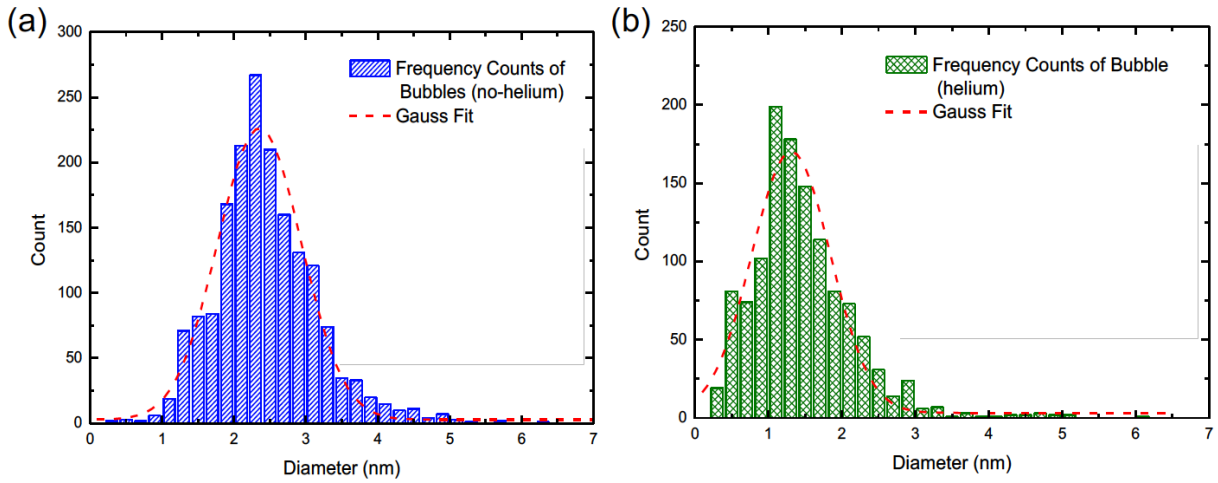

Figure 8. Cavity size distribution in neutron irradiated 3C-SiC (a) without and (b) with in-situ helium implantation.

The SiC samples experiencing simultaneous neutron irradiation and He implantation displayed certain similarities and distinctions in comparison with the non-He neutron irradiated samples. The similarity involves the presence of abundant cavities in the grain interior with similar Gaussian size distribution, as shown in Figure 8 (b). These observed cavities are more likely the He bubbles considering the intensive He implantation within this damaged area. The average size of visible He bubbles is 1.3nm, less than that of non-He neutron-irradiated SiC. The reduced bubble size is due to the fact that the vacancy clusters capturing He atoms become much more stable, and thus, the mobility of them reduces. A significant difference in the microstructure observed in this sample was that large He bubbles exist along the grain boundaries or stacking faults, which are all faceted. Grain boundaries are working as strong sinks for mobile species (i.e., helium, vacancy, etc.) contained in the studied materials. Similar phenomena were also observed in neutron- and ion-irradiated SiC at elevated temperatures [14, 26, 28].

Conclusions

The microstructural evolution in 3C-SiC subject to simultaneous He implantation and neutron irradiation at 500°C to 30 dpa was examined before and after TDS measurements by using TEM. The TDS measurements on both neutron-irradiated and ion-implanted samples were also performed to capture the fundamentals of He-defect interactions in 3C-SiC. The main results obtained are summarized as follows:

(1) The designed Ni foil implanter is an efficient way to provide in-situ He-implantation to SiC exposed to neutron irradiation at desired He/dpa ratios and He concentrations relative to the real service environment.

(2) The major irradiation defects in 3C-SiC following neutron irradiation without in-situ He implantation are still Frank faulted loop, same as other studies of neutron irradiated (irradiation temperature < 1100°C) and ion irradiated (irradiation temperature <1000°C) SiC. The presence of implanted He promoted the formation of He bubbles in SiC at such low irradiation temperature to 30dpa, indicating helium stabilized the defect clusters.
(3) Thermal He desorption spectra of ion-implanted and neutron-irradiated 3C-SiC display complete different features, which strongly depends on the initial microstructures of samples. The lack of comprehensive theoretical studies of He-defect interactions in SiC limited the current understanding of the experimental data.
(4) The microstructure of neutron-irradiated 3C-SiC with in-situ He implantation following TDS measurements showed the existence of large faceted He bubbles along grain boundaries and stacking faults. The average cavity size in the grain interior is smaller than that of non-He neutron-irradiated SiC samples but with similar Gaussian size distribution. The existence of He prohibited the growth of cavities by decreasing the mobility of vacancy and its clusters.

References

[1] Snead, L.L., et al., *Handbook of SiC properties for fuel performance modeling.* Journal of Nuclear Materials, 2007. **371**(1-3): p. 329-377.
[2] Price, R.J., *Properties of Silicon Carbide for Nuclear Fuel Particle Coatings.* Nuclear Technology, 1977. **35**: p. 320-336.
[3] Zinkle, S.J., K.A. Terrani, and L.L. Snead, *Motivation for utilizing new high-performance advanced materials in nuclear energy systems.* Current Opinion in Solid State and Materials Science, 2016. **20**(6): p. 401-410.
[4] Hasegawa, A., et al., *Critical issues and current status of SiC/SiC composites for fusion.* Journal of Nuclear Materials, 2000. **283-287**: p. 128-137.
[5] Snead, L.L., et al., *Status of silicon carbide composites for fusion.* Journal of Nuclear Materials, 1996. **233-237**: p. 26-36.
[6] Katoh, Y., H. Kishimoto, and A. Kohyama, *The influences of irradiation temperature and helium production on the dimensional stability of silicon carbide.* Journal of Nuclear Materials, 2002. **307-311**: p. 1221-1226.
[7] Van Ginhoven, R.M., et al., *Theoretical study of helium insertion and diffusion in 3C-SiC.* Journal of Nuclear Materials, 2006. **348**(1-2): p. 51-59.
[8] Sun, D., et al., *Interaction between helium and intrinsic point defects in 3C-SiC single crystal.* Journal of Applied Physics, 2017. **121**: p. 225111.
[9] Oliviero, E., et al., *Helium implantation defects in SiC studied by thermal helium desorption spectrometry.* Nuclear Instruments and Methods in Physics Research B, 2002. **186**: p. 223-228.
[10] Svetukhin, V.V., A.S. Kadochkin, and V.D. Risovanyi, *Determining the parameters of helium accumulation centers in irradiated silicon carbide from thermodesorption spectra.* Technical Physics Letters, 2013. **39**(2): p. 226-228.
[11] Barbot, J.F., et al., *Helium implantation into 4H-SiC.* physica status solidi (a), 2009. **206**(8): p. 1916-1923.
[12] Smith, R.J., et al., *NRA and ERDA investigation of helium retention in SiC as a function of irradiation and annealing.* Nuclear Instruments and Methods in Physics Research Section B: Beam Interactions with Materials and Atoms, 2004. **219-220**: p. 631-635.
[13] Nogami, S. and A. Hasegawa, *Indentation Properties of Silicon Carbide after Neutron Irradiation and Helium Implantation.* IOP Conference Series: Materials Science and Engineering, 2011. **18**(16): p. 162007.
[14] Kondo, S., T. Hinoki, and A. Kohyama, *Synergistic Effects of Heavy Ion and Helium Irradiation on Microstructural and Dimensional Change in beta-SiC.* Materials Transactions, 2005. **46**(6): p. 1388-1392.
[15] Taguchi, T., et al., *Synergistic effects of implanted helium and hydrogen and the effect of irradiation temperature on the microstructure of SiC/SiC composites.* Journal of Nuclear Materials, 2004. **335**(3): p. 508-514.

[16] Chen, J. and P. Jung, *Effect of helium on radiation damage in a SiC/C composite.* Ceramics International, 2000. **26**: p. 513-516.
[17] Pramono, Y., M. Imai, and T. Yano, *Helium Release and Physical Property Change of Neutron-Irradiated α-SiC Containing B4C of Different10B Concentrations.* Journal of Nuclear Science and Technology, 2003. **40**(7): p. 531-536.
[18] Pramono, Y., K. Sasaki, and T. Yano, *Release and Diffusion Rate of Helium in Neutron-Irradiated SiC.* Journal of Nuclear Science and Technology, 2004. **41**(7): p. 751-755.
[19] Yamamoto, T., et al., *The transport and fate of helium in nanostructured ferritic alloys at fusion relevant He/dpa ratios and dpa rates.* Journal of Nuclear Materials, 2007. **367-370**: p. 399-410.
[20] Campbell, A.A., et al., *Method for analyzing passive silicon carbide thermometry with a continuous dilatometer to determine irradiation temperature.* Nuclear Instruments and Methods in Physics Research Section B: Beam Interactions with Materials and Atoms, 2016. **370**: p. 49-58.
[21] Hu, X., et al., *Impact of neutron irradiation on thermal helium desorption from iron.* Journal of Nuclear Materials, 2017. **489**: p. 109-117.
[22] Bockstedte, M., A. Mattausch, and O. Pankratov, *Ab initiostudy of the migration of intrinsic defects in3C−SiC.* Physical Review B, 2003. **68**(20).
[23] Gao, F., et al., *Ab initioand empirical-potential studies of defect properties in3C−SiC.* Physical Review B, 2001. **64**(24).
[24] Kirkegaard, P., J.V. Olsen, and M. Eldrup, *A software package for analysing positron lifetime spectra.* 2016.
[25] Hu, X., et al., *Positron annihilation spectroscopy investigation of vacancy defects in neutron-irradiated 3C-SiC.* Physical Review B, 2017. **95**(10).
[26] Katoh, Y., et al., *Microstructural development in cubic silicon carbide during irradiation at elevated temperatures.* Journal of Nuclear Materials, 2006. **351**(1-3): p. 228-240.
[27] Koyanagi, T., et al., *Neutron-irradiation creep of silicon carbide materials beyond the initial transient.* Journal of Nuclear Materials, 2016. **478**: p. 97-111.
[28] Chen, K.F., et al., *Quantifying helium distribution in dual-ion beam irradiated SiCf/SiC composites by electron energy loss spectroscopy.* Progress in Nuclear Energy, 2012. **57**: p. 46-51.
[29] Hu, X., D. Xu, and B.D. Wirth, *Quantifying He-point defect interactions in Fe through coordinated experimental and modeling studies of He-ion implanted single-crystal Fe.* Journal of Nuclear Materials, 2013. **442**(1-3): p. S649-S654.
[30] Xu, D. and B.D. Wirth, *Post-implantation thermal desorption of helium from poly- and single-crystalline iron.* Journal of Nuclear Materials, 2009. **386-388**: p. 395-399.
[31] Cherniak, D.J., et al., *Diffusion of helium in SiC and implications for retention of cosmogenic He.* Geochimica et Cosmochimica Acta, 2016. **192**: p. 248-257.
[32] Jung, P., *Diffusion and retention of helium in graphite and silicon carbide.* Journal of Nuclear Materials, 1992. **191-194**: p. 377-381.

3.5 PRECIPITATES AND VOIDS IN CUBIC SILICON CARBIDE IMPLANTED WITH $^{25}Mg^{+}$ IONS—Weilin Jiang, Steven R. Spurgeon, Jia Liu, Daniel K. Schreiber, Hee Joon Jung, Arun Devaraj, Danny J. Edwards, Charles H. Henager Jr., Richard J. Kurtz (Pacific Northwest National Laboratory), and Yongqiang Wang (Los Alamos National Laboratory)

This is an extended abstract presenting some of the major results of a paper recently published in the *Journal of Nuclear Materials* https://doi.org/10.1016/j.jnucmat.2017.10.046 [1].

ABSTRACT

This study reports on the formation of ^{25}Mg-bearing precipitates and voids in cubic phase silicon carbide (3C-SiC) single crystals implanted to 9.6×10^{16} $^{25}Mg^{+}/cm^{2}$ at 673 K and subsequently annealed at 1073 and 1573 K for 2, 6 and 12 h in an Ar environment. Unidirectionally aligned tetrahedral precipitates are observed around the Mg profile peak, many of which are likely cubic MgC_2 and tetragonal Mg_2Si particles or their precursor structures. There is also evidence that suggests a possible formation of core (MgC_2)-shell (Mg_2Si) structure in some of the large precipitates. In addition, small spherical voids are observed near the surface, along with the larger faceted voids in the region of maximum vacancy concentration. ^{25}Mg segregation takes place with a dominant fraction of small atomic clusters. The study provides important results needed to fully assess SiC for potential fusion applications.

HIGHLIGHTS

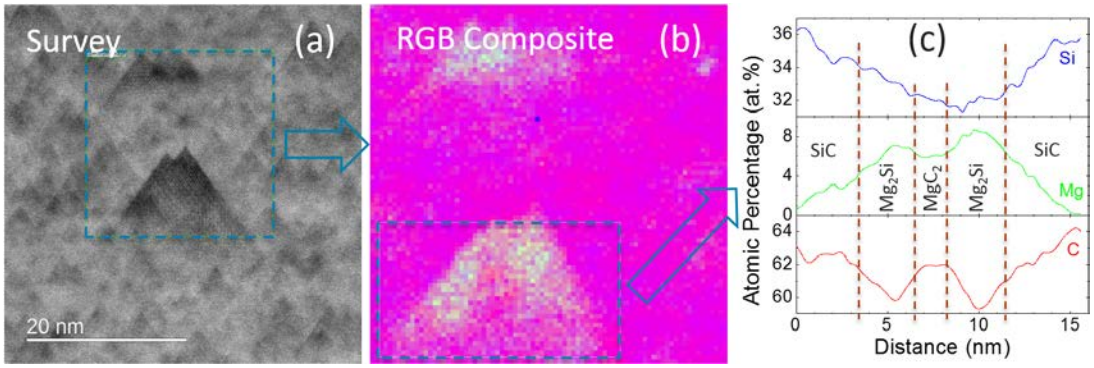

Figure 1. (a) HAADF-STEM image of 3C-SiC implanted to 9.6×10^{16} $^{25}Mg/cm^{2}$ and annealed at 1573 K for 12 h. (b) STEM-EELS map of all the elements. (c) Elemental profiles across a selected region.

Figure 1(a) shows a high concentration of unidirectionally aligned tetrahedral precipitates formed near the Mg profile peak in 3C-SiC implanted to 9.6×10^{16} $^{25}Mg^{+}/cm^{2}$ at 673 K and annealed at 1573 K for 12 h in an Ar environment. A composite STEM-EELS map and the elemental concentration profiles across a large precipitate are shown in Figures 1(b) and 1(c), respectively. While the Si concentration shows a broad valley, the C concentration exhibits a peak near the center of the precipitate, which is located at the minimum intensity of the double Mg peak profile. The overall higher concentrations of Si and C may be attributed to the predominant composition in the volume of the STEM-EELS analysis due to the film thickness. From Figure 1(c), the Mg-bearing

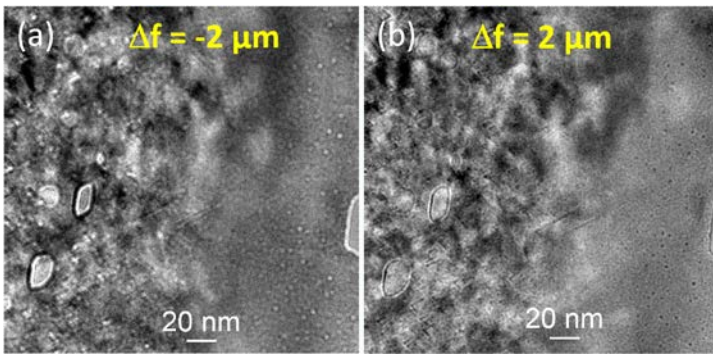

Figure 2. (a) Under- and (b) over-focus bright-field TEM micrographs in the same sample as in Figure 1.

precipitate appears to have a core-shell structure of SiC, Mg_2Si, MgC_2, Mg_2Si, and SiC across the volume, as indicated in the figure. The data may suggest the formation of the precipitates or precursor structures of Mg_2Si and MgC_2 in the neighborhood. It should be noted that image overlap due to specimen thickness effects could produce similar compositional variations in a one-dimensional plot. Figure 2 provides evidence for the formation of small spherical voids in the near-surface region and larger faceted voids near the vacancy peak.

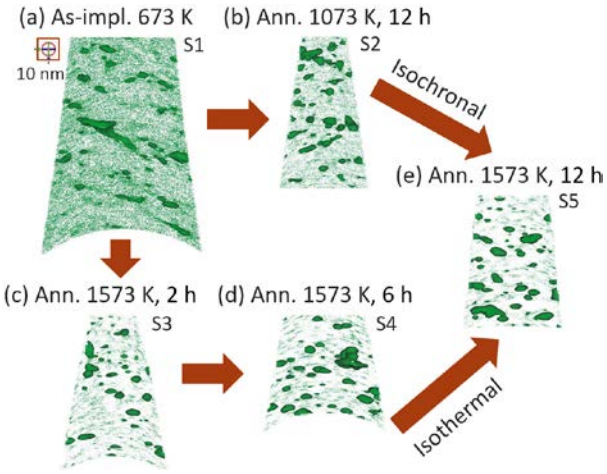

Figure 3. Isoconcentration surfaces at 10 at.% ^{25}Mg in 3C-SiC (a) implanted to 9.6×10^{16} $^{25}Mg/cm^2$ at 673 K and annealed at (b) 1073 K, 12 h, (c) 1573 K, 2 h, (d) 1573 K, 6 h, and (e) 1573 K, 12 h in Ar.

A series of isoconcentration surfaces at 10 at.% ^{25}Mg are shown in Figure 3 as a function of annealing temperature and duration in isochronal and isothermal annealing processes, respectively. For 12 h isochronal annealing, the density of the green dots that represent ^{25}Mg atomic clusters decreases with increasing temperature from 1073 to 1573 K. A similar trend is also observed with increasing duration from 2 to 12 h in the isothermal annealing at 1573 K, but the change is more gradual.

Table 1. APT results for ^{25}Mg-bearing precipitates in 3C-SiC

Sample ID	Max Isoconc. Surf. (^{25}Mg%)	^{25}Mg Conc. Peak (at.%)	^{25}Mg Conc. Matrix (at.%)	Precipitate Size (nm) Gyration Dia. ± Dev.	Precipitate Size (nm) Max. Ext. Dia. ± Dev.	Ave. N ± Dev. of ^{25}Mg in Precipitate (counts)	Precipitate Number (counts)	Precipitate Density (cm^{-3})
S1	23	19	5.7	4.5 ± 6.8	11.5 ± 17.6	1439±3373	138	6.1×10^{17}
S2	34	26	4.3	2.4 ± 2.9	6.7 ± 8.0	567±692	72	1.5×10^{18}
S3	60	46	1.9	2.7 ± 4.0	8.4 ± 11.0	583±756	89	1.5×10^{18}
S4	75	48	1.8	2.5 ± 3.1	7.8 ± 8.9	917±1347	107	1.5×10^{18}
S5	85	48	1.4	2.4 ± 2.7	7.5 ± 8.5	680±1007	93	1.6×10^{18}

The precipitate size and number density are analyzed and summarized in Table 1. The precipitate size shows a maximum value of 11.5 ± 17.6 nm for the as-implanted 3C-SiC at 673 K (S1). Thermal annealing at 1073 K for 12 h (S2) reduces the precipitate size to 6.7 ± 8.0 nm. Further annealing at 1573 K for 12 h (S5) increases the size only slightly to 7.5 ± 8.5 nm. Isothermal annealing at 1573 K does not significantly change the average precipitate size. The largest precipitate size for S1 may be a result of irradiation-enhanced diffusion and precipitation. The reduction in the size may be associated with phase decomposition during annealing, followed by precipitation below the melting points of the precipitates (~1073 K) during cooling. Thus, the duration at the same high annealing temperature (1573 K) is not expected to significantly affect precipitate size. The precipitate number density is relatively low (6.1×10^{17} cm^{-3}) for S1, increases significantly to 1.5×10^{18} cm^{-3} at 1073 K (S2) and then slightly to 1.6×10^{18} cm^{-3} at 1573 K (S5) during the 12 h isochronal annealing; it also first increases to 1.5×10^{18} cm^{-3} for 2 h (S3), and then remains nearly unchanged for 6 h (S4) and 12 h (S5) during the isothermal annealing at 1573 K.

References

[1] W. Jiang, S. R. Spurgeon, J. Liu, D. K. Schreiber, H. J. Jung, A. Devaraj, D. J. Edwards, C. H. Henager Jr., R. J. Kurtz, and Y. Wang, Journal of Nuclear Materials 498 (2018) 321-331; https://doi.org/10.1016/j.jnucmat.2017.10.046.

4. HIGH HEAT FLUX MATERIALS AND COMPONENT TESTING

4.1 TEM CHARACTERIZATION OF MULTIMODAL PRECIPITATES IN NOVEL COPPER ALLOYS FOR FUSION ENERGY APPLICATIONS—Ying Yang (Oak Ridge National Laboratory), Ling Wang (University of Tennessee at Knoxville), Steven J. Zinkle (University of Tennessee at Knoxville and Oak Ridge National Lab), and Lance Snead (Stony Brook University)

OBJECTIVE

This study aims at developing high strength; high conductivity Cu alloys with improved thermal creep strength for long pulse fusion high heat flux structures, through an accelerated approach of computational thermodynamics guided alloy design.

SUMMARY

Detailed transmission electron microscopy (TEM) compositional analysis has been conducted for the Cu-Cr-Nb-Zr alloy Cu-2Cr-1.35Nb-0.15Zr. Multiple precipitates have been identified, featured by large grain boundary Cr_2Nb-Laves-phase and Cr-rich (Cr,Fe) precipitates, and smaller matrix Cr precipitates. Fe contamination has been found in the samples.

PROGRESS AND STATUS

TEM composition characterization

The TEM samples were lifted out using a Field Electron and Ion Company (FEI) Versa 3D focused-ion-beam (FIB) system. The matrix and grain boundary precipitates were characterized using a Japan Electron Optics Laboratory (JEOL) 2100F TEM. The energy dispersive x-ray spectroscopy (EDS) capability of an FEI Talos F200X TEM was employed for compositional analysis.

The TEM composition characterization was performed on the solutionized and aged 1CCNZ-a-70 alloy, Cu-2Cr-1.35Nb-0.15Zr. Three types of precipitates have been identified: large grain boundary Laves phase, coarse Cr particles, and fine-scale Cr matrix precipitates. A cluster of Cr_2(Nb,Zr) C14 Laves precipitates at a grain boundary is shown in Figure 1 (a). The Laves-phase precipitates were found to contain internal stacking faults and have a size range from 350 nm to 1 um. The composition maps of Cu, Cr, Nb and Zr are shown in Figures 1 (b~e). The Laves phase mainly consists of Cr and Nb, with a trace amount of uniformly distributed Zr. A Cr-rich phase is observed together with the Laves phase (Figures 1c-f). Both the Cr_2(Nb,Zr) and Cr-rich phase should form during solidification, as predicted phases from solidification.

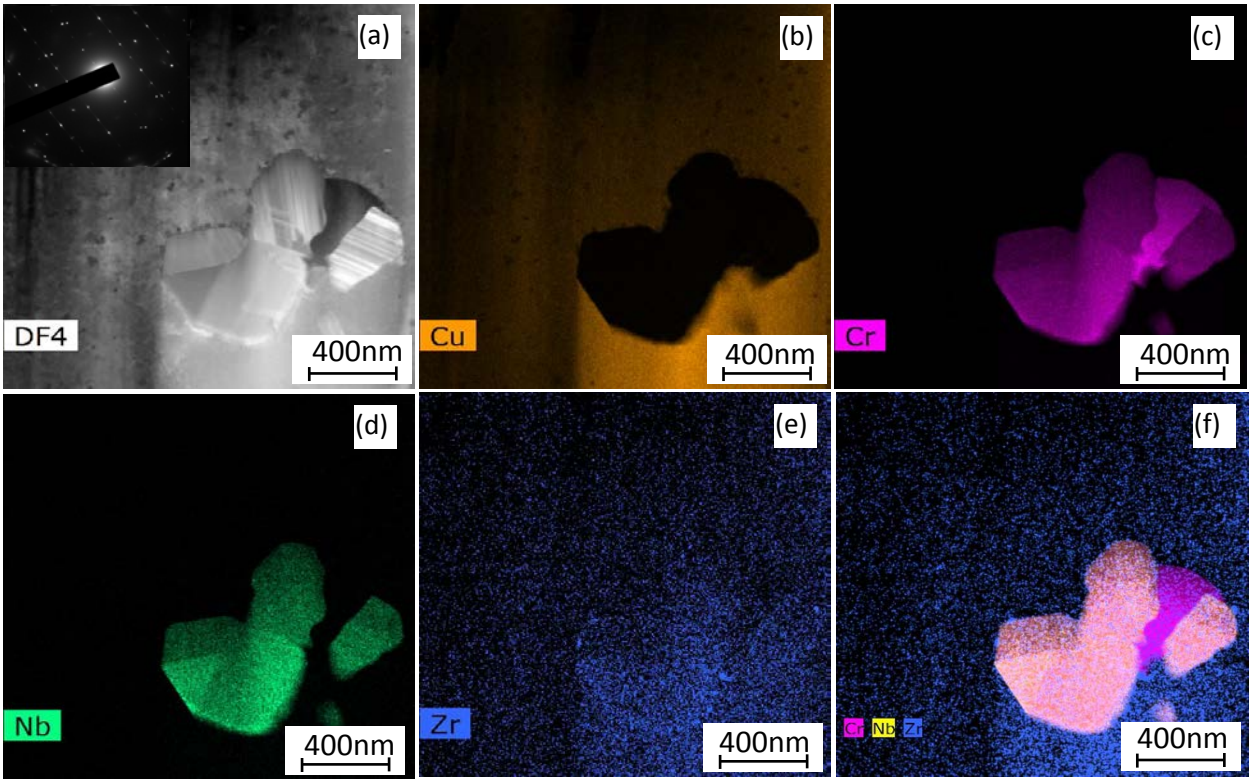

Figure 1. (a) Bright field TEM image of the 1CCNZ-a-70 alloy showing Cr_2(Nb,Zr) C14-Laves phase precipitates along a grain boundary; the insert image is the precipitate diffraction pattern. (b) ~(e) the individual and composite composition maps of Cu, Cr, Nb, Zr. (f) three-elemental-composition map of Cr, Nb and Zr, indicating that Zr is uniformly distributed both in the matrix and Laves phases.

The second type of observed precipitate is the relatively coarse Cr phase with a diameter between 150 nm and 350 nm, as shown with the four precipitates in Figure 2 (a~b) either at grain boundaries or in the grain interior. Figure 2 (Cr~Fe) are the composition maps of Cu, Cr, Nb and Zr for the precipitates observable in the bright field TEM image in Figure. 2b. Fe contamination was identified in this phase, which was probably introduced during the crushing process of the pre-alloy constituents using the steel mortar. The unintentional Fe contamination (which was not modeled in our computational thermodynamic simulations) was confined to the relatively coarse Cr-rich particles. Based on equilibrium calculation results, these relatively large Cr precipitates are probably formed during the solutioning process at 970°C through grain boundary diffusion.

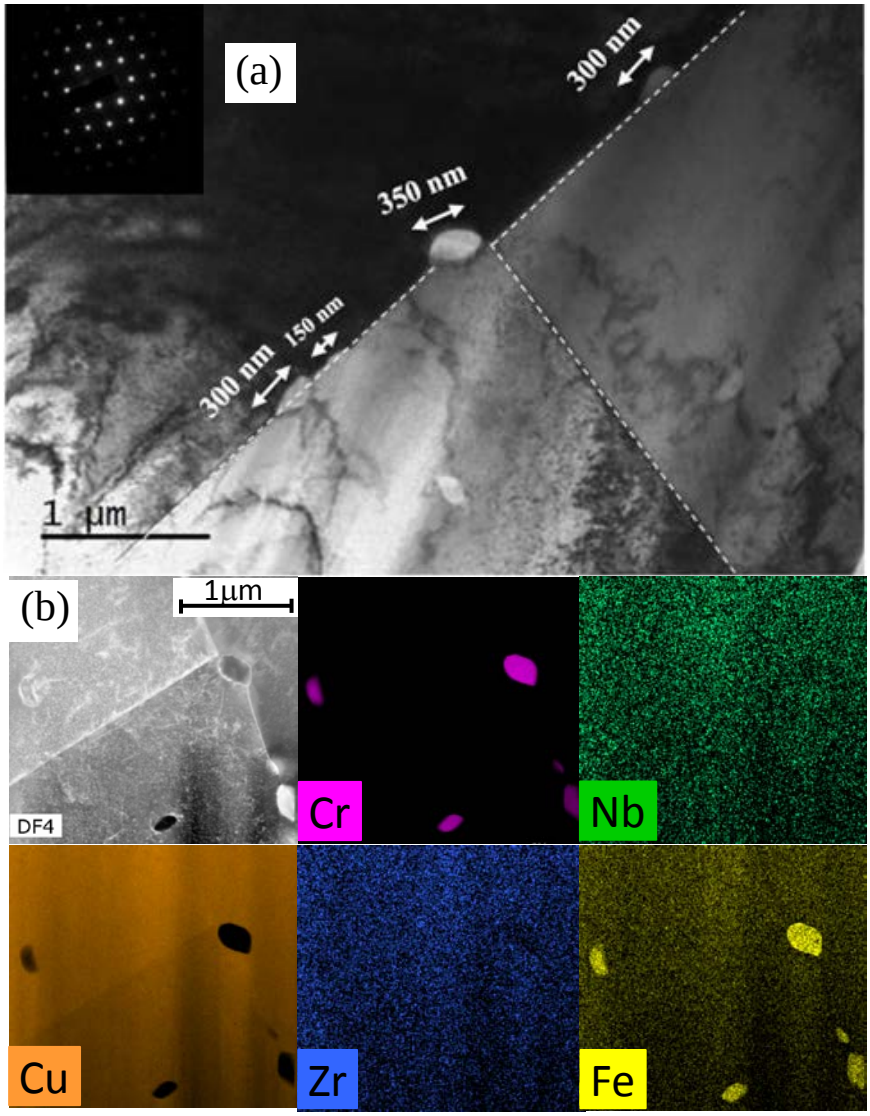

Figure 2. (a) TEM image of the 1CCNZ-a-70 alloy showing the coarse Cr precipitates; the insert image is the diffraction pattern of the Cu matrix on the left (darker) grain. Figures (Cr) ~(Fe) are the individual composition maps of Cu, Cr, Nb, Zr and Fe.

The third type of precipitate is the Cr matrix precipitate, which has been reported in the previous semiannual reports. This type of Cr precipitate is formed during the 475°C aging process. Figures 3(a) and (b) are magnified images selected from the area in the dark grain in Figure 2(a) showing a uniform distribution and nearly spherical shape of Cr precipitates with a typical diameter of 5 to 10 nm. Many of the precipitates are coherent with the matrix, judging from the BF image under two beam conditions when the so-called no contrast line appears in normal direction to the diffraction ***g*** vector. The density of Cr precipitates is approximately $1.3 \times 10^{22}/m^3$. The predicted $Cu_{51}Zr_4$ or Cu_5Zr intermetallic compounds were not observed under TEM, which is probably due to their very small volume fraction (~0.1% predicted from equilibrium calculation; nearly an order of magnitude smaller volume fraction than the Cr matrix precipitates). A second possibility for the absence of the Cu-Zr precipitates might be due to sluggish

formation kinetics at 475°C. However, previous studies on Cu-Cr-Zr alloys have observed a moderate density of Cu-Zr precipitates with sizes several times larger than the Cr matrix precipitates following aging at temperatures near 475°C. Therefore, it seems more likely that Zr participation in Laves phase precipitation has diminished the amount of Zr available for Cu-Zr precipitation during the final aging treatment for the Cu-2Cr-1.35Nb-0.15Zr alloy. In the vicinity of coarser grain boundary Cr-rich ppts, there is a precipitate denuded zone, as shown in Figures 3(c) and (d). The Cr-rich precipitate is the same as that in Figure 2 (a) and (b). The formation of coarser Cr-rich precipitates during the solutioning process depleted Cr close to a grain boundary, therefore leading to the formation of a denuded zone. However, it is not clear why the denuded zone only happened on one side of the grain boundary. The crystallographic orientation of grains might have a role on the diffusivity of Cr.

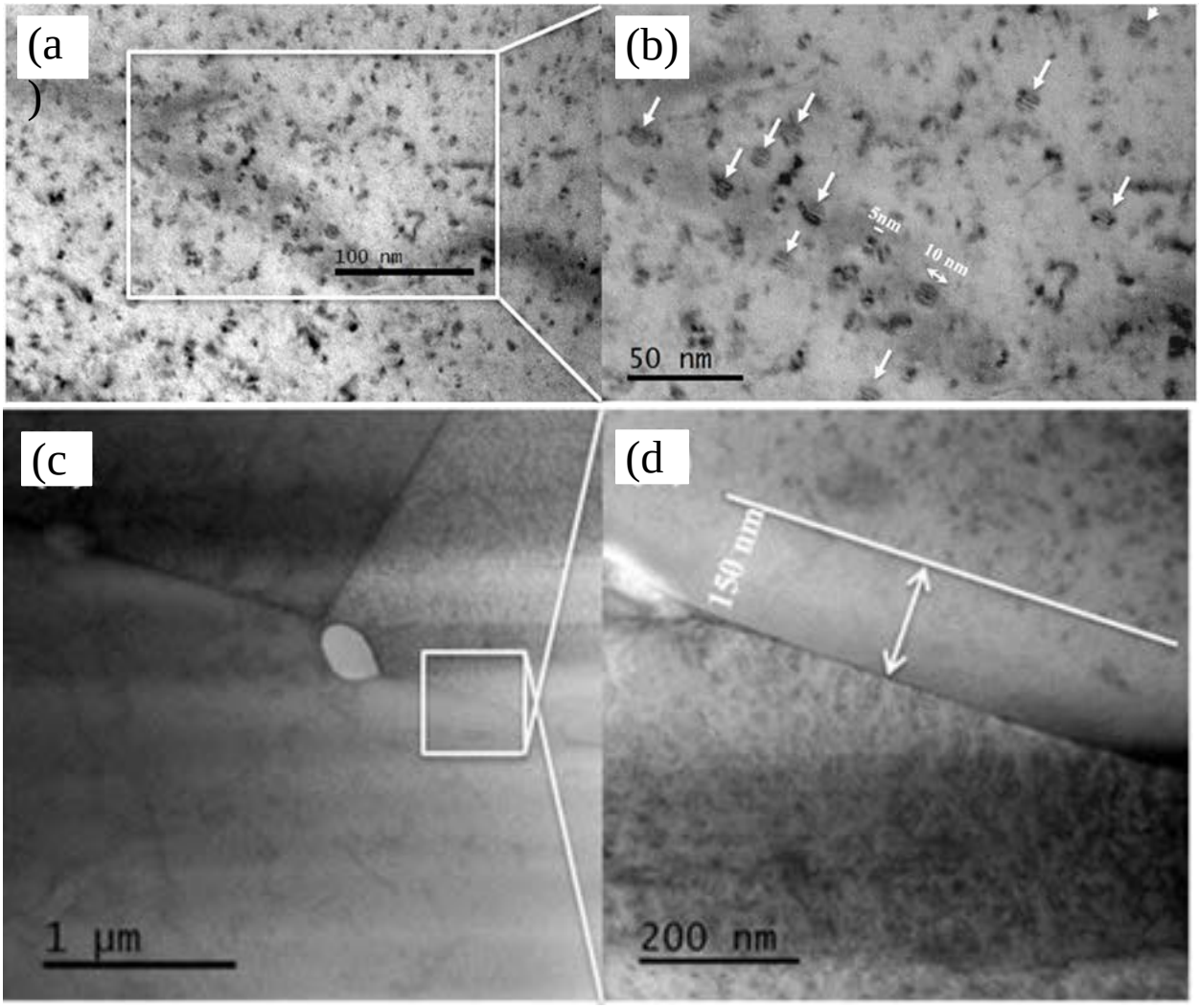

Figure 3. (a~b) TEM image of the 1CCNZ-a-70 alloy showing the fine Cr matrix precipitates. (c-d) TEM images of grain boundary denuded zone in the vicinity of coarser Cr precipitates.

4.2 NEUTRON IRRADIATION EFFECTS IN TUNGSTEN—L.M. Garrison, Y. Katoh (Oak Ridge National Laboratory)

OBJECTIVE

The objective of this work is to evaluate the effects of neutron irradiation on the mechanical properties and microstructure of tungsten-based materials to aid in developing plasma-facing materials for fusion reactors.

SUMMARY

The aim of this work is to evaluate tungsten for potential use as part of a plasma-facing component for future fusion reactors. Single crystal tungsten tensile specimens in the tensile-axis [110] and [100] orientations have been neutron irradiated at temperatures of 90-830°C to fast fluences of 0.01 to 20×10^{25} n/m^2 (E>0.1 MeV) in the mixed-spectrum High Flux Isotope Reactor (HFIR). Analysis of the tensile behavior of these materials reveals that single crystal tungsten exhibits little to no strain hardening after irradiation. The modulus of resilience and modulus of toughness were calculated from the tensile data of the irradiated materials. The [110] orientation tungsten had a maximum modulus of tungsten for all doses at 300°C test temperature, while the [100] orientation tungsten had its maximum at 650°C.

PROGRESS AND STATUS

The tensile test results of the single crystal tungsten from the TITAN campaign have been reported previously. A trend in the tensile results was observed that for many of the irradiated materials, the ultimate tensile strength (UTS) occurred shortly after the yield stress (YS) was reached. In fact, only unirradiated material had uniform elongations (UE) greater than 5% (Figure 1). As dose increased initially, the UE decreased below 5% for all samples. As dose increased further, for samples tested at temperatures up to 500°C, the UE is further reduced to less than 0.5%. The samples with less than 0.5% UE experience no strain hardening.

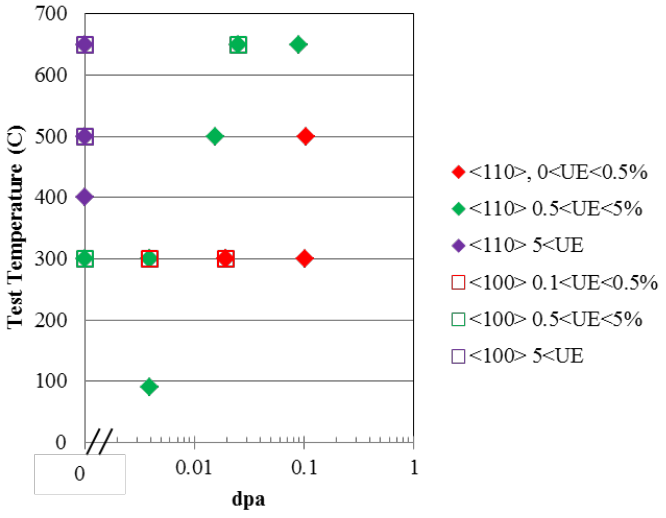

Figure 1. Neutron irradiation reduces the UE of single crystal tungsten of both orientations for ductile tests (those with total elongation ≥ 0.2%).

The modulus of resilience (U_R) is defined as the integral under the stress-strain curve from zero to the strain at the yield point, which is approximately equal to the numerical integration of the stress strain data points (Equation 1).

$$U_R = \frac{1}{100}\int_0^{\epsilon_y} \sigma d\epsilon \approx \sum_{i=1}^{n_y-1} \frac{(\sigma_{i+1}+\sigma_i)}{2}\frac{(\epsilon_{i+1}-\epsilon_i)}{100} \quad (1)$$

In Equation 1, ϵ is the strain expressed as a percentage, ϵ_y is the strain percentage value corresponding to the 0.2% offset yield point, σ is the stress in units MPa, i is the counter for the stress and strain data points in the list, and n_y is the number in the list of data points corresponding to the 0.2% offset yield.

For ductile samples, a triangle approximation was used for the modulus of resilience, U_{R_D} instead of the integral (Equation 2). For the values reported here, the second half of Equation 2 was used, where σ_y is the yield stress and E is a standard elastic modulus of tungsten of 400 GPa. Multiplying the elastic modulus by the unitless factor of m/m allows the modulus of resilience to be expressed in units of MJ/m^3. For brittle samples a modified modulus of resilience (U_{R_B}) was calculated by using the ultimate tensile strength (σ_U), which is equal to the fracture strength, instead of the yield strength (Equation 3).

$$U_{R\_D} \approx \frac{1}{200}\sigma_y\epsilon_y = \frac{1}{2}\frac{(\sigma_y)^2}{E} \quad (2)$$

$$U_{R\_B} \approx \frac{1}{200}\sigma_U\epsilon_U = \frac{1}{2}\frac{(\sigma_U)^2}{E} \quad (3)$$

The modulus of toughness (U_T) is defined as the integral under the stress-strain curve from zero to the fracture point. This is approximately equal to the numerical integration of the stress-strain data points, Equation 4, in which parameters are defined as for the modulus of resilience and additionally ϵ_f is the strain at fracture and n is the number of the final data point in the list of stress-strain points.

$$U_T = \frac{1}{100}\int_0^{\epsilon_f} \sigma d\epsilon \approx \sum_{i=1}^{n-1} \frac{(\sigma_{i+1}+\sigma_i)}{2}\frac{(\epsilon_{i+1}-\epsilon_i)}{100} \quad (4)$$

The modulus of toughness can be divided into the area under the curve up to the yield point, which is the modulus of resilience U_R, plus the area under the remainder of the curve. A further slight approximation is made in that the area under the curve from the yield point to the fracture point is calculated as the area under the curve of the stress-strain values where the elastic strain contribution has been removed. The area under the plastic deformation area of the curve is labeled U_P, and is depicted as the grey shaded region in Figure 2. Figure 2 also illustrates that for ductile samples U_T is significantly larger than U_R. In Equation 5, symbols are defined as in Equations 1-4 and also ϵ_{p_i} is the list of plastic strain values. For the modulus of toughness results discussed below, the Equation 5 version of the definition is used.

$$U_T \approx \frac{1}{200}\sigma_y\epsilon_y + \sum_{i=n_y}^{n-1} \frac{(\sigma_{i+1}+\sigma_i)}{2}\frac{\left(\epsilon_{p\_(i+1)}-\epsilon_{p\_i}\right)}{100} = U_R + U_P \quad (5)$$

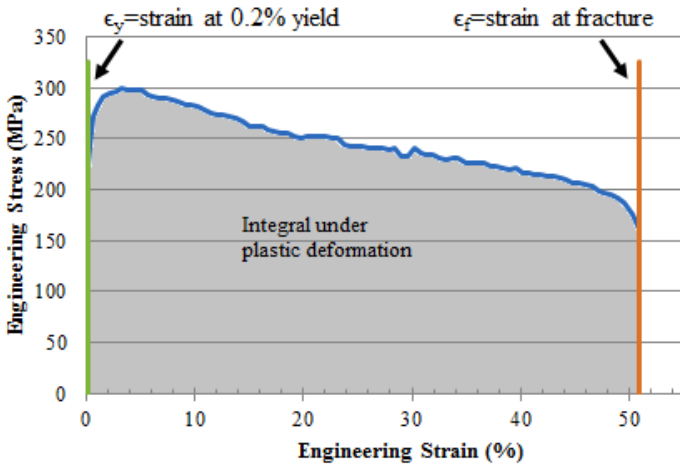

Figure 2. Single crystal unirradiated tungsten tested at 300°C data is used as an example with the elastic strain contribution removed. The shaded area under the curve is labeled U_P, and when added to the modulus of resilience, U_R, it equals the modulus of toughness, U_T.

The modulus of resilience for ductile samples using Equation 2 and brittle samples using Equation 3 are plotted versus test temperature in Figure 3. As is clear in Equations 2-3, the modulus of resilience is proportional to the yield stress (ductile samples) or ultimate tensile strength (brittle samples). Thus, the same trends seen in yield strength and ultimate tensile strength also hold true for the trends in modulus of resilience. The modulus of resilience decreases with increasing test temperature (Figure 3) because the yield strength decreases with increasing test temperature. Also, because the UTS for tests at 22 and 90°C is highest at 0.02 dpa, the modulus of resilience at those test temperatures is also highest for material irradiated to 0.02 dpa. All the modulus of resilience values are in the range 0-2 MJ/m^3.

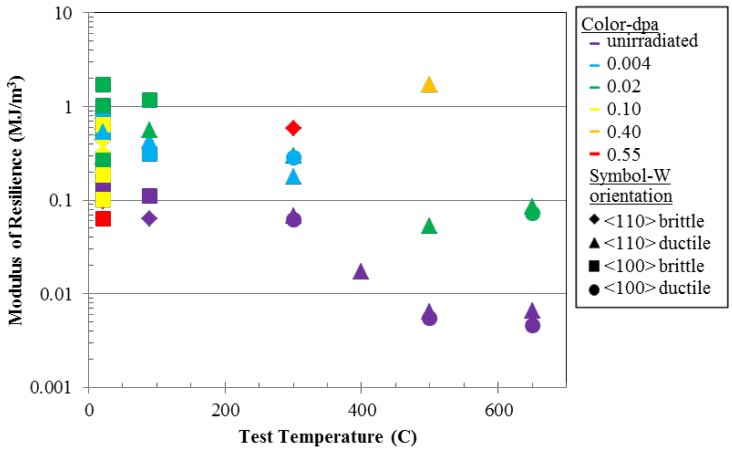

Figure 3. Modulus of resilience for both crystal orientations of tungsten.

In contrast to the modulus of resilience, the modulus of toughness (as defined in Equation 5) does not have a strong dependence on UTS (Figure 4a). Most of the unirradiated samples have lower UTS values and higher modulus of toughness values than the irradiated samples. There does appear to be a drop of modulus of toughness for material that had UTS values above ~600 MPa, but there are also fewer data points in that region, so a trend is difficult to determine.

The correlation between modulus of toughness and TE is clearer (Figure 4b). While there is scatter in the data, as TE increases, so does the modulus of toughness. In the upper right corner of the figure are the unirradiated materials, which had both the longest TE and highest modulus of toughness values. Aside from most of the unirradiated data points being grouped together, there is not a clear trend with increasing dose. However, it is clear that the materials with the lowest TE also have the lowest modulus of toughness.

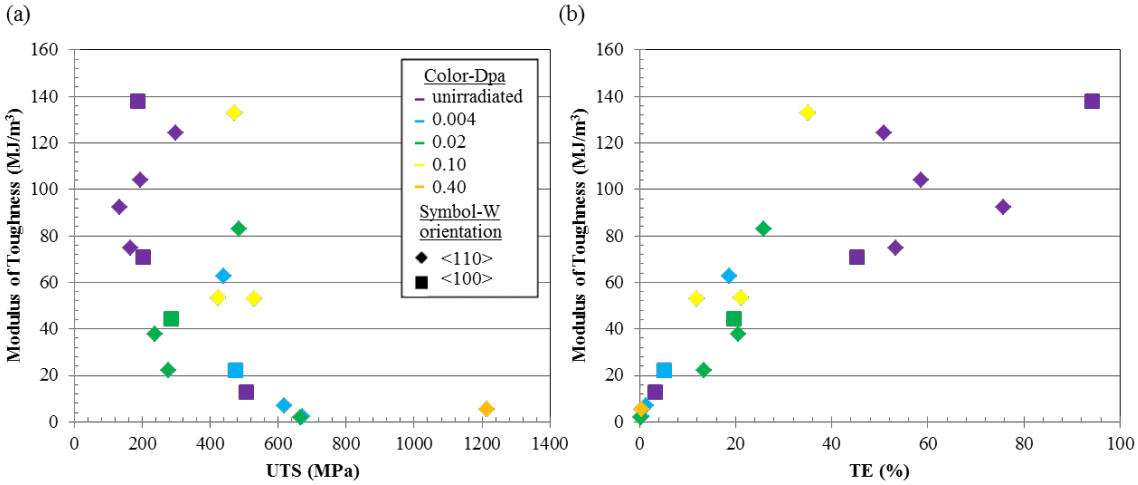

Figure 4. Modulus of toughness versus (a) UTS and (b) TE. The legend is the same for both parts of the figure.

Initially the unirradiated tungsten had high values of modulus of toughness, but there was a drop in the modulus of toughness at the lowest dose of 0.004 dpa (Figure 5a). After that point, the modulus of toughness increased with increasing dose until at 0.1 dpa the material irradiated at 360-460°C has a modulus of toughness equal to the unirradiated case. In fact, the material irradiated at 360-460°C (and tested at 300°C) had a higher modulus of toughness than any other irradiation temperature (Figure 5a). Generally the second highest modulus of toughness was for material irradiated in the higher temperature zone of 690-830°C, and the lowest modulus values were from material irradiated at 90°C. Thus, the material irradiated at 360-460°C and tested at 300°C appears to have the most favorable combination of some irradiation hardening to increase the UTS, still retaining enough ductility to have a reasonable TE, and not being at a high enough temperature where UTS is severely reduced. However, this trend only continues through ~0.1 dpa where the modulus of toughness reaches a high of 133 MJ/m^3 because the next dose tested, 0.55 dpa, was brittle and had a modulus of toughness of only 0.58 MJ/m^3. Only those materials with plastic deformation of 0.2% TE and longer are plotted on Figure 5, and their modulus of toughness values range between 5 and 150 MJ/m^3. The brittle materials by definition have little to no plastic deformation, so $U_P \approx 0$ and from Equation 5, $U_T = U_R$. Because the highest U_R measured was under 2 MJ/m^3, the U_T for brittle materials would not be distinguished in the scale on Figure 5 so they were not plotted.

The transition to fully ductile at 300°C test temperature is mirrored in the sharp increase in modulus of toughness at that temperature (Figure 5b). For unirradiated <100> orientation tungsten, the modulus of toughness linearly increases from 300°C to a maximum modulus of toughness at 650°C test temperature. For unirradiated <110> orientation tungsten, the modulus of toughness is highest at 300°C, linearly drops as temperature increases to 500°C, and then increases slightly at 650°C. The <110> orientation tungsten irradiated to 0.02 and 0.1 follow the same pattern with the highest modulus of toughness at 300°C test temperature. For the other doses, there are not enough data points to see if the trend continues.

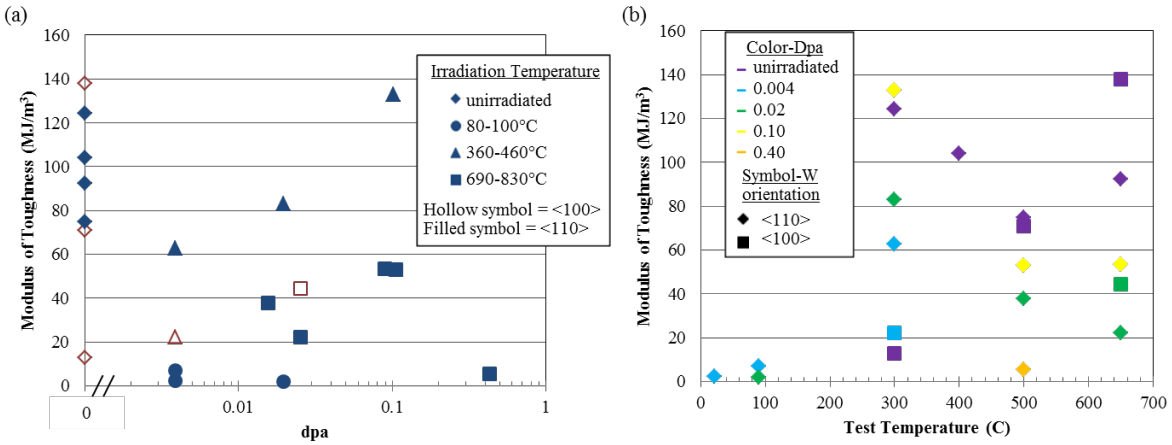

Figure 5. The modulus of toughness for the ductile materials is plotted (a) versus dose (dpa) and (b) versus tensile test temperature.

4.3 NEUTRON IRRADIATION EFFECTS IN TUNGSTEN-COPPER COMPOSITES—L.M. Garrison, Yutai Katoh (Oak Ridge National Laboratory)

OBJECTIVE

The aim of this work is to evaluate tungsten-copper based composites for potential use in plasma-facing component of future fusion reactors.

SUMMARY

As part of the TITAN program, two types of tungsten-copper composites were irradiated in High Flux Isotope Reactor (HFIR) at temperatures from 300 to 900°C and fast neutron fluences of 0.01 to 20 $\times 10^{25}$ n/m^2 at E>0.1 MeV. One material was a tungsten-copper laminate composite composed of 0.1 mm alternating layers of tungsten and copper. The other material was a tungsten-copper powder sintered composite, with 75% W and 25% Cu. Tensile tests at 22°C and elevated temperatures of unirradiated and irradiated tungsten-copper sintered composite have been completed.

PROGRESS AND STATUS

Previous analysis of the tungsten-copper laminate composites irradiated in the TITAN program showed that the laminate composites quickly loose ductility after low dose irradiation. Because the tungsten and copper layers are continuous, once a crack forms in a tungsten layer, it causes a sudden transfer of stress to the remaining layers. After neutron irradiation above approximately 0.02 dpa, the tungsten-copper laminate had no ductility in 22°C tensile tests.

As an alternative to the tungsten-copper laminate composite, a powder sintered tungsten copper composite with 75 wt.% W and 25 wt.% Cu was investigated. This material was produced by Mi-Tech Metals Inc. Tungsten, Indianapolis, Indiana. The sintered composite will be referred to by its engraved code KW. A polished surface of one of the KW composites is shown in Figure 1. There are sharp boundaries between the rounded W particles and the Cu. As expected, no interlayer or mixed phase formed between the elements.

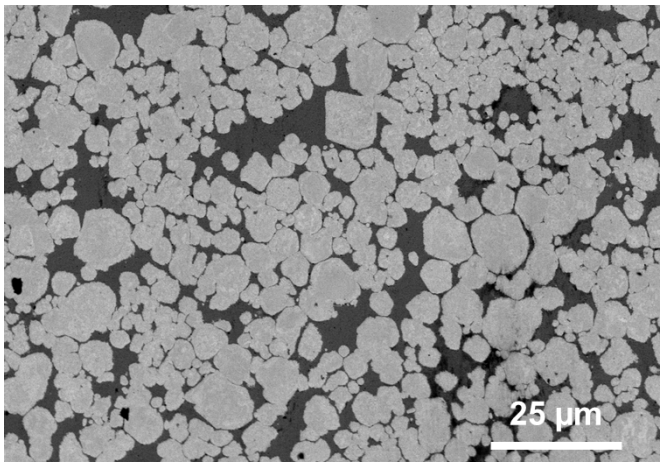

Figure 1. SEM image of the powder sintered tungsten copper composite.

Previously, tensile and Vickers hardness tests were completed on selected unirradiated and irradiated KW samples at room temperature. During this reporting period, elevated temperature tests were completed on unirradiated and irradiated KW samples, Table 1. The tensile yield stress (YS), ultimate tensile strength (UTS), uniform elongation (UE), and total elongation (TE) are listed. For these materials,

the displacements per atom (dpa) are calculated for the tungsten using the conversion 0.195 dpa=1E25 n/m^2 (E>0.1 MeV), as given by M. E. Sawan, Fusion Eng. Des., 87(5-6), 551-555 (2012).

Individual unirradiated samples are labeled by their Sample Identification (ID) and their test temperature, for example, KW23-22 for the unirradiated sample KW23 tested at 22°C. For irradiated samples, the labels include the Sample ID, dpa, irradiation temperature, and test temperature in that order. For example, KW02-0.02-450-22 was irradiated to 0.02 dpa at 450°C and tested at 22°C.

Table 1. Tensile and hardness data for the tungsten-copper particle composite

Capsule	ID	T_{irr} (°C)	Fast Fluence ($\times 10^{25}$ n/m^2, E>0.1 MeV)	DPA	Test Temp. (°C)	YS (MPa)	UTS (MPa)	UE (%)	TE (%)	Vickers hardness (HV)
Control	KW22	—	—	0	22	483	599	4.80	7.14	—
Control	KW23	—	—	0	22	466	577	5.58	7.42	—
TB-300-1	KW00	410	0.02	0.004	22	502	622	3.70	5.94	223.8
TB-300-2	KW02	450	0.1	0.02	22	532	649	3.72	5.74	238.2
TB-300-3	KW04	420	0.52	0.10	22	546	634	3.28	5.13	238.4
TB-500-1	KW08	750	0.08	0.02	22	464	586	4.97	8.40	—
TB-650-1	KW15	780	0.13	0.03	22	473	611	4.67	7.21	252.4
TB-650-2	KW16	760	0.46	0.09	22	534	634	4.19	6.49	—
TB-500-2	KW11	670	0.54	0.11	22	528	622	3.36	5.04	314.9
TB-500-3	KW12	630	9	1.8	22	791	828	0.93	0.98	320.2
Control	KW24	—	—	0	300	311	381	6.16	18.03	—
Control	KW25	—	—	0	400	250	315	8.82	13.99	—
Control	KW26	—	—	0	500	188	244	5	9.33	—
Control	KW27	—	—	0	600	133	173	2.81	7.03	—
Control	KW28	—	—	0	700	137	141	0.5	0.5	—
Control	KW29	—	—	0	800	—	—	—	—	—
TB-300-1	KW01	410	0.02	0.004	410	266	309	6	10.57	—
TB-300-2	KW03	450	0.1	0.02	450	272	303	3.44	8.07	—
TB-300-3	KW05	420	0.52	0.10	420	391	391	0.24	3.46	—
TB-500-1	KW09	750	0.08	0.02	750	94	114	3.13	7.28	—
TB-650-1	KW14	780	0.13	0.03	780	83	105	1.72	7.12	—
TB-650-2	KW17	760	0.46	0.09	760	107	122	1.39	5.78	—
TB-500-3	KW13	630	9	1.8	630	282	329	1.3	2.08	—

For the tensile data shown in the following figures, the contribution of the elastic strain has been removed so that only the plastic extension is shown. This minimizes the influence of test frame compliance on the data.

Unirradiated Tensile Data

The KW unirradiated material tested at 22°C had a TE of 7.42% (Figure 2). Of the temperatures tested, the greatest ductility was observed at 300°C with 18% TE. As test temperature was increased beyond 300°C, TE and UTS decreased. At 700°C, only 0.5% TE was observed. A sample, KW28, was attempted to be tested at 800°C, but as soon as force was applied to the material at 800°C, it failed. This indicates that the tungsten-copper sintered composite has no useful engineering strength in the unirradiated condition at 800°C.

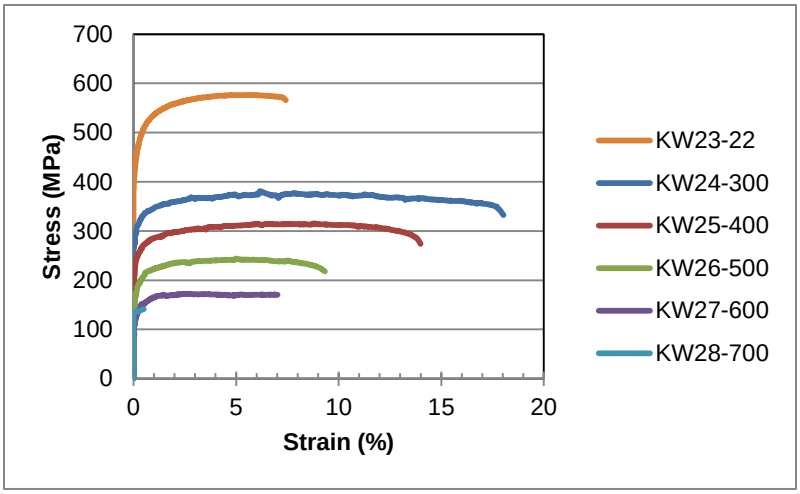

Figure 2. Tensile data for unirradiated KW material tested at temperatures of 22-700°C. Only the plastic strain is shown.

Tensile data for KW composite, irradiated at 360-460°C

Figure 3a shows the room temperature tensile curves for the KW material irradiated to different doses at temperatures between 410-450°C. With increasing dose, the total elongation was reduced. There was a slight increase in ultimate strength with increasing dose, but all irradiated material values are similar when tested at 22°C. For the material tested at the irradiation temperature (Figure 3b), there is a noticeable increase in UTS and decrease in TE for the material irradiated to 0.1 dpa. For material irradiated to less than 0.1 dpa, the UTS when tested at the irradiation temperature are reduced approximately by half compared to the 22°C test value. The TE is increased from 5-6% at 22°C to 8-11% when tested at the irradiation temperatures.

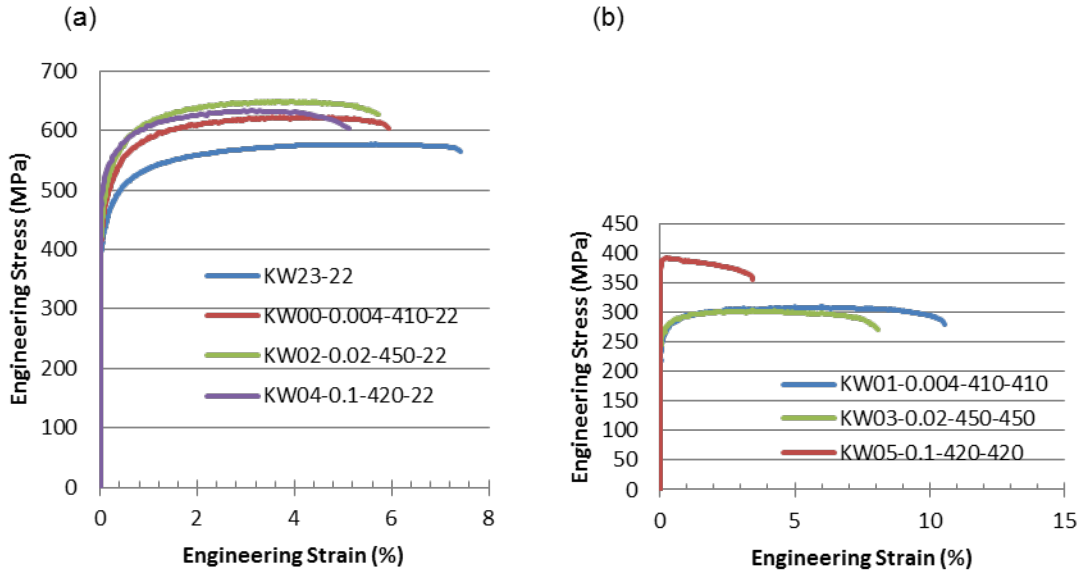

Figure 3. Tungsten-copper sintered composite irradiated at 410-450°C and tensile tested at (a) room temperature and (b) the irradiation temperature. Only the plastic strain is shown and approximately the same scale is used for both parts of the figure.

Tensile data for KW composite, irradiated at 630-780°C

After irradiation in the higher temperature range, from 630-780°C, and tensile tested at room temperature, the KW tensile results are similar to the lower temperature group up to 0.11 dpa (Figure 4a). However, at the highest dose tested, 1.8 dpa, there is a sharp increase in UTS and drop in TE. It is thus postulated that between 0.11 and 1.8 dpa the defect structure changes or accumulates to a critical level that in turn causes the changes in the mechanical behavior. For the material irradiated to the same conditions but tensile tested at the irradiation temperatures, the same pattern is seen with a change in behavior after 1.8 dpa, but all the UTS values are reduced (Figure 4b).

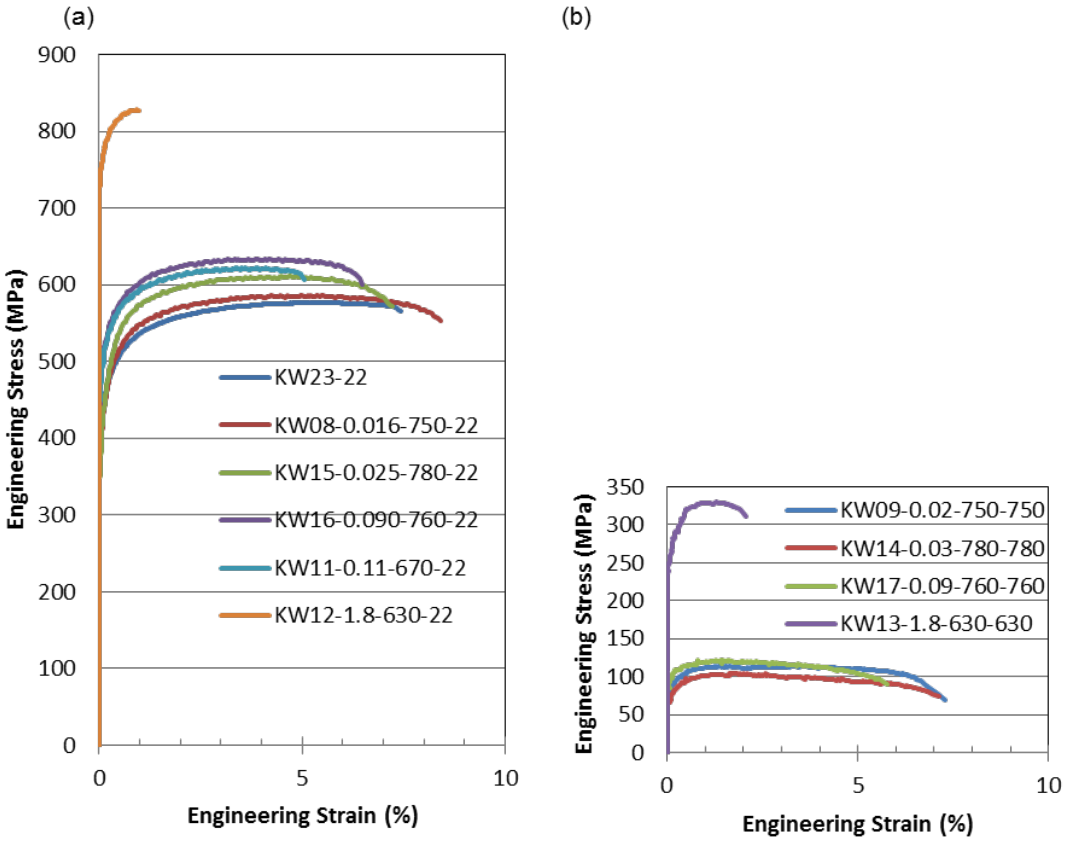

Figure 4. Tungsten-copper sintered composite irradiated at 630-780°C and tested at (a) room temperature and (b) the irradiation temperature. Only the plastic strain is shown and approximately the same scale is used for both parts of the figure.

4.4 ON THE FRACTURE BEHAVIOR OF WNiFe HEAVY METAL ALLOY HYBRIDS

—M.E. Alam, G. R. Odette (University of California Santa Barbara)

OBJECTIVE

The objective of this research is to develop tungsten-coated tungsten heavy alloy composites as divertor material.

SUMMARY

The strength and fracture toughness properties of four ductile phase toughened (DPT) commercially available tungsten (W)-based heavy metal alloy composites (WNiFe), reinforced with 3 to 10 (wt.%) of a NiFe phase, were previously thoroughly characterized from room to liquid nitrogen (LN_2) temperatures. All the alloys manifested a sub-zero brittle-to-ductile transition temperature (BDTT) ranging from -50ºC to -150ºC, depending on the amount of the ductile NiFe phase. In this study, pure W was coated on the WNiFe alloys by spark plasma sintering (SPS) at 1350ºC under a 50 MPa pressure load. Three-point bend (3PB) bars were fabricated and room temperature toughness tests were conducted to understand the crack formation and propagation mechanisms from the pure W coating up, to or into, the WNiFe alloy through or near the W:WNiFe interface. The results show that the pure W coating on the 90 and 92.5WNiFe alloy hybrid exhibits mode-I fracture and ductile phase toughening, while the 95 and 97WNiFe alloy hybrid exhibit a mode-II toughening mechanism, with deflected cracks at the W:WNiFe interface, possibly due to higher W-coating porosities in these cases.

PROGRESS AND STATUS

Introduction

Due to high melting temperature, good conductivity, low sputtering rates and high-temperature strength, tungsten (W), and its alloys, are currently considered the most promising candidates for plasma facing component for future fusion reactor divertor applications [1]. This application requires that structural W-based alloys and structures have sufficient fracture toughness to withstand the severe thermal-mechanical environment of a divertor. It is likely that monolithic W is intrinsically too brittle for this task. Previously a series of WNiFe (90, 92.5, 95 and 97 wt.% W with 7:3 = Ni:Fe) heavy metal alloys were shown to have much higher room temperature toughness (> 10x) and much lower BDTT temperatures (-150 to -50 ºC) than monolithic W (several hundred °C), depending on their ductile phase NiFe content [2]. In the work reported here, the fracture behavior of pure W:WNiFe alloy hybrid coupons, fabricated by SPS, were explored. Room temperature toughness tests were performed on the W:WNiFe hybrid coupons to: a) observe crack propagation paths after they initiate in the pure W coating; and, b) estimate the effective W:WNiFe hybrid coupon toughness.

Experimental Procedure

Pure W powder (size: 4-6 µm, purity: 99.95%, Stanford Materials) was used to coat four commercially available (Mi-Tech Metals, Indianapolis, Indiana, United States of Ameria) liquid-phase sintered WNiFe heavy metal alloy composites containing 90, 92.5, 95 and 97 wt.% W and a 7:3 Ni:Fe ductile phase. The coating was fabricated by SPS. First, 20mm diameter-2mm thick discs were cut from WNiFe alloys by electrical discharge machining (EDM). The discs were ground with 80µm to 1µm SiC paper to remove residual stresses and oxide layers formed during EDMing, and cleaned ultrasonically for 15 minutes in alcohol. Twenty mm diameter graphite and Nb foils were used to lubricate the SPS loading stack-up and to reduce tungsten carbide formation, respectively. The graphite shaft/ram and foils, Nb foils, W powder and the WNiFe alloy disc were stacked inside a 20.7mm inner diameter graphite die, as shown in Figure 1a. The stack-up consisted of elemental W powder, which was weighed inside an argon-filled glove box (containing less than 10 ppm oxygen) and poured on top of WNiFe disc, followed by the Nb and graphite foils and the graphite shaft. The W:WNiFe hybrid coupons were consolidated and bonded in vacuum

under a 50MPa compressive pressure at a sintering temperature of 1350ºC, with 10 min dwell time. The sintering temperature was restricted due to the lower melting temperatures of Ni (~1450ºC) and Fe (~1540ºC). Both the heating and cooling stages were performed at 50ºC/min. The amount of W powder was selected to produce a 2 mm thick coating after consolidation, resulting in ~20mm diameter-4mm thick W:WNiFe hybrid coupons (Figure 1b).

The EDM was then used to fabricate single-edged notch three-point bend (3PB) specimens with nominal dimensions of 16 mm length, 3.3 mm width and 1.67 mm thickness (Figure 1c). Pre-Cracking was not performed, and the notch depth of a/W ≈ 0.4 was selected to place the initial neutral axis in the WNiFe disc, in order to provide a driving force for the W-initiated crack to penetrate into the WNiFe alloy. In addition, a shallower a/W ≈ 0.15 notch, with the neutral axis in W side of the hybrid coupon, was used in some tests on the W:90WNiFe hybrid. A 810 MTS servo-hydraulic universal testing machine was used to load hybrid bend bars, and a Questar long-distance (telescopic) optical microscope with 3-axis positioning system was used to observe *in-situ* crack initiation and propagation at a frame rate of 6/min. The sides of the 3PB bars were sanded with a sequence of 2000 grit, 9µ, 3µ and 1µ paper to provide a better surface finish for crack imaging. The toughness tests were carried out at a crosshead speed of 0.04mm/min. While not fully applicable, American Society for Testing and Materials (ASTM) E1921 type procedures were generally used to evaluate both the elastic and plastic components of fracture toughness of hybrid bend bars [3]. The plastic K_{Jc} were calculated at the maximum load (P_m) in the load-displacement (P-d) curve. Three to four specimens were tested for each WNiFe alloy ductile phase NiFe content.

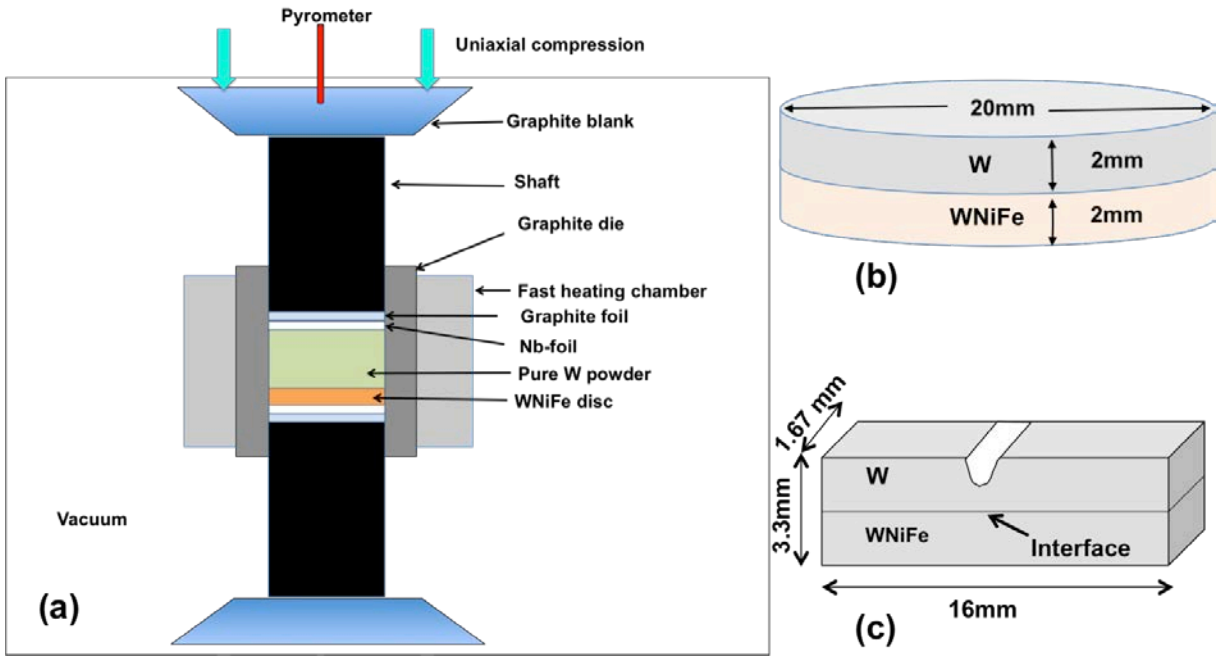

Figure 1. Schematic diagrams of: (a) SPS process set up; (b) a W-coated WNiFe hybrid disc; and, (c) the 3PB bar used for fracture testing.

Results

Microstructure

Scanning Electron Microscopy (SEM) micrographs of the polished W-coated-WNiFe alloy hybrids reveal roughly spheroidal W particles surrounded in the interconnected skeleton of a ductile NiFe phase in

WNiFe alloy side (top part of Figure 2a). Note the NiFe phase also contains about 30% W after liquid metal sintering. Note, there is a clean, and apparently well-bonded interface. A low volume fraction of pores in the W coating is also observed, especially in the 95 and 97WNiFe hybrids.

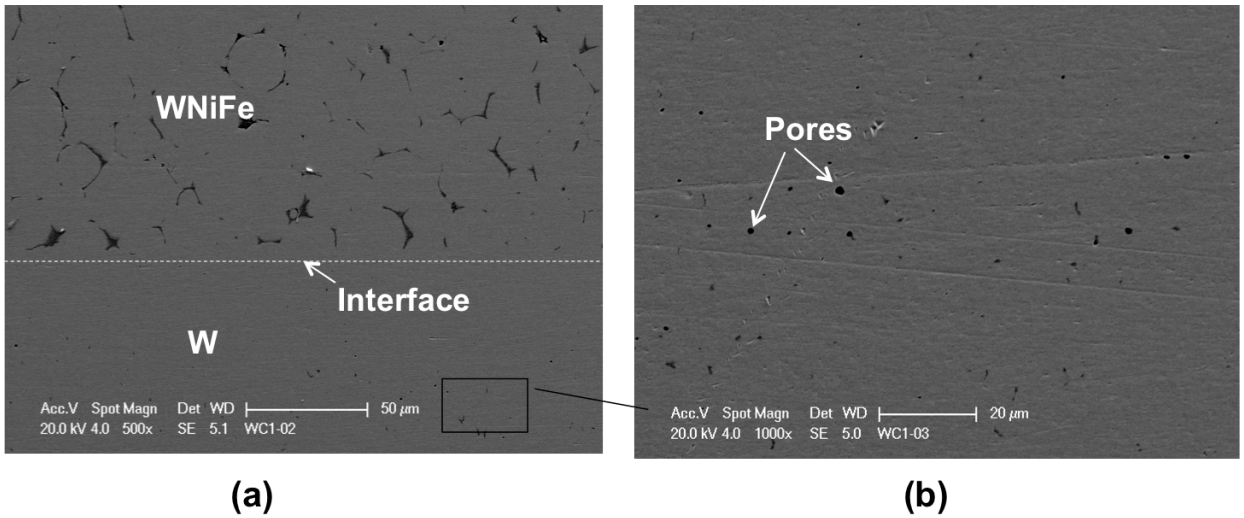

Figure 2. (a) The clean and well-bonded interface between W and WNiFe; and, (b) pores in the pure W coating.

Fracture Toughness

As reported previously, fracture toughness tests on 90-97WNiFe alloys were conducted from room temperature (RT) down to liquid nitrogen (LN_2) temperatures [2]. In summary, all alloys tested at RT show continuous load drop after the maximum load (P_m) with increasing displacement (d), indicating stable crack growth. The average maximum load K_{Jc} was ≈ 96 ± 20 MPa$\sqrt{m}$. The toughness generally decreases with deceases in the NiFe(W) ductile phase content, and is minimum at 97W. Stable ductile tearing is still observed in the 90WNiFe alloy at -100ºC, while somewhat mixed (stable + unstable) crack growth occurs at -150ºC [2]. Brittle fracture is observed at the LN_2 temperature in all cases. The corresponding transition temperatures for the other alloys were ≈ -100 ºC, -75 ºC, and -50 ºC for the 92.5, 95 and 97.5W alloys, respectively.

New RT fracture toughness tests were carried out on the hybrid 3PB bars. Figure 3 shows the result for a deeply notched (a/W ≈ 0.4) 3PB bar of the W:90WNiFe hybrid coupon, including the P-d curve (Figure 3a) along with a profile view of the propagated crack (Figure 3b), and a profile view showing the sequence of crack propagation (Figure 3c). The load increases to Point-1, associated with the brittle elastic fracture toughness of pure W, then suddenly drops, as crack growth initiates from W-notch, and propagates through W matrix to the W:90WNiFe interface, as a large pop-in event. The load then increases again until the arrested blunting crack penetrates into the 90WNiFe alloy. The load decreases thereafter under stable growth in the WNiFe alloy. The second a/W = 0.4 test behaved in a similar fashion.

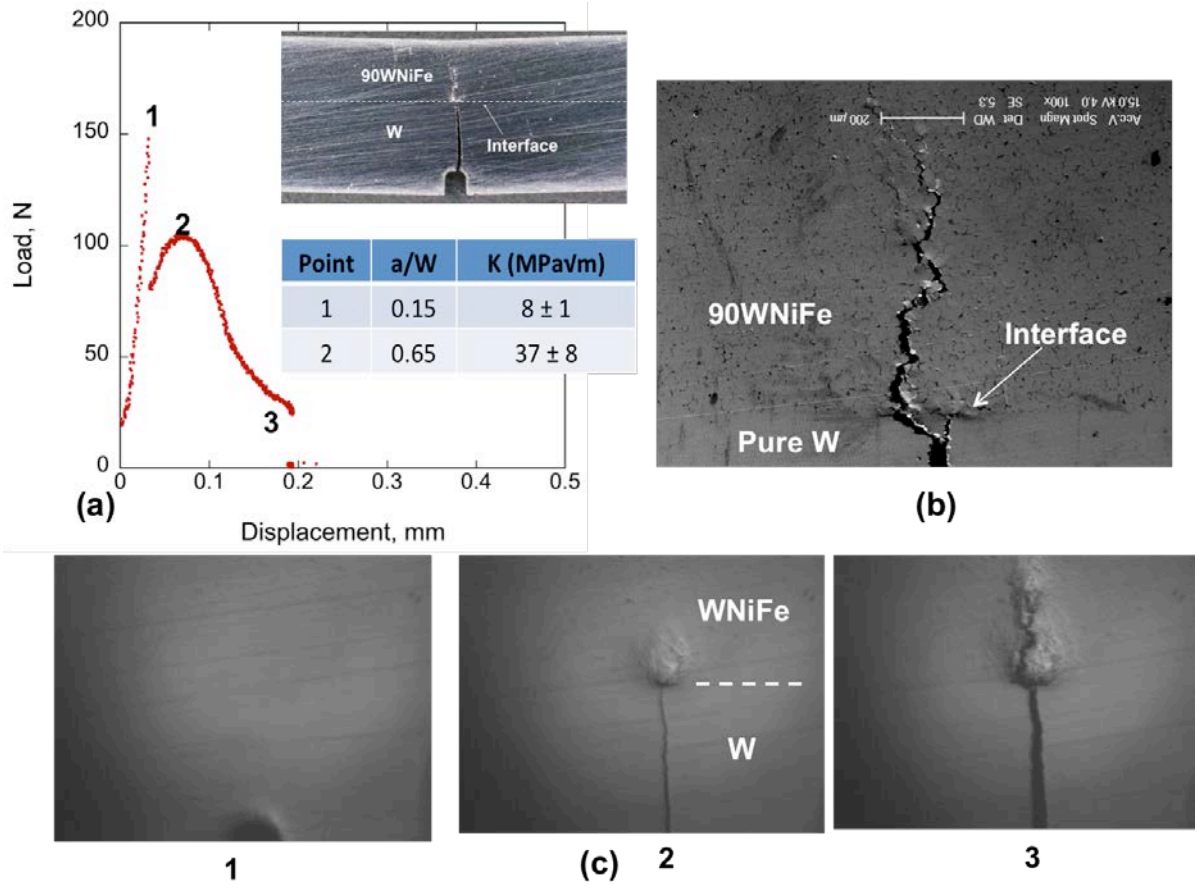

Figure 3. Characterization of cracking in the W:90WNiFe hybrid: (a) the load-displacement (P-d) curve with the W and peak load 90WNiFe alloy toughness values and a profile view of the tested specimen; (b) a SEM micrographs of propagated crack; and (c) in-situ optical micrographs associated with the numbered loading points.

Two other tests were conducted with smaller initial a/W ≈ 0.15, so that the initial neutral axis lies in W, rather than the 90WNiFe alloy side. The initiation toughness of pure W was same for all tests that averaged K_{IC} ≈ 8 ± 1 MPa√m (see Table 1). Crack propagation was also similar to that described above. However, maximum load toughness of 90WNiFe is slightly higher for smaller notch specimens with K_{Jc} values of averaging ≈ 44 ± 4 MPa√m than deeper notched specimens at ≈ 32 ± 2 MPa√m (Table 1). Note these values are much lower than those for the as-received 90WNiFe alloy (95 ± 20 MPa√m) [2]. The lower maximum load toughness is probably due the the effects of the W side of the interface on the crack blunting needed to initiate growth in the 90WNiFe alloy.

The tests on the other alloy compositions were all made with 3PB bars with deep notches. Figure 4 shows a representative P-d curve for W:92.5WNiFe hybrid along with *in-situ* optical micrographs and a SEM fractograph. Similar to W/90WNiFe hybrid, the W/92.5WNiFe load increased up to Point-1 marking the W toughness, followed by sudden load-drop due to crack propagation to arrest at the interface. The load then increased to Point-2 marking the blunting and re-initiation of stable crack growth in the 92.5WNiFe alloy. The W toughness was ≈ 9 ± 2 MPa√m, while the average 92.5WNiFe alloy toughness was slightly lower (32 ± 16 MPa√m) than that for 90WNiFe hybrid (37 ± 8 MPa√m, see Table 1). However, one of the W/92.5WNiFe shows higher K_{Jc} toughness as the crack slightly deflected at the interface, but later penetrated into and propagates through the WNiFe alloy.

Table 1. Notch depth and toughness values of pure W and WNiFe hybrid composites

Hybrid composites	Initial a/W, p-1	K_{IC}, MPa√m	a/W for WNiFe, p-2	K_{Jc}, MPa√m
W/90WNiFe	0.404	8.8	0.651	30.0
	0.402	7.8	0.629	33.2
	0.154	6.7	0.612	47.3
	0.154	7.6	0.682	40.3
	Average	**7.7 ± 0.8**	**Average**	**37.7 ± 7.7**
W/92.5WNiFe	0.349	6.4	0.603	22.5
	0.356	11.4	0.61	22.0
	0.355	9.4	0.59	50.5
	Average	**9.3 ± 2.5**	**Average**	**31.7 ± 16.3**

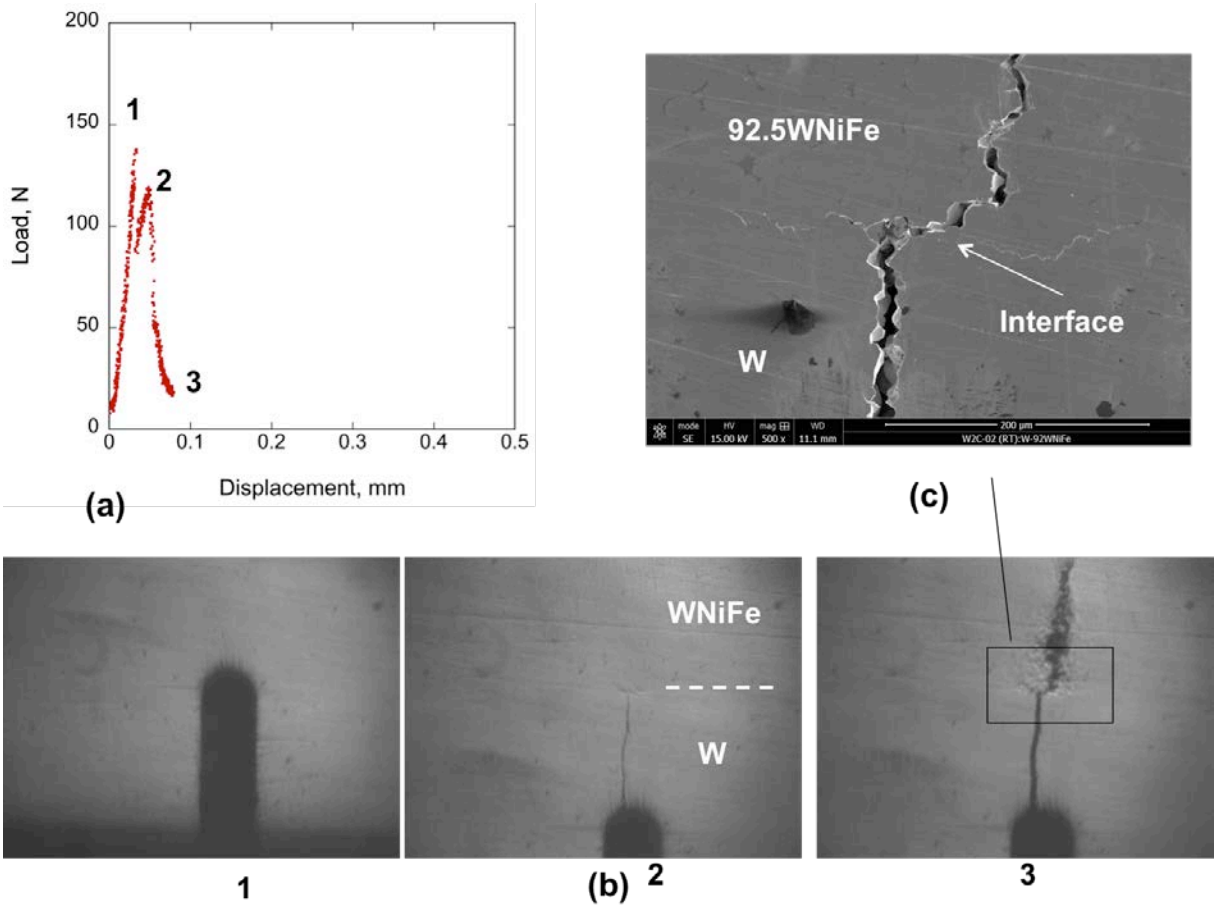

Figure 4. Characterization of cracking in the W:92.5WNiFe hybrid: (a) the load-displacement (P-d) curve; (b) in-situ optical micrographs associated with the numbered loading points; and, (c) a SEM micrograph of propagated crack.

Figures 5 and 6 show load-displacement curves along with micrographs for W-coated 95WNiFe and 97WNiFe hybrids, respectively. Unlike the W:90 and 92.5WNiFe hybrids, the load continuously increases as cracks arrests and is deflected perpendicular to the loading direction, running along, or near, the interface. One possible reason for selection of the crack deflection path is the higher porosity observed on the W side for the 95 and 97WNiFe hybrids (Figures 3c, 5c,f, and 6b). The pores may make the interface debonding an easier path for crack to propagate in these cases, rather than penetrating into and propagating through the 95 and 97.5WNiFe alloy. Crack deflection leads to a load displacement curve that continuously increases up to the end of the test. Thus it is not formally possible to define a maximum-load toughness, but the effective toughness and resistance curve behavior is very high. Note, the W coating cracked internally under preloading condition, again possibly due to the larger amount of porosity in the W. Although the pores may improve the toughness of 95 and 97WNiFe hybrids, it may have detrimental effects on other properties (like strength), or the functionality of W components.

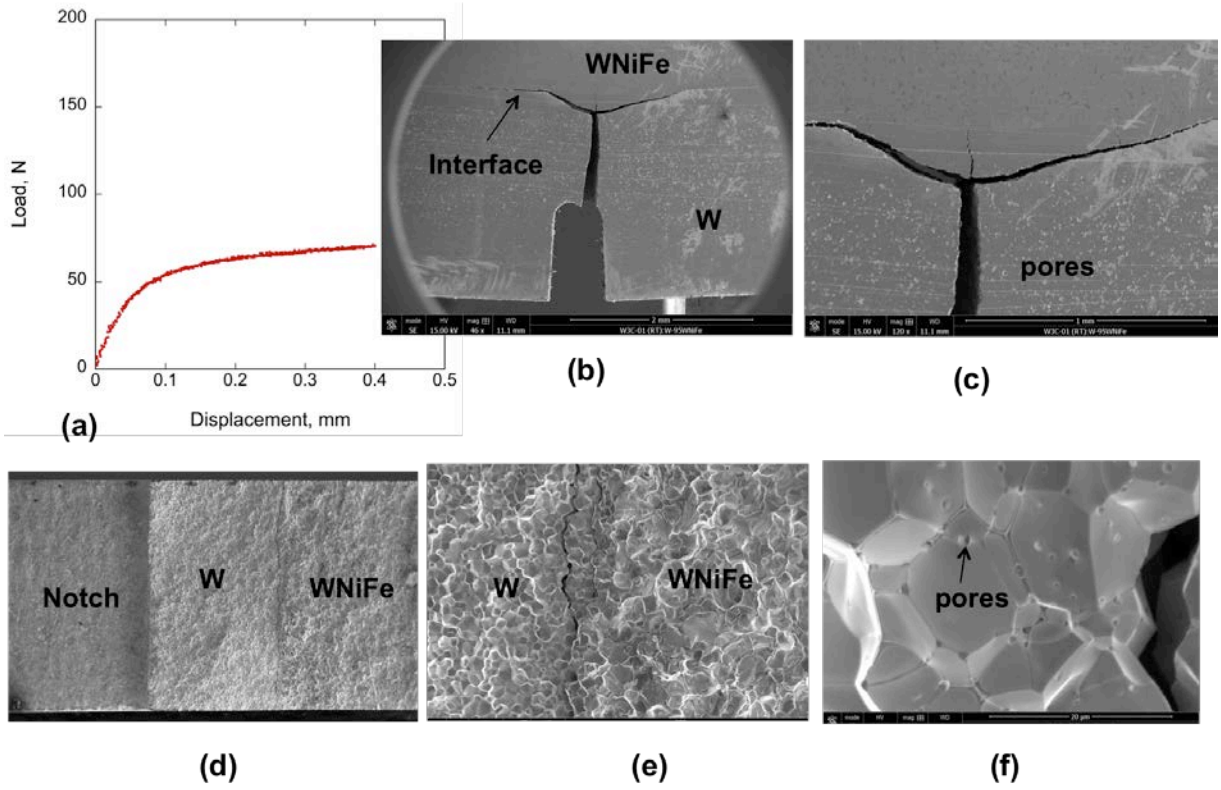

Figure 5. Characterization of cracking in the W:95WNiFe hybrid: (a) the load-displacement (P-d) curve; (b) and (c) profile images of the crack showing a 90° deflection and propagation along or near the W:95WNiFe hybrid interface; and, (d) to (f) micrographs of the fracture surfaces at increasing magnification.

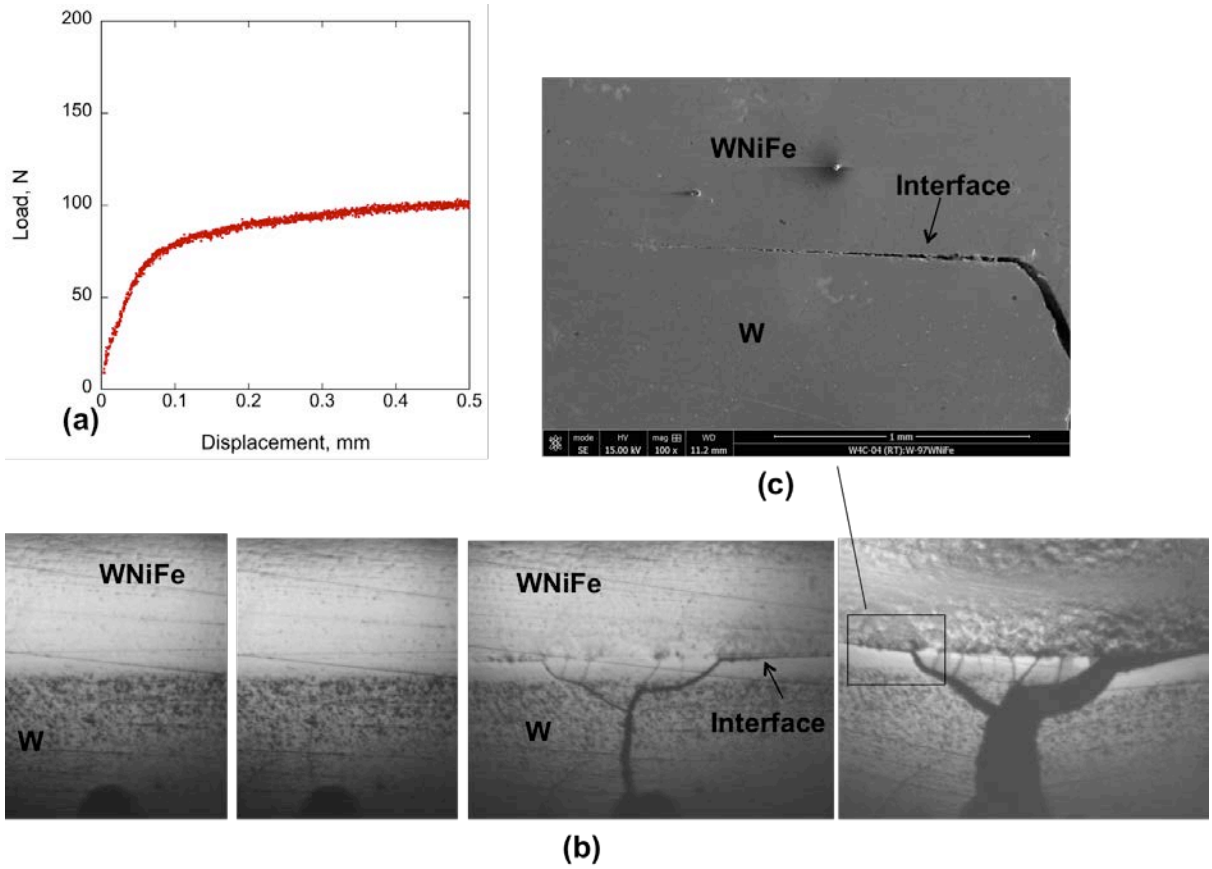

Figure 6. Characterization of cracking in the W:97WNiFe hybrid: (a) load-displacement (P-d) curve, (b) in-situ optical micrographs with crack propagation along the interface; and, (c) a SEM micrograph of the deflected crack at the interface.

Ongoing and Future Work

- Pre-cracking the 90 to 97WNiFe 3PB bars has been completed, and they will be tested to evaluate high-temperature toughness.
- Thermal shock tests will be performed on these WNiFe alloy and hybrids.
- Special fracture specimens will be tested measure interface toughness and strength.

Acknowledgement

We like to acknowledge the support provided by United States Department of Energy (DOE) through the Office of Fusion Energy Sciences (DOE Pacific Northwest National Laboratory (PNNL) Tungsten: 8-442520-22403-3 ROF02).

References

[1] M. Rieth, S. L. Dudarev et al., "Recent progress in research on tungsten materials for nuclear fusion applications in Europe", Journal of Nuclear Materials 432 (2013) 482-500.

[2] M.E. Alam, S. Pal, K. Fields, G. R. Odette, "Mechanical properties characterization of 90-97wt% WNiFe heavy alloys", DOE/ER-0313/61 (2016), DOE Fusion Reactor Materials Program Semiannual Progress Report, 61 (2016) 73-82.

[3] ASTM E1921-13a, Standard Test Method for Determination of Reference Temperature, T_o, for Ferritic Steels in the Transition Range, ASTM International, West Conshohocken, PA, 2013.

4.5 HIGH-HEAT FLUX TESTING OF LOW-LEVEL IRRADIATED MATERIALS USING PLASMA ARC LAMPS—A.S. Sabau, Y. Katoh (Oak Ridge National Laboratory)

OBJECTIVE

The objective of this work, part of the PHENIX collaboration with Japan, is testing of irradiated materials that are candidate divertor component materials and mock-up divertor components under high-heat flux using Plasma Arc Lamps (PAL).

SUMMARY

In this reporting period, the effort was mainly focused on designing and fabrication of a new reflector to increase the heat flux to its maximum achievable for the maximum arc temperature of the PAL. After a significant delay, the fabrication of the new reflector was completed and successfully tested.

PROGRESS AND STATUS

Effort was conducted in two main areas in order to attain the maximum incident heat flux from PAL with the new reflector of 12 MW/m^2: (a) designing and fabrication of a new reflector and (b) instrumenting the test section with a lift mechanism of the dome test section.

The new reflector was designed by Mattson Technologies, Inc. Mattson Technologies conducted simulations for various reflector shapes using a proprietary model of the volumetric distribution of the heat source within the plasma arc, which is confined in a quartz tube. The actual thicknesses of quartz fixtures (windows, dome or cylinder) used for radiological containment were considered in the model simulations conducted at Mattson Technologies, illustrated in Figure 1.

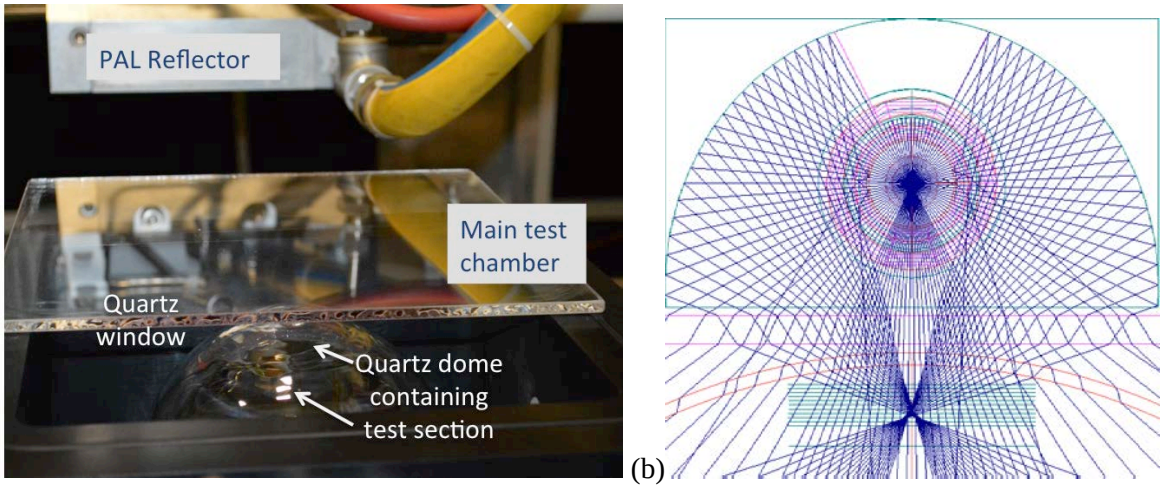

Figure 1. The main configuration components of the PAL experimental setup (PAL reflector, quartz window, and quartz dome): (a) picture of the setup and (b) schematic of ray tracing toward the specimen.

Mattson Technologies provided Oak Ridge National Laboratory (ORNL) with schematics for various reflector shapes simulated (e.g., Figure 1b). Several positions of the specimen with respect to the top surface of the quartz dome and reflector surface shapes were investigated by Mattson Technologies Inc. to maximize the heat flux for our high-heat flux testing. The calculated incident heat flux from the new line-focus reflector is shown in Figure 2, together with the measured data for incident heat flux provided by the uniform heat flux reflector. The maximum incident heat flux that was estimated to be attained for a dome configuration is 12 MW/m^2.

The reflector was successfully installed (Figure 3). To allow for greater flexibility in heat flux selection, an extension was provided to the reflector. Without the extension, the line-focus reflector can be used with the flat quartz window (Figure 1a). With the extension, the reflector surface become larger and the heat flux is increased only when the quartz dome is inserted within the reflector. Thus, the new reflector can be operated in two configurations, i.e., with and without the extension. A picture of the operating reflector without its extension is shown in Figure 3a. A picture of the operating reflector with the extension is shown in Figure 3b. In Figure 3b, the heat flux sensor is placed within the quartz dome at the appropriate target-reflector distance. More detail on the heat flux placement is shown in Figure 3c. The measured incident heat flux at various operating currents is shown in Figure 4 for the old reflector and the new reflector (with the extension). The absorbed heat flux into W from the new PAL line-focus reflector and old uniform heat-flux reflector was estimated by assuming an emissivity of the W surface of 0.47.

An overall schematic of the new reflector (without its extension) is shown in Figure 5, in order to illustrate how pyrometers and/or cameras can be mounted for direct line-of-sight to the specimen surface. Figure 5b shows a picture taken during PAL operation in which confinement dome the light irradiation from the right view port can be clearly seen. In Figure 5c, a view of the pyrometer laser spot from the side-view of the reflector can be seen.

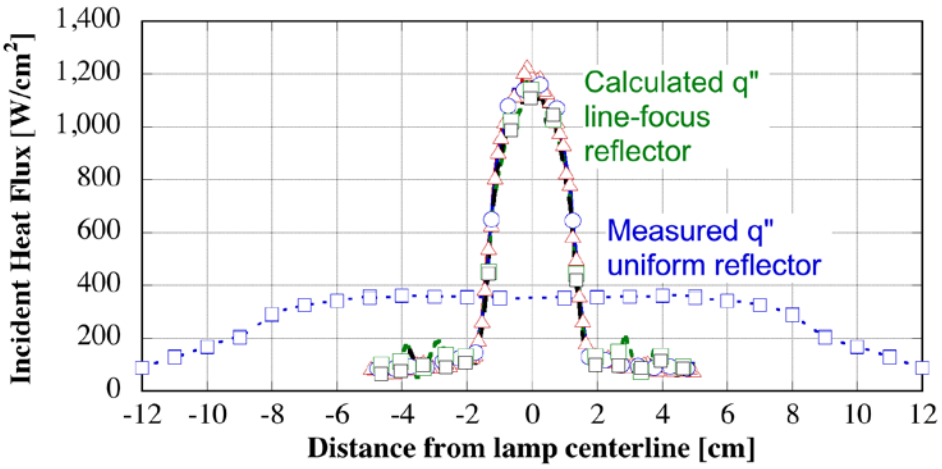

Figure 2. Incident heat flux from the plasma-arc lamp: numerical simulation results for new, line-focus reflector, and measured data for old uniform heat-flux reflector.

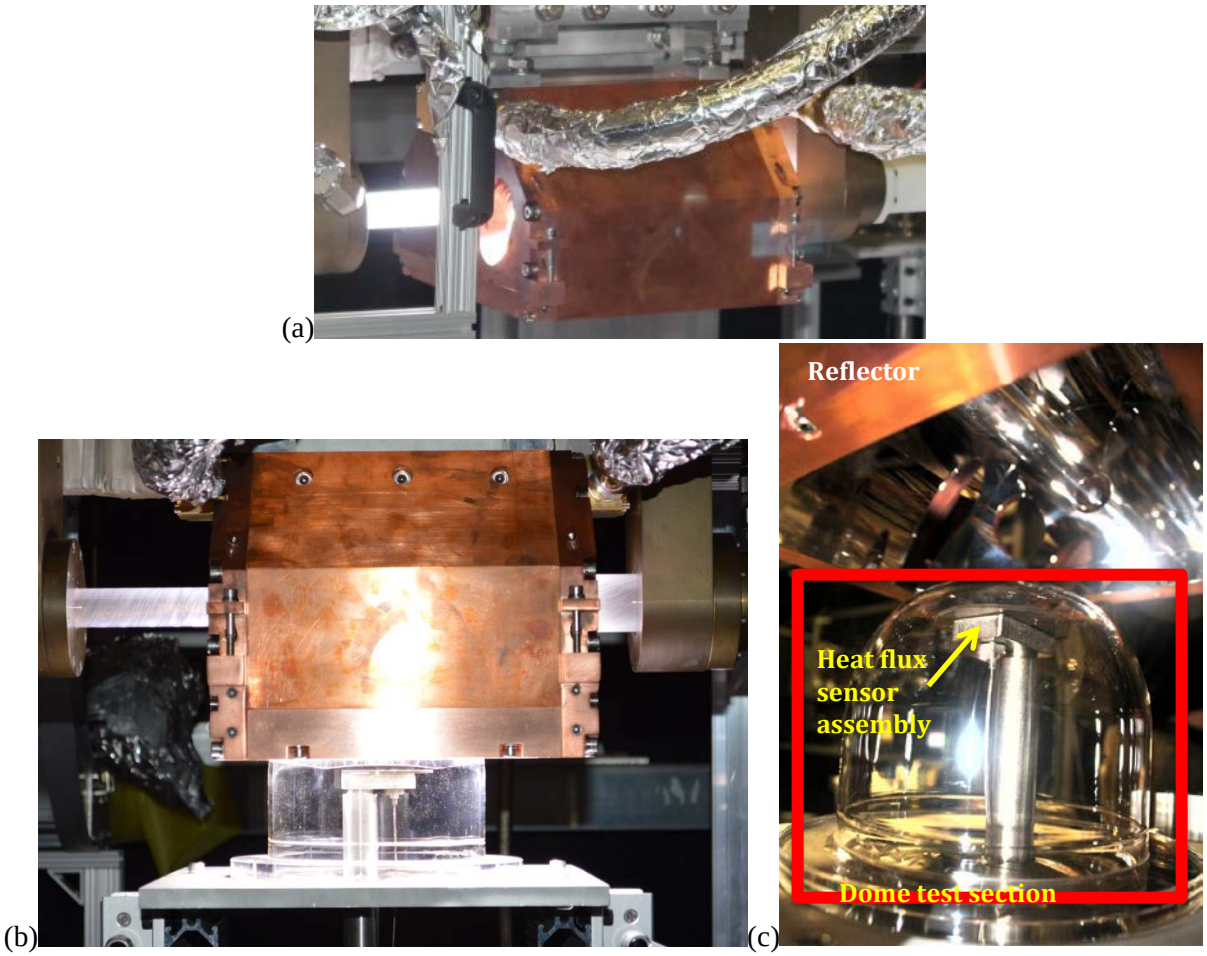

Figure 3. Pictures showing the new reflector and setup for heat flux measurements: (a) new reflector without extension, (b) front view of new reflector with extension, and (c) view from below of the new reflector. (b, c) The heat flux sensor is placed within the quartz dome at the appropriate target-reflector distance.

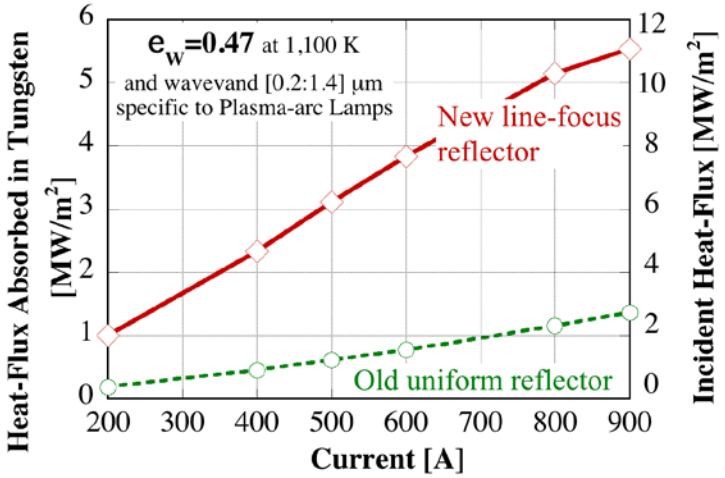

Figure 4. Measured incident heat flux and estimated absorbed heat flux into W from the new PAL line-focus reflector and old uniform heat-flux reflector.

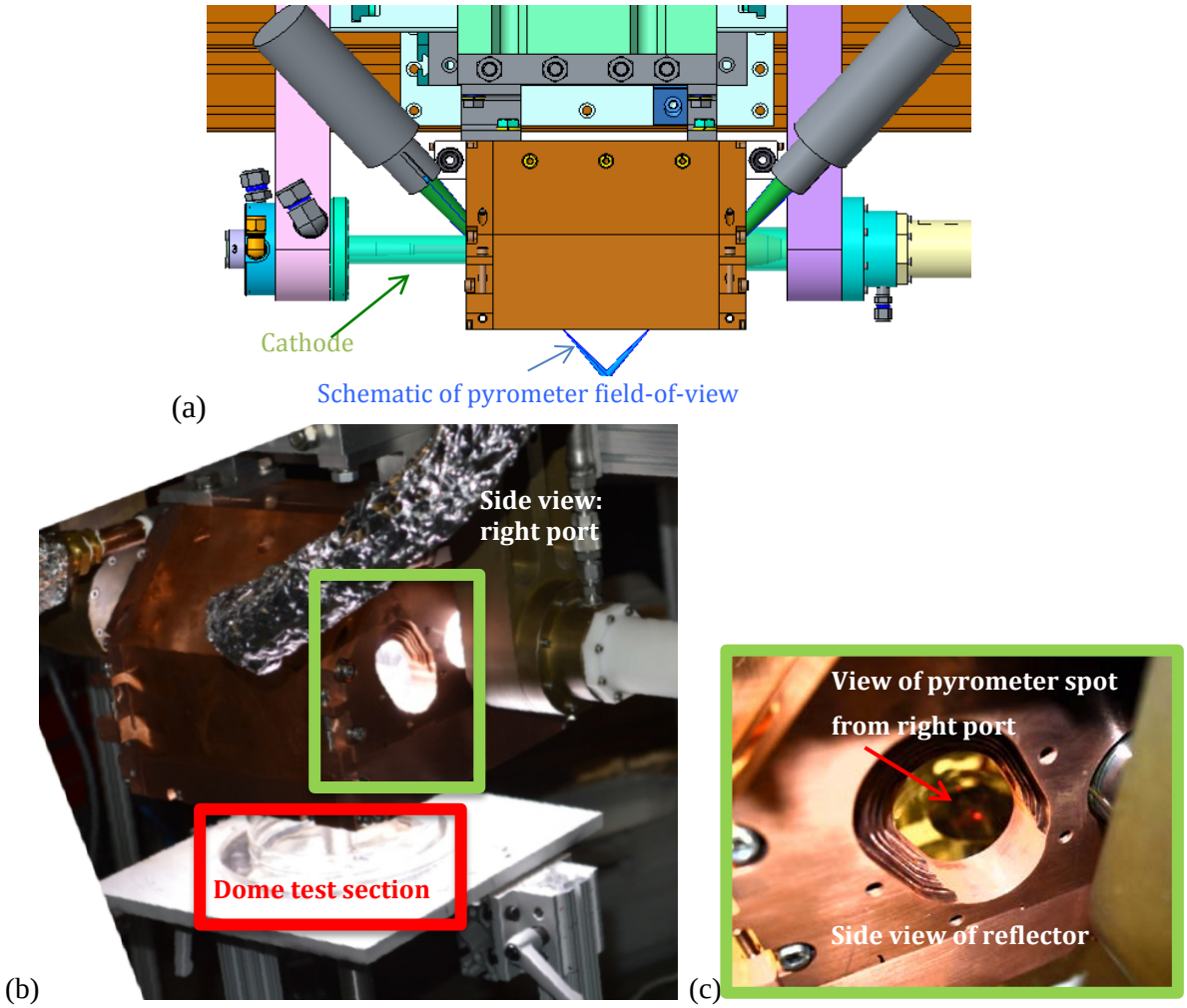

Figure 5. New reflector: (a) schematic showing how pyrometer and/or cameras can be mounted for direct line-of-sight to the specimen surface, (b) pictures during PAL operation showing the illumination of the confinement dome and the light irradiation from the right view port, and (c) view of the pyrometer laser spot from the side-view of the reflector.

5. MAGNETIC AND DIAGNOSTIC SYSTEM MATERIALS

No contributions this reporting period.

6. FUSION CORROSION AND COMPATIBILITY SCIENCE

6.1 LIQUID METAL COMPATIBILITY IN STATIC Li, Sn and Sn-Li—J. Jun and B. A. Pint (Oak Ridge National Laboratory)

OBJECTIVE

This task is evaluating the maximum use temperature for structural steel compatibility for plasma facing components with liquid metal candidates, such as Li, Sn and Sn-20Li. A literature review is in progress and a small series of isothermal capsule experiments were conducted to confirm published results, including determining if a surface oxide can significantly improve compatibility.

SUMMARY

A set of 1000 h isothermal capsule experiments was completed on alloys F82H (Fe-8Cr-2W) and Kanthal APMT (Fe-20Cr-5Al-3Mo) at 400°C (Sn and Sn-20Li) and 600°C (Li). One set of APMT specimens were pre-oxidized at 1000°C to form a thin alumina layer prior to the capsule test as a potential dissolution barrier and a second set was exposed without pre-oxidation. The specimens exposed to Sn and Sn-Li are being cleaned (to remove residual liquid metal) before measuring the mass change. The specimens exposed to Li were cleaned with NH_3 and small mass gains were noted for the bare alloys and small mass losses for the pre-oxidized APMT specimens. Mass change values were compared to those in the literature.

PROGRESS AND STATUS

Introduction

As part of a United States (US) working group evaluating liquid metal (LM) plasma facing components (PFC), this project is assessing compatibility with reduced activation ferritic martensitic (RAFM) structural steels. Using a liquid metal to protect the surface of a PFC has been discussed and investigated for many years [1-3]. It offers the possibility of replenishing the surface during plasma operation but this assumes the liquid metal has a relatively low vapor pressure and good compatibility with the underlying components, including the pumping system to deliver the liquid during operation. A number of candidates such as Ga and In can be eliminated because of their very poor compatibility with conventional alloys. Among the remaining candidates, Li has relatively good compatibility but a high vapor pressure, while Sn offers a much lower vapor pressure but questionable compatibility [4-6]. Based on the initial findings of a literature review that is currently in progress, a test matrix was developed for isothermal capsule testing to supplement literature data for Sn, Sn-20Li and Li as the most likely LM PFC candidates.

Experimental Procedure

The test matrix is shown in Table 1. Isothermal capsule experiments were conducted for 1000 h with specimens in inner Mo capsules and outer type 304 stainless steel (SS) capsules to protect the Mo from degradation during the experiment. High purity Sn and Li were loaded in an Ar-filled glove box to minimize contamination prior to closure welding the Mo and SS capsules. A typical ferritic-martensitic structural steel, F82H (Fe-8Cr-2W) was selected for the initial evaluation in Li, Sn and Sn-20Li. To avoid the complication of aluminizing F82H, a commercial alumina-forming steel, Kanthal APMT (Fe-20Cr-5Al-3Mo), was selected to determine if a pre-oxidation to form a stable oxide could inhibit dissolution in Li, Sn and Sn-20Li. Uncoated F82H would form a mixed Fe- and Cr-rich oxide with a complex structure.

However, APMT is well-known to form an external alumina layer or scale. A pre-oxidation treatment for 2 h at 1000°C was selected to form a uniform, single-phase, α-Al_2O_3 scale [7], which is much more thermodynamically stable than any Fe- or Cr-rich oxide.

Table 1 also shows the specimen list with coupons (~3x10x20 mm) of F82H exposed in each condition. For APMT, both coupons and 25mm-long, type SS-3 tensile specimens were exposed. These are similar to the specimens being exposed in the Pb-Li thermal convection loops [8,9]. Relatively thick coupons (1.5-2 mm) were used in these experiments to help prevent complete consumption, particularly in the capsules containing Sn. Before and after exposure, the specimen mass was measured using a Mettler-Toledo model XP205 microbalance with an accuracy of ±0.04 mg or ~0.01 mg/cm^2. After exposure, the Li was removed using NH_3[10]. Subsequently, the specimens were rinsed with ethanol, 50:50 ethanol and water and, finally, deionized water. The Sn removal was attempted using sodium hydroxide in a 0.5M solution [11], which was ineffective. The next cleaning process attempted will be dipping the specimens in liquid Li at 250°C [6,12].

Table 1. Test matrix for evaluation of liquid metal compatibility

Liquid/Temperature	F82H	APMT	1000°C-2h pre-oxidized APMT
Sn at 400°C	X	XX	XX
Sn-20Li at 400°C	X	XX	XX
Li at 600°C	X	XX	XX

X: coupon only, XX: coupon + tensile specimen

Results

Example images of the specimens after exposure are shown in Figure 1, which illustrates that the specimens were coated to varying degrees in Sn and/or Li after the 1000 h exposure at 400° or 600°C. Table 2 shows the measured specimen mass change for the specimens exposed to Li after cleaning with NH_3. Mass gains were observed for the bare specimens, while mass losses were observed for the pre-oxidized specimens. For comparison with literature data from different times [12,13], the rates were normalized and plotted in Figure 2. All of the mass losses are small, the literature mass losses can be converted to metal loss rates of 1.35~1.58 μm·y^{-1} for Fe-9Cr-2W assuming a density of 7.8 g·cm^{-3}. The mass losses for the pre-oxidized APMT specimens may suggest a reaction with the pre-oxidized α-Al_2O_3 surface layer, which is less stable than Li oxide [14]. Characterization of the post-cleaning surfaces is in progress.

The removal of the Sn from the other specimens is in progress. It was possible to dissolve pure Sn in 0.5M NaOH solution but very little dissolution occurred for the specimens. Scanning electron microscopy/energy dispersive x-ray analysis of one specimen showed Sn, O and Cr peaks, which suggests that some reaction did occur with the substrate and the change in composition may inhibit removal. Thus, a new cleaning process with liquid Li will be attempted next.

A review of the literature is in progress. As indicated by the data in Figure 2, it is sometimes difficult to make comparisons among studies because different procedures and exposure times were used. One of the key parameters for determining compatibility in liquid metals is solubility. Figure 3 compares solubility

of several elements in Li and Pb, illustrating the well-known difference in Ni solubility in the two cases. Similar solubility data for Sn or Sn-Li has not been located.

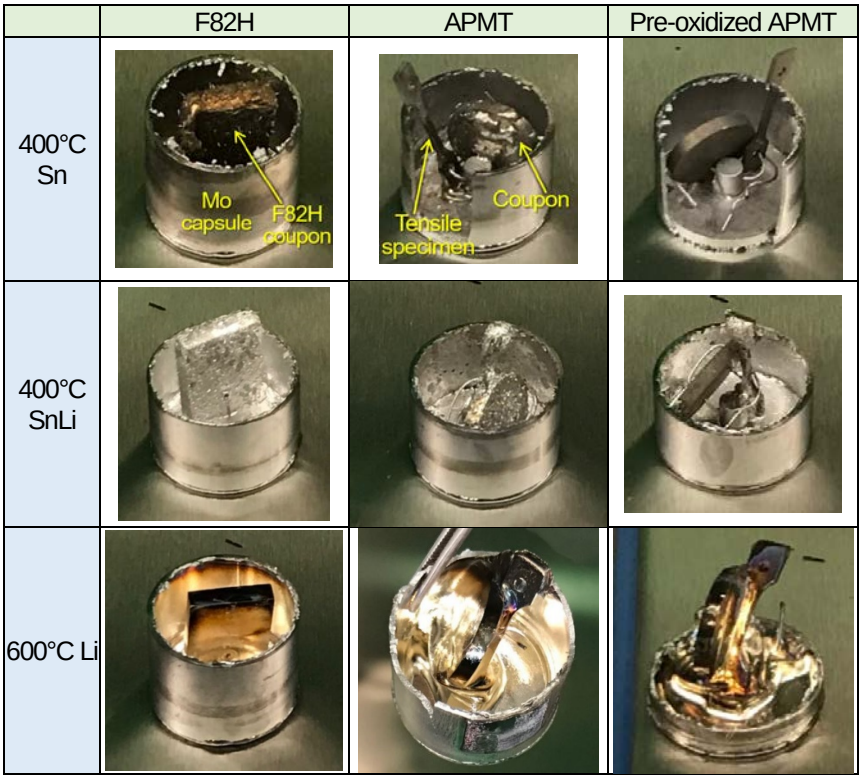

Figure 1. Opened Mo capsules containing F82H and APMT specimens after 1000 h isothermal liquid Li, SnLi and Sn exposure. The diameter of Mo capsule is approximately 1 inch.

Table 2. Mass change of F82 and APMT after 1000 h-600°C Li exposure

600°C Li, 1000 h test	Mass change mg·cm^{-2}	
	Coupon	Tensile specimen
F82H	0.12	—
APMT	0.34	0.24
Pre-oxidized APMT	-0.17	-0.52

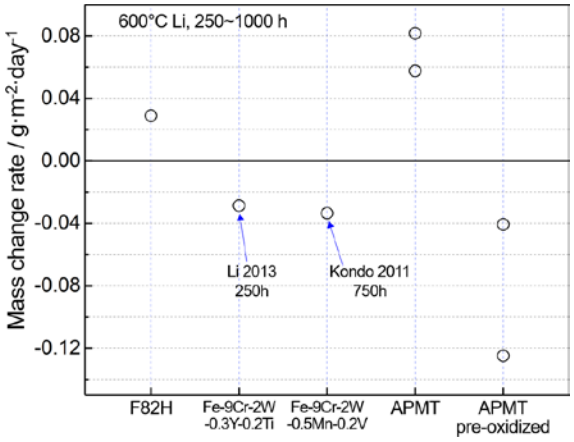

Figure 2. Mass change rate of FeCrW (F82H, Fe-9Cr-2W-0.3Y-0.2Ti and Fe-9Cr-2W-0.5Mn-0.2V) and FeCrAl (APMT with and without pre-oxidation) alloys after 250, 750 and 1000 h isothermal Li exposure at 600°C. Literature mass loss data from references 12 and13.

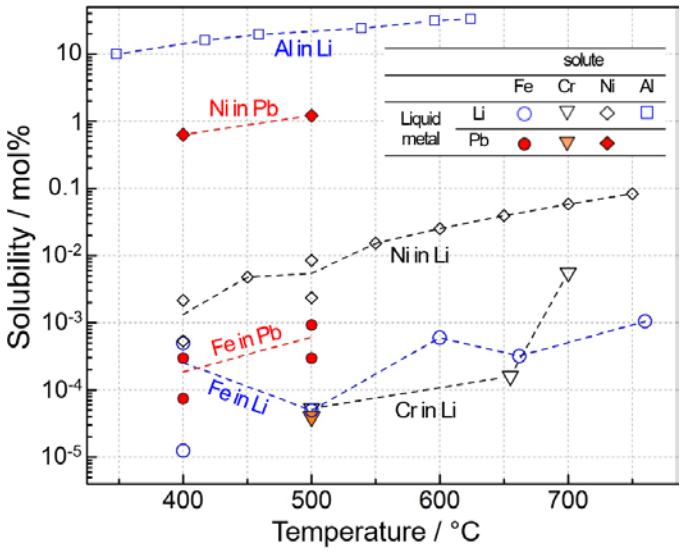

Figure 3. Solubility of Fe, Ni, Cr and Al in liquid Li and Pb as a function of temperature.

References

[1] S. V. Mirnov, V. N. Demyanenko and E. V. Muravev, J. Nucl. Mater. 196 (1992) 45.
[2] D. G. Whyte, et al., Fusion Eng. Design 72 (2004) 133.
[3] S. V. Mirnov and V. A. Evtikhin, VA, Fusion Eng. Design 81 (2006) 113.
[4] S. J. Zinkle and N. M. Ghoniem, Fusion Eng. Design 51-52 (2000) 55.
[5] S. Sharafat, N. Ghoniem and S. Zinkle, J. Nucl. Mater. 329–333 (2004) 1429.
[6] M. Kondo, M. Ishiib and T. Muroga, Fusion Eng. Design 98–99 (2015) 2003.
[7] B. A. Pint and K. L. More, J. Nucl. Mater. 376 (2008) 108.
[8] S. J. Pawel and K. A. Unocic, J. Nucl. Mater. 492 (2017) 41.
[9] B. A. Pint and J. Jun, DOE-ER-0313/61 (2016) 100.

[10] *Tenth International Symposium on Chemical Reaction Engineering* edited by J. R. Bourne, W. Regenass and W. Richarz, Vol. 43 of Chemical engineering science, Elsevier (2017).
[11] W.S. Jun, P.S. Yun, E.C. Lee, Hydrometallurgy 73 (2004) 71.
[12] M. Kondo, et al., J. Nucl. Mater. 417 (2011) 1200.
[13] Y. Li, H. Abe, T. Nagasaka, T. Muroga, M. Kondo, J. Nucl. Mater. 443 (2013) 200.
[14] P. Hubberstey, J. Nucl. Mater. 247 (1997) 208.

6.2 LIQUID METAL COMPATIBILITY IN FLOWING SYSTEMS—J. Jun and B. A. Pint (Oak Ridge National Laboratory)

OBJECTIVE

This task is investigating the possibility of increasing the Pb-Li temperature in the dual coolant lead-lithium (DCLL) blanket concept in order to improve the overall system efficiency. Alloys based on FeCrAl are potential candidates and monometallic thermal convection loops of a commercial FeCrAl alloy are being built and operated to establish a maximum operating temperature for operation in flowing eutectic Pb-Li.

SUMMARY

A series of monometallic thermal convection loops (TCLs) fabricated using dispersion strengthened FeCrAl (Kanthal APMT, Fe-21Cr-5Al-3Mo) tubing are being operated for 1000 h with increasing peak temperatures. Further characterization was completed on the APMT specimens exposed to commercial Pb-17Li in the hot and cold legs of the second TCL with a peak temperature of 600° ± 1.5˚C. The APMT specimens pre-oxidized to form alumina prior to exposure tended to have low mass changes (i.e. reduced dissolution) but the oxide spalled after exposure. The specimens that were exposed without pre-oxidation showed larger mass losses (i.e. more dissolution before the oxide layer formed) but the oxide was much more adherent. The third TCL with a peak temperature of 650° ± 1.5˚C was assembled and operated continuously for 1000 h in September-October 2017. Mass change, post-exposure tensile properties and initial characterization of the reaction products is reported. Similar mass change behavior was observed in the 650°C TCL as in the 550° and 600°C TCLs. No loss of ductility was observed after exposure.

PROGRESS AND STATUS

Introduction

The DCLL blanket concept (eutectic Pb-17 at.%Li and He coolants) is the leading United States (US) design for a test blanket module (TBM) for International Thermonuclear Experimental Reactor (ITER) and for a DEMOnstration Power Station (DEMO)-type fusion reactor [1]. With reduced activation ferritic martensitic (RAFM) steel as the structural material, the DCLL is limited to ~475°C metal temperature because Fe and Cr readily dissolve in PbLi above 500°C and Eurofer 97 plugged a PbLi loop at 550°C [2-3]. With the addition of Al to Fe-Cr alloys, isothermal compatibility tests have shown low mass losses at up to 800°C [4-7]. Thermodynamic evaluations [8,9] indicated that Al_2O_3 should be stable in PbLi and inhibit dissolution by forming at the alloy surface, however, capsule studies found that a preformed α-Al_2O_3 surface layer transformed to $LiAlO_2$ during exposures at 600°-800°C [4,10]. To further evaluate the PbLi compatibility of FeCrAl-type, exposures in flowing PbLi are needed where changes in solubility with temperature can drive mass transfer [2,11]. In 2014, a monometallic TCL was operated for 1000 h with a peak temperature of 550°C using commercial Fe-21Cr-5Al-3Mo alloy (Kanthal APMT) tubing and specimens in the hot and cold legs [12-15]. This was the first time that PbLi was flowed at 550°C without plugging flow and only small mass losses were noted after the exposure. In 2016, a second monometallic APMT TCL was operated for 1000 h with a peak temperature of 600°C, and the mass change, characterization and room temperature tensile properties of APMT specimens from the second TCL were reported [16, 17]. The third TCL with a peak temperature of 650°C was completed in October 2017. Pre-oxidation of APMT to form alumina before PbLi exposure was used in all cases. However, in

the 650°C TCL the pre-oxidation condition was changed for most of the specimens to 2h at 1000°C [10] to reduce the alumina thickness and potentially improve post-exposure oxide adhesion compared to the manufacturers recommended pre-oxidation of 8 h at 1050°C, which was used in the first TCL. In each TCL, several specimens were exposed without pre-oxidation to quantify the effect of pre-oxidation. Mass change and post-exposure tensile properties of the APMT specimens in the hot and cold legs of the TCL are reported. Initial characterization of the reaction products also is reported.

Experimental Procedure

The details of the TCL construction and operation have been previously described [12-16]. Similar to the two previous TCLs, the third TCL was ~1 m tall and 0.5 m wide and heated on one side by resistively heated furnaces (i.e. the hot leg). The third TCL contained hot and cold leg specimen chains of 20 SS-3 type (25 x 4 x 0.9 mm) and 2 rectangular type (25 x 18.5 x 1 mm^3) APMT spacer specimens. All specimens were connected with APMT wire. Most of the specimens were pre-oxidized for 2 h at 1000°C in ambient air to form an α-Al_2O_3 surface layer or scale [10]. Each chain had four specimens with no pre-oxidation treatment and two specimens pre-oxidized for 8 h at 1050°C, which was the main pre-oxidation condition used in the first two TCL experiments. Rectangular coupons of unalloyed tungsten were attached at the bottom of each specimen chain to act as a "sinker" to keep the relatively low-density specimen chains from floating in the PbLi test fluid, and to act as "spacers" to keep the specimen chain centered within the tubing and liquid metal flow path.

The same batch of commercial purity Pb-17Li was used in all three TCLs with impurity levels of 1200 ppmw O, 240 ppmw C and <10 ppmw N (average of 6 samples) and no metallic impurities above the detection limit of ~1 ppmw [15]. Six thermocouples in thermowells that protruded about 0.3 cm into the flow path at the top, bottom and middle of each leg monitored the temperature during operation. The temperature data were used to estimate the exposure temperature of each specimen in the hot and cold legs. The temperature gradient in the TCL was ~120°C from 530-650°C and the velocity was measured at ~0.4 m/min by heating a section of the tubing using a gas torch and tracking the temperature spike as the heated liquid moved around the TCL. Following 1000 h of operation at 650°C, the Pb-Li was drained into the dump tank at the bottom of the cold leg. After removal, specimens were soaked in cleaning solution (1:1:1 mixture of ethanol, hydrogen peroxide, and acetic acid) while within the TCL (as an assembled chain) and again upon removal from the TCL (as individual specimens). The mass change of all specimens was measured and tensile specimens were tested at room temperature with a 0.001 s^{-1} strain rate. Specimens were examined by scanning transmission electron microscopy (SEM) equipped with energy dispersive x-ray spectroscopy (EDS) and Cu-plated prior to metallographic sectioning to protect the surface oxide. Spallation was quantified using image analysis using ImageJ software.

Results

The post-exposure specimen mass change data from the 650°C TCL is plotted versus the estimated temperature in the hot leg (HL) and cold leg (CL) in Figure 1a. Pre-oxidation of APMT effectively lowered the mass loss, but was not strongly dependent on exposure temperature in the TCL. The mass change from all the specimens in the three TCLs is shown in Figure 1b for comparison. The specimens that were not pre-oxidized showed more mass loss in each case. Figure 2 shows the post-exposure room temperature tensile properties plotted versus the estimated temperature in the HL and CL and compared to baseline as-received properties (shaded ranges) [15]. In addition, APMT specimens were annealed in argon-filled, sealed quartz ampoule for 1000 h at 550°, 600° and 650°C to isolate the effect of the

temperature exposure from the effect of Pb-Li exposure. Post-exposure yield and ultimate tensile stress (YS and UTS) were similar to the as-received and Ar-annealed results, Figure 2a. Uniform and total plastic elongation (UPE and TPE) versus exposure temperature are compared to as-received and Ar-annealed results in Figure 2b. A slight reduction in ductility was noted after Pb-Li exposure and after annealing. In each case, the tensile results did not appear to be strongly affected by pre-oxidation.

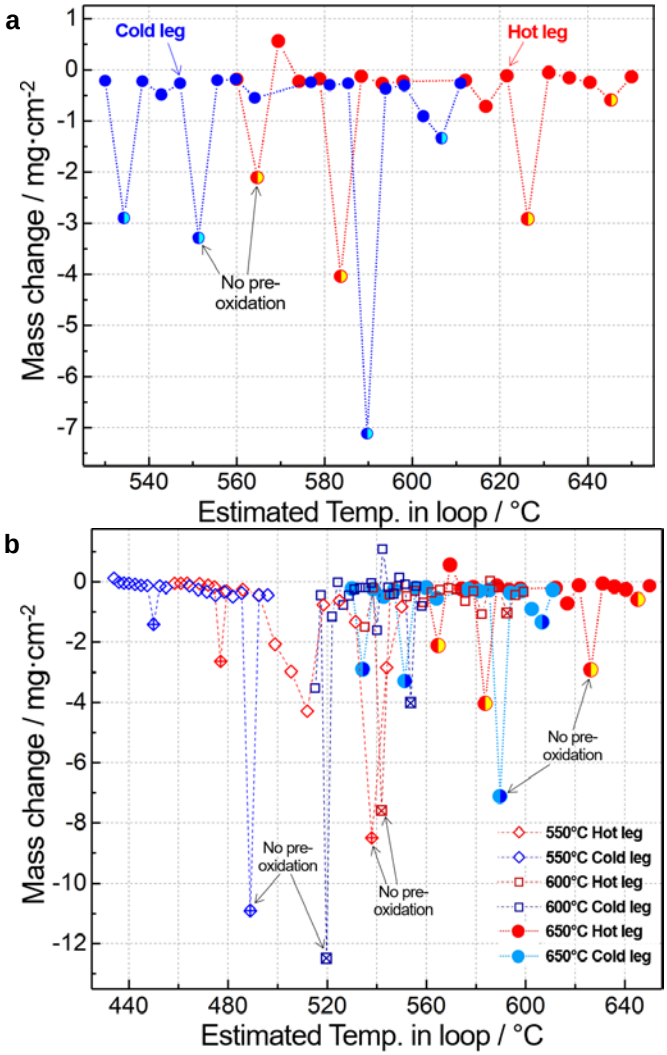

Figure 1. Mass change of APMT specimens after 1000 h in flowing Pb-Li versus estimated exposure temperature in (a) 650°C TCL and (b) all three (550, 600 & 650°C) TCLs.

The surface morphology of APMT specimens from the 600°C TCL are shown in Figure 3. For pre-oxidized specimens (8 h at 1050°C), remnants of the pre-formed oxide scale can be distinguished from smooth spalled area (Figures 3b and 3d). Meanwhile, as-received APMT (i.e. no pre-oxidation) appeared to have a rougher surface (Figures 3a and 3c) and some cracking of the oxide (Figure 3a). Considering the higher mass losses of as-received APMT (-12.49 and -1.04 mg·cm^{-2}), the rougher surface morphology suggests a non-uniform dissolution as was observed in the 550°C TCL [15]. Figure 3e shows images of the specimens in Figures 3a-3d. Without pre-oxidation, the oxide appeared more uniform with no

indication of spallation. In contrast, the bright regions on the pre-oxidized specimens corresponded to areas of oxide spallation (i.e. exposed bare metal).

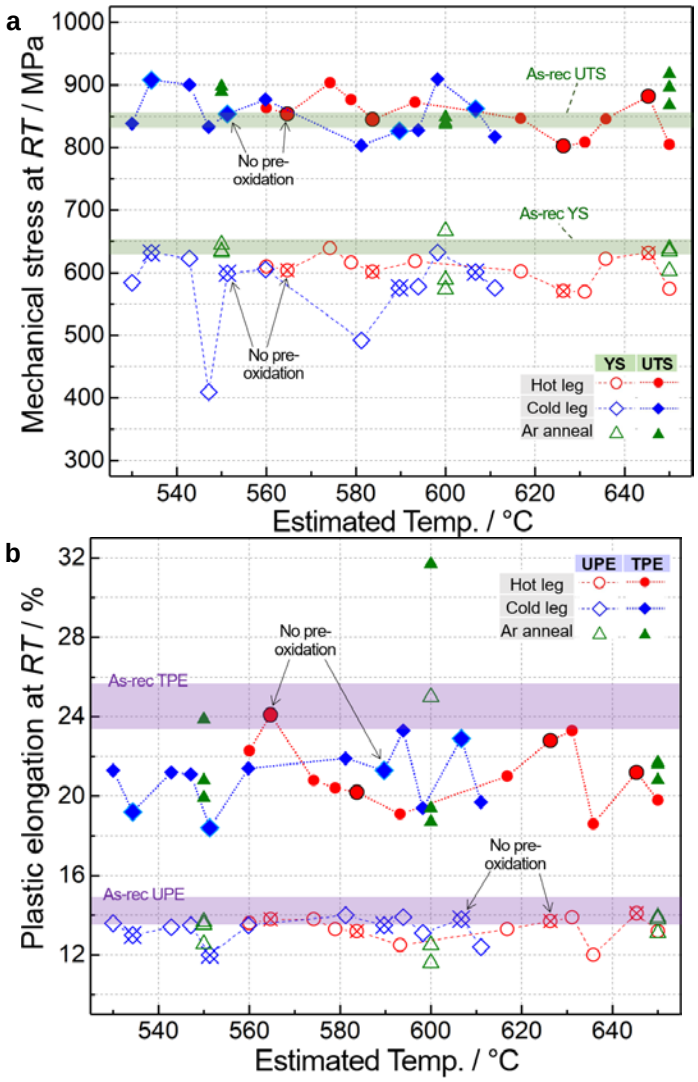

Figure 2. Room temperature tensile properties of APMT specimens versus estimated exposure temperature, (a) yield & ultimate tensile stresses and (b) uniform and total plastic elongation. Values after Pb-Li exposure are compared to annealed specimens and pre-oxidation conditions are noted. The shaded regions note as-received properties.

Figure 4 shows SEM/EDS results on an as-received APMT specimen exposed in the 600°C TCL hot leg that exhibited a mass loss of -7.59 mg·cm^{-2}. For the plan view, Figure 4a, variations in the Fe and Cr EDS maps indicate where the surface oxide is thicker, Figure 4b. Of course, EDS cannot detect Li, if it is present. In section, Figure 4c, Al and O were enriched at the surface, Figure 4d. The surface was not flat, suggesting dissolution occurred. Figure 5 shows similar SEM/EDS analysis of pre-oxidized specimens exposed at 549° (Figures 5a and 5b) and 586°C (Figures 5c and 5d). For the plan view image, Figure 5a, the oxide is rich in Al and O and the spalled areas are rich in Fe, Cr and Mo, Figure 5b. For the polished cross-section, Figure 5c, the surface oxide is enriched in Al and O and Mo appears to be enriched along the alloy grain boundaries [18], Figure 5d.

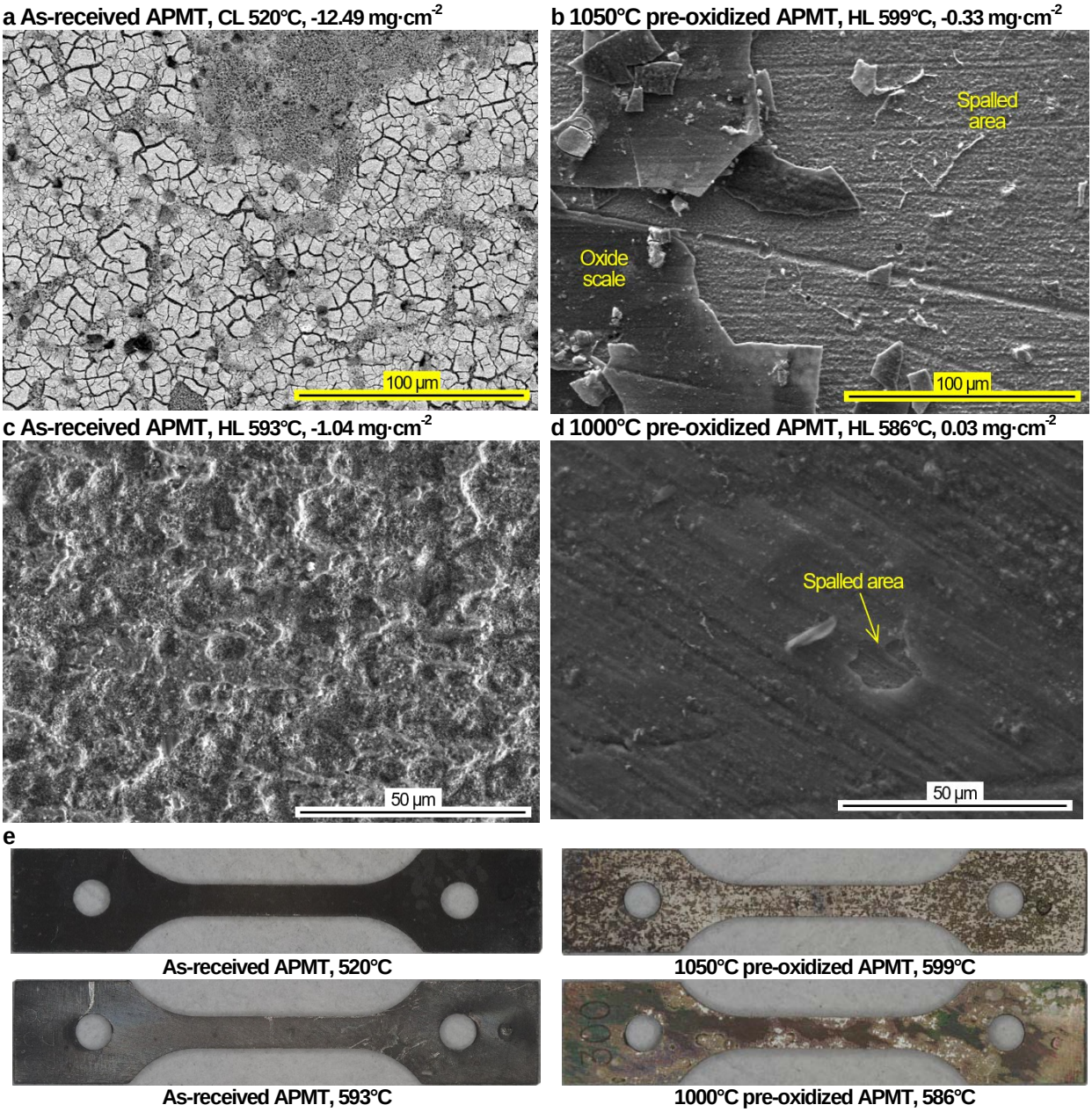

Figure 3. Surface SEM images of APMT specimens exposed in 600°C TCL with estimated exposure temperature with (a, c) no pre-oxidation and (b, d) pre-oxidized; (e) macro images of specimens in (a-d). (a) is back-scattered (BSE) image and others are secondary electron (SE) images.

In order to determine if the spallation correlated with exposure temperature or mass change, the amount of spalled "bright" area was quantified using image analysis of the tensile specimen images, such as those shown in Figure 3e. For the specimens in the 600°C TCL, the results are shown in Figure 6. Figure 6a indicates that the amount of spallation increased with exposure temperature. Also, the specimens pre-oxidized at 1000°C for 2 h showed less spallation than those pre-oxidized at 1050°C at 8 h. Thus, the lower temperature pre-oxidation was used for the 650°C TCL. Figure 6b shows a slight

correlation between mass loss and spallation. Intuitively, the mass loss should increase as more of the scale was lost due to spallation. A similar analysis is in progress for the specimens from the 650°C TCL.

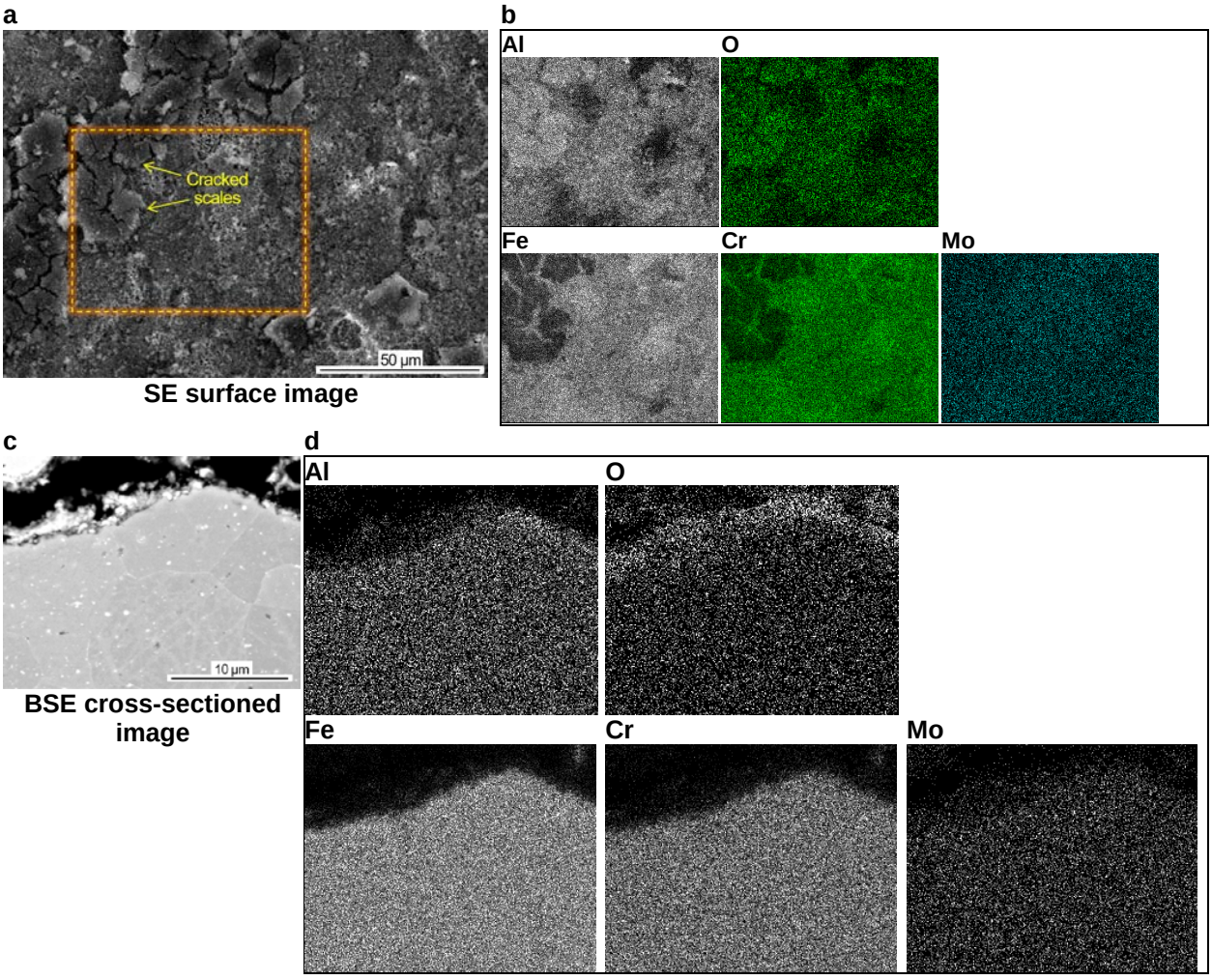

Figure 4. As-received APMT exposed to 542°C PbLi in HL: (a) SE surface image, (b) EDS mapping of selected region in (a), (c) BSE cross-sectioned image and (d) EDS mapping of (c).

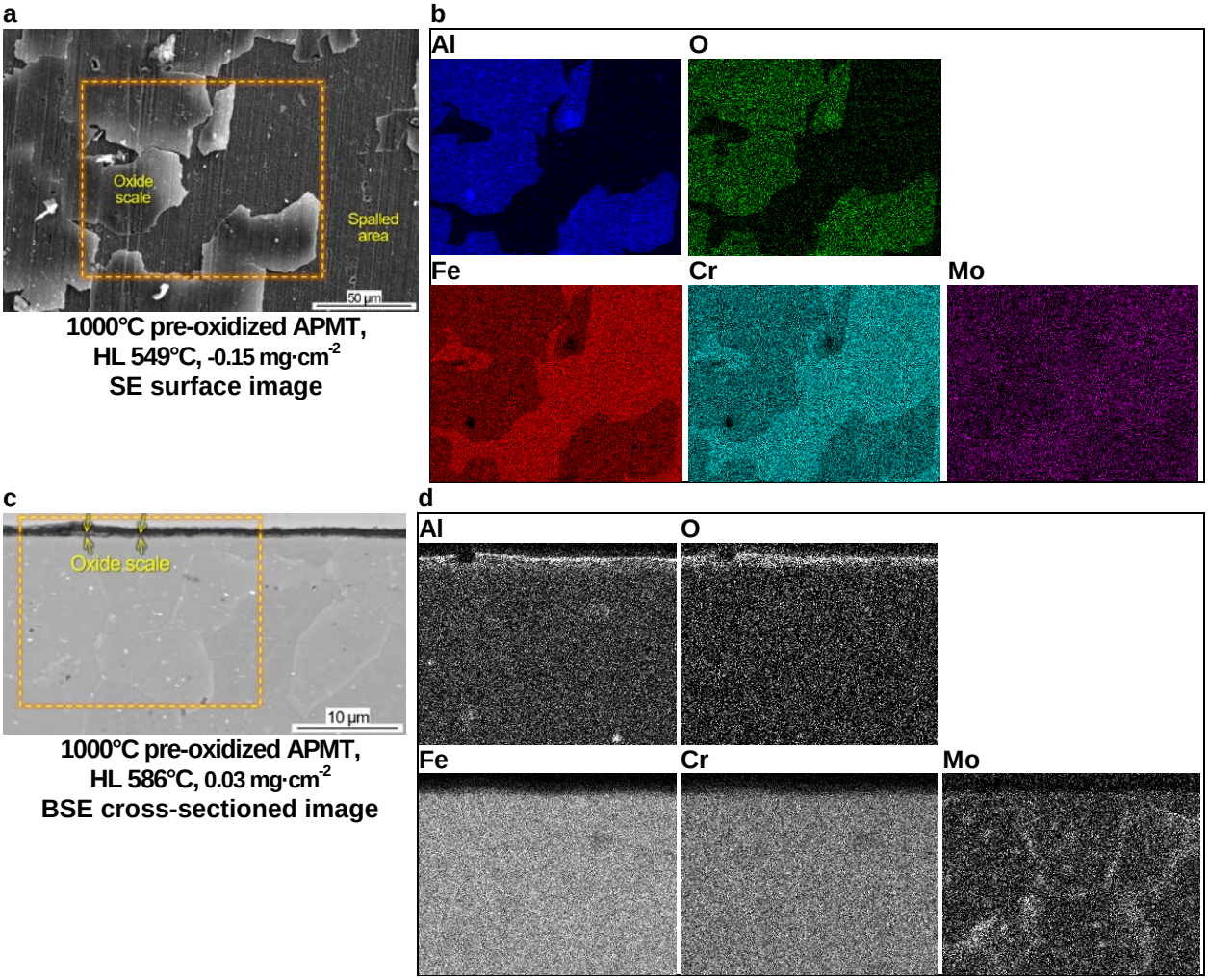

Figure 5. Pre-oxidized APMT (2 h at 1000°C) (a) SE plan view after exposure in HL at 549°C and (b) EDS maps of (a); (c) BSE section image of 586°C HL specimen and (d) EDS maps of (c).

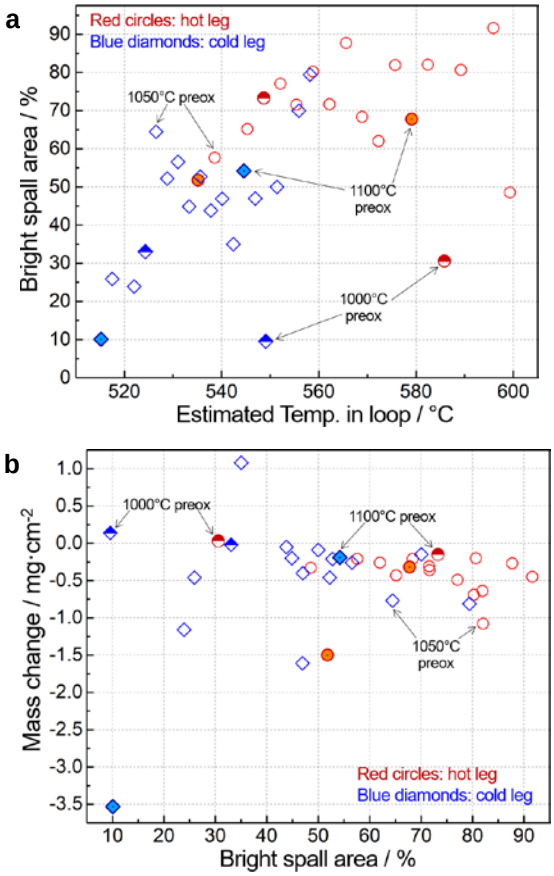

Figure 6. Estimated spallation area plotted versus (a) estimated exposure temperature and (b) specimen mass change in 600°C TCL. Three different pre-oxidation conditions were used.

References

[1] M. Abdou, et al., Fusion Sci. Technol., 47 (2005) 475.
[2] O. K. Chopra, et al., Fusion Technol., 8 (1985) 1956.
[3] J. Konys, et al., J. Nucl. Mater. 386-88 (2009) 678.
[4] B. A. Pint, L. R. Walker and K. A. Unocic, Mater. High Temp. 29 (2012) 129.
[5] K. A. Unocic and B. A. Pint, J. Nucl. Mater. 455 (2014) 330.
[6] B. A. Pint, S. Dryepondt, K. A. Unocic and D. T. Hoelzer, JOM 66 (2014) 2458.
[7] K. A. Unocic, D. T. Hoelzer and B. A. Pint, Mater. High Temp. 32 (2015) 123.
[8] P. Hubberstey, T. Sample and A. Terlain, Fusion Technol., 28 (1995) 1194-9.
[9] P. Hubberstey, J. Nucl. Mater. 247 (1997) 208.
[10] B. A. Pint and K. L. More, J. Nucl. Mater. 376 (2008) 108.
[11] J. H. DeVan, J. Nucl. Mater., 85-86 (1979) 249.
[12] S. J. Pawel, DOE-ER-0313/56 (2014) 178.
[13] S. J. Pawel, DOE-ER-0313/57 (2014) 132.
[14] S. J. Pawel, DOE-ER-0313/58 (2015) 185.
[15] S. J. Pawel and K. A. Unocic, J. Nucl. Mater. 492 (2017) 41.
[16] B. A. Pint and S. J. Pawel, DOE-ER-0313/60 (2016) 137.
[17] B. A. Pint and J. Jun, DOE/ER-0313/61 (2016) 133.
[18] N. Li, S. S. Parker and E. S. Wood, LA-UR-17-28480 (2017).

7. MECHANISMS AND ANALYSIS

7.1 HIGH-TEMPERATURE NEUTRON-IRRADIATION OF Ti-BASED $M_{n+1}AX_n$ PHASES—Matheus A. Tunes and Philip D. Edmondson **(**Oak Ridge National Laboratory)

OBJECTIVE

The overarching objective of this work is to perform detailed microstructural characterization of high temperature, neutron-irradiated Ti-based $M_{n+1}AX_n$ phases to provide a comparative microstructure database in support of the use of such materials in nuclear fusion applications.

SUMMARY

The $M_{n+1}AX_n$ phase alloys have been proposed for use in nuclear fusion reactors, but their radiation behavior has not yet been analyzed and understood when exposed to high temperature neutron-irradiation. Here, a transmission electron microscopy (TEM) based characterization of two Mn+1AXn alloys irradiated to 2 and 10 displacements per atom (dpa) at 1273 K has been performed. Initial results indicate that the defect microstructure is different when compared to lower temperature irradiations, with significant dislocation lines and networks being formed.

PROGRESS AND STATUS

Introduction

The $M_{n+1}AX_n$ phases can be defined as a recent class of engineered ternary compounds based on the mixing of an early transition metal (M), an element (A) from the IIIA-VIA groups of the periodic table with (X) carbon, nitrogen or both that produces a multi-layered crystal structure with both ceramic and metallic atomic planes. Due to its high-temperature oxidation resistance and superior mechanical strength when compared to pure ceramic compounds, there have been considerable efforts to assess the radiation tolerance of $M_{n+1}AX_n$ phases under displacive radiation aiming at its application within a fusion reactor core. The most recent research on the neutron-irradiation resistance of such materials has been concentrated on the analysis of radiation effects at moderate temperatures (573–973 K) and at low doses (0.1–1 displacement-per-atom or dpa). Among the several compounds studied, Ti_3SiC_2, Ti_3AlC_2 and Ti_2AlC were found to be the most promising candidates with the generation of a few dislocation loops and black spots on the basal planes [1]. In this work, we report on the effects of high-temperature (1273 K) neutron irradiation of Ti_3SiC_2 and Ti_2AlC and at dose levels of 2 and 10 dpa.

Experimental Procedure

Materials

Samples were irradiated in the High-Flux Isotope Reactor (HFIR) and the microstructural characterization has been carried out at the Low Activation Materials Laboratory (LAMDA) at the Oak Ridge National Laboratory (ORNL). The characterization of the radiation damage has been performed using conventional TEM techniques such as Bright-Field TEM (BFTEM), Dark-Field TEM (DFTEM) and $\vec{b} \cdot \vec{g} = 0$ condition for dislocation loop analysis.

Results

In contradiction to recent published results on the neutron irradiation effects of Ti-based $M_{n+1}AX_n$ phases, this work has identified different types of defects in such microstructures, including dislocation loops, dislocation lines, cavities and stacking faults. Additionally, there is strong evidence that the areal density of radiation-induced defects has increased significantly from 2 to 10 dpa (see Figure 1) which contradicts recent predictions in literature on the presumed self-healing and high dynamic recovery potentials of such compounds. We also found evidences for radiation-induced recrystallization in both microstructures at 10 dpa, although in all cases studied, the $M_{n+1}AX_n$ phases did not suffered amorphization. The results obtained thus far is suggestive of a different defect recovery occurring at elevated temperatures compared to those that have been observed in the lower temperature irradiations that have been published in the current literature.

Research Schedule and Progress

The electron microscopy characterization of the irradiated Ti-based $M_{n+1}AX_n$ phases is planned to be completed by the end of January 2018, including the analysis of pristine samples. A scientific manuscript is currently being prepared.

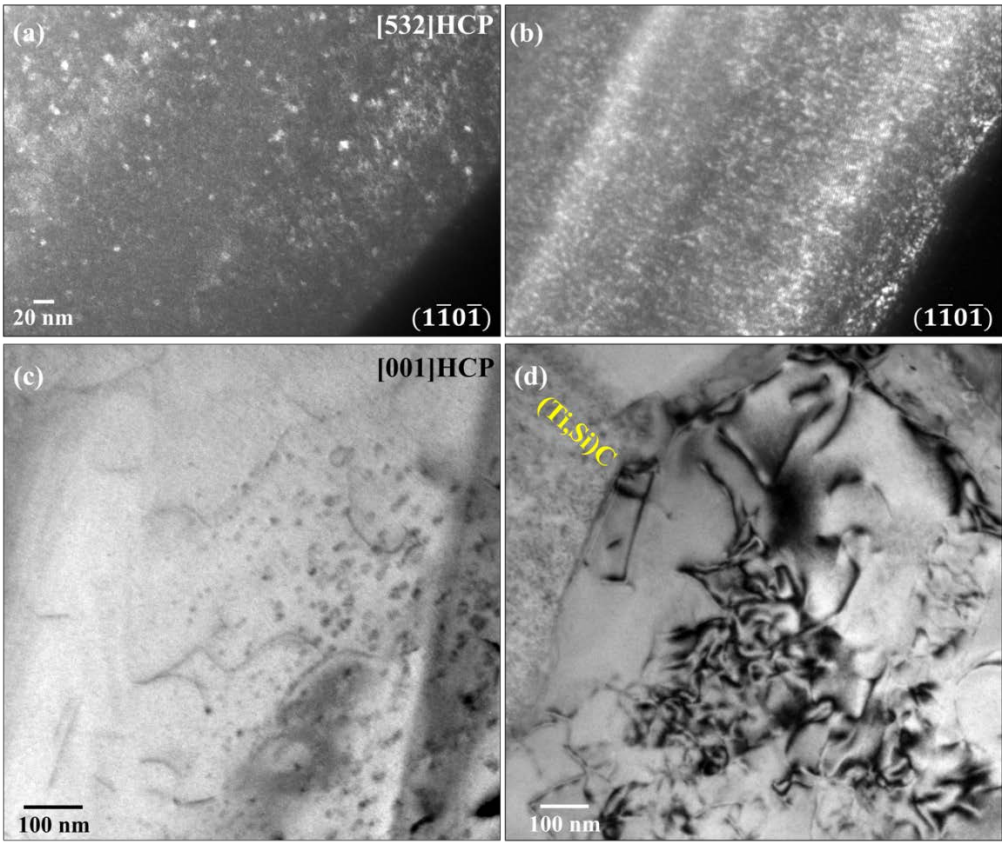

Figure 1. The DFTEM micrographs (a,b) exhibit the evolution of black spots in the microstructure of the Ti_2AlC at 2 and 10 dpa, respectively. The BFTEM micrographs (c,d) revealed dislocation loops and dislocation lines on the basal planes observed at 2 dpa have evolved to complex dislocation networks at 10 dpa. For both cases, the areal density of defects has increased from 2 to 10 dpa.

References

[1] D.J. Tallman, E.N. Hoffman, E.N. Caspi, B.L. Garcia-Diaz, G. Kohse, R.L. Sindelar, M.W. Barsoum, Effect of neutron irradiation on select MAX phases, Acta Mater. 85 (2015) 132–143. doi:10.1016/j.actamat.2014.10.068.

7.2 GENERATION AND INTERACTION MECHANISMS OF PRISMATIC DISLOCATION LOOPS IN FCC METALS—Can Erel, Giacomo Po, Tamer Crosby, and Nasr Ghoniem (University of California, Los Angeles)

*Extended abstract of a paper published in Computational Materials Science **140 (**2017) 32-46.*

The early stages of plastic deformation of fcc metals are characterized by the appearance of long dislocation dipoles and prismatic loops. Because they cannot self-annihilate by glide, prismatic loops are persistent debris, believed to play a significant role in strain hardening and patterning processes of both uni-axially and cyclically loaded fcc metals. Several characteristic features of plastic deformation can be directly related the formation, migration, and accumulation of prismatic dipolar dislocation loops. Much smaller prismatic loops are also produced in both fcc and bcc metals as a result of irradiation with energetic ions or neutrons. Collision cascades form a rich vacancy core surrounded by Self-Interstitial Atom (SIA) clusters. Because of the importance of these defects as obstacles to dislocation motion, and their influence on the formation of clear dislocation channels, they have been the subject of recent attention. We investigate the mechanisms of prismatic dipolar loop formation, motion, interactions, and large-scale patterning in fcc metals utilizing Discrete Dislocation Dynamics (DDD) [1]. We identify two main formation mechanisms; both enabled by cross-slip of screw dislocations. The first is termed Super-Jog-Drag-Truncation (SJDT), and the second is the Offset-Double-Cross-Slip (ODCS) mechanism. DD simulations show that the ODCS mechanism is a precursor to the SJDT mechanism, which then leads to the formation of prismatic dipolar loop arrays. It is shown that successive SJDT events enable a knitting mechanism that can generate long strings of prismatic loop arrays, consistent with experiments. We show that fully sessile dislocation segments arise in several loop-loop interactions, leading to Frank-Read and single-arm type sources. A new stable butterfly configuration is found when two (111) [011] prismatic loops interact to form glissile segments on conjugate glide planes, joined by one sessile segment that pins this structure. Absorption of prismatic loops by screw segments and the formation of helical turns is reproduced by DD simulations, consistent with earlier MD results [2]. An efficient new tripolar transport mechanism is found to contribute to the clustering of prismatic dipolar loops near Persistent Slip Band (PSB) channel walls during fatigue loading.

In summary, the following unique findings are drawn from the present study:

1. A new mechanism of knitting dislocation loop arrays has been shown to produce large arrays of dipolar loop strings of nearly equal size, consistent with the experimental observations of Carstensen (1998) [3];
2. New sessile dislocation configurations have been discovered as result of dislocation-dipolar loop, and loop-loop interactions (see Figure 1). Such sessile segments can act as strong dislocation obstacles, as well as provide new Frank-Read type sources;
3. A new tripolar drag mechanism was discovered. This transport mechanism is shown to lead to the formation of long, tight dipoles near PSB walls; and
4. The present dislocation dynamics calculations have confirmed literature MD simulations of dislocation-loop interactions, thus establishing the high fidelity and accuracy of DDD simulations.

Acknowledgements

The authors wish to acknowledge the support of the United States Department of Energy (DOE), Office of Fusion Energy, through the DOE award number DE- FG02-03ER54708 at University of California Los Angeles (UCLA), and the Air Force Office of Scientific Research (AFOSR), through award number FA9550-16-1-0444 with UCLA.

References

[1] Can Erel, Giacomo Po, Tamer Crosby, Nasr Ghoniem, “Generation and Interaction Mechanisms of Prismatic Dislocation Loops in FCC Metals,” Computational Materials Science **140**, 32-46, 2017.
[2] Nomoto, A., Soneda, N., Takahashi, A., Ishino, S. “Interaction analysis between edge dislocation and self-interstitial type dislocation loop in bcc iron using molecular dynamics.” Materials Transactions **46**

(3), 463–468, 2005.
[3] Carstensen, J. V. “Structural evolution and mechanisms of fatigue in polycrystalline brass.” Risø National Laboratory, Report # Risø-R- 1005(EN), 1998.

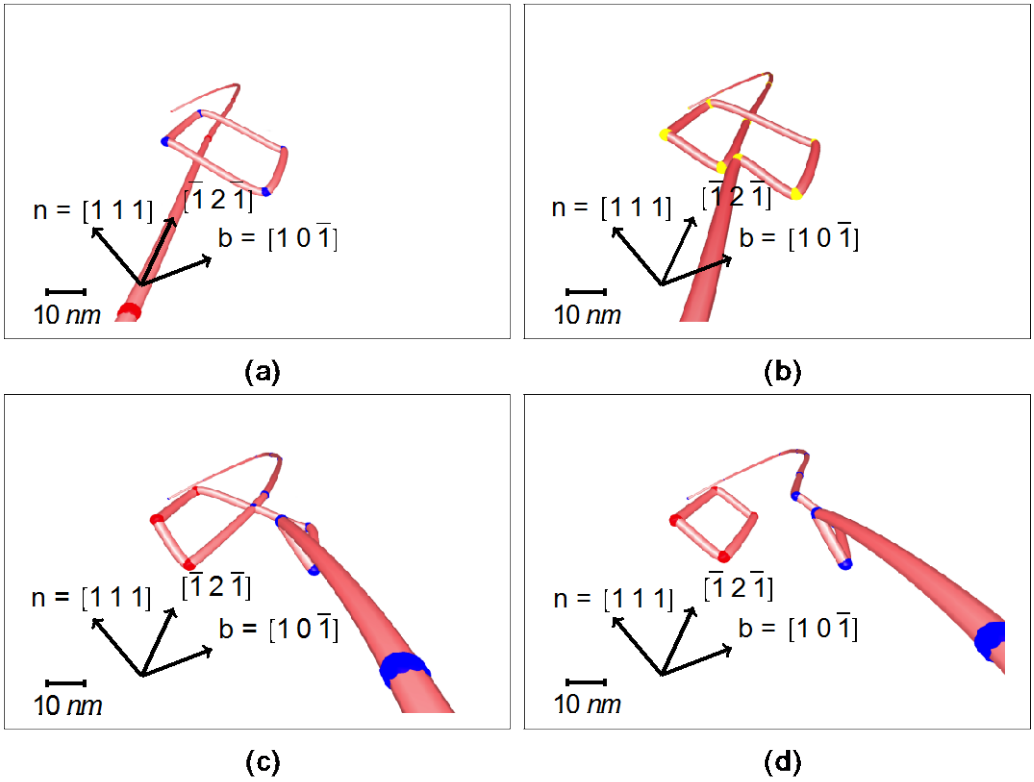

Figure 1. Mechanism of dipolar loop chopping by an edge dislocation. The sequence of events leading to loop chopping confirms the MD simulations of (Nomoto et al., 2005).

7.3 DEPENDENCE OF HARDENING AND SATURATION STRESS IN PERSISTENT SLIP BANDS ON STRAIN AMPLITUDE DURING CYCLIC FATIGUE LOADING—Can Erel, Giacomo Po, and Nasr Ghoniem (University of California, Los Angeles)

*Extended abstract of a paper published in Philosophical Magazine **97 (32)**, (2017) 2947-2970.*

The localization of plastic strain into Persistent Slip Bands (PSBs) is the most distinguishing feature of fatigued Face-centered cubic (FCC) crystals. The stress-strain behavior of a small volume containing a few PSBs is almost the same as that of the whole crystal in which they are embedded. This striking feature is a direct result of the fact that, once PSBs form, the applied strain is almost entirely accommodated by increasing the volume of the material containing PSBs. The behavior takes place at a critical stress value (so-called saturation stress), which, once attained, plastic deformation is accommodated by nucleation of more PSBs, and not by changing the deformation behavior within them. In addition to this significant observation about PSBs, their interaction with the free surface leads to roughening and ultimately fatigue crack nucleation. Cyclic loading of FCC single crystals leads to the formation of PSBs over a wide range of applied strain amplitudes.

The hardening and saturation stress associated with cyclic loading of Cu single crystals are reproduced with 3-D discrete dislocation dynamics simulations [1]. Evolution of the dislocation microstructure in PSB channels and walls during cyclic loading is shown to explain key features of plastic deformation. Screw dislocation segments are found to deposit edge components near PSB channel walls resulting in the nucleation of half-loops that expand into neighboring channels. The saturation stress is found to be $\tau_s \approx$ 34 MPa at an applied strain amplitude, $\gamma_p = 7.5 \times 10^{-3}$, within the range of experimental observations [2,3]. It is shown that once PSBs are formed, subsequent cycling at lower strain amplitudes does not lead to their elimination, but the cyclic stress–strain behavior is modified. At lower values of γ_p of previously formed PSBs, the saturation stress is found to decrease to $\tau_s \approx 24$ MPa at $\gamma_p = 1.5 \times 10{-}3$. Plastic energy dissipation in hysteresis loops is also significantly reduced but not removed. However, some reverse plasticity is shown to take place upon unloading at low values of γ_p, and is a direct result of strain recovery of loops that expand into neighboring channels during the loading phase.

In summary, the following aspects were revealed by the present investigation:

(1) The saturation stress dependence on the applied strain, and its consistency with experimental observations.
(2) Reverse plasticity behavior at low applied strain amplitudes in pre-deformed PSBs.
(3) Dislocation permeation through PSB walls, and the consequence on the shape of the hysteresis loop.
(4) The origin of hardening in hysteresis loops as it relates to screw dislocations overcoming opposing screw dislocations at various inter-planar distances, dipolar loops at the interface between walls and channels, and the bowing out of edge segments into adjacent channels.
(5) The avalanche behavior of dislocations associated with the collective interaction between dense edge segments at PSB walls when the saturation stress is reached.
(6) Plastic energy dissipation in hysteresis loops is significantly reduced at lower applied strain amplitudes of pre-deformed PSBs, but not eliminated. The PSB formation phenomenon cannot thus be viewed as a reversible phase transition, as postulated in some literature.

Acknowledgements

The authors wish to acknowledge the support of the United States Department of Energy (DOE), Office of Fusion Energy, through the DOE award number DE- FG02-03ER54708 at University of California Los Angeles (UCLA), and the Air Force Office of Scientific Research (AFOSR), through award number FA9550-16-1-0444 with UCLA.

References

[1] Can Erel, Giacomo Po, and Nasr Ghoniem, "Dependence of Hardening and Saturation Stress in Persistent Slip Bands on Strain Amplitude During Cyclic Fatigue Loading," *Philosophical Magazine* **97 (32)**, 2947-2970, 2017.

[2] H Mughrabi, F Ackermann, and K Herz. "Persistent slip bands in fatigued face-centered and body-centered cubic metals." *Fatigue Mechanisms*, 1979.

[3] H Mughrabi. "Microscopic mechanisms of metal fatigue." *Strength of metals and alloys*, 569 1980.

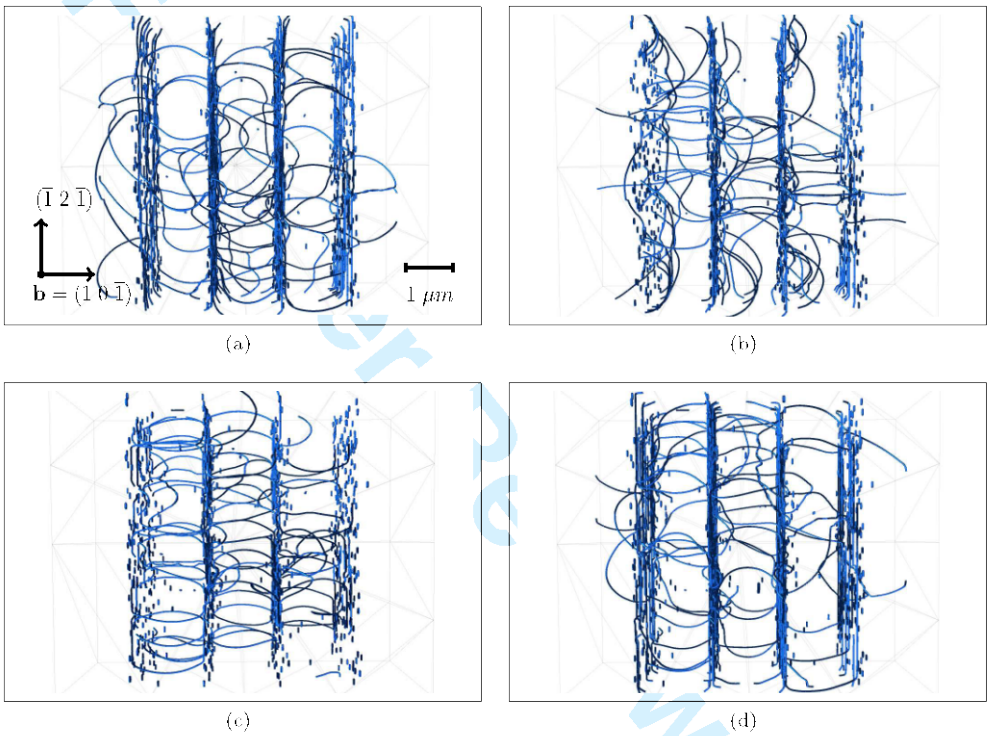

Figure 1. Dislocation microstructure accompanying the states a) A, b) B, c) C and d) D, $\gamma_p = 7.5 \times 10^{-3}$. Note the significant bowing out of edge segments at the interface between channels and walls in state B, and the very well-organized structure in state D, where dislocations have nearly rectangular racetrack configurations.

7.4 TOWARDS BEND-CONTOUR-FREE DISLOCATION IMAGING VIA DIFFRACTION CONTRAST STEM—Yuanyuan Zhu, Danny Edwards, Mychailo Toloczko, Richard J. Kurtz (Pacific Northwest National Laboratory), and Colin Ophus (Lawrence Berkeley National Laboratory)

Extended abstract of a manuscript under the review by Ultramicroscopy.

Dislocation imaging using transmission electron microscopy (TEM) has been an invaluable tool for characterizing crystallographic defects in metals. Compared to conventional TEM (CTEM), diffraction contrast imaging scanning transmission electron microscopy (DCI STEM) provides better defect contrast with almost negligible bend contour artifacts, enabling more reliable analysis of dislocation structures. To fully understand the behavior of defect contrast, we investigated the image formation process and found that DCI STEM alleviates bend contours by averaging out the rocking-curve oscillation in reciprocal space. Combining DCI STEM with analytical techniques already available in STEM imaging mode, we propose a new routine for comprehensive characterization of crystallographic defects as well as chemical information. This way of obtaining clearer and more comprehensive microscopy data tailored for nuclear structural alloys paves the way to improved determination and understanding of irradiation effects.

HIGHLIGHTS

Figure 1 schematically illustrates a new workflow that is capable of comprehensive microstructural and chemical characterization of irradiation-induced defects under a single imaging mode. Considering that foil thickness is important for an accurate estimation of dislocation density and precipitate number density, STEM-based electron energy loss spectroscopy (EELS) is the first step to provide TEM foil thickness information. Next, STEM dislocation imaging is conducted in selected regions with suitable foil thickness. Over the same sample region, STEM-based energy-dispersive X-ray spectroscopy (EDS) is

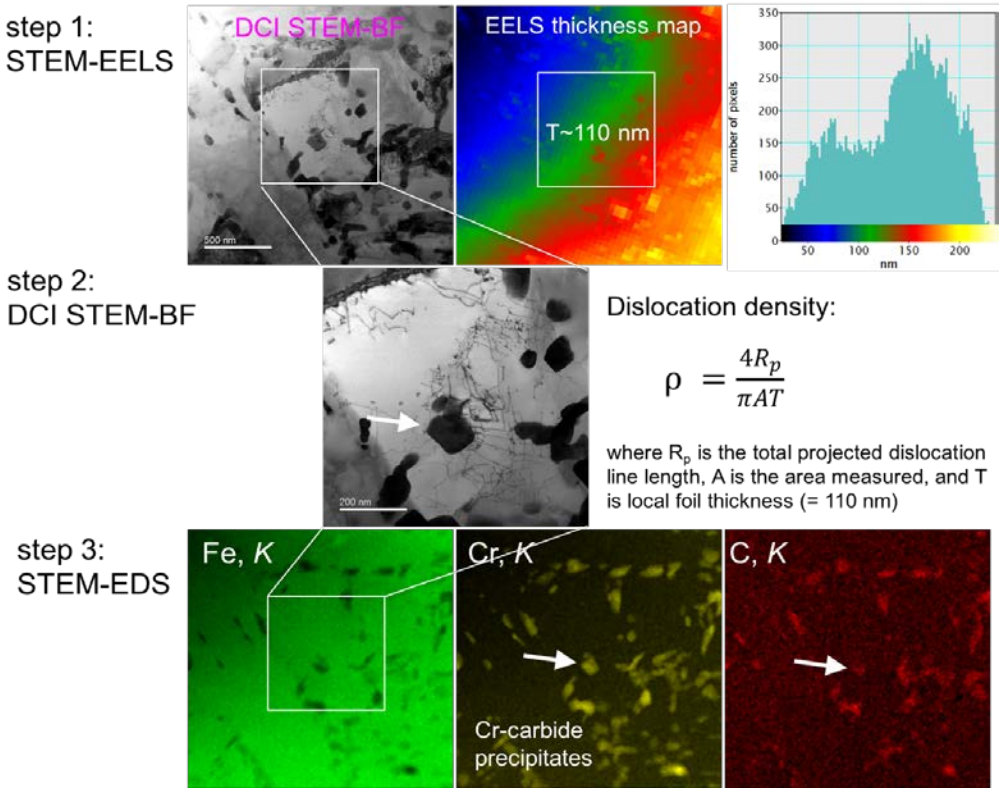

Figure 1. The workflow of a comprehensive defect characterization in STEM mode.

then performed to provide complementary chemical information in the same area of interest.

This is made possible due to the development of DCI STEM. Although previous studies have proven that, with proper parameters, DCI STEM satisfies the dynamical theory of diffraction contrast including ***g*** • ***b*** criteria, it has not been clear how DCI STEM suppresses bend contours nor how different STEM parameters affect the contrast of dislocation images. In this work, we investigated the image formation process in STEM mode (Figure 2) and found both the STEM convergence and collection semi-angles, α_S and β_S, need to be reasonably large (around a few mrad) to alleviate the bend contours that often dominate the background contrast of TEM dislocation images. Unlike the parallel electron beam in CTEM, the converged STEM electron probe opens a cone in reciprocal space that accesses the rocking-curve oscillation; then a sufficiently large β_S (~ α_S) behaves like a "mask" averaging out this oscillation,

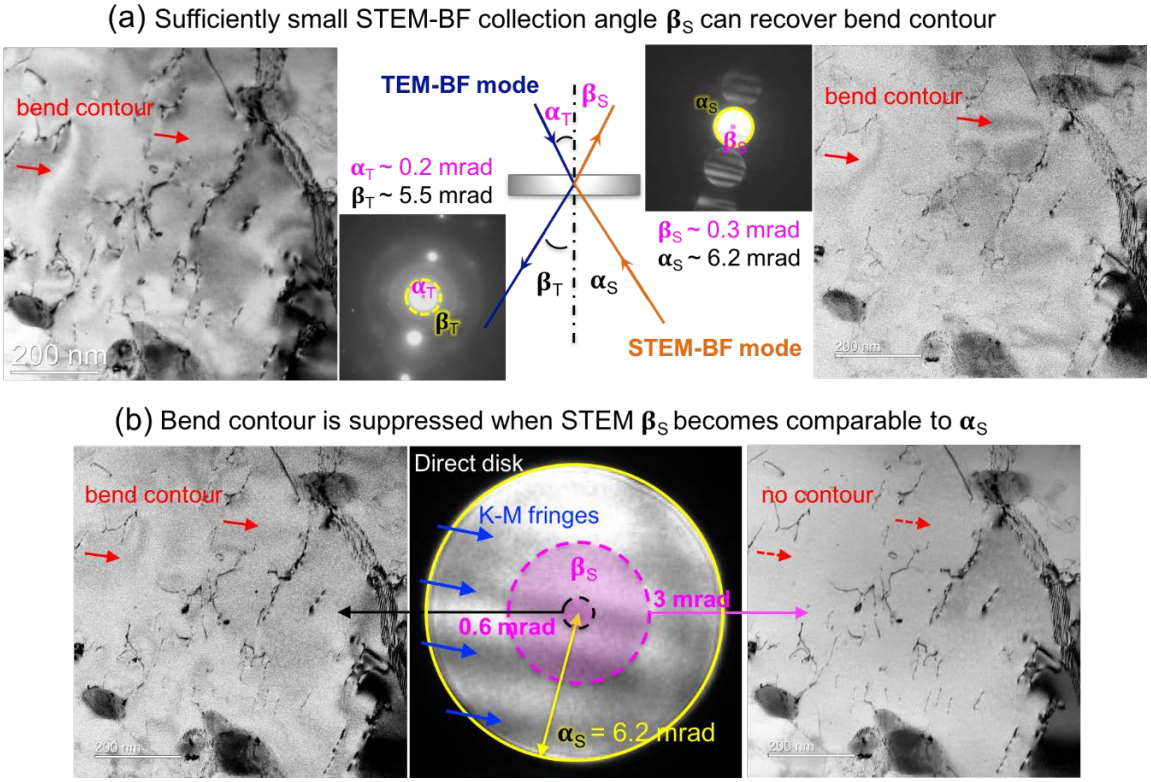

Figure 2. The influence of STEM bright field (BF) collection semi-angle β_S size on the presence of bend contours in dislocation imaging in STEM mode.

leading to a uniform background when imaging dislocations. It is particularly powerful in resolving complex microstructures containing a high density of dislocations, grain boundaries, and precipitates as typically observed in nuclear structural alloys. Moreover, we found relatively thick foils do not significantly degrade the DCI STEM image quality, an inherent advantage over CTEM images, which are usually limited to < 200 nm of foil thickness for any appreciable dislocation density (~ 10^{15} per m^2). Thus, the improvement in dislocation imaging coupled with the ability to simultaneously capture chemical information in STEM mode allows a faster, more comprehensive characterization of crystallographic defects and chemical information in a single imaging mode. This streamlined characterization can advance understanding of the interactions between irradiation-induced defects or between these defects and matrix grain structures, and can facilitate comparisons among nuclear alloys exposed to different irradiation conditions.

8. MODELING PROCESSES IN FUSION SYSTEM MATERIALS

8.1 RADIATION EFFECTS ON COHERENT PRECIPITATES IN BINARY Cu-1%Co ALLOYS—Ling Wang and Steven J. Zinkle (University of Tennessee, Knoxville)

OBJECTIVE

This study aims at providing initial information on the ballistic stability of different types of precipitates in different binary model alloys.

SUMMARY

Transmission Electron Microscopy (TEM) observations of the loss of coherency in Co-rich precipitates in heavy ion irradiated Cu-1%Co alloys serve as a 'diagnostic monitor' providing an indicator of the radiation defect migration behavior, since the interaction between radiation defects and coherent precipitates produces loss of precipitate coherency. Semi-coherent precipitates were observed in ion irradiated Cu-1%Co binary alloys, coexisting with coherent precipitates, well beyond the nominal maximum 600 nm depth of the irradiated region due to the migration behavior of interstitials under 1MeV Ni ion irradiation at 350°C to a peak dose of 12 dpa. The observed extent of the loss of coherency regime of 1700 nm beyond the nominal ion irradiation zone is significantly larger than expected 3-D motion mean free path, calculated as 127 nm, and more close to the calculated 1-D migration mean free path of 5600 nm for the initial precipitate size and density, indicating that most of the radiation-produced clusters exhibit 1-D motion.

PROGRESS AND STATUS

Introduction

Computer simulations of defect clusters in face centered cubic and body centered cubic metals [1-3] predict that defect clusters with sizes from ~5 to >50 vacancies or self-interstitial atoms (SIAs) may be highly mobile and exhibit predominantly one-dimensional (1-D) migration behavior. Since vacancy clusters become thermally unstable at temperatures above ~150°C (Recovery Stage V) due to typical binding energies of ~1 eV whereas SIA clusters are typically stable up to temperatures above ~700°C due to SIA cluster binding energies of >3 eV [2], glissile SIA clusters are of particular importance for operating temperatures relevant for nuclear energy applications. However, experimental confirmations of highly glissile 1-D migration of defect clusters is incomplete, and mainly consist of occasional observations of 1-D motion of SIA [4] or vacancy [5] clusters.

Experimental Procedure

Based on previous reports [6], a Cu-1%Co binary alloy was heat treated (Table 1) to produce uniformly distributed coherent Co-rich precipitates in Cu matrix with a measured number density of $4.3\times10^{20}/m^3$. The precipitate sink strength [7] is listed as $2\pi Nd$, where N and d are the precipitate density and diameter (Table 2). Following heat treatment, this alloy was mechanically polished to a mirror like surface and then irradiated at room temperature or 350°C with 1 MeV Ni+ ions in the Ion Beam Materials Laboratory at the University of Tennessee Knoxville (UTK). The damage range calculated by Stopping and Range of Ions in Matter (SRIM) 2013 code (Kinchin-Pease simulation mode) was around 600 nm and the peak dose was 12 dpa, assuming displacement threshold energy of 30 eV for pure copper.

Cross-sectional TEM foils were prepared via focused ion beam (FIB) lift-out techniques by using an Field Electron and Ion Company (FEI) Quanta 3D 200i Dual Beam workstation. In order to reduce un-wanted FIB-induced damage and surface oxide layers, all samples were further thinned using Ar+ ions at 900eV in a Fischione Nanomill 1040 system with an incidence angle of ±10° for 3 min, and then cleaned in a Fischione 1020 Plasma Cleaner for another 3 min. Conventional TEM examination was performed in a Japan Electron Optics Laboratory (JEOL) 2100F operated at 200kV. X-ray energy dispersive

spectroscopy (EDS) mapping was performed in an FEI Talos F200X scanning/transmission electron (S/TEM), using a SuperX four-detector EDS system.

Results

It is known that freely-migrating point defects, generated by neutron or ion irradiation, can be absorbed at sinks such as grain boundaries, dislocations, surfaces and precipitate interfaces [7]. In this study, the average grain diameter is around 150 μm in our bulk sample (much larger than the ion irradiated regions investigated in this work) and the dislocation density was very low. Therefore, the majority of the irradiation-induced point defects can be trapped at the interface between Co-precipitates and the matrix because of their affinity in terms of lattice strain. As a neutral sink, coherent precipitates act as traps that capture a defect but preserve its identity until it is annihilated by the opposite type defect. The precipitate coherency can be envisioned by considering that a certain volume of the matrix (copper) is removed and replaced by a different volume of product phase (Co-precipitate). The difference in volume leads to a dilatational strain which is negative, due to the smaller lattice parameter of Co compared to Cu matrix induced volume change. The interface of the coherent precipitate with the matrix can be modeled as containing a distribution of saturable traps. The bright field (BF) TEM images of Cu-1%Co specimens with the sink strength of $5.9\times10^{13}/m^2$ irradiated at 350°C to a peak dose of 12 dpa are shown in the middle of Figure 1. Here, three interesting regions may be observed, each of which is depicted in several high magnifications BF and dark field (DF) images. The first region is called ‘incoherent region’ and it’s visible through the whole irradiated region, where the depth from the irradiated surface is around 600 nm. In this region, Co-precipitates lose coherency due to absorption of interstitials and vacancies at the interface of the coherent precipitate with the matrix and become totally incoherent with the matrix. In other words, the precipitate loss of coherency is indicative that the coherency strain is relieved by absorbing radiation defects [4]. The corresponding high magnification TEM image of those incoherent precipitates is shown in Figure 2. The second region we call ‘coherent region’; it has uniformly distributed coherent and spherical precipitates and is located a couple of micrometers deeper than the irradiated region. The third region occurs between the irradiated incoherent region and deep unirradiated coherent regions and consists of a combination of incoherent and coherent precipitates; approximately 90% of the Co-precipitates become incoherent with some small loops. This transition region extends from the irradiated maximum depth (“end of range”) to 1700 nm beyond the end of range.

Figure 2 shows three high magnifications TEM images of incoherent ‘cauliflower like’ shape Co-precipitates at three different depths within the ion irradiated region at 350°C. The zone axis is <100>.

Figure 3 shows an EDS mapping of one of the above Cu-1%Co alloys irradiated with 1 MeV Ni ions at room temperature to a peak dose of 12 dpa. Co-precipitates exhibited stable size and density as in the incoherent region. The precipitate mean diameter was 29 nm in the ion irradiated region, 26 nm in the intermediate region and 23 nm as original mean diameter.

Compared to predicted 1-D and 3-D migration of SIA clusters in homogeneously distributed precipitate sinks [8], Table 2 showed partial loss of precipitate coherency results that are consistent with 1-D defect cluster motion as the observed extent of the loss of coherency regime (1700 nm beyond the calculated ion damage range) is significantly larger than 3-D motion mean free path, calculated as 127 nm, and is more close to the calculated 1-D motion mean free path of 5600 nm for the initial precipitate size and density, indicating the most SIA clusters would migrate in 1-D motion.

Conclusions

Semi-coherent precipitates were observed in ion irradiated Cu-1%Co binary alloys, coexisting with coherent precipitates well beyond the nominal maximum 600 nm depth of the irradiated region due to the migration behavior of interstitials under irradiation condition at 350°C. The loss of coherency in these Co-precipitates acts as a ‘diagnostic monitor’ providing an indicator of the radiation defect migration behavior

upon heavy ion irradiation, since the interaction between radiation defects and coherent precipitates produces loss of precipitate coherency.

Table 1. Pre-ion irradiation heat treatment and precipitate size, density and sink strength

Alloy	Solution Annealed	Cooling	Aging	Cooling
Cu-1%Co	1000℃/1h	WQ	600℃/1h	AC

Table 2. Calculation results by 1-D vs. 3-D migration of SIA clusters on microstructural evolution

Alloys	ppt. size range (nm)	ppt. mean size (nm)	Density (m^{-3})	Sink strength ~2πNd (m^{-2})	3-D motion $\lambda\sim(\pi r^2N)^{-1}$ (nm)	1-D motion $\lambda\sim(4\pi rN)^{-1/2}$ (nm)	Observed BEOR loss of coherency (nm)
Cu-1%Co	14~32	23	4.3×10^{20}	5.9×10^{13}	127	5600	~1700

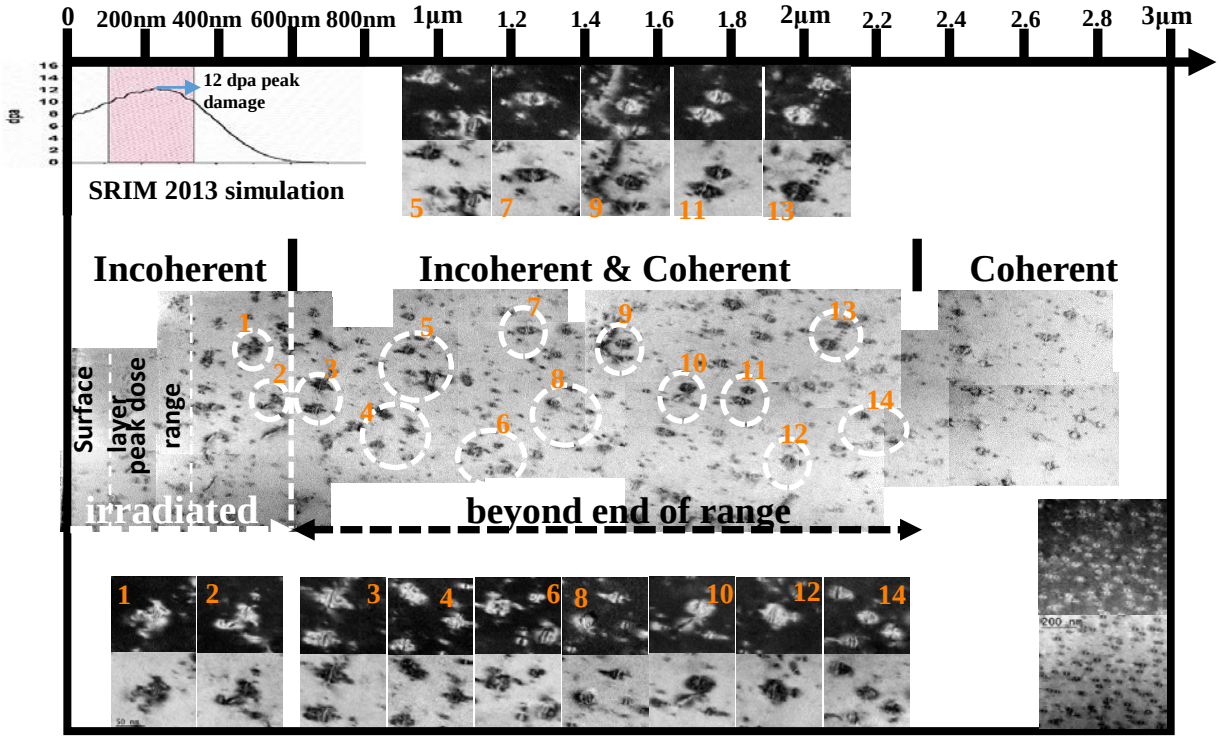

Figure 1. The BF TEM images of Cu-1%Co binary alloys irradiated at 350°C to a peak dose of 12 dpa. The displacement damage depth profile is shown in the upper left inset figure.

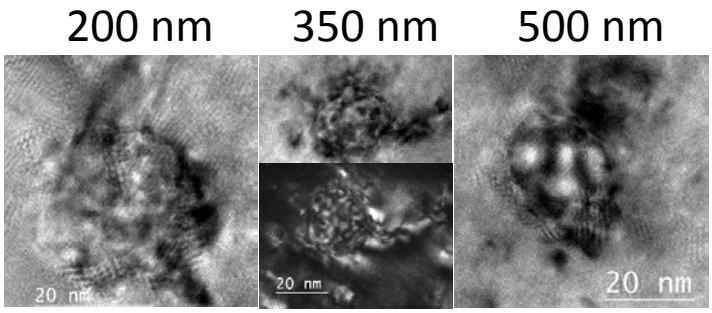

Figure 2. High magnification TEM images of incoherent 'cauliflower like' shape Co-precipitates at three different depths.

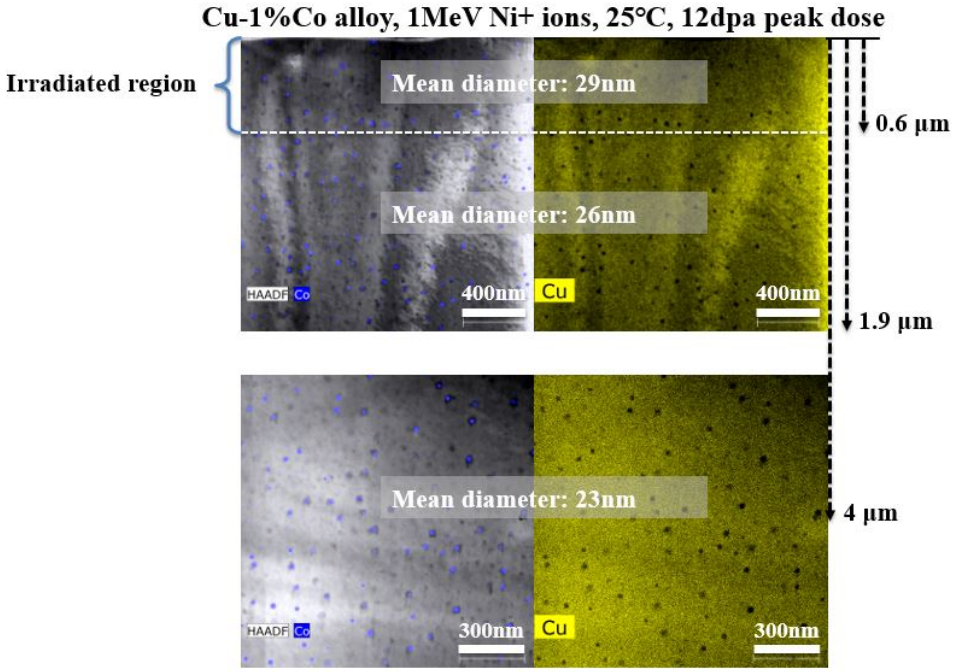

Figure 3. The EDS mapping of Cu-1%Co irradiated with 1MeV Ni ions at room temperature to a peak damage level of 12 dpa. The mean diameter of Co-precipitates in irradiated region (incoherent precipitates) is 29 nm, 26 nm in the region up to ~1 □m beyond the nominal irradiated region, and 23 nm in the original unirradiated regions.

Future work

The next step is to investigate the sink strength dependence on the extent of the loss of coherency regime through different precipitation treatment on Cu-1%Co binary alloys. Further experimental studies are needed to quantify the irradiation temperature- and dose rate-dependent conditions where sink strength become significant in radiation defect migration behavior.

References

[1] Y.N. Osetsky, D.J. Bacon, A. Serra, B.N. Singh, & S.I. Golubov, One-dimensional atomic transport by clusters of self-interstitial atoms in iron and copper. Philosophical Magazine 83 (2003) 61-91.

[2] Y.N. Osetsky, D.J. Bacon, A. Serra, B.N. Singh, S.I. Golubov, Stability and mobility of defect clusters and dislocation loops in metals, J. Nucl. Mater., 276 (2000) 65-77.

[3] H.L. Heinisch, H. Trinkaus, & B.N. Singh, Kinetic Monte Carlo studies of the reaction kinetics of crystal defects that diffuse one-dimensionally with occasional transverse migration. Journal of Nuclear Materials 367-370 (2007) 332-337.

[4] K. Arakawa, K. Ono, M. Isshiki, K. Mimura, M. Uchikoshi, H. Mori, Observation of the one-dimensional diffusion of nanometer-sized dislocation loops, Science, 318 (2007) 956-959.

[5] Y. Matsukawa, S.J. Zinkle, One-dimensional fast migration of vacancy clusters in metals, Science, 318 (2007) 959-962.

[6] G. R. Woolhouse, M. Ipohorski. On the Interaction between Radiation Damage and Coherent Precipitates. Proc. Royal Society A 324 (1971) 415-431.

[7] L.K. Mansur, Theory and experimental background on dimensional changes in irradiated alloys, J. Nucl. Mater., 216 (1994) 97-123.

[8] H. Trinkaus, H.L. Heinisch, A.V. Barashev, S.I. Golubov, B.N. Singh, 1D to 3D diffusion-reaction kinetics of defects in crystals, Phys. Rev. B, 66 (2002) 060105.

8.2 DEVELOPMENT OF INTERATOMIC POTENTIALS IN TUNGSTEN-RHENIUM SYSTEMS—W. Setyawan and R. J. Kurtz (Pacific Northwest National Laboratory), N. Gao (Institute of Modern Physics, Chinese Academy of Science, China)

Extended Abstract of a paper submitted to Physical Review Materials.

The objective of this research is to develop interatomic potentials for exploring radiation damage in W in the presence of solid transmutation product Re and radiation-induced precipitation of W-Re intermetallic phases. A tungsten-rhenium classical interatomic potential is developed within the embedded atom method interaction framework. A force-matching method is employed to fit the potential to *ab initio* forces, energies, and stresses. Simulated annealing is combined with the conjugate gradient technique to search for an optimum potential from over 1300 initial trial sets. The potential is designed for studying point defects in tungsten-rhenium systems. It gives good predictions of the formation energies of Re defects in tungsten and the binding energies of tungsten self-interstitial clusters with Re. The trend on the binding energies of small clusters of WW111 dumbbells with a substitutional Re atom is shown in Figure 1. The trend is compared to that calculated with the density functional theory (DFT) and a published potential (Bon17) [1].

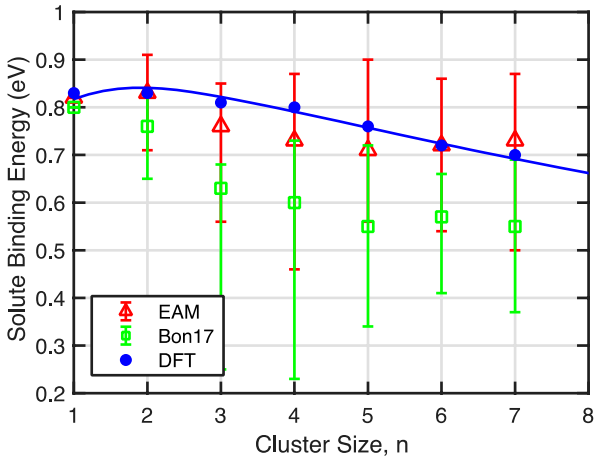

Figure 1. Binding energy of size-*n* WW111 clusters to a Re atom substituting one of the W dumbbell atoms. Results obtained using the fitted W-Re embedded-atom method (EAM) potential, a published Bon17 potential [1], and DFT [2]. The data points represent the average over the three most stable clusters. The tic marks represent the minimum and maximum values. The fit curve shows the fit over the DFT data as done in Ref. [2].

The potential is further evaluated for describing the formation energies of structures in the σ and χ intermetallic phases. The predicted convex-hulls of formation energies are in excellent agreement with the *ab initio* results as shown in Figure 2. In Figure 2, the convex-hull for each phase is drawn connecting the stable structures within the phase. Structures labelled as σ-20 and χ-4 represent the stable structures with Re concentration closest to that in the respective stoichiometric σ (WRe) and χ (WRe_3) compounds, i.e. 50% and 75% respectively. As evident from Figure 2, the fitted EAM potential performs significantly better than the Bon17 potential in reproducing the DFT results. In fact, the formation energy of the σ-20 and χ-4 is within 8 and 16 meV of the DFT values, respectively, while with Bon17 potential the differences are 55 and 201 meV.

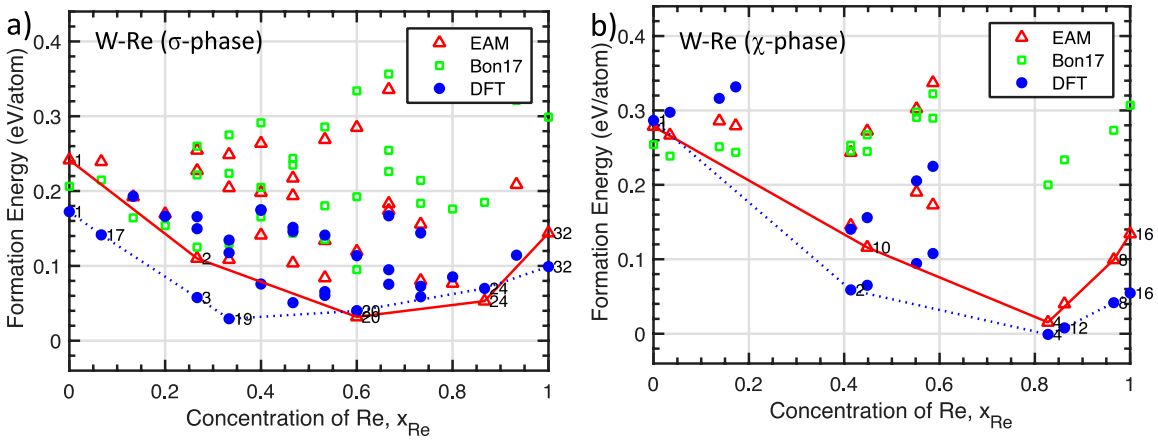

Figure 2. Formation energy of W-Re structures in the σ and χ phases with respect to bcc W and hcp Re. The stable structures in each phase are connected with a common-tangent line forming a convex-hull. The indices of the stable structures are shown.

The potential is also suitable for modeling intrinsic defects in a pure Re. The predicted formation energies of vacancy and interstitial defects are in good agreement with DFT. Specifically, the potential correctly predicts that the basal configurations BO and BS and the non-basal configurations C, O, S, and T are stable, while the basal BT and BC are unstable and spontaneously relax to the BO configuration. The interstitial configurations are depicted in Figure 3. In addition, DFT calculations show that C and T are the most stable configurations with the same formation energy of 6.52 eV. The potential also predicts C and T as the two most stable configurations with a formation energy of 6.29 eV and 6.40 eV, respectively. This is in contrast to Bon17 potential which incorrectly predicts BO to be the ground state configuration with a very high formation energy of 11.96 eV.

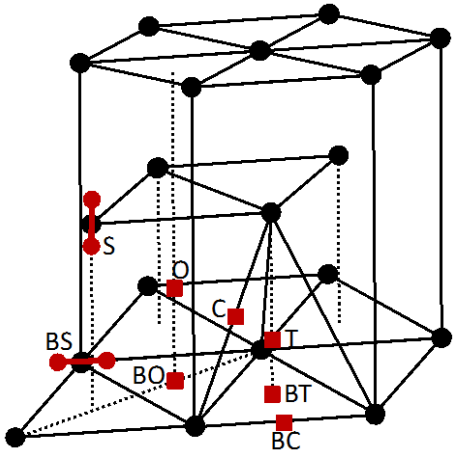

Figure 3. Interstitial configurations in an hexagonal close-packed lattice, namely crowdion (C), octahedral (O), split dumbbell (S), tetrahedral (T), basal projections of octahedral (BO) and tetrahedral (BT), basal crowdion (BC), and basal split dumbbell (BS).

Furthermore, by including liquid structures in the force-matching fit, the developed potential also performs better in describing the melting behavior of Re than the Bon17 potential. To validate the melting behavior, the melting temperature is determined by monitoring the crystalline/liquid interface of a two-phase system at zero external pressure. The fitted potential predicts the melting temperature of Re at 3130 K in good agreement with the experimental value of 3459 K, compared to Bon17 potential which predicts 4836 K.

Acknowledgement

We would like to acknowledge the support by National Natural Science Foundation of China (11375242, 11675230) and by the Youth Innovation Promotion Association Chinese Academy of Sciences.

References

[1] G. Bonny, A. Bakaev, D. Terentyev, Y. A. Mastrikov, *Journal of Applied Physics* 121 (2017) 165107.
[2] W. Setyawan, G. Nandipati, R. J. Kurtz, *Journal of Nuclear Materials* 484 (2017) 30.

8.3 OKMC STUDY OF DEFECT ACCUMULATION IN TUNGSTEN AT ROOM TEMPERATURE DUE TO RADIATION CORRESPONDING TO PKA SPECTRA OF 14-MeV-NEUTRON AND HIGH-FLUX ISOTOPE REACTOR (HFIR)—G. Nandipati, W. Setyawan, K. J. Roche, R. J. Kurtz (Pacific Northwest National Laboratory) and B. D. Wirth (University of Tennessee)

OBJECTIVE

The objective of this work is to understand differences in damage accumulation in pure tungsten (W) at room temperature due to radiation with primary knock-on atom (PKA) spectra corresponding to a 14 MeV-Neutron source and the High-Flux Isotope Reactor (HFIR) using the object kinetic Monte Carlo (OKMC) method.

SUMMARY

Using *KSOME* [1,2], OKMC simulations of radiation damage at room temperature (300 K) in pure, polycrystalline tungsten with a grain size of 2 μm were carried out. Preliminary simulation results are presented for damage accumulation in W when subjected to neutron bombardment with a PKA spectrum corresponding a 14 MeV-Neutron source for dose rates of $2.3 \times (10^{-4} - 10^{-8})$ dpa/s and HFIR for dose rates of $5.8 \times (10^{-4} - 10^{-8})$ dpa/s. During the initial stage of irradiation, both the number density of vacancies and vacancy clusters increase linearly with dose ($< 5 \times 10^{-2}$ dpa) and saturate with increasing dose. As expected, the density of vacancies and vacancy clusters and their average size are independent of dose rate, except for the lowest dose rate studied. Due to dissociation of di-vacancies, a small, but a noticeable increase in the vacancy cluster density is observed at the lowest dose rate studied. Nevertheless, the qualitative behavior of damage accumulation as a function of dose and dose rate is the same for both PKA spectra.

PROGRESS AND STATUS

Introduction

Simulations were performed using a non-cubic box with dimensions 95.10 x 96.37 x 97.00 nm^3 ($300a_0$ x $304a_0$ x $306a_0$, where a_0 is the lattice constant of tungsten), with each axis parallel to an $a_0\langle 100\rangle$ type direction. Each defect can hop to one of eight possible body-centered cubic nearest neighbor lattice sites at a distance of $a_0/2\langle 111\rangle$. Finite periodic boundary conditions were adopted in all three directions i.e. periodic boundary conditions are applied, but whenever a mobile object moves a distance larger than the average grain size, it is removed from the simulation, and it is no longer tracked. In the present simulations, we used an average grain size of 2 μm and no intragranular traps (dislocations or impurities) were considered.

The values of the binding energies of defects used in the present annealing simulations were taken from the *ab initio* calculations of Becquart *et al*. [3] while the migration barriers were taken from molecular dynamic (MD) simulations [4] using an embedded-atom method (EAM) potential for W [5]. In the present simulations, self-interstitial atom (SIA) clusters larger than size five were constrained to diffuse in 1D along one of four ⟨111⟩ directions. The SIA clusters up to size five can change their direction of 1D motion via rotation and thereby perform a mixed 1D/3D migration. The activation barrier for changing direction from one ⟨111⟩ direction to another is 0.38 eV [6]. The direction of 1D motion was assigned randomly to the SIAs at the start of a simulation, and interstitial clusters of all sizes are assumed to be glissile. Their migration/diffusion rates decrease with increasing cluster size (n) according to $\nu_o n^{-1}$ ($\nu_o = 6 \times 10^{12}$ s^{-1}) while the migration barrier is taken to be independent of cluster size.

For a single vacancy, the activation barrier for diffusion is taken as 1.30 eV [7], and vacancy clusters larger than five are assumed to be immobile. However, at room temperature vacancy clusters of all sizes are immobile but can emit mono-vacancies. The vacancy (SIA) dissociation rate is given by $\Gamma_d = \nu_d \exp((E_m + E_d)/k_B T)$, where E_d is the binding energy of a vacancy (SIA) to a vacancy (SIA) cluster, and E_m

is the migration energy of a single vacancy (SIA). We have assumed that defect clusters of all sizes and types are spherical objects, and their capture radii are obtained from Ref. [3].

An extensive database of cascades with PKA energies ranging from 10 keV to 200 keV, generated at 300 K using MD simulations [7, 8] was used to carry out the present simulations. Individual cascades were randomly selected from the cascade database based on the PKA spectrum being considered and were inserted into the simulation box at random positions based on the cascade production rate. The production rate of cascades, which is the number of cascades produced in the simulation cell per second, dose rates and the accumulated DPA (displacements per atom) are calculated based on the NRT displacements per cascade (ν_{NRT}) [9]. Also note that unless explicitly specified, the term 'PKA energy' represents the damage energy (E_{MD}) and not the recoil energy (E_{PKA}) of a PKA.

Results

Figures 1 and 2 show the densities of individual vacancies and vacancy clusters, and the average vacancy cluster radius as a function of dose for various dose rates for 14 MeV-Neutron and HFIR irradiation, respectively, at 300 K. During the initial stages of irradiation, a large fraction of the SIAs are absorbed at grain boundaries leading to a linear increase the density of individual vacancies with dose that can be seen in Figures 1(a) and 2(a). After this linear regime, an increasing fraction of the SIAs recombine with vacancies resulting in a gradual decrease of the damage (vacancy) accumulation rate. Finally, when all SIAs produced by a cascade recombine, the vacancy density approaches saturation. Accordingly, only the information regarding vacancies is shown in Figures 1 and 2. Also, note that only order-of-magnitude of dose rates are shown in the figures.

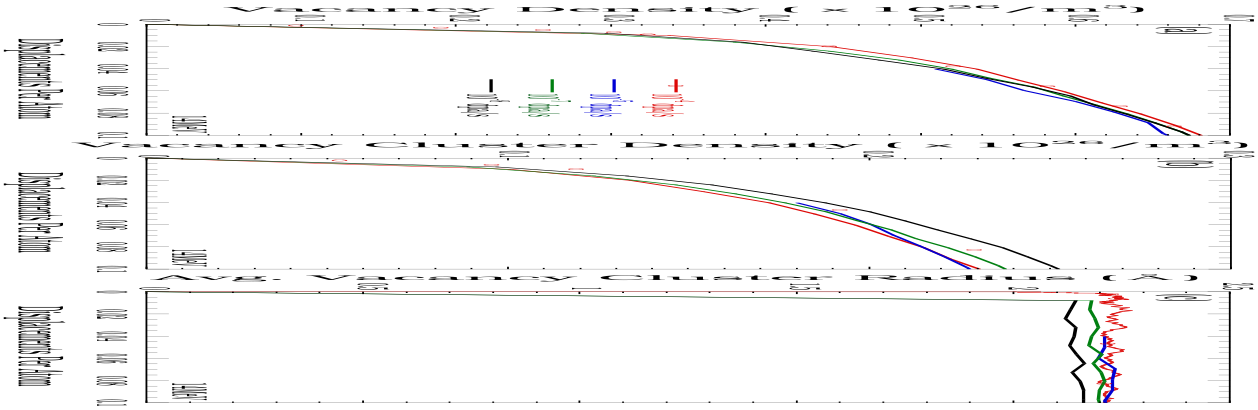

Figure 1. Comparison of (a) vacancy density, (b) vacancy cluster density and (c) average vacancy cluster radius as a function of dose at various dose rates for a 14 MeV-Neutron PKA spectrum.

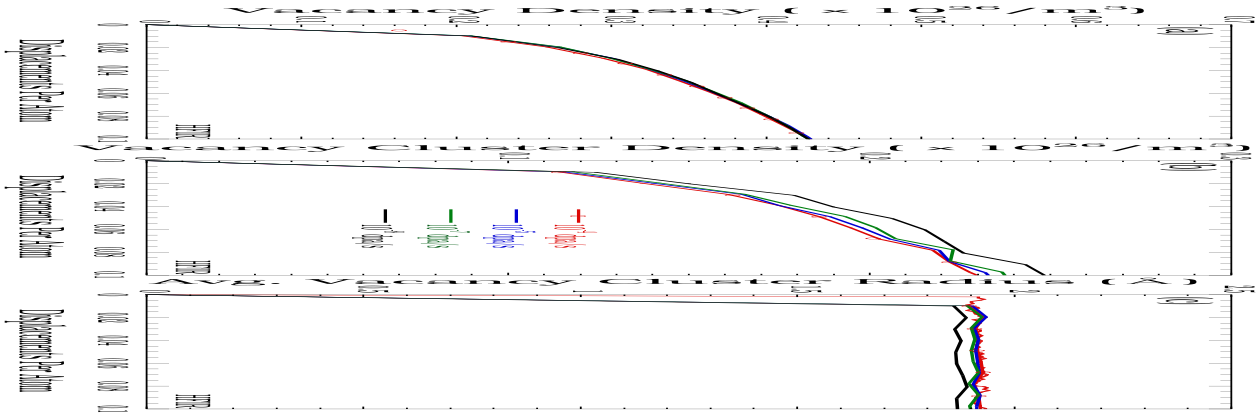

Figure 2. Comparison of (a) vacancy density, (b) vacancy cluster density and (c) average vacancy cluster radius as a function of dose at various dose rates for the HFIR PKA spectrum.

At 300 K, SIA clusters are the only diffusing defect species, and during irradiation they are either absorbed at grain boundaries, especially during the initial stages or recombine, at much shorter time scales when compared to the time interval between consecutive cascade insertions. Therefore, as expected, there is no effect of dose rate on the damage accumulation for both PKA spectra. This is typical of damage accumulation at temperatures where vacancies are immobile. Note that the same amount of irradiation damage is produced by both PKA spectra, regardless of the time required to reach a given dose. However, the surviving damage at that dose differs between the two PKA spectra due to the difference in the production rates of various defect cluster sizes. For the 14 MeV-Neutron source, higher production rates of large defect clusters results in faster accumulation of surviving damage when compared to HFIR irradiation, which can be seen by comparing the slopes of the linear-region in Figures 1(a) and 2(a). Production of larger defect clusters result in a lower fraction of diffusing defect species, which in turn reduces recombination resulting in a higher surviving damage. Nevertheless, for both PKA spectra the start of the non-linear regime seems to occur at approximately (slightly later in the HFIR's case) the same dose (see Figures 1(a) and 2(a)).

At temperatures where vacancies are immobile or diffuse slowly, the vacancy density, the vacancy cluster density, and the average vacancy cluster radius are expected to be independent of dose rate. However, for both PKA spectra, from Figures 1(b) and 2(b), and Figures 1(c) and 2(c), it is evident that the expected behavior is not observed at the lowest dose rate studied. The increase in the vacancy cluster density and a corresponding decrease in the average vacancy cluster radius at the lowest dose rate is due to vacancy dissociation. We think this is due to the repulsive binding energy of di-vacancies, which makes their dissociation rate much higher than their diffusion rate. This behavior is much more noticeable for HFIR irradiation because of the higher production rate of small vacancy clusters. Note that at fusion-reactor relevant temperatures, di-vacancies dissociate as soon as they are formed. However, at room temperature and especially for higher dose rates, the dissociation rate is slower than the cascade production rate, and even di-vacancy clusters tend to grow rather than dissociating.

Qualitatively, the damage accumulation behavior as a function of dose and dose rate observed in the present simulations is similar to that observed in our previous irradiation simulations of tungsten at 300K using only the cascades of a particular PKA energy, i.e. PKA spectrum corresponds to a delta function at that PKA energy [10]. The number density of vacancies and vacancy clusters increased linearly during the initial stages and saturated with increasing dose, in individual simulations using PKA energies (E_{MD}) of 40, 50, 60, 75, 100 keV. In contrast, in the individual simulations using cascades with PKA energies of 10, 20 and 30 keV damage accumulation increased linearly with dose up to 1.0 dpa, the maximum dose studied. Interestingly, even though the average E_{MD} of the HFIR PKA spectrum between 10-200 keV (E_{MD}) is approximately 28 keV, the behavior of damage accumulation is considerably different from that is obtained in the irradiation simulation using only the 30 keV cascades.

Acknowledgement

These simulations were performed using the CONSTANCE cluster at Pacific Northwest National Laboratory.

References

[1] G. Nandipati *et al* Semiannual Progress Report DOE/ER-0313/54, June 2013, 179-183.
[2] G. Nandipati, *et al* J. Nucl. Mater. (2015) 462 338–334.
[3] C. S. Becquart *et al.* J. Nucl. Mater. 403 (2010) 75.
[4] T. Faney, N. Juslin, B. D. Wirth, (*private communication)*.
[5] N. Juslin, B. D. Wirth, J. Nucl. Mater. 432(2013)61.
[6] D. A. Trentyev, L. Malerba, M. Hou, Phys. Rev. B 75 (2007) 104108.
[7] W. Setyawan, *et al* J. Nucl. Mater. (2015) 462 329–337.
[8] W. Setyawan *et al* Semi-annual Progress Report DOE/ER-0313/58 June2015 272-277.
[9] M. J. Norgett, M. T. Robinson, I. M. Torrens, Nucl. Eng. Des. 33 (1975) 50.
[10] G. Nandipati *et al* Semiannual Progress Report DOE/ER-0313/59, June 2016, 178-182.

8.4 MODELING DUCTILE-PHASE TOUGHENED TUNGSTEN FOR PLASMA-FACING MATERIALS: PROGRESS IN DAMAGE FINITE ELEMENT ANALYSIS OF TUNGSTEN-COPPER BEND BAR TESTS—B.N. Nguyen, C.H. Henager, Jr., N.R. Overman, R.J. Kurtz (Pacific Northwest National Laboratory)

OBJECTIVE

The objective of this study is to investigate the deformation behavior of ductile phase toughened W-composites such as W-Cu and W-Ni-Fe using a multiscale finite element model that involves a microstructural dual-phase model where the constituent phases (i.e., W, Cu, Ni-Fe) are finely discretized and are described by a continuum damage model. Such a model is suitable for modeling deformation, cracking, and crack bridging for W-Cu, W-Ni-Fe, and other ductile phase toughened W-composites, or more generally, any multi-phase composite structure where two or more phases undergo cooperative deformation in a composite system. During the current report period, we further validated the dual-phase microstructural approach by simulating the response as well as damage and fracture development of W-Cu un-notched and notched (SENB) specimens subjected to three-point bending and comparing the predictions to the corresponding experimental results to validate the model [1].

SUMMARY

A promising approach to increasing fracture toughness and decreasing the ductile-brittle transition temperature (DBTT) of a W-alloy is by ductile-phase toughening (DPT) [2-4]. In this approach, a ductile phase is included in a brittle matrix to increase the overall work of fracture for the material. There is a need for improved mechanical property models of such composite systems to optimize these structural materials with regard to high-temperature strength and fracture toughness for fusion-energy applications. We have further investigated the deformation behavior of a W-Cu composite, and refined the developed microstructural approach to predict crack initiation, propagation and load-displacement response controlled by DPT mechanisms. This report summarizes the validation of the dual-phase microstructural models developed for W-Cu un-notched and notched specimens subjected to three-point bending.

PROGRESS AND STATUS

Introduction

Tungsten (W) and W-alloys are the solid materials of choice for plasma-facing components (PFCs) of future fusion reactors, such as the International Thermonuclear Experimental Reactor (ITER) and Demonstration Power Plant (DEMO), due to their high melting point, strength at high temperatures, high thermal conductivity, low coefficient of thermal expansion, and low sputtering yield [5-7]. However, W and most W-alloys exhibit low fracture toughness and a high DBTT that would render them as brittle materials during reactor operations [5,7,8]. The DBTT for unirradiated W-alloys typically ranges from 573K to 1273K (300 to 1000˚C), and in a reactor environment radiation hardening would further elevate this range [7,9,10]. The W-alloys toughened by engineered reinforcement architectures, such as DPT, are strong candidates for PFCs. The principles of DPT are illustrated in Figure 1, which shows an actual and schematic illustration of ductile bridging ligaments stretching across an open crack in a brittle W matrix material [1]. The W-Cu is a DPT composite for model development purposes only.

Model Development

The approach used to build the finite element (FE) model for a W-Cu single-edge-notched bend (SENB) bar ((16 mm x 3.3 mm x 1.65 mm) is presented in [11,1]. This approach generates homogenized, meshed regions adjacent to the dual-phase meshed region shown in Figure 2a to create a fully meshed model of a bend bar that corresponds to the physical dimensions of an actual W-Cu SENB specimen. During the current report period, this approach was also applied to build a model for the un-notched W-Cu three-point bend specimen shown in Figure 2b. The dimensions of the un-notched specimen are: 16 mm x 3.24

mm x 1.55 mm. The dimensions of its supports, loading pin and bar as well as the support span are the same as those for the SENB specimen [1]. Because of cracking found along the specimen bottom surface after bending experiments, the width of the dual-phase domain (6.6 mm) considered for the un-notched specimen is significantly larger than the width of the dual-phase domain for the SENB specimen (4.72 mm). The as-created FE meshes shown in Figures 2a and 2b for the bend specimens possess three regions: the dual phase W-Cu microstructural region where damage, fracture and large deformation occur, and two adjacent continuum homogenized W-Cu linear elastic regions. Meshing for the silicon carbide (SiC) supports and loading pins was performed using their actual dimensions (diameter = 3.1 mm) and support span (13 mm). The SiC loading bar that applied the displacements to the loading pin was also modeled. All contacts between different entities of the models (Figure 2) are assumed to be frictionless.

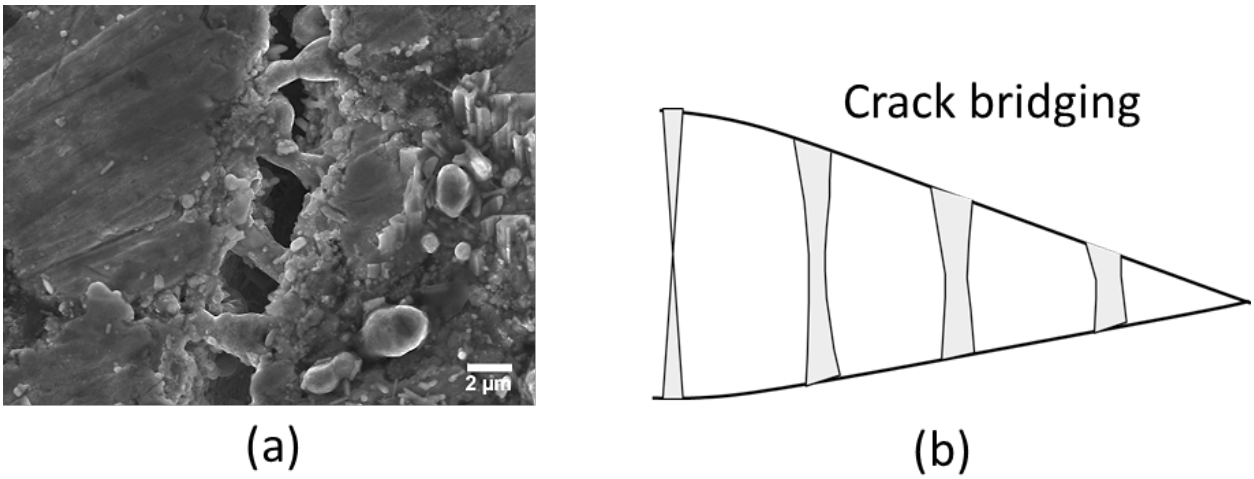

Figure 1. a) Scanning electron microscope (SEM) images of a crack in W-Cu tested at 632˚C in argon showing Cu ligaments bridging a crack [1]. b) A steady-state bridging zone shown schematically in 2D.

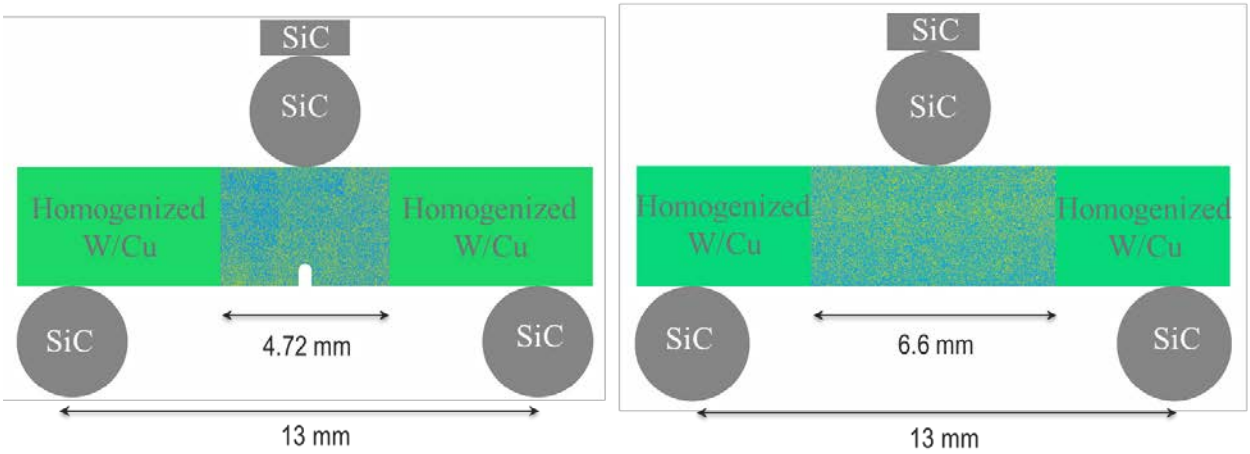

Figure 2. (a) The FE mesh of the W-Cu SENB specimen (3.3 mm x 1.6 mm x 16 mm). (b) The FE mesh of the W-Cu un-notched specimen (16 mm x 3.24 mm x 1.55 mm). The dual-phase microstructural domains are finely discretized with the constituent phases identified by color (yellow: copper; blue tungsten) [1].

The constitutive behaviors of W and of Cu considered in the analyses are described by an elastic-plastic damage model implemented in Pacific Northwest National Laboratory's (PNNL's) Eshelby-Mori-Tanaka Approach to Non-Linear Analysis (EMTA-NLA) [12] that acts as a user-subroutine module of ABAQUS. The model treats the different behaviors in tension and compression by only allowing damage evolution for a tensile stress state. While the stress/strain behaviors of *macroscale* Cu (e.g., [13]) and *macroscale* W (e.g., [14]) are rather well-known, the same kinds of elastic-plastic responses of these metals at the micron-scale of the microstructure (~grain size) are not known and constitute a challenge in this research. This problem is known as the size effect on material strength that has been reported for various materials including metals and ceramics. In this work, the reported stress/strain data for bulk Cu and W [13-14] were used as initial guesses. A series of FE analyses of the specimen models was performed to adjust model parameters until the predicted damage and fracture patterns as well as load-displacement responses reasonably agree with the corresponding experimental results. Thus, a single set of model parameters identified for each material (i.e., Cu or W) were used in the analyses of both specimen models [1].

Results

The FE models for the W-Cu SENB and un-notched specimens subjected to three-point bending were analyzed by ABAQUS. The crack propagation patterns for the W-Cu SENB specimen discussed in our previous report [11] are shown in Figure 3 for a comparison with the results for the un-notched specimen. Damage is quantified by a damage indicator that varies from 0 to 1. If the failure indicator is equal to 1, total failure (or fracture) occurs and is captured by a vanishing element method. In the SENB specimen, the cracks are found to meander and link up to form a main crack that propagates into the material close to the vertical centerline of the dual-phase domain. Figure 3a also shows the damage and crack patterns in the dual-phase domain for the un-notched specimen at an advanced stage of fracture. Many micro cracks meander and link up to form a main crack that propagates into the material nearly in the center of the dual-phase domain. In addition, a number of smaller cracks are predicted along the tensile surface of the specimen, meandering nearly parallel to the main crack. Figure 3b shows the cracked regions observed in experiments (performed at room temperature) on the SENB and un-notched specimens that validate model predictions for crack patterns and propagations. The predicted load-displacement responses for these specimens reported in Figures 4a and 4b agrees reasonably well with the experimental data.

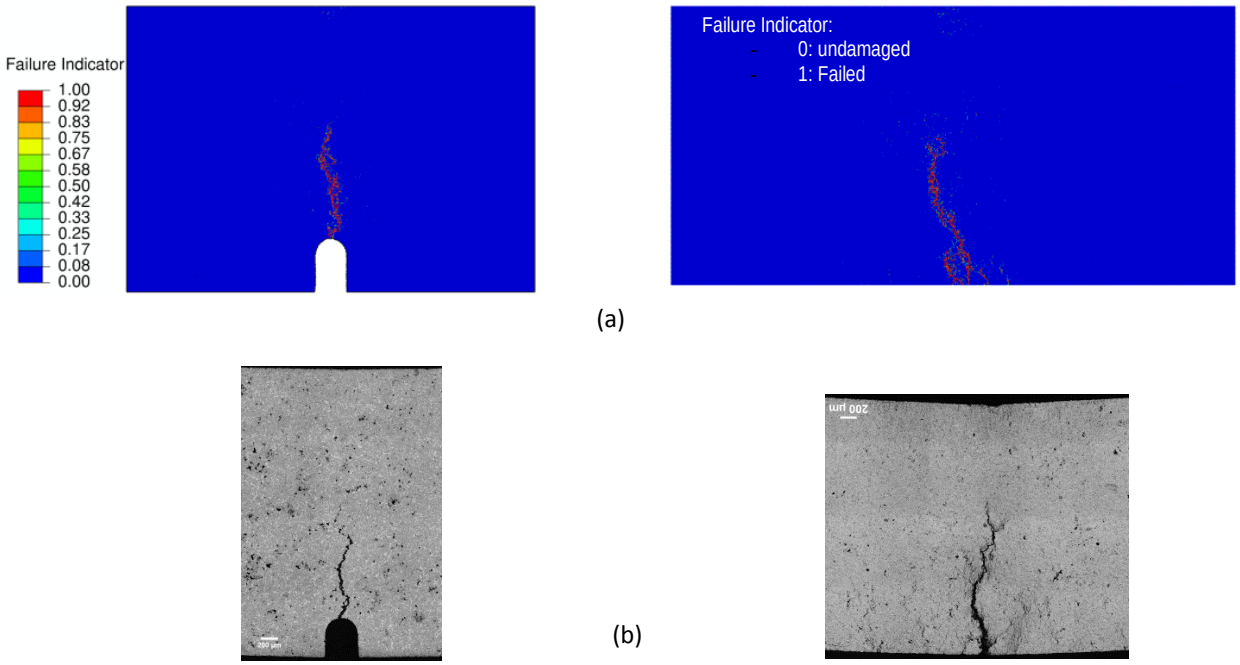

Figure 3. Predicted damage distributions and crack patterns (a) compared to experiments (b) in the microstructural regions of the W-Cu SENB (left) and un-notched (right) specimens [1].

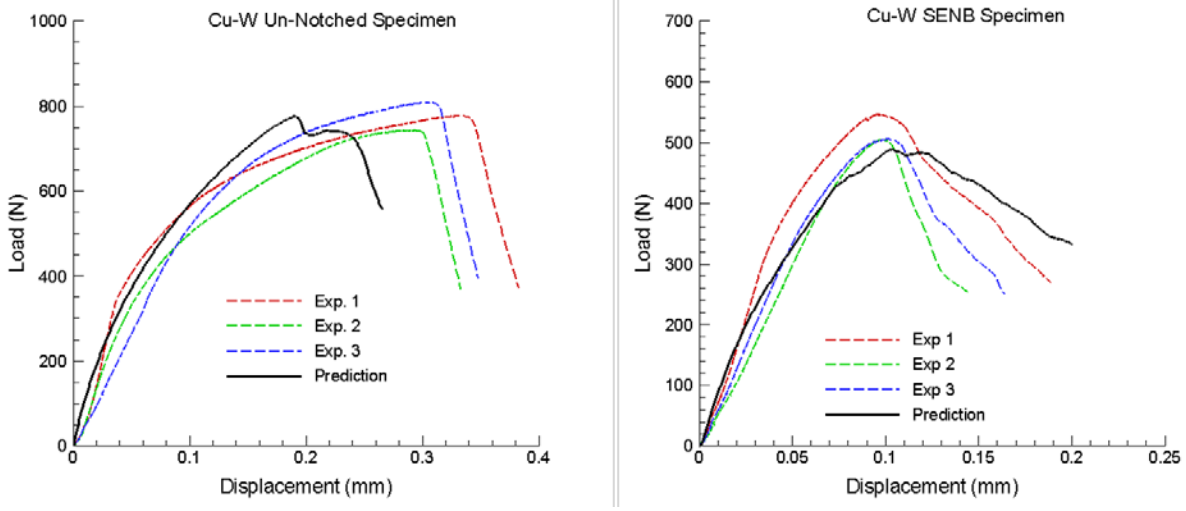

Figure 4. Predicted load-displacement responses compared to experimental results for the W-Cu notched (left) and SENB (right) specimens [1].

Conclusions

During this report period, important progress has been made in both modeling and experimental efforts to develop ductile phase-toughened tungsten for plasma-facing applications. We have finalized and experimentally validated a dual-phase microstructural approach to simulate W-Cu un-notched and SENB specimen tests. The current model predictions show good agreement with our recent experimental data with respect to load-displacement curves and crack patterns as well as propagation directions in the W-Cu composite. The model can effectively capture the bridging mechanism responsible for retarding crack

propagation. The developed approach appears to be robust and can be further enhanced to tailor the mechanical properties of DPT composites provided the constitutive properties are known.

Future Work

The developed approach is being applied to study W-Ni-Fe composites through similar bend bar tests and analyses.

References

[1] Nguyen, B.N., C.H. Henager, Jr, N.R. Overman, and R.J. Kurtz. 2018. A Multiscale Microstructural Approach to Ductile-Phase Toughened Tungsten for Plasma-Facing Materials. Journal of Nuclear Materials (Submitted).
[2] Deve, H.E., A.G. Evans, G.R. Odette, R. Mehrabian, M.L. Emiliani, and R.J. Hecht, Acta metallurgica et materialia, 1990. 38(8): p. 1491-502.
[3] Erdogan, F. and P.F. Joseph, J. Am. Ceram. Soc., 1989. 72(2): p. 262-270.
[4] Sigl, L.S., P.A. Mataga, B.J. Dalgleish, R.M. McMeeking, and A.G. Evans, Acta Metall., 1988. 36(4): p. 945-953.
[5] Rieth, M., J.L. Boutard, S.L. Dudarev, T. Ahlgren, S. Antusch, N. Baluc, M.F. Barthe, C.S. Becquart, L. Ciupinski, J.B. Correia, C. Domain, J. Fikar, E. Fortuna, C.C. Fu, E. Gaganidze, T.L. Galan, C. Garcia-Rosales, B. Gludovatz, H. Greuner, K. Heinola, N. Holstein, N. Juslin, F. Koch, W. Krauss, K.J. Kurzydlowski, J. Linke, C. Linsmeier, N. Luzginova, H. Maier, M.S. Martinez, J.M. Missiaen, M. Muhammed, A. Munoz, M. Muzyk, K. Nordlund, D. Nguyen-Manh, P. Norajitra, J. Opschoor, G. Pintsuk, R. Pippan, G. Ritz, L. Romaner, D. Rupp, R. Schaublin, J. Schlosser, I. Uytdenhouwen, J.G. Van Der Laan, L. Veleva, L. Ventelon, S. Wahlberg, F. Willaime, S. Wurster, and M.A. Yar, J. Nucl. Mater., 2011. 417: p. 463-467.
[6] Pitts, R.A., A. Kukushkin, A. Loarte, A. Martin, M. Merola, C.E. Kessel, V. Komarov, and M. Shimada, Physica Scripta Volume T, 2009. 2009(T138): p. 014001 (10 pp.).
[7] Mertens, P., T. Hirai, M. Knaup, O. Neubauer, V. Philipps, J. Rapp, V. Riccardo, S. Sadakov, B. Schweer, A. Terra, I. Uytdenhouwen, and U. Samm, Fusion Eng. Des., 2009. 84(7-11): p. 1289-93.
[8] Mertens, P., V. Philipps, G. Pintsuk, V. Riccardo, U. Samm, V. Thompson, and I. Uytdenhouwen, Physica Scripta Volume T, 2009. 2009(T138): p. 014032 (5 pp.).
[9] Gludovatz, B., S. Wurster, A. Hoffmann, and R. Pippan, Int. J. Refract. Met. Hard Mater., 2010. 28(6): p. 674-8.
[10] Zinkle, S.J. and N.M. Ghoniem, Fusion Eng. Des., 2000. 51-52: p. 55-71.
[11] Nguyen B.N., C.H. Henager, Jr, and R.J. Kurtz. 2017. "Modeling Ductile-Phase Toughened Tungsten for Plasma-Facing Materials: Progress in Damage Finite Element Analysis of the Tungsten-Copper Bend Bar Tests." Chapter 8.4 in Fusion Materials Semiannual Progress Report For the Period Ending December 31, 2016, vol. 61; DOE/ER-0313/61, ed. FW Wiffen and S Melton, pp. 171-177, Oak Ridge National Laboratory, Oak Ridge, TN.
[12] Nguyen, B.N., EMTA-NLA User's Guide. Pacific Northwest National Laboratory, Richland, WA, 2010, PNNL-20013.
[13] Sandstrom, R. and Hallgren, Stress strain flow curves for Cu-OFP, Royal Institute of Technology, Swedish Nuclear Fuel and Waste Management Co, 2009, R-09-14.
[14] Dummer T., J.C. Lasalvia, G. Ravichadran, and M.A. Meyers. Acta Materialia, 1998, 146(17): p. 6267-90.

8.5 MODELING THE EFFECTS OF HELIUM BUBBLES ON THE STRESS-STRAIN BEHAVIOR OF IRON GRAIN BOUNDARIES BY A MECHANISTIC FINITE ELEMENT APPROACH USING MOLECULAR DYNAMICS DATA—B.N. Nguyen, R.J. Kurtz (Pacific Northwest National Laboratory), and F. Gao (University of Michigan)

OBJECTIVE

The objective of this study is to investigate the effects of helium (He) bubbles on the stress-strain behavior of iron (α-Fe) grain boundaries (GB) by a mechanistic finite element (FE) approach using a continuum damage mechanics (CDM) description of the material behavior informed by molecular dynamics (MD) data. The approach developed finely discretizes an α-Fe bicrystal system in which the elastic-plastic crystals are connected one to another by cohesive elements. Helium bubbles accumulated at the GB are explicitly modeled through an equivalent hollow sphere under internal pressure and located in the middle of the modeling domain. Finite element analyses of this bicrystal system subjected to tensile loading, periodic boundary conditions and internal He pressure were performed using the ABAQUS FE package. The modeling results reveal a very significant effect of vacancy and high-pressure He bubble on the stress-strain response of the bicrystal system.

SUMMARY

The same bicrystal configuration given in [1] was finely discretized in 2-D plane-strain finite elements. The GB between the two α-Fe crystals was described by cohesive elements. This bicrystal system also includes an equivalent hollow sphere under internal pressure in the middle of the GB to model the effects of pressurized He bubbles on stress, strain and damage distributions. The radius of the equivalent sphere was determined assuming the presence of two or four vacancies in the system. The constitutive behavior of the crystals obeys a CDM elastic-plastic model with isotropic hardening while the cohesive elements follow a traction-separation law. Stress/strain data from an MD analysis of the same bicrystal system [1-2] without He bubbles were used to identify material parameters for the continuum constitutive models. This modeling approach appears to be a very efficient method to quantify the effects He bubbles on the stress-strain behavior and strength of an α-Fe GB.

PROGRESS AND STATUS

Background

Ferritic/martensitic steels are considered to be prime candidate materials for structural applications in future fusion reactors [3]. In such applications, these materials are exposed to high energy neutrons leading to He formation due to transmutation reactions. Formation of He is of particular concern because it can cause hardening and increases in the ductile-to-brittle transition temperature (DBTT) [4-5] and swelling as a result of nucleation and growth of He bubbles [6]. Helium also weakens GBs by lowering GB cohesive stress or promoting GB nucleation, growth and coalescence of GB cavities, which can lead to intergranular fracture at high temperature [7]. As it is very difficult to experimentally quantify the effects of nano-scale He bubbles on the material integrity, computational methods such MD simulations have been very helpful to elucidate the degradation mechanisms associated with He bubble formation. Although there are a significant number of atomistic studies of He in bulk α-Fe e.g., [8-29], work on He at α-Fe GBs is less extensive [1,30-40]. A promising and efficient approach to model the effects of He on the material integrity is by FE modeling of the bicrystal system in which CDM is used to describe the constitutive behavior of α-Fe and cohesive elements are used to model the GB behavior. The MD data of the homologue model are explored to identify the material parameters for the continuum constitutive models. Such an approach is termed mechanistic as it uses a CDM description informed by MD analysis results.

Model Development

The FE models to study the effects of He bubbles were developed based on the bicrystal system configuration for MD analysis given in [1]. Shi et al. [1] performed MD simulations of bicrystal α-Fe systems containing symmetric tilt boundaries with <110> and <100> tilt axes to investigate the effects of He vacancy (He-V) cluster size and He density on bicrystal tensile deformation behavior. Figures 1a and 1b show the FE models developed for plane-strain analyses of the α-Fe bicrystal systems containing the clean GB (without He bubbles) and the GB involving two vacancies depicted by an equivalent hollow sphere occupied by He at a given pressure. In these models the two crystals were connected one to another by cohesive elements. The dimensions of the modeling domains are 8 nm x 25 nm. In order to use the MD data given in [1-2], periodic boundary conditions were prescribed on the vertical boundaries of the modeling domains shown in Figures 1a and 1b, and in addition, the vertical displacements of the bottom boundaries were fixed while uniform vertical displacement loadings were incrementally applied on the top surfaces. The loading for the model with He bubbles (Figure 1b) also involved the prescribed internal pressure ramping up to a maximum value at the first loading step before application of the vertical displacement at the next loading step. The model with a clean GB (Figure 1a) was used to identify the material parameters for the constitutive laws used in the analyses. Subsequently, the same set of model parameters was used in all the analyses to determine the effect of the He bubble on the stress-strain response of the *as-formed* bicrystal system.

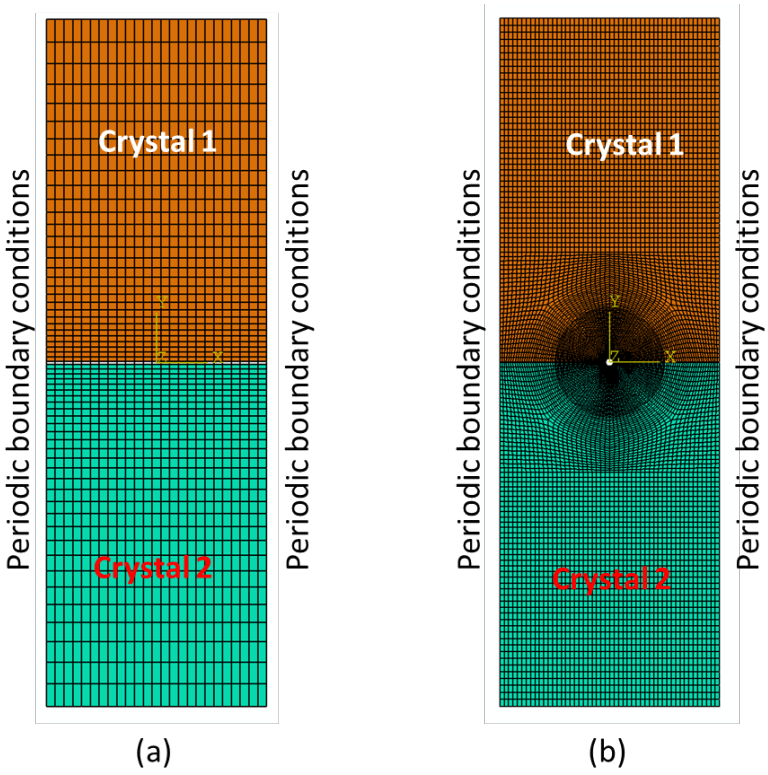

Figure 1. FE models for the α-Fe bicrystal system subjected to periodic boundary conditions along the vertical boundaries and tensile loading in the vertical direction (y-direction) – (a) model with clean GB, and (b) model with two vacancies depicted by an equivalent hollow sphere occupied by He.

Results

A series of ABAQUS analyses was first conducted for the model with clean GB based on the crystal lattice configuration specified in [1-2] (i.e, Σ11{332}) to identify the material parameters for the constitutive laws used for the bicrystal system. In this work, the elastic-plastic model with isotropic hardening and isotropic damage available in the ABAQUS material model options was used for the crystals while cohesive elements were used to describe the behavior of the GB. Figures 2a and 2b respectively illustrate the plots of the equivalent Von Mises stress and stress S_{yy} versus the applied strain e_{yy} (labelled as CDM) compared to the corresponding MD data from [1-2]. Good correlations between CDM and MD results allowed identification of the material parameters for use in subsequent analyses of the model with He bubbles.

Next, we conducted ABAQUS analyses of the model presented in Figure 1b to study the effects of He bubbles on the stress-strain response of the bicrystal system. The FE mesh shown in Figure 1b was carefully designed to capture damage and fracture initiated and propagated from the pressurized sphere as expected due to stress concentrations in this area. As mentioned earlier, the He pressure was applied inside the hollow sphere incrementally to a prescribed level during the first loading step. At the next loading step while maintaining the He pressure at the maximum prescribed level, uniform vertical displacements were applied on the top model boundary incrementally until the system completely failed. Figure 3 illustrates the contour of damage and fracture in the bicrystal system at the onset of total failure for different prescribed levels of He pressure. Damage is described by a failure indicator (damage variable) of the CDM model. A FE fails if the failure indicator is equal to 1. Figure 3 shows an important effect of He pressure on the damage and fracture pattern in the system. At high He pressure, damage and fracture are more localized in the central region while at lower He pressure damage and fracture tend to propagate along ±45° directions and also toward remote areas from the open sphere.

The most important results from these FE analyses using CDM are the determination of the effects of He bubbles on the stress-strain response of the bicrystal system as shown in Figures 4a and 4b. Figure 4a shows the predicted equivalent Von Mises stress versus applied strain for increasing levels of He pressure. First, even without He, the presence of vacancies at the GB reduces its strength and ductility significantly. With increasing He pressure there is a gradual reduction of both failure strain and strength. In Figure 4a, at 26 GPa He pressure, the stress-strain response exhibits limited ductility. To illustrate the strength reduction due to increasing He bubble pressure, Figure 4b provides the equivalent Von Mises fracture stress (the peaks of the curves in Figure 4a) as a function of He bubble pressure. As mentioned earlier, the strength of the system with a clean GB is significantly higher than a system with vacancies. However, Figure 4b indicates that for small to moderate He pressures (< 12 GPa), the effects of He bubbles on the material strength is rather small, but this effect becomes more and more pronounced at higher He pressures. We also conducted similar analyses for a bicrystal system with four vacancies and the results for the equivalent Von Mises stress at fracture are given in Figure 4. As expected, increasing the number of vacancies further reduces the strength of the system. However, it is necessary to use a model with larger dimensions to investigate bubbles with larger number of vacancies.

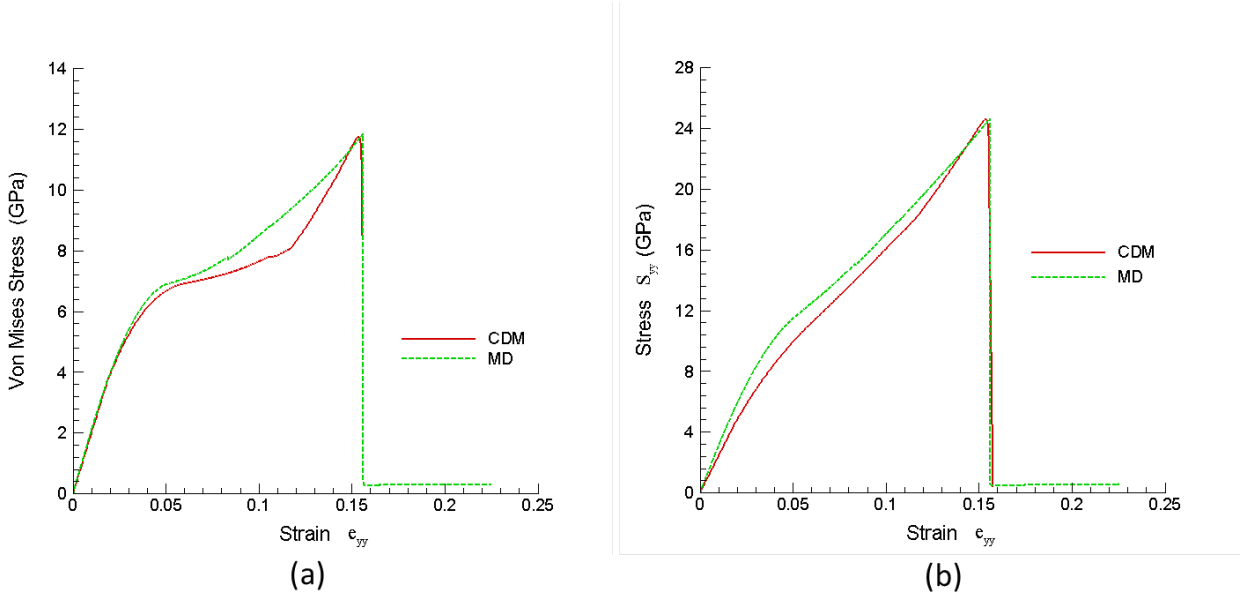

Figure 2. (a) Von Mises stress vs. applied strain e_{yy}, and (b) Stress S_{yy} vs. applied strain e_{yy} predicted by FE analysis using CDM compared to the corresponding MD data [1-2].

Conclusions

During this report period, important progress has been made to develop a mechanistic FE approach informed by MD data to investigate the effects of He bubbles on the stress-strain behavior of an α-Fe bicrystal system. The analysis results using this approach show an important effect of vacancies and He pressure at high levels that reduce material ductility and strength substantially. Current model predictions show good agreement with MD results for the analogue system reported in [1]. The developed approach appears to be very efficient in terms of computation time compared to MD simulations. Thus, it can serve as a very good complimentary approach to MD simulations to study He bubbles or other radiation effects on the material integrity.

Future Work

There is a need to further assess the material stress-strain response through truly uniaxial simulations. To this end we will perform similar MD analyses of larger bicrystal systems subjected to purely uniaxial loading.

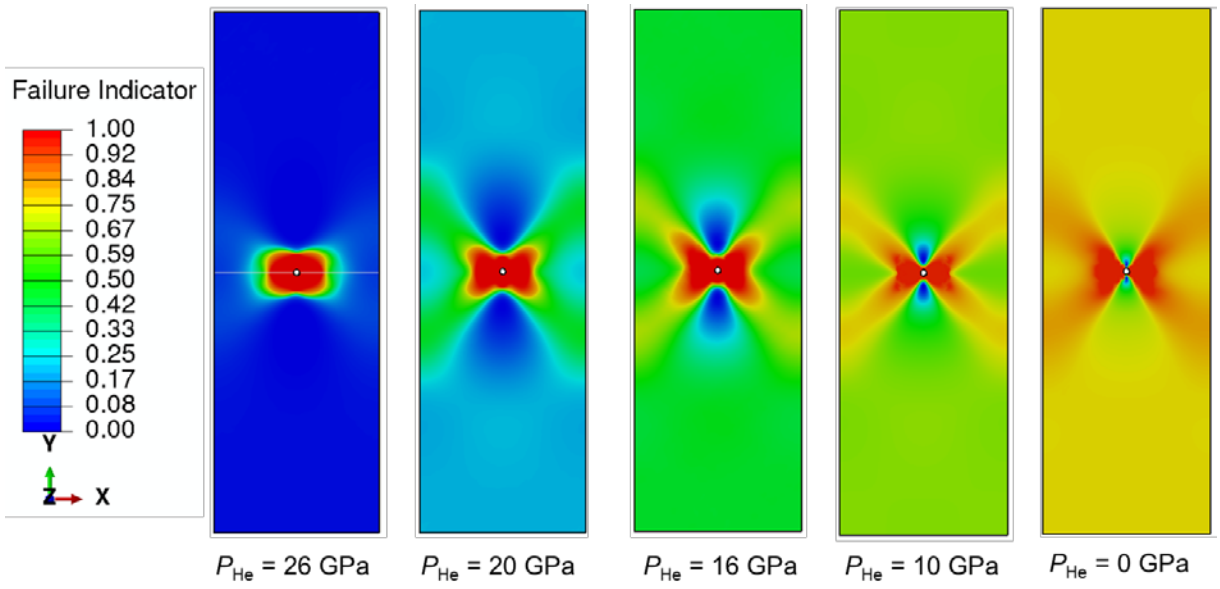

Figure 3. Damage distributions depicted by the failure indicator (1: failed, 0: undamaged) for different levels of He pressure in the bicrystal system with 2 vacancies.

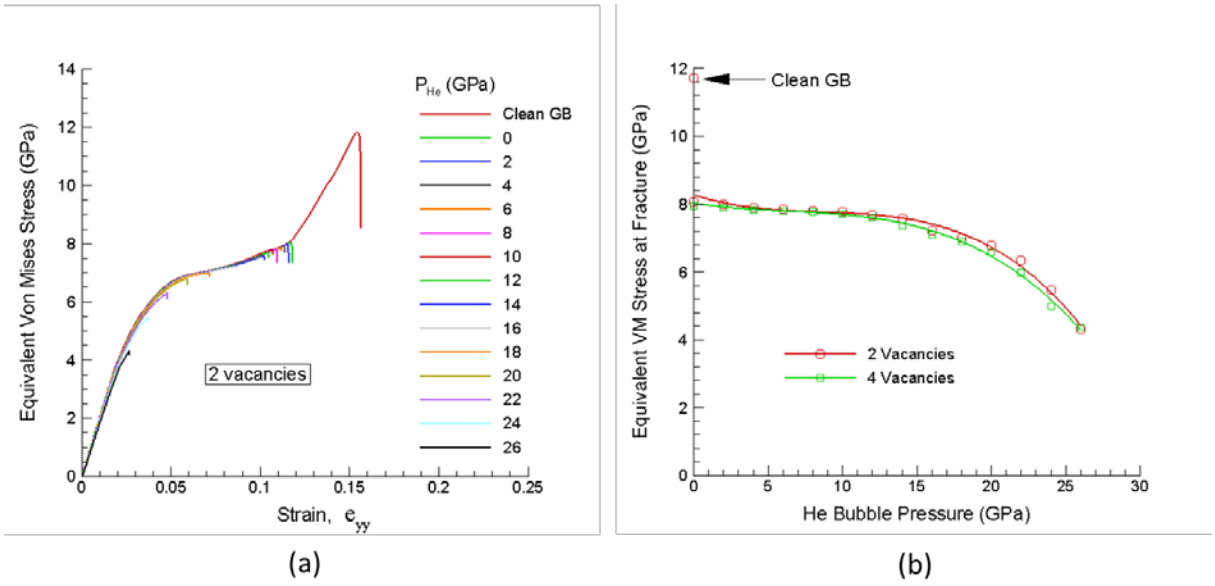

Figure 4. (a) Equivalent Von Mises stress vs. applied strain, and (b) Equivalent Von Mises stress at fracture as a function of the He bubble pressure predicted by the FE analysis using CDM.

References

[1] J. Shi, L. Peng, M. Ye, F. Gao, IEEE Trans. Plasma Sci. 45(2) (2017) 289-293.
[2] F. Gao, *Personal communication*.
[3] A. Kohyama, A. Hishinuma, D.S. Gelles, R.L. Klueh, W. Dietz, K. Ehrlich, J. Nucl. Mater. 233–237 (1996) 138–147.
[4] N. Baluc, R. Schaublin, C. Bailat, F. Paschoud, M. Victoria, J. Nucl. Mater. 283–287 (2000) 731–735.
[5] X. Jia, Y. Dai, J. Nucl. Mater. 323 (2003) 360–367.
[6] F.A. Garner, Materials Science and Technology, Vol. 10A, VCH, Germany, 1994 (Chapter 6).

[7] H. Trinkaus, J. Nucl. Mater. 133–134 (1985) 105–112.
[8] C.C. Fu, F. Willaime, Phys. Rev. Lett. 92 (17) (2004) 175503.
[9] Yang, L., F. Gao, Z.Q. Zhu, S.M. Peng, X.G. Long, X.S. Zhou, H.L. Heinisch, R.J. Kurtz, X.T. Zu, J. Nuc. Mater. 441 (2013) 6.
[10] Yang, L., H.Q. Deng, F. Gao, H.L. Heinisch, R.J. Kurtz, S.Y. Hu, Y.L. Li, X.T. Zu, Nucl. Inst. Meth. Phys. Res. B 303 (2013) 68.
[11] Heinisch, H.L., Gao, F., Kurtz, R.J., Phil. Mag. 90 (2010) 885.
[12] Yang L., Zu, X.T., Gao, F., Peng, S.M., Heinisch, H.L., Kurtz, R.J., Physica B 405 (2010) 1754.
[13] Yang L, XT Zu, F Gao, HL Heinisch, RJ Kurtz, Nucl. Inst. Meth. Phys. Res. B 267 (2009) 3046.
[14] Zu XT, L Yang, F Gao, SM Peng, XG Long, HL Heinisch, RJ Kurtz, Phys. Rev. B 80 (2009) 0541041.
[15] Yang, L., Zu, X.T., Wang, Z.G., Gao, F., Wang, XY, Heinisch, H.L., Kurtz, R.J., Nucl. Inst. Meth. Phys. Res. B 265 (2008) 541.
[16] Pu, J., Yang, L., Gao, F., Heinisch, H.L., Kurtz, R.J., and Zu., X.T., Nucl. Inst. Meth. Phys. Res. B 266 (2008) 3993.
[17] Yang, L., Zu, X.T., Wang, Z.G., Gao, F., Heinisch, H.L., Kurtz, R.J., Wang, X.Y., Liu, K.Z., J. Nuc. Mater. 374 (2008) 437.
[18] Yang, L., Zu, X.T., Wang, Z.G., Yang, H.T., Gao, F., Heinisch, H.L., Kurtz, R.J., J. of App. Phys. 103 (2008) 063528.
[19] Yang, L., Zu, X.T., Xiao, H.Y., Gao, F., Heinisch, H.L., Kurtz, R.J., Wang, Z.G., and Liu, K.Z., Nucl. Inst. Meth. Phys. Res. B 255 (2007) 63.
[20] Yang, L., Zu, X.T., Xiao, H.Y., Gao, F., Heinisch, H.L., and Kurtz, R.J., Physica B 391 (2007) 179.
[21] Heinisch, H.L., Gao, F., and Kurtz, R.J., J. Nuc. Mater., 367 (2007) 311.
[22] Heinisch, H.L., Gao, F., Kurtz, R.J, Le, E.A., J. Nuc. Mater. 351 (2006) 141.
[23] Yang, L., Zu, X.T., Xiao, H.Y., Gao, F., Heinisch, H.L., Kurtz, R.J., Liu, K., App. Phys. Lett. 88 (9) (2006) 091915.
[24] Yang, L., Zu, X.T., Xiao, H.Y., Gao, F., Liu, K., Heinisch, H.L., Kurtz, R.J., Yang, S.Z., Mater. Sci. Eng. A 427 (2006) 343.
[25] T. Seletskaia, Yu.N. Osetsky, R.E. Stoller, G.M. Stocks, J. Nucl. Mater. 351 (2006) 109–118.
[26] K. Morishita, R. Sugano, B.D. Wirth, J. Nucl. Mater. 323 (2003) 243–250.
[27] L. Ventelon, B. Wirth, C. Domain, J. Nucl. Mater. 351 (2006) 119–132.
[28] G. Lucas, R. Shäublin, J. Phys.: Condens. Matter 20 (2008) 415206.
[29] N. Juslin, K. Nordlund, J. Nucl. Mater. 382 (2008) 143–146.
[30] G. Lucas, R. Schäublin, J. Nucl. Mater. 386–388 (2009) 360–362.
[31] Deng, H.Q., W.Y. Hu, F. Gao, H.L. Heinisch, S.Y. Hu, Y.L. Li, R.J. Kurtz, J. Nuc. Mater. 442 (2013) S667.
[32] Heinisch HL, F Gao, RJ Kurtz, in proceedings ASTM 23rd Symposium on Effects of Radiation on Materials, (2009) 190.
[33] Gao F, HL Heinisch, RJ Kurtz, J. Nuc. Mater. 386 (2009) 390.
[34] Kurtz RJ, HL Heinisch, F Gao, J. Nuc. Mater. 382 (2008) 134.
[35] Gao, F., Heinisch, H.L., and Kurtz, R.J., J. Nuc. Mater. 367 (2007) 446.
[36] Heinisch, H.L., F. Gao, R.J. Kurtz, J. ASTM Inter. 4 2007).
[37] Gao, F., Heinisch, H.L., Kurtz, R.J., J. Nuc. Mater. 351 (2006) 133.
[38] Kurtz R.J., Heinisch H.L.,, J. Nuc. Mater. 329-333 (2004) 1199.
[39] T. Suzudo, H. Kaburaki, M. Yamaguchi, J. Nucl. Mater. 417 (2011) 1102–1105.
[40] T. Suzudo, T. Tsuru, M. Yamaguchi, H. Kaburaki, J. Nucl. Mater. 442 (2013) S655–S659.
[41] D. Terentyev, X. Hea, A. Serra, J. Kuriplach, Comp. Mater. Sci. 49 (2010) 419–429.

8.6 MECHANICAL PROPERTIES AND RADIATION EFFECTS IN FUSION MATERIALS—Yury Osetskiy (Oak Ridge National Laboratory)

Extended abstract of research in progress.

The purpose of this research is understanding low-level mechanisms of radiation damage and mechanical properties degradation of fusion materials under fusion irradiation conditions. We use molecular dynamics (MD) to study interactions between moving dislocations and important for fusion materials obstacles that are oxide particles, secondary phase precipitates, voids and He-filled bubbles. A large database of MD results is accumulated and is under treatment now using theoretical models for materials plasticity. We are investigating a number of effects that include such effects as applied strain rate, ambient temperature and dislocation-obstacle interaction geometry. At this stage, we have investigated effects of He pressure inside bubbles to microstructure evolution and mechanical properties.

The He bubbles equilibrium was studied earlier in [1] and we have noticed that He filled bubbles always has a positive binding with He atoms. Even highly over-pressurized He-vacancy clusters prefer to attract He atoms and emit interstitial atom as was observed in *ab initio* modeling [2]. At this stage of our research we have investigated larger scale effects related to over-pressurized state of He filled bubbles in Fe.

Several effects were observed and studied using large scale MD modeling together with Oak Ridge National Laboratory (ORNL)-derived potential for Fe-He interactions [1]. The most significant to the microstructure evolution is a spontaneous formation of dislocation network near the over-pressurized bubbles. The effect depends on the bubble size and He/VAC ratio. Examples are presented in Figure1. This effect predicts that under the conditions of continuous irradiation and fast He production He filled bubbles will not only grow (due to vacancy supersaturation) but may also create a new dislocation network. The probability to emit dislocations at the same level of He/VAC ratio increases for large bubbles as demonstrated in Figure1. Small bubbles, 2-4nm, emit dislocation when the flow of He atoms significantly exceeds that of vacancies. Large bubbles, ≥6nm, can emit dislocations even when the flow of He atoms is weaker than that of vacancies, i.e. at He/VAC<1. The expected effect is a formation of a new network with mainly edge-type dislocations that should contribute into the whole process of microstructure evolution. For example, existence of edge dislocation network near bubbles decreases a flow of point defects to bubble and therefore increasing their effective He/VAC ratio. The general effect is an enhancement of defect recombination through increasing of the total dislocation network length.

References

[1] R.E.Stoller and Yu.N.Osetsky, An atomistic assessment of helium behavior in iron, *J.Nuclear. Mater,* **455** (2014) 258-262.

[2] T. Seletskaia, Yu.N. Osetsky, R. E. Stoller and G. M. Stocks, Calculation of helium defect clustering properties in iron using a multi-scale approach. *J. Nucl. Mater.* **351** (2006) 109-118.

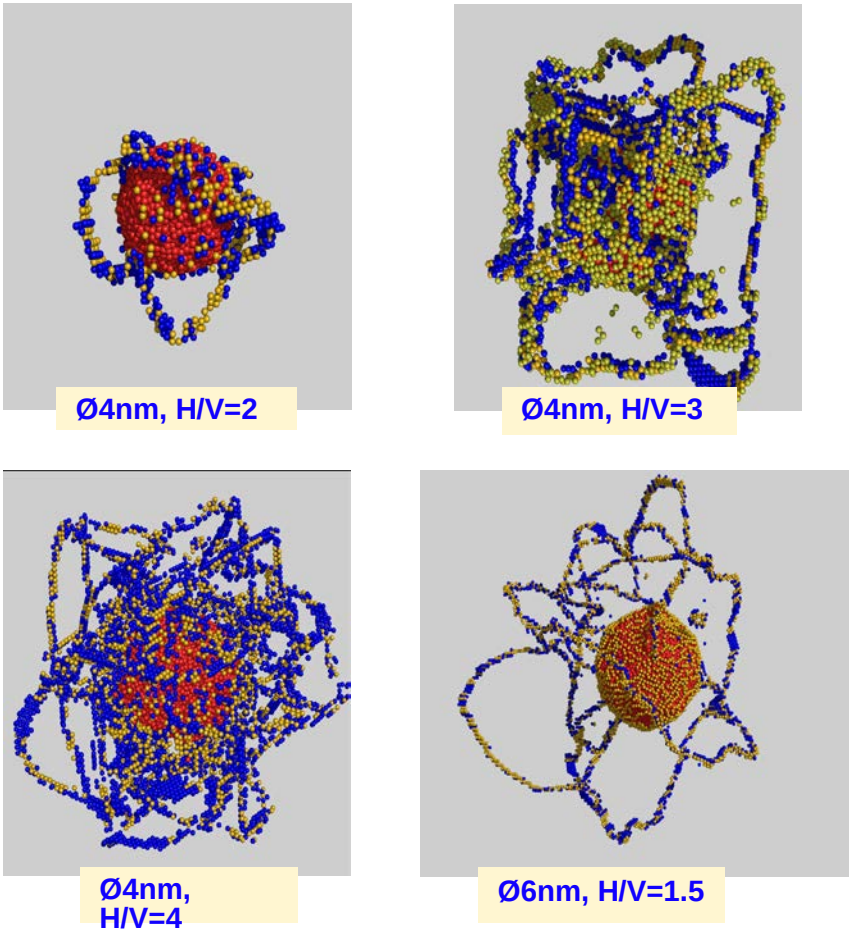

Figure 1. Equilibrium configuration of 4 and 6 nm bubbles with different He/VAC ratio modelled at 300K. Red circles are He atoms, blue and yellow are atoms (with different than perfect bcc lattice coordination numbers) belonging to the bubble surface or/and the edge dislocation core formed around the bubble during equilibration.

9. FUSION SYSTEM DESIGN

No contributions this reporting period.

10. IRRADIATION METHODS, EXPERIMENTS AND SCHEDULES

10.1 STRAIN EVALUATION USING A NON-CONTACT DEFORMATION MEASUREMENT SYSTEM IN TENSILE TESTS OF IRRADIATED F82H AND 9Cr ODS STEELS—H. Sakasegawa, T. Kato, H. Tanigawa, M. Ando (National Institutes for Quantum and Radiological Science and Technology), X. Chen, J.W. Geringer, Y. Katoh (Oak Ridge National Laboratory)

OBJECTIVE

It is important to obtain more accurate strain data in post irradiation tensile testing for the current design activity of fusion blankets using reduced activation ferritic/martensitic steels as their structural material. This is because they show significant irradiation embrittlement accompanying irradiation hardening within a few dpa at low temperatures. In this work, we developed a non-contact deformation measurement system to evaluate the irradiation effect on material ductility. This work is part of the United States Department of Energy (US DOE) – National Institutes for Quantum and Radiological Science and Technology fusion materials collaboration.

SUMMARY

In our developed non-contact deformation measurement system, the distance between painted marks within the specimen gauge section was measured using a high resolution video camera to evaluate the specimen deformation during room temperature tensile testing. The test materials were F82H and 9Cr oxide dispersion strengthened (ODS) steels irradiated in High Flux Isotope Reactor (HFIR) up to ≈ 71 dpa at about 573 K. The system yielded accurate stress strain curves without deformations other than the specimen gage section, and the elongation was less than that calculated from cross-head displacement. This system can contribute to expanding the technically reliable database for the design activity of fusion reactor blanket, including the effects of irradiation on tensile properties.

PROGRESS AND STATUS

Introduction

Post irradiation tensile testing is the most fundamental method to evaluate mechanical properties after irradiation. In the past, changes in material strengths such as yield and ultimate tensile strength after irradiation have been measured without major issues, but it has been hard to obtain accurate strain measurements from small size specimens. This is because the specimen size is often too small to utilize the conventional strain gages used for full size specimens. Instead, cross-head displacement has alternatively been used to measure strain. However, the strain calculated from cross-head displacement generally includes deformation from specimen shoulders, fixtures, and the test frame in addition to the deformation from the specimen gage section. In the current design activity for fusion blankets using reduced activation ferritic/martensitic steel as their structural material, it is desired to obtain more accurate strain data. This is because significant irradiation embrittlement accompanying irradiation hardening has been observed within a few dpa at temperatures less than about 573 K, which is near the lower operation temperature of the Japanese water cooled blanket design [1]. In particular, the uniform elongation (UE) of F82H was almost zero after irradiation [2]. It is indispensable to accurately evaluate the irradiation effect on material ductility. In this work, we developed a non-contact deformation measurement system to meet this need.

Experimental Procedure

Figures 1 (a) and (b) show the non-contact deformation measurement system (NCDMS) before and after installation into the hot cell 2 at Building 3025E. Its specifications are listed in Table 1. The video camera is a 2,100 million-pixels monochrome camera and has resolution high enough to properly observe the entire gauge section of SS-J3 type tensile specimens. The camera frame rate is two frames per second. The lens is telecentric with the chief ray parallel to its optical axis. The telecentric lens is preferable for dimension measurement, since this gives high measurement accuracy in depth of field and there are no changes in the observed image between centeral and peripheral portions. The light for the camera is co-axial light-emitting diode (LED) and can be easily attached to the side port of telecentric lens. The video camera and lens with LED light were attached to the camera mount made for the tensile test frame inside hot cell. The position of video camera can be adjusted in three dimensions, horizontal, vertical and front-back positions using positioning screws which can be

adjusted with manipulators. This allows analyzable images of specimen to be taken during tensile testing. When the video camera is not in use, the mount arm rotates and the video camera is kept away from the irradiated specimen to prevent it from receiving undesired radiation damage.

Figure 2 shows the analysis procedure applied in this work. Two visible marks were painted on the specimen gauge using a permanent paint marker pen. The distance between the two paint marks was measured to calculate strain, as shown in Figure 2 (a). Figure 2 (b) shows an example of data recorded. The measured pixel distance and the calculated strain are shown on the left and right vertical axes, respectively. It should be noted that two regions, one for lower strain rate and the other for faster strain rate, were found during tensile testing, though the cross-head speed was set at a constant speed of 0.508 mm/min. The former and latter regions correspond to elastic and plastic regions, respectively. The lower strain rate in the elastic region obviously indicates that the cross-head displacement includes deformations from specimen shoulders, fixtures, and the test frame in addition to the deformation from the specimen gauge section. This explains why the stress-strain slope based on the strain calculated from cross-head displacement has been much lower than the expected value of Young's modulus value.

The materials tested were F82H IEA, mod 3, 1.4% Ni58, 1.4% Ni60 heats, and JNC 9Cr ODS steel developed at Japan Atomic Energy Agency (formerly Japan Nuclear Cycle Development Institute, JNC). The chemical composition and heat treatment conditions are given in Table 2. F82H mod 3 heat contains higher tantalum than IEA to obtain better irradiation resistances and high temperature mechanical properties. The F82H 1.4% Ni58 heat was prepared to study transmutation helium and the heat with Ni60 is used to study the alloying effect of Ni in F82H. Their tensile specimens of SS-J3 type were irradiated in HFIR JP29 capsule from January 2005 to July 2013. F82H IEA and 1.4% Ni58 heats were irradiated up to 70 dpa and mod 3 and 1.4% Ni60 heats were irradiated up to 71 dpa, with damage levels calculated from the dosimetry analysis [3]. The irradiation temperature was 574 K on average, based on the thermometry analysis and to the same as the planned irradiation temperature of 573K [4]. The JNC 9Cr ODS was irradiated up to 48 dpa at 606 K, though its planned irradiation temperature was 773 K [3, 5]. The reason why the analyzed irradiation temperature was different from the planned one is still being investigated, focusing on the capsule design and the possible deformation under irradiation during the long irradiation period of eight years. It is worth evaluating the tensile property of JNC 9Cr ODS steel applying the NCDMS for obtaining a fundamental understanding of the irradiation behavior of 9Cr ODS steel. Room temperature tensile test was performed with shoulder loading at a constant cross-head displacement speed of 0.508 mm/min, as mentioned above.

Results

Figure 3 shows the result of room temperature tensile tests of (a) F82H IEA, (b) F82H mod 3, (c) F82H 1.4% Ni58, (d) F82H 1.4% Ni60, and (e) 9Cr ODS steels using NCDMS. In the figure, stress-strain curves calculated from cross-head displacement were also shown. The application of NCDMS obviously yielded more accurate stress-strain curves. Total elongation (TE) was less than that calculated from cross-head displacement, which indicates that the deformations other than the specimen gauge section were successfully excluded. Four F82H heats except for 9Cr ODS showed a typical stress strain curve after irradiation with comparable yield stress (YS) and ultimate tensile stress (UTS) values, and much shortened UE [2, 6]. In Figure 3 (a) of F82H IEA heat, the modulus of 217 GPa for unirradiated F82H can fit data points in the elastic region [7], though some scatter is seen in the points. In Figure 3 (b) of F82H mod 3 heat, the same modulus can also fit data points in the elastic region with less scattered points compared to F82H IEA heat. In the case of F82H mod 3 heat, the paint marks on the specimen gauge section gave the better contrast easily detectable by NCDMS, as shown in Figure 2 (a). The more ideal the marks are painted on the specimen gauge, the more accurately the analysis can be performed with less scatter. However, irradiated specimens were often partly or entirely oxidized and had darkened surfaces, which makes it difficult to paint ideal marks using hot cell manipulators. It is an important issue which needs further developments to clearly paint marks on the surface of irradiated specimen in future work. In Figure 3 (c) of F82H 1.4% Ni58 heat, an unexpected stress-strain curve was obtained with lower tensile strength and lower elongation [2, 5, 6] and the measured Young's modulus was 107 GPa. This is discussed below. In Figure 3 (d) of F82H 1.4% Ni60 heat, though some plots deviate from the modulus line, the Young's modulus of F82H can also fit data plots.

In Figure 3 (e) of 9Cr ODS steel, the reported modulus of 209 GPa for unirradiated 9Cr-ODS steel can fit the data points of the irradiated sample in the elastic region [8]. Compared to the four F82H heats, it shows a greater UE and there is no sharp drop in stress after reaching UTS, which are favorable tensile properties as a structural material. However, the TE is lower than the other steels.

Table 3 summarizes the tensile properties of YS, UTS, UE, and TE. In this work, TE values have uncertainty of a few percent in absolute value due to measurement uncertainty in the distance between painted marks. It is important to develop a mark painting method that can be used with manipulators inside the hot cell to obtaining more accurate results in future work. Clearly detectable contrast of the reference marks can reduce such errors. F82H IEA heat shows more irradiation hardening than F82H mod 3 heat, but their elongations are comparable. The result for F82H 1.4% Ni58 needs attention before comparing the results of Ni58 and Ni60 doped F82H heats to establish transmuted helium effects, since its stress strain curve was unexpected.

Figure 4 shows detailed information about the fracture behavior of F82H 1.4% 58Ni. Necking was observed at the portion near the upper fixture edge, as shown in Figure 4 (a), and the specimen ruptured there with less reduction of area, as shown in Figure 4 (b). Figure 4 (c) shows the distance between the upper and lower fixtures (1) and gauge deformation without the necking portion (2). During tensile testing of the particular specimen of F82H 1.4% Ni58, the fixtures did not move steadily and some fluctuations were observed in the movement. Due to the unstable movement of fixtures, compression deformation was observed for the specimen gauge section. This means that appropriate tensile deformation was not applied due to some misalignments of fixtures and the specimen, which directly ruined the Young's modulus and may invalidate the strength and elongations listed in Table 3 for F82H 1.4% Ni58. Although, it was not possible to study transmuted helium effects in the comparison of Ni58 and Ni60 doped F82H heats in this work, but NCDMS gave the dynamic information of tensile testing and materials fracture behaviors which is helpful for verifying tensile test results.

In future work, the irradiation database of F82H will be expanded by using NCDMS in room temperature tensile tests of other unirradiated and irradiated specimens as well as elevated temperature tensile tests with result from further developments.

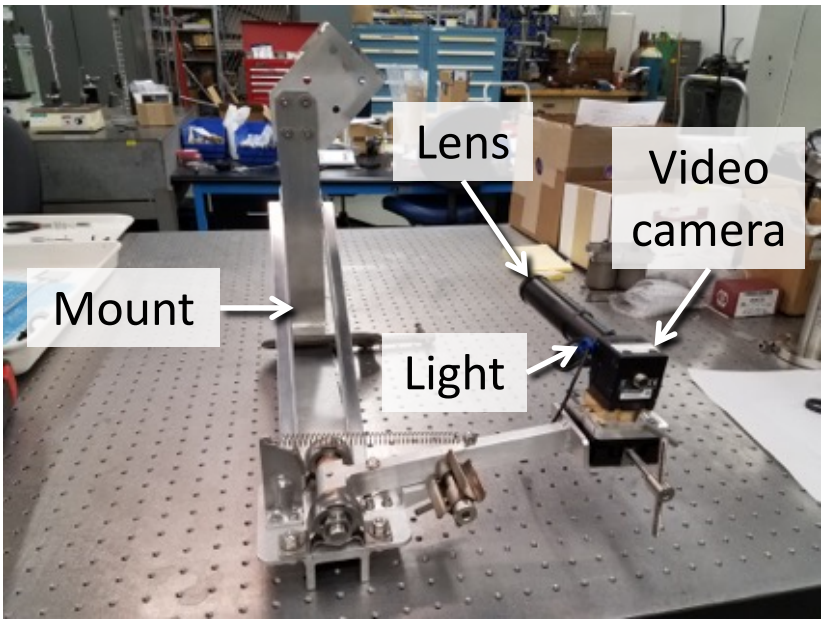

(a) Before installation

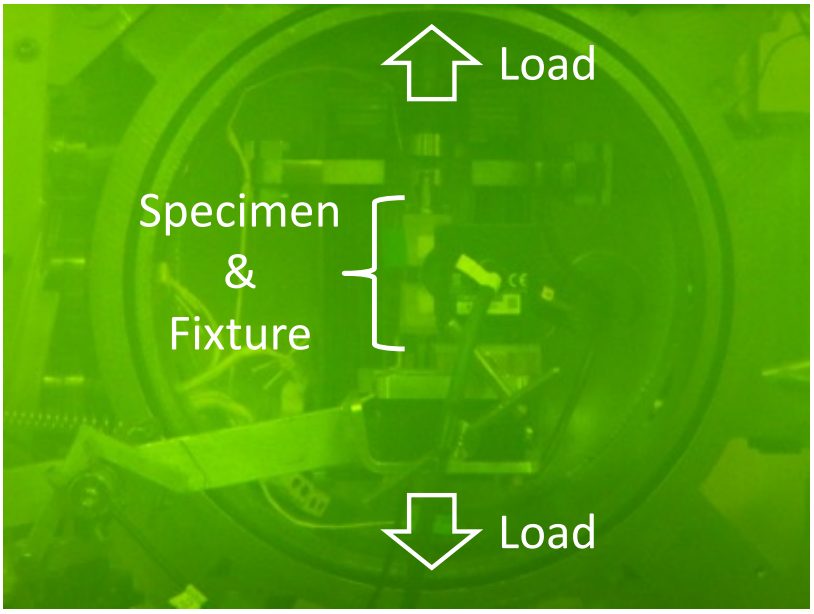

(b) After installation

Figure 1. Non-contact deformation measurement system.

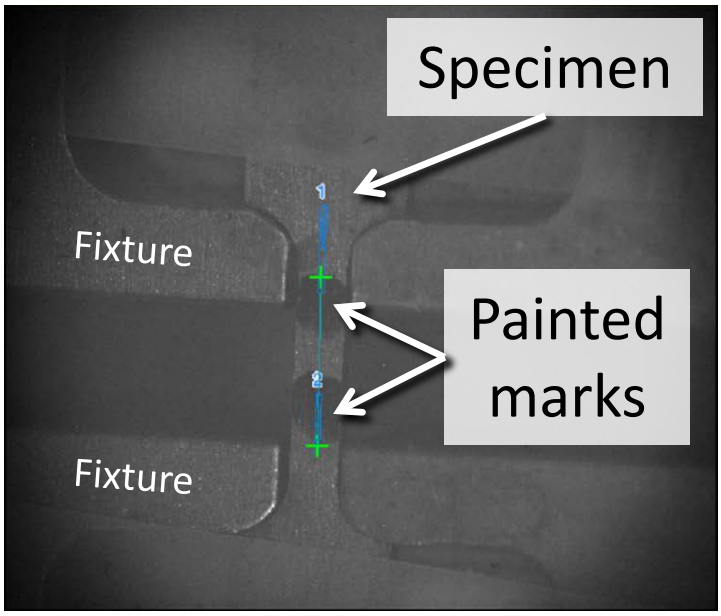

(a) Painted marks on specimen gauge

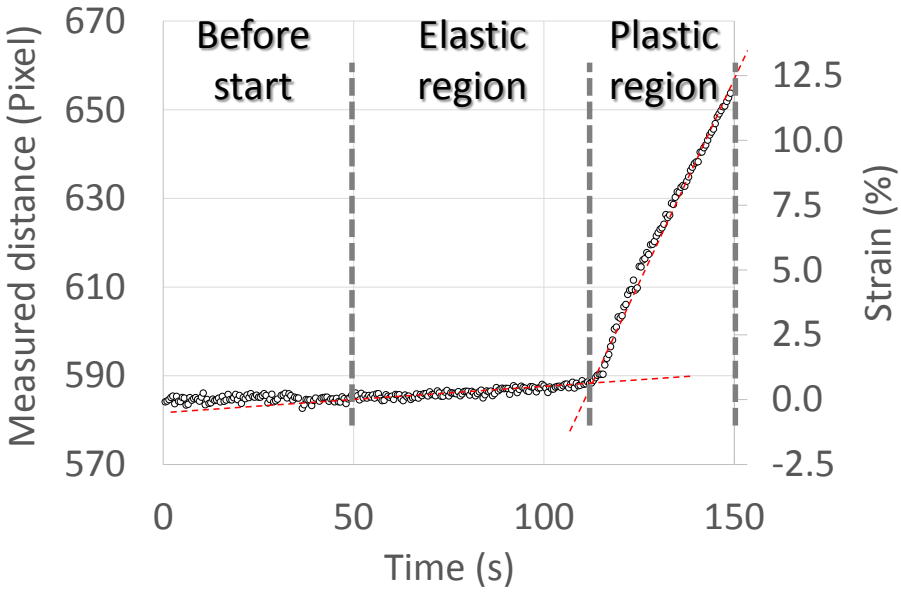

(b) Measured deformation

Figure 2. Analysis procedure for determining tensile strain.

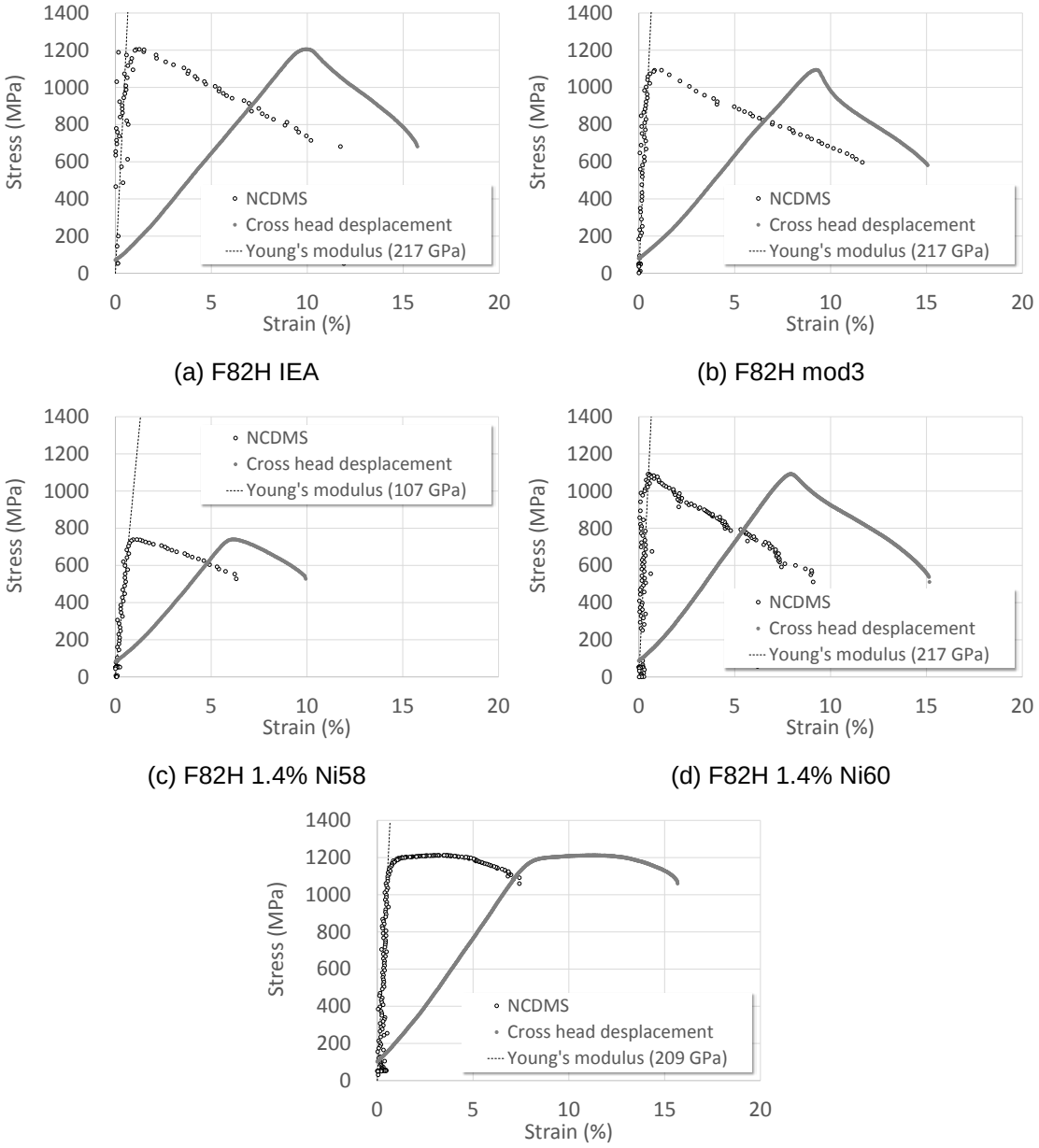

(a) F82H IEA

(b) F82H mod3

(c) F82H 1.4% Ni58

(d) F82H 1.4% Ni60

(e) JNC 9Cr ODS

Figure 3. Room temperature tensile test result for five alloy variants irradiated in HFIR experiment capsule JP29.

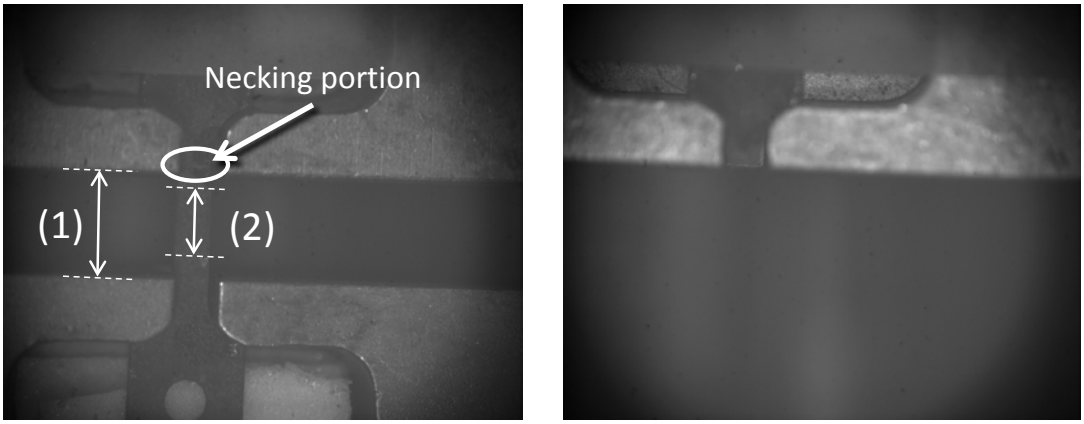

(a) Before rupture (b) After rupture

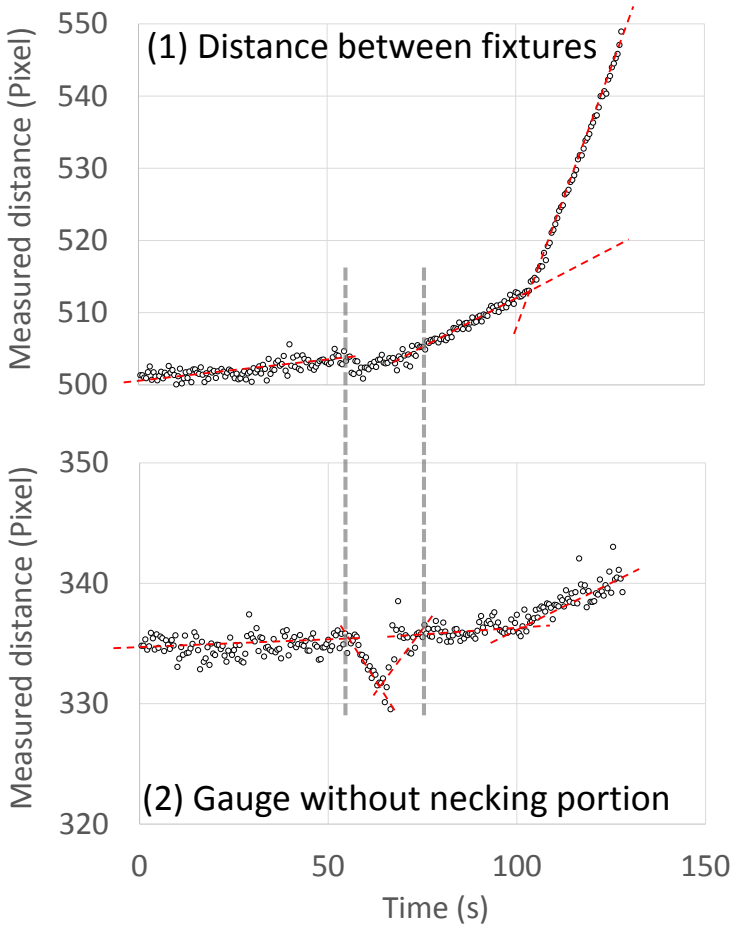

(c) Measured distances

Figure 4. Room temperature fracture behavior of irradiated F82H 1.4% Ni58.

Acknowledgements

This research was sponsored by the National Institutes for Quantum and Radiological Science and Technology (Japan Atomic Energy Research Institute) and the Office of Fusion Energy Sciences, US DOE, under contracts NFE-17-06547 and DE-AC05-OR22725, respectively, with UT-Battelle, LLC.

References

[1] K. Tobita, S. Nishio, H. Tanigawa, M. Enoeda, T. Isono, H. Nakamura, D. Tsuru, S. Suzuki, T. Hayashi, K. Tsuchiya, T. Hayashi, T. Nishitani, and The DEMO design team, “Torus configuration and materials selection on a fusion DEMO reactor, SlimCS”, Journal of Nuclear Materials 386-388 (2009), 888-892.

[2] H. Tanigawa, K. Shiba, A. Möslang, R.E. Stoller, R. Lindau, M.A. Sokolov, G.R. Odette, R.J. Kurtz, and S. Jitsukawa, “Status and key issues of reduced activation ferritic/martensitic steels as the structural material for a DEMO blanket”, Journal of Nuclear Materials 417 (2011), 9-15.

[3] L.R. Greenwood, B. D. Pierson, M. G. Cantaloub, and T. Trang-Le, “NEUTRON FLUENCE MEASUREMENTS AND RADIATION DAMAGE CALCULATIONS FOR THE JP28 AND JP29 EXPERIMENTS IN HFIR”, Fusion Materials Semi-annual Progress Report, DOE/ER-0313 Semi-Annual Progress Reports, (2017), in press.

[4] H. Sakasegawa, H. Tanigawa, T. Hirose, M. Ando, Y. Katoh, C.O. Stevens, and M.R. McAlister, “TENSILE FRACTURE MECHANISM OF HFIR-HEAVILY-IRRADIATED F82Hs”, DOE/ER-0313 Semi-Annual Progress Reports, 59 (2015) 22-25.

[5] H. Sakasegawa, M. Ando, H. Tanigawa, T. Hirose, X. Chen, J.W. Geringer, and Y. Katoh, “IRRADIATION HARDENING BEHAVIOR OF F82H IN JP28 AND 29”, Fusion Materials Semi-annual Progress Report, DOE/ER-0313 Semi-Annual Progress Reports (2017), in press.

[6] H. Tanigawa, E. Gaganidze, T. Hirose, M. Ando, S.J. Zinkle, R. Lindau, and E. Diegele, “Development of benchmark reduced activation ferritic/martensitic steels for fusion energy applications”, Nuclear Fusion 57 (2017), 092004.

[7] K. Shiba, A. Hishinuma, A. Tohyama, and K. Masamura, “Properties of Low Activation Ferritic Steel F82H IEA heat - Interrim Report of IEA Round-robin Tests (1) -”, JAERI Tech 97-038 (1997).

[8] T. Kaito, S. Mizuta, T. Uwaba, S. Otsuka, and S. Ukai, “The Tentative Materials Strength Standard of ODS Ferritic Steel Claddings”, JNC-TN9400 2005-015 (2005).

10.2 HFIR IRRADIATION EXPERIMENTS—J.P. Robertson, Y. Katoh, J.L. McDuffee, C. Bryan (Oak Ridge National Laboratory)

SUMMARY

Neutron irradiation experiments were performed in support of the research and development of fusion reactor materials using various materials irradiation facilities in the High Flux Isotope Reactor (HFIR).

The HFIR operated for three complete cycles between July 1 and December 31, 2017. It completed Cycle 473 on July 8 (2149.23 MWD), Cycle 474 on August 19 (2112.43 MWD), Cycle 475 on September 29 (2070.56 MWD), and Cycle 476 on December 8, 2017 (2051.05 MWD).

During this time frame, 11 target zone rabbit capsules underwent HFIR irradiation. These capsules are listed in Table 1 along with condensed information on material, specimen type, temperature, fluence, and period of irradiation.

The full length capsule RB-19J contained tungsten and F82H alloys in various specimen configurations, operating at 250/300, 500, 800, or 1200°C. The experiment used a Gd thermal neutron shield. It ran for four cycles, completing irradiation at the end of Cycle 469. It was transported to the Building 3525 hot cells and disassembled into its component specimen holders in December 2017.

Table 1. HFIR fusion materials program rabbit capsules continuing irradiation into 2018

Experiment Designation	Primary Materials	Specimen Types	Irradiation Temperature (°C)	Max Exposure (dpa)	Number of Reactor Cycles	HFIR Cycles Start – End		
F13A6	FeCrAlY Steel	Bend bar	300	50	29	451	-	505
JCR11-05	SiC/SiC	bend bars	950	200	115	444	-	590
JCR11-07	SiC/SiC	Mini bend bars	950	100	47	444	-	523
JCR11-08	SiC/SiC	Mini bend bars	950	200	85	444	-	561
SCF8	SiC/SiC	Bend bars	600	100	45	457	-	521
SCF9	SiC/SiC	Bend bars	600	200	90	457	-	566
SCF11	SiC/SiC	Bend bars	950	100	57	458	-	533
FHC01	F82H	Creep tube	300	3.7	2	475	-	476
FHC02	F82H	Creep tube	300	3.7	2	475	-	476
FHC03	F82H	Creep tube	300	3.7	2	475	-	476
FHC04	F82H	Creep tube	300	3.7	2	475	-	476